Università degli Studi di Trieste
Scuola di dottorato in Fisica
XXIV Ciclo del Dottorato di Ricerca in Fisica

Tesi di Dottorato

Non-equilibrium phase diagram of $Bi_2Sr_2Y_{0.08}Ca_{0.92}Cu_2O_{8+\delta}$ cuprate superconductors revealed by ultrafast optical spectroscopy

Federico Cilento

Responsabile del Dottorato di Ricerca:
Prof. Paolo Camerini

Relatore e Supervisore:
Prof. Fulvio Parmigiani

Anno Accademico 2010/2011

Contents

Chapter 1

Introduction

1.1 Introduction

100 years after K. Onnes observed the superconductivity phenomenon in Mercury [142], this phase of matter remains one of the most fascinating, mysterious, debated and intriguing problems in the condensed matter physics. From its discovery and for many decades, little progressess have been made, and the maximum transition temperature to the superconducting state was set around 20 K. In 1957 Bardeen, Cooper and Schrieffer formulated the BCS theory, capable to explain the physical behavior and the microscopic mechanisms behind these conventional superconductors. Only in 1986 Bednorz and Muller [21] discovered that layered copper oxide compounds could sustain superconductivity at unsuspectedly high temperatures ($\sim$30 K). Soon after, the critical temperature T_c of these doped copper oxide-based compounds exceded the boiling temperature of the liquid nitrogen and soon after it raised singnificantly above 100 K. For this reason these materials are nowadays known as high temperature superconductors (HTSCs). Among high temperature superconductors, beyond cuprates, other superconducting families exist: pnictides and calchogenides (Iron based superconductors, discovered in 2006 [103]), Fullerenes (Cs_3C_{60} has T_c=38 K), Heavy Fermion Systems (UPt_3) and Organic Superconductors. The term high-temperature in this classification refers mainly to the unconventional physics beyond them, rather than to the actual T_c, that is often lower than that of conventional superconductors. Within this thesis work, however, the term high temperature superconductors / superconductivity will be referred to cuprates. The high transition temperature of cuprates cannot be explained in the frame of the BCS theory and today, 25 years later, a comprehensive microscopic theory capable to explain the phenomenon of superconductivity in copper-oxide based superconductors is still lacking. This despite the huge efforts of the scientific community to solve this intriguing problem. Nowadays, more than 100.000 scientific papers related to the superconductivity has been published since 1911, and new interesting experimental findings are paving the

road to the knowledge of the HTSCs physics.

Following a novel approach started about 10 years ago, my PhD thesis faces the high-temperature superconductivity problem from the perspective of non-equilibrium physics.

High-temperature superconductors obey to the general electro-dynamics phenomenology of the conventional superconductors, but the microscopic mechanisms that give rise to the superconducting state remain an open question.

Before discussing this problem, let me remind here that the key breakthrough in understanding the mechanism leading to superconductivity was obtained by L. Cooper in 1956 [40]. An intuitive and over-simplified picture can be gained by considering that an electron moving through a crystal lattice attracts the positively charged ions, while a second electron can feel a surplus of positive charge from which it is attracted. If the the attractive potential is larger than the Coulomb repulsive potential between the two electrons, then an electron-electron effective attractive interaction is established. Electrons are thus coupled, forming bound pairs known as Cooper Pairs (CPs). In BCS systems, the pairing is mediatd by phonons (i.e., lattice vibrations). To gain the lowest energy state, the two paired electrons must have opposite spin (S=0). This pairing mechanism has the characteristic of transforming a fermionic particles system into a bosonic particle system obeying to a different distribution statistic. The main result is that an infinite number of particles can occupy the same quantum state. This state is the key element of the superconductivity in condensed matter. In BCS theory, the pairing process and the pairs condensation into a collective state (the superconductive state) extending over macroscopic dimensions are simultaneous effects, to some extents similar to the condensation of bosons in a ground state characterized by a wavefunction extending over macroscopic dimensions, i.e., a wavefunction with a phase coherent over macroscopic lenghtscales.

The phase transition to the superconducting state, occurring at the characteristic temperature T_c, is accompanied by an energy gain for the system, and an energy gap, Δ, opens between the occupied and the unoccupied electronic states. This is the so-called superconducting gap, and its magnitude is equal to the pair binding energy. Δ is of the order of few meV in BCS superconductors [175]. The energy difference between the normal and the superconductive phase is termed condensation energy, and is proportional to $N(E_F)\Delta^2$ ($N(E_F)$ being the density of states at the Fermi Energy). In BCS superconductors, where the pairing is mediated by phonons, the gap is isotropic in the k-space, showing an s-wave like symmetry and a magnitude that depends on the temperature, being zero at T=T_c, and maximum at T=0. The $\Delta(T)$ value is governed by the so-called 'gap equation'.

Instead, for HTSC it is not clear the nature and the origin of the microscopic mechanism leading to an attractive interaction among electrons, to form Cooper Pairs. The phonon mediated attraction, alone, seems not enough to justify such high critical temperatures. The point is whether phonons are involved in the pairing mechanism together with other mediators, or whether the pairing is purely mediated by a bosonic glue of electronic origin. It must be pointed out that, in contrast to BCS superconductors, HTSCs show a pairing gap with a d-wave like symmetry [49].

In order to clarify the microscopic mechanisms leading to high-temperature superconductivity in cuprates, a huge effort has been done in these last decades, using mostly spectroscopies in the frequency domain or other probes at equilibrium. These studies have produced several important information but leaving the main physics behind the HTCS phenomenon unveiled. Only in this last decade, spectroscopies in the time domain have been considered to study the superconducting phase transition out of equilibrium with the aim of identifying, through different lifetimes, mechanisms having close energy scales. In particular, these experiments started by considering that in copper-oxyde based superconductors it exists a clear interplay between high (few eV) and low (few meV) energy scale physics, as evidenced by the spectral weight transfer between interband and intraband spectral regions observed by conventional optical measurements. This behavior, which has only recently been addressed [80], is typical of HTSC, whereas it is absent in conventional superconductors, where the spectral weight removed from the gap spectral region is enterely recovered by the condensate contribution at zero frequency.

In addition, for HTSC also the normal state is not completely understood. In fact, the ground state is a non-Fermi Liquid. HTSC are strongly correlated electronic materials, and the strong electronic correlations make them charge-transfer insulators, when undoped.

The nature of the pseudogap phase and of the phase diagram of HTSCs (that probably can only be understood together), are the very elusive aspects.

Therefore, here I am going to face the problem of high temperature superconductivity by a non-equilibrium approach, using the ultrafast optical pump-probe technique, in the time and frequency domain. The scope is to disentangle the electronic dynamics from the thermal dynamics, since the first happens on timescales much shorter than thermal heating, being the latter related to the phonons thermalization.

In the recent past, the all-optical pump-probe technique, though powerful in providing information about the temporal dynamics of the excitations underlying the different physical phases under scrutiny, failed to address the microscopic mechanism at the origin of the observed signals and dynamics. The main reason being the lack of energy resolution. Usually, pump-probe measurements have been performed at fixed energy (1.55 eV, i.e., 800 nm, the fundamental of conventional Ti:Sapphire lasers). The knowledge of the dynamics at only one wavelength is not sufficient to explore the microscopic mechanisms at the origin of the time-resolved optical signal. With this thesis work, I tried to overcome this limit.

In fact, an important part of my research has been devoted to develop different pump-probe setups, in which the monochromatic probe has been replaced

by broadband or tunable probe pulses. This novel technique will be termed time-resolved spectroscopy.
This technique allows revealing the quasiparticles dynamics with a spectral resolution typical of the conventional optical spectroscopies. Therefore, these experiments unlocked the gate to observe the time evolution of the dielectric function in the 0.5-2.2 eV spectral range, with a temporal resolution of $\sim$100 fs. The information that can be extracted from such kind of measurements are much more with respect to that achieved by the conventional, one-color time resolved approach.
Thanks to the richness of the non-equilibrium spectroscopic information obtained, I have been able to characterize the three most important phases composing the phase diagram of a copper-oxide based high-temperature superconductor, i.e., the normal state, the pseudogap phase, and the superconducting phase. As a result, an all-optical formulation, based on non-equilibrium spectroscopic measurements, of the phase diagram of a hole-doped copper oxide based superconductor, has been proposed.

1.2 Overview

My PhD thesis work tackles some open questions in the field of unconventional superconductivity in cuprates. The results I obtained come from the experimental evidences emerged by probing different Y-Bi2212 superconducting samples ($Bi_2Sr_2Y_{0.08}Ca_{0.92}Cu_2O_{8+\delta}$, being δ the doping) in the normal, pseudogap and superconducting phases, by the novel time-resolved spectroscopy technique I developed. Each phase is characterized by a peculiar time-resolved optical signal in the time and energy domains. In particular, the following points have been addressed:

- The mechanisms leading to electron pairing and to the formation of Cooper Pairs in HTSCs are object of debate since long time. I analyzed the problem of electron-boson coupling in HTSCs starting from the experimental evidences of time-resolved spectroscopy in the normal state of Y-Bi2212. A clear indication is that electrons are strongly coupled with bosonic excitations of electronic origin, characterized by a small specific heat. The simultaneous analysis of experimental data in both the time and the energy domains revealed that the subset of bosonic excitations of electronic origin can account, alone, for the high critical temperature of the material. This finding suggests that pairing in HTSC is mainly of electronic origin. Possible candidates for the bosons of electronic origin are antiferromagnetic spin flucutations or current loops.

- The pseudogap phase is the most elusive phase of the HTSC phase diagram. Here, by the novel non-equilibrium spectroscopic approach, I disentangled the various effects taking place in this phase, when the system is brought out of equilibrium by an ultrashort laser pulse. In particular, three contributions have been revealed: a thermal heating, a filling of the gap in the density of states, and an intensity-dependent modification of the electron-boson coupling. These effects helps in the interpretation of the nature of the pseudogap. In particular, the fact that the pseudogap is indeed one phase, with relative long-range order, is argued by the evidence of a magnetic excitation mode which originates and couples with electron at temperature T^*, which scales with doping. This T^* line delimits a region of p-T space in which the electron-boson coupling is temperature-dependent.

- In HTSCs, in contrast to BCS superconductors, an interplay between physics at very different energy scales, namely, the one related to the condensate formation, and the one related to interband transitions, has been revealed by static spectroscopies. Nevertheless, the origin of this interplay remained elusive. Here, thanks to the non-equilibrium approach and the spectroscopic information, I have been able to reveal the origin of such interplay. In particular, I demonstrated that two high-energy optical transitions, at 1.5 and 2 eV, are modified by the condensate formation. This finding is precluded to equilibrium techniques, since thermal heating effects overwhelm the small contibution to the signal originating from the condensate formation. Moreover, I revealed that the spectral weight transfer from interband transitions to low-energy scales, accounts for a direct, superconductivity-induced carriers kinetic energy gain in the underdoped side of the phase diagram, which changes in a BCS-like, superconductivity-induced carriers kinetic energy loss in the overdoped side of the phase diagram. This change happens close to the optimal doping level required to attain the maximum T_c.
- Different scenarios exist in the literature about the phase diagram of an High-T_c. In this respect, our findings regarding i) a T^* line delimiting a region with temperature-dependent electron-boson coupling, and ii) a different direction for the superconductivity-induced spectral weight transfer from high- to low-energy scales, changing exactly at the optimal doping level, suggest that the phase diagram of an High-T_c is governed by a quantum critical point at T=0, inside the superconducting dome.

Finally, I briefly summarize the content of the chapters:

- Chapter 2 contains an overview of the basic physics and of the main open questions in the field of HTSCs. In particular, the different scenarios for the copper-oxide-based compounds phase diagrams are discussed.
- Chapter 3 contains a short review of the equilibrium optical properties of HTSCs. The relevant models for the dielectric function are discussed, with particular emphasis on the formalisms of the Extended Drude model (EDM). The main focus is the interpretation of the equilibrium optical properties of cuprate superconductors.

- Chapter 4 reports on the non-equilibrium physics of HTSCs. The established results in the field of time-resolved optics on cuprates are briefly reviewed. The models commonly used to interpret the non-equilibrium dynamics in metals and superconductors in the normal state, namely, the two/three temperature models, are analyzed in detail. Finally, the novel *differential dielectric function approach*, that is at the base of this work, being used to interpret all the experimental evidences, is formulated and commented.

- Chapter 5 describes the different time-resolved setups developed to perform non-equilibrium measurements. The steps toward the implementation of the spectral resolution in addition to conventional time-resolved measurements are presented. In particular, two complementary setups, based respectively on a visible supercontinuum probe pulse and on an infrared tunable probe pulse, are described in detail. Time-resolved optical spectroscopy is presented. Finally, a section aimed at the description of the various methods developed for the characterization of the ultrashort white light pulses concludes this chapter.

- Chapter 6 describes the results of the non-equilibrium spectroscopic technique in the normal state of Y-Bi2212 superconductors. The unambiguous experimental evidence is that, after a time shorter than the electron-phonon thermalization, the observed time-resolved optical signal in the energy domain is only explained by a scenario in which electrons are already thermalized with some bosonic degrees of freedom, having a small specific heat and a strong coupling with the electrons. The transient spectral response is interpreted within the differential dielectric function approach. Through a model constraining the temporal and spectral evolution of the time-resolved optical signal, I proved that the coupling strenght and spectral distribution of these modes is compatible with bosons of electronic origin. This boson subset, alone, justifies the high critical temperature of the compound. This suggests that the pairing in cuprates is mainly of electronic origin.

- Chapter 7 reports on the interpretation of the transient spectral signal observed in the pseudogap phase of cuprates. Here I argue that several spectral contributions, arising from different physical mechanisms, add to produce the observed signal. By disentangling them, I proved that beyond a thermal contribution arising from the simple heating of the system, a transient modification of the glue function and an impulsive closing of the pseudogap gap are enough to reproduce the observed signal. In the pseudogap, the electron-boson coupling is fluence-dependent.

- Chapter 8 reports on the experimental evidences of time-resolved spectroscopy in the superconducting phase of Y-Bi2212. The spectrally and temporally resolved measurements clearly demonstrate that below T_c, two high-energy interband oscillators (at 1.5 and 2 eV) are entangled with the superconducting condensate formation: the interplay between high- and low-energy physics in cuprates is confirmed; moreover, its origin has been revealed. An important result is that the modification of the high-energy states accounts for a superconductivity-induced carriers direct kinetic energy gain, in the underdoped side of the phase diagram, evolving toward a BCS-like carriers kinetic energy loss on the overdoped side of the phase diagram. The transition happens close to the optimal doping level. This information, together with the knowledge of the onset temperature of the temperature-dependent electron-boson coupling, lead us to argue that the High-T_c phase diagram is characterized by a quantum critical point at $T=0$, inside the superconducting dome. The critical line of such phase diagram delimits a region in which the glue function acquires a temperature dependence.

- Chapter 9 finally contains the conclusion of this thesis work, summarizes the most important results and delineates the perspective of this work, with emphasis on the questions that need a further clarification.

Chapter 2

Superconductivity with High Critical Temperature

2.1 Introduction

In this chapter I will briefly describe the electronic structure of copper-oxide based superconductors, that leads to many phenomena, such as the superconductivity at high critical temperature and the pseudogap phenomenon. I will present the leading models and scenarios for the pseudogap phase and the proposed phase diagram of these compounds, which will be relevant in supporting our experimental findings. I will then introduce the formalisms developed to relate the superconducting critical temperature T_c to the electron-boson coupling strength, λ. This chapter ends with a description of the physical properties of $Bi_2Sr_2CaCu_2O_{8+\delta}$ (also termed as Bi2212), and in particular of the Yttrium substituted compound Y-Bi2212, which is the compound investigated in this work.

2.2 Electronic properties of copper-oxide based superconductors

After 25 years have passed since the discovery of high temperature superconductivity in cuprates [21], no consensus has been reached yet on its physical origin. This is due mainly to a lack of understanding of the state of matter from which the superconductivity arises [140]. In optimally (OP) and underdoped (UD) materials, the ground state exhibits a pseudogap at temperatures large compared to the superconducting transition temperature T_c [186, 83]. On the contrary, overdoped (OD) materials do not exhibit a pseudogap. The physical origin of the pseudogap behavior, and whether it constitutes a distinct phase of matter is still an open question.

In spite of the apparent complexity of their unit cell, cuprates turn out to be simple materials from the structural point of view. The structure is composed of Cu-O planes (where each Copper ion is fourfold coordinated with Oxygen ions), which are separated by spacer layers. Despite the complications arising from the different kinds of crystal structures supporting superconductivity, the essential structure for superconductivity at high critical temperature is that of the Cu-O planes. The transition temperature T_c varies considerably from structure to structure, and in general it is higher the more the number of Cu-O planes per unit cell is (this is true up to three Cu-O planes per unit cell). The low energy electronic structure of the planes is characterized by a single energy band [147]. This single two-dimensional energy band near the Fermi Energy is what makes cuprates attractive from a theoretical point of view. From this apparently simple electronic structure, a lot of phenomena arises, as can be argued by looking at the general phase diagram of a cuprate superconductor, presented in Fig. 2.1. Superconductivity is effective in the so-called 'superconducting dome', delimited by the solid blue line. The maximum critical temperature T_c is reached at the so-called optimal doping (OP), p_{opt}. Two regions are naturally defined as the underdoped region (UD, $p<p_{opt}$) and the overdoped region (OD, $p>p_{opt}$).

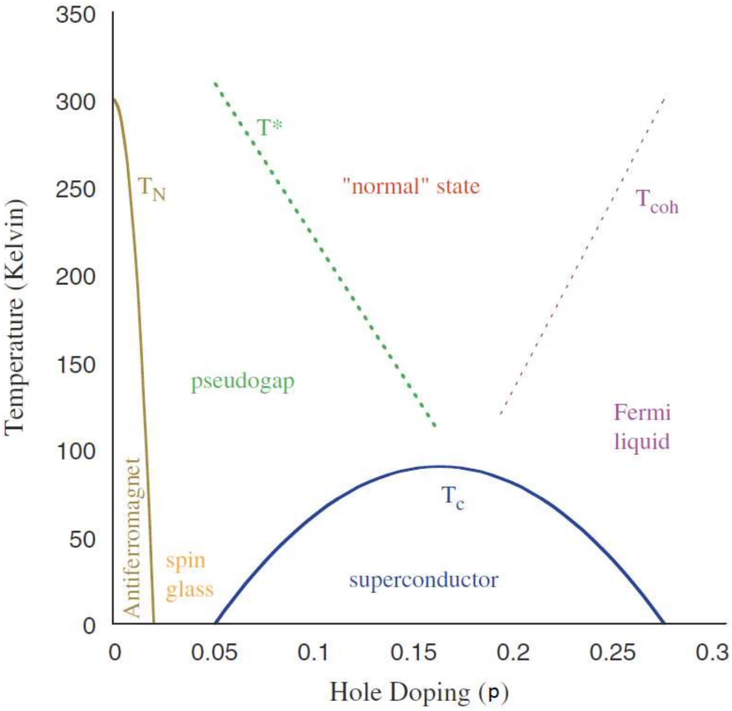

Figure 2.1: The phase diagram of copper-oxyde based superconductors is reprted. p is the number of doped holes per Copper ion. Solid lines represent true, thermodynamic phase transitions, while dotted lines indicate crossover behavior.

Electronic structure of copper-oxide based superconductors

In the parent compound material, that is the undoped material, the lowest-lying energy band is half filled, which corresponds to a d^9 configuration for the Copper ions. This can be justified by recalling the CuO$_2$ coordination for Copper and Oxygen in the Cu-O planes, and that each Oxygen ion is strongly electro-negative, attracting two electrons (O$\rightarrow$O^{2-}, having electronic configuration 2p^6). The result is that Copper ions are left in a 3d^9 configuration. Conventional band theory predicts such compounds to be metals (an odd number of electrons is present at each Copper site), but the material turns out to be an insulator instead. The energy gap for the parent compounds is of the order of 2 eV. The origin of the insulating behavior in strongly correlated electronic materials was well described by N. Mott [135], as an effect of the strong electron-electron correlations.

More generally, all transition metal oxides are insulators. This is due to the fact that the transition metal 3d levels and oxygen 2p levels are separated by an energy larger than the energy spread of these levels, due to band formation. Thus separate 3d and 2p energy bands are obtained. The Coulomb repulsion on the transition metal site is usually very large, and the 3d band undergoes a Mott-Hubbard splitting into an upper and a lower Hubbard bands, separated by an energy scale termed U, which is typically 8-10 eV. The gap is thus of the charge-transfer (CT) type (in contrast to the Mott-Hubbard gap type), separating the filled oxygen 2p valence band from the empty 3d conduction band (the upper Hubbard band) [147]. In cuprates the picture is more involved [161]. Copper ion (d^9) 3d energy level is above, but relatively close to, the Oxygen (p^6) 2p energy level. The tetragonal environment of the Cu ion leads to the single 3d hole having d$_{x^2-y^2}$ symmetry. Thus, in cuprates, the dominant energy is the bonding-antibonding splitting involving a quantum mechanical admixture of the Copper 3d$_{x^2-y^2}$ orbital and the planar Oxygen 2p$_x$ and 2p$_y$ orbitals (as sketched in Fig. 2.2a). The final result is that in the parent compound (undoped material), a half filled band, which is the antibonding combination of these three orbitals, is obtained, while the bonding, non-bonding, and the rest of the Cu and O orbitals are filled. As argued by Anderson [151], it is the copper-oxygen antibonding band which undergoes Mott-Hubbard splitting, forming an insulating gap of the order of 2 eV in the parent compound. The effective U is indeed reduced because of the Copper-Oxygen orbital admixture. Finally, upon doping the compound, a structure reminiscent of the CT gap moves to higher energies, while the gap is filled by states. The Fermi Energy lies in the hybridized Copper-Oxygen band, having a bandwidth of about 1.5 eV. Fig. 2.2b summarizes the density of states in this situation.

For the hole-doped compounds, an important electronic configuration is worth to be described, since it constitutes the ground state. The electronic sys-

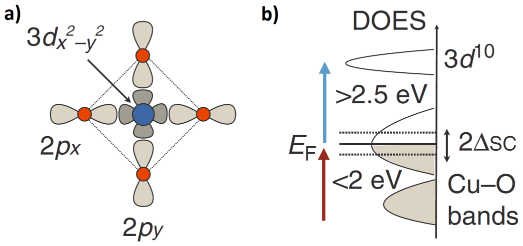

Figure 2.2: a) Cu and O electronic orbitals responsible for the covalent bonding between Copper and Oxygen atoms in the CuO planes. b) Density of states for Cu and O bands. E_F is the Fermi Energy.

tem can gain energy because of the hole hopping between Cu and O orbitals, given by the antiferromagnetic superexchange interaction between the holes of the Cu-O system. In particular, the most stable configuration, known as the Zhang-Rice singlet (ZRS), is obtained as a fully symmetric linear combination of the four oxygen holes states around the Copper site, with the Copper hole spin that couples anti-ferromagnetically to the (shared) Oxygen hole spin. Finally, this singlet state can hop from site to site like a single hole does in a simple single-band Hubbard model [188]. A sketch of the ZRS is reported in Fig. 2.3. Spin-resolved photoemission measurements [23] confirmed that the lowest energy excitations have a singlet nature, providing a direct support to the stability of the Zhang-Rice singlet in hole-doped cuprates.

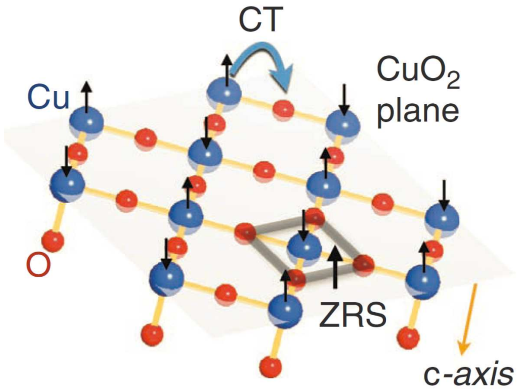

Figure 2.3: The atomic structure of the CuO plane is reported. The Zhang-Rice singlet (ZRS) and the in-plane charge-transfer process between Cu and O atoms is evidenced. Copper atoms are depicted in blue, while Oxygen atoms in red. Arrows indicate the direction of the spin in the antiferromagnetic phase.

Hubbard and t-J models

The Hubbard and the t-J models are the simplest models able to catch the

basic physics of strongly correlated materials.
The electronic hopping from one site to the other, required for conductivity to occur, would cost an energy due to Coluomb repulsion (for electrons in the same site), which is indicated with U (Hubbard U). In undoped cuprates, the Hubbard U well exceeds the kinetic energy gain due to hopping (t), and electrons become localized (the material is thus insulating). The Hamiltonian representing this picture is the well-known Hubbard Hamiltonian 2.1 (Hubbard Model) [150].

$$H = -t \sum_{\langle i,j \rangle,\sigma} \left(c^{\dagger}_{i,\sigma} c_{j,\sigma} + H.C. \right) + U \sum_{i} n_{i,\downarrow} n_{i,\uparrow} \tag{2.1}$$

The first term describes the quantum hopping of electrons between nearest-neighbor sites, while the second term accounts for the strong coulomb interaction for electrons occupying the same site.
In the insulating state, the spins of the Cu ions are arranged antiferromagnetically, forming a Neel lattice. The energy gain due to this ordering is known as the superexchange energy J, with: $J \propto t^2/U$ [150].
Despite its apparent simplicity, the Hubbard model is very difficult to solve. For doped materials, a simplification of the (one-band) Hubbard model exists, by considering its limit for large U. This model is known as t-J model. In this limit, the upper Hubbard band is projected out (considering a hole-doped material), and the effect of U becomes virtual [46], leading to a superexchange interaction between Copper spins (since two parallel spins are not allowed to occupy the same Copper site, while antiparallel spins can). This leads to the energy saving of t^2/U, from second-order perturbation theory. t-J Hamiltonian is:

$$H = -t \sum_{\langle i,j \rangle,\sigma} \left(c^{\dagger}_{i,\sigma} c_{j,\sigma} + H.C. \right) + J \sum_{\langle i,j \rangle} \left(\overrightarrow{S_i} \cdot \overrightarrow{S_j} + \frac{1}{4} n_{i,\downarrow} n_{i,\uparrow} \right) \tag{2.2}$$

The t-J Hamiltonian is widely used as a starting point to describe the electronic properties of copper-oxide based high-temperature superconductors.

Superconductivity and evidence of a pseudogap

When a cuprate is doped (here I will refer to the case of hole doping), the physical properties of the material drastically change. These materials exhibit superconductivity at high critical temperatures and a so-called 'pseudogap'. Hole doping can be obtained either by chemical substitution of elements in the spacer layers, or directly by modifying the oxygen content ($\delta \neq 0$ for a doped compound). In both cases, the result is that, to maintain charge neutrality, electrons are pulled away from the CuO_2 planes, forming holes in these planes. The hole concentration is indicated with p. Upon increasing the doping level p from zero, the material becomes a bad metal. At about 5% doping (p=0.05), a superconducting state emerges at low temperatures. The T_c rapidly increases with further doping, reaching a maximum value at about 16% doping (p=0.16), termed the optimal doping (OP) level. Further doping makes T_c to fall to zero, at about 25% doping (p=0.25). Increasing doping further, the material becomes an ordinary metal.

The superconducting ground state is isomorphic with that of the BCS theory [13, 14], since it consists of a condensate composed of Cooper Pairs [40]. The main difference is the symmetry of the gap. In the original BCS theory, the pairs have an s-wave symmetry. On the contrary, the cuprate pairing gap has a d-wave symmetry (the superconducting gap is no more isotropic in k-space, but it is maximum in the antinodal direction of the Brillouin zone (ΓM), and zero in the nodal direction (ΓY) of the Brillouin zone), as demonstrated by several experiments [45, 32]. This fact led to the speculation that the pairing in the cuprates has a different origin from that of conventional superconductors.

Since superconductivity is an instability of the normal state, to understand its origin it is mandatory to understand the nature of the normal state from which it arises. For cuprates, this is where the real controversy begins [140, 137]. Indeed, measurements of the spin response of cuprates below the optimal doping level revealed a reduction in the imaginary part of the low frequency dynamic spin susceptibility, at a temperature larger than T_c [186]. Other magnetic susceptibility measurements [50] showed a suppression of the uniform static susceptibility at temperatures significantly higher than T_c. Similar evidences has been revealed by the decrease of the spin-lattice relaxation rate in NMR experiments on underdoped cuprates [18], and anomalies revealed by tunnelling experiments [130, 172], c-axis optical conductivity [149], specific heat experiments [119] and angle-resolved photoemission experiments [177] have been reported. On the contrary, this kind of depressions occur in conventional superconductors only at T_c. The quenching of these magnetic susceptibilities indicates that a sort of pre-pairing is taking place. This also implies the opening of an energy gap in the density of states, as evidenced by ARPES studies [49]. In cuprates, the temperature at which these quenching phenomenon begin is termed T^*, while no additional anomaly at T_c are shown: a quenching analogous to spin singlet formation of conventional superconductors does not set in at T_c, but at T^*. In particular, T^* increases upon reducing the doping, on the contrary to what happens for T_c. Quenching sets in at higher temperatures as the Charge-Transfer insulating phase is approached.

This point constitutes the main open question in the HTSC field. No consensus exists about the relation existing among the 'spin gap' or pseudogap and the superconducting phase [89, 137, 173]. By analogy with the conventional superconductors case, one possibility is that the pseudogap is also associated with spin singlet formation. This would indicate a sort of pre-pairing of electrons. In this scenario, the pseudogap is thought to be a 'friend' of superconductivity [137]. On the contrary, since any instability typically results in an energy gap, and such an energy gap leads by definition to a depression of the electronic density of states, some feel the pseudogap does not necessarily imply spin singlet formation. In these scenarios, the pseudogap is thought as something unrelated with the phenomenon of superconductivity, or something which impedes the superconductivity formation (superconductivity 'foe') [137].

The understanding of the pseudogap phenomenon is intimately connected to the understanding of the whole phase diagram of the material: each theory for the phase diagram predicts a different nature for the pseudogap phenomenon. The next section will be devoted to the presentation of the most releveant schemes for the copper-oxide based superconductor phase diagram.

2.3 Models for the phase diagram

The critical parameter that determines the properties of a copper-oxygen based superconductor is the concentration of holes (p) in the Copper-Oxygen planes. The phase diagram obtained by modifying p has been sketched in Fig. 2.1, in the p-T (doping-temperature) parameters space. The UD region is characterized by the enigmatic pseudogap phase. This paragraph is aimed to the description of the most relevant models for this phase [89, 173].

The models reported in the literature design two main scenarios [137].
The first one involves preformed Cooper pairs at temperature $T<T^*$, which become phase coherent only for $T<T_c$. An important theory pointing into this direction is contained in a work by Emery and Kivelson [70]. In this theory, the loss of coherence of the condensate at $T>T_c$ is explained in terms of phase fluctuations that, due to the low density of the superconducting carriers as compared to the standard 3D BCS superconductors, destroy the long range order without breaking the Cooper Pairs. Another theory supporting this first scenario is based on the notion of spin-charge separation [114, 133]. A single hole is described as a bound state of a fermionic particle, called spinon, carrying only the spin, and a bosonic particle, called holon, carrying only the charge. In strongly correlated electron systems, this dual nature of the charge carriers becomes more evident, with spinons and holons behaving like independent partieles. In a mean-field description, spinons pair together forming a gap in the spin excitation spectrum, interpreted as the pseudogap, while holons undergo Bose-Einstein condensation at T_c, making the system superconductive.
The opposite scenario is that in which the pseudogap is considered as a phase, characterized by an hidden order, in competition with superconductivity [33, 181]. Various candidates for this order have been proposed. In particular, stripe and antiferromagnetic order, d-density wave order (DDW), or current loops, all break a particular symmetry of the system.

The fact that the T^* temperature decreases moving towards the OD region of the phase diagram is experimentally established, but the precise structure of the phase diagram, and particularly the T^* dependence on the hole density p, is still subject of discussion. Two different behaviors for the pseudogap line $T^*(p)$ are expected, depending on the actual scenario [89], as can be seen by looking at Fig. 2.4.

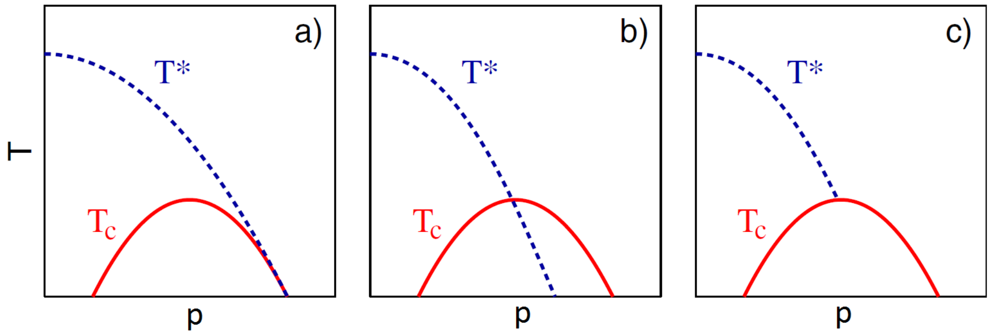

Figure 2.4: Three scenarios for the interplay of pseudogap (blue dashed line) and superconductivity (red solid line) in the p-T phase diagram of HTSC are reported. In a), the pseudogap merges gradually with the superconducting gap in the strongly overdoped region. In b) and c) the pseudogap line intersects the superconducting dome, at about optimal doping. In most descriptions, the pseudogap line is identified with a crossover with a characteristic temperature T^* rather than a true thermodynamic phase transition. In a), $T^*>T_c$ at all dopings. In b), $T^*<T_c$ beyond optimal doping. In c), T^* does not exist inside the superconducting dome. From [89], adapted from [140].

In the first scenario, in which the pseudogap would be a precursor of superconductivity, the T^* line is supposed to be tangent to the OD limit of the superconducting dome. On the contrary, in the scenario of a pseudogap competing with superconductivity, the T^* line should enter the superconducting dome at about optimal doping, and extending into the superconducting dome itself. In this case, a region where superconductivity coexists with the psendogap is expected. In this scenario, the phase diagram would be governed by a quantum critical point (QCP) inside the superconducting dome, at T=0. In this respect, a model of Copper-Oxygen bonding and antibonding bands proposed by C. Varma [95, 180] provides for a continuous transition (as a function of hole density p and temperature T) to a phase in which a pair of oppositely directed currents circulate in each unit cell (loop-current electronic order). This phase preserves the translational symmetry of the lattice, while breaks time-reversal invariance and fourfold rotational symmetry [95]. This circulating current phase terminates at a critical point for p=p_{QCP} and T=0. This scenario is depicted in Fig. 2.5.

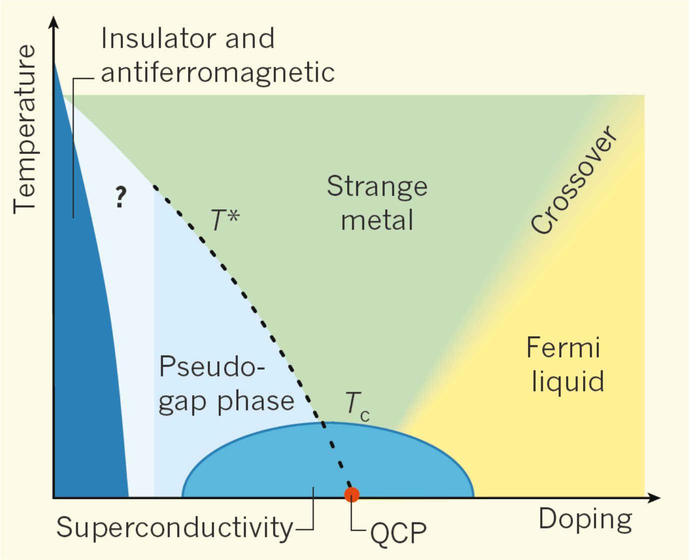

Figure 2.5: The QCP-governed phase diagram proposed by C. Varma is reported. At very low levels of hole doping, cuprates are insulating and antiferromagnetic. At increased doping levels, they become conducting, and the exact temperature and doping level determine which phase of matter they will be in. At temperatures below T_c, they become superconducting, and at temperatures above T_c but below T^* they fall into the pseudogap phase. The boundary of the pseudogap region at low doping levels is unknown. The transition between the Fermi-liquid phase and the strange-metal phase occurs gradually, by crossover. QCP denotes the quantum critical point at which the temperature T^* goes to absolute zero. This QCP origins a critical region (the pseudogap) in which the ground state is given by pairs of electron-current-loops flowing within each of the material unit cells, and producing a pair of oppositely directed magnetic moments. From [180].

2.4 The Electron-Boson coupling in HTSC

The electron-phonon interaction (that can be generalized to a more universal electron-boson interaction) affects and determines many physical properties of solid state materials (such as the optical properties, the resistivity, the specific heat). Moreover, it constitutes the attractive interaction - essential in the superconductivity framework - which binds together pairs of electrons, forming the so-called Cooper Pairs (CP), as pointed out by Cooper [40]. This holds without exceptions for the conventional superconductors (metals, compounds or simple alloys). It is universally accepted that in conventional superconductors the pairing comes entirely and solely from the electron-phonon interaction, whose strength determines the material T_c (pairing and pair condensation are simultaneous effects in the BCS theory [13, 14]). Actually the BCS theory is only valid in the so-called weak-coupling regime (even if many phenomena are satisfactorily described even when the weak coupling requirement is violated). Its generalization to the strong-coupling regime case is due to Eliashberg [69, 134, 126], but the main features of the theory remains the same. Usually, the origin of the net attractive interaction which forms the CP is termed glue. In the BCS theory and its extensions, the glue is given by phonons.

Electron-phonon interaction is thus an essential topic to be investigated in the framework of high-temperature superconductivity, to highlight differences or similarity with respect to the BCS case. Upon determining the electron-phonon coupling strength in High-Tc materials, it is possible to point out whether the material is in the weak or strong coupling regime, and possibly whether other bosons contribute (entirely or cooperatively) to the pairing. Indeed, no consensus has been reached yet on the nature of the (bosonic) glue in the High-Tc: a strong debate is on whether the pairing is due to phonons [44, 56, 113, 120, 167], spin fluctuations [2, 35, 162], or both (bosons of phononic or electronic origin). Many techniques have been exploited to measure the electron-phonon coupling constant, both in metals and superconductors. Nevertheless, the obtained results are contrasting. Among these techniques, which probe the equilibrium properties of the material, I may cite ARPES, inelastic neutron scattering, tunneling spectroscopy, optical conductivity. Extracting information from these static, equilibrium measurements is a task of high difficulty, since complex procedures of data inversion are needed. Reverting to the time-resolved point of view, the electron-phonon coupling strength can be derived in a straightforward way, instead. The non-equilibrium approach revealed the more direct way of extracting these information, since it allows to access the temporal domain: the timescale of the return-to-equilibrium of an excited system of electrons and phonons is related (see section 4.3.1) to the electron-phonon coupling strenght. The first experimental results taking advantage of the temporal resolution are dated 1990 for studies with optical measurements [25, 24] and 2007 for studies with (time-resolved) ARPES [145]. A common model (some alternative models are reported in [96, 75]) employed to extract the electron-phonon coupling is the Two-Temperatures model (and its evolution to the three temperatures model, in the case of strongly correlated systems and anisotropic systems), developed by Anisimov (1974) [10] and Allen (1987) [7]. This model will be described in detail in Chapter 4 (section 3), together with its evolutions. Now, a few words are worth to be spent about the definition of the electron-phonon coupling strength and its relation with the material T_c.

The theory of strong coupling superconductivity is based on the Green's-function method of the many-body theory, with the theory of strong coupling which is a generalization of the theory of normal metals, by Migdal (1957) [126]. Some important quantities enter the theory. $F(\Omega)$, being Ω the phonon frequency, is the phonon density of states (PDOS), which constitutes the phonons spectrum. $\alpha^2(\Omega)$ is the phonon-frequency-dependent electron-phonon interaction. A very common quantity for the theory is the temperature independent, material dependent product $\alpha^2(\Omega)F(\Omega)$, which enters in the definition of the (frequency integrated) electron-phonon coupling constant λ. The expression $\alpha^2(\Omega)F(\Omega)$ is usually called 'the glue function'. λ represents an effective coupling:

$$\lambda = 2\int_0^\infty \alpha^2(\Omega)F(\Omega)\Omega^{-1}d\Omega \tag{2.3}$$

λ is the same as $\lambda\left\langle\Omega^0\right\rangle$, being $\lambda\left\langle\Omega^n\right\rangle$ the moments of $\alpha^2(\Omega)F(\Omega)$, appearing in the superconductivity theory:

$$\lambda\left\langle\Omega^0\right\rangle = 2\int_0^\infty \left[\alpha^2(\Omega)F(\Omega)\Omega^{-1}\right]\Omega^n d\Omega$$

Often, a characteristic phonon frequency $\tilde{\Omega}$ is defined, as an average over $\alpha^2(\Omega)F(\Omega)$. Following the literature, at least three possibilities are reported: "linear" (Dynes), "quadratic" (Kresin$-$Wolf), "log" (Allen$-$Dynes, Carbotte): $\tilde{\Omega} = \langle\Omega\rangle$, $\tilde{\Omega} = \left\langle\Omega^2\right\rangle^{1/2}$, $\tilde{\Omega} = \langle\ln(\Omega)\rangle$. From simple comparison with the BCS-limit case and for the better agreement with the data, the best choice for the mean phonon frequency will turn out to be the "log" one.
The mean values come from the expression:

$$\langle f(\Omega)\rangle = \frac{2}{\lambda}\int_0^\infty \left[\alpha^2(\Omega)F(\Omega)\Omega^{-1}\right] f(\Omega)d\Omega$$

thus:

$$\langle\Omega\rangle = \frac{2}{\lambda}\int_0^\infty \alpha^2(\Omega)F(\Omega)d\Omega \equiv \frac{2A}{\lambda}$$
$$\left\langle\Omega^2\right\rangle = \frac{2}{\lambda}\int_0^\infty \alpha^2(\Omega)F(\Omega)\Omega d\Omega$$
$$\langle\ln(\Omega)\rangle = \frac{2}{\lambda}\int_0^\infty \alpha^2(\Omega)F(\Omega)\ln(\Omega)d\Omega$$

Expressions for $T_c = T_c(\lambda)$
The electron-phonon coupling constant λ is an important parameter because it enters the (approximate) expressions determining the material's T_c, in the various coupling strength formalisms. The problem arises since a correct explicit expression for T_c depends on the strength of the coupling, thus some limiting cases are analyzed.
I start with the weak-coupling regime ($\lambda \leqslant 0.3$), in which the BCS theory fully holds. The BCS result actually reads:

$$k_B T_c \approx 1.13\hbar\Omega_D \exp(-1/N(0)V)$$

where $N(0)V = (\lambda - \mu^*)$ $(\lambda > \mu^*)$.
The net attractive pairing potential V is proportional to an attractive part,

λ (originating from the electron-phonon interaction) and a repulsive part, μ^* (originating from electron-electron Coulomb interaction). In the above formulae, $N(0)$ is the density of states (per spin) at the Fermi Energy, and Ω_D is the Debye frequency (or a typical phonon frequency) of the material. The BCS theory assumes the coupling is with just one phonon mode (with $\Omega = \Omega_D$): following the derivation of the above formula, one argues that the correct expression for the mean value $\tilde{\Omega}$ is given by the log-average:

$$\tilde{\Omega} = \langle \ln(\Omega) \rangle \tag{2.4}$$

and that, by definition, in the BCS theory it holds: $\tilde{\Omega} = \Omega_D$.
The above BCS relation indicates that in general T_c is much smaller than the material Debye frequency, Ω_D. Even in many metallic, conventional superconductors, it turns out that λ is not in the weak-coupling regime (1.4 in Pb, 1.6 in Hg), so that new theories should be developed.
For larger values of λ ($\lambda \lesssim 1.5$), i.e., in the strong coupling regime, the relation T_c vs λ is given by the famous McMillan formula [125] (later modified and improved by Dynes [62] and by Allen&Dynes [8]), which derives from the Eliashberg theory:

$$k_B T_c \approx \frac{\hbar\tilde{\Omega}}{1.2} \exp\left(\frac{-1.04(1+\lambda)}{\lambda - \mu^*(1+0.62\lambda)}\right) \tag{2.5}$$

This relation reduces to the BCS one in the weak coupling limit, $\lambda \ll 1$. It should be noted that in the above expression the coefficients 1/1.2, 1.04, 0.62 are the result of a fitting procedure of a more general expression to data from real materials: this expression is thus 'semi-phenomenological'.
Finally, if the coupling constant λ is large ($\lambda > 1.5$), McMillan equation stops being satisfactory, and one should use different expressions for the critical temperature T_c (indeed, McMillan equation leads to a saturation of T_c for $\lambda \to \infty$, while the exact result does not: the effect of a maximum T_c is an artifact of the approximations done, and is not intrinsic to the Eliashberg theory from which it follows). A comprehensive review of these relations can be found in [110, 28]. The conclusion is that, if the material is characterized by large values of $\tilde{\Omega}$ and λ, it can have a very high T_c. This can be the case when some high-energy boson-exchange mechanism are operative, as it is the case in copper-oxide based superconductors. Regarding the fact of achieving large values of the electron-phonon coupling constant λ, the problem is related to the framework of lattice or other instabilities, which are not accounted for by the superconductivity theories. λ cannot increase indefinitely, indeed the lattice would surely reach a point when it is no longer stable because of the very large electron-phonon interaction, eventually leading to polaron formation. At present, there is no universally accepted and quantitative stability criterion [28].
Up to now, I considered for the glue function the expression $\alpha^2(\Omega)F(\Omega)$, indicating the frequency dependent electron-phonon interaction. The glue function

can be generalized to include other possible scattering mechanisms / channels for the electrons, for example, with spin fluctuations, charge fluctuations or loop currents. The coupling between electrons and spin fluctuations is indicated in a similar manner as: $I^2(\Omega)\chi(\Omega)$. Thus, the total glue can be written as: $\Pi(\Omega) = \alpha^2(\Omega)F(\Omega) + I^2(\Omega)\chi(\Omega) + ...$ In this framework, λ assumes the more general meaning of an electron-boson coupling constant. A strong debate exists on whether the electron-phonon interaction alone can provide the high critical temperatures typical of the cuprate superconductors [110].

Considering the total glue function $\Pi(\Omega)$ as a source of pairing for electrons is the ultimate step for the coupling theories which propose bosonic 'mediators' for the formation of Cooper Pairs. It must be noted that these theories, which consider a "retarded" attraction mediated by the exchange of bosonic excitations forming the bosonic glue, and not the only ones that have been proposed. They are set against the theories for which the pairing comes directly by the ("non-retarded") Coulomb interaction, without the need of mediators [151, 9, 146].

The presented approximate relations for $T_c = T_c(\lambda, \tilde{\Omega})$ are of paramount importance since they relate the material T_c to average values of the quantity $\Pi(\Omega)$, i.e., λ and $\tilde{\Omega}$. In section 4.3 I will present some models which allow to estimate, from time-resolved pump-probe measurements, the parameter λ. The valuse for λ obtained by measurements in the time-domain can be compared to the values obtained by relation 2.3, which integrates the total Glue Function $\Pi(\Omega)$ obtained from static optical measurements (section 3.7.2).

2.5 Bi2212 Crystal Structure

$Bi_2Sr_2Ca_{m-1}Cu_mO_{2m+4+\delta}$, often abbreviated with BSCCO (Bismuth-Strontium-Calcium-Copper-Oxyde) to highlight the chemical elements it contains, is one of the most important members of the high critical temperature copper oxide based (cuprate) superconductors. In the above formula, m indicates the number of Copper-Oxygen (Cu-O_2) planes in the conventional unit cell of the material, while δ indicates the doping level, obtained through modification of the Oxygen concentration. In the BSCCO compound, the variation of the Oxygen stoichiometry δ results in an effective hole-doping mechanism. Cuprates are characterized by a layered structure, with Cu-O_2 planes separated by spacer layers that act as charge reservoirs.

Among the more than 20 distinct phases in which the BSCCO compound can be synthetized, differing for the stoichiometric ratios and the growing process, only three show high temperature superconductivity properties. They are indicated with Bi2201 (the one-plane Copper-Oxygen compound, having T_{cmax}=20 K), Bi2212 (the two-planes Copper-Oxygen compound, having T_{cmax}=90 K), and Bi2223 (the three-planes Copper-Oxygen compound, having T_{cmax}=110 K). The main difference between the three compound resides only in the number m of Cu-O planes contained in the conventional unit cell.

Most of the measurements presented in this thesis work are carried out on the two-layered compound (m=2), which formula is $Bi_2Sr_2Ca_1Cu_2O_{8+\delta}$ (I will refer to this compound simply by Bi2212). In particular, I will study peculiar Yttrium substituted samples, in which some Ca atoms are substituted by Y ones to stabilize the crystal structure and simultaneously increase the maximum critical temperature with respect to the conventional compound. Both these requirements are achieved for 8% Y substitution: the chemical formula of this compound is: $Bi_2Sr_2Y_{0.08}Ca_{0.92}Cu_2O_{8+\delta}$. I will refer to this compound by Y-Bi2212.

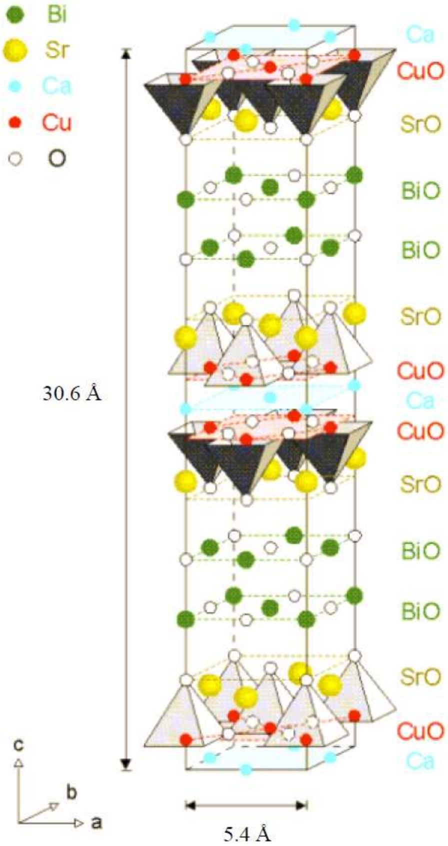

Figure 2.6: The $Bi_2Sr_2Ca_1Cu_2O_{8+\delta}$ unit cell, evidencing the complex material crystal structure, is reported.

Fig. 2.6 shows the conventional unit cell of Bi2212, from which it is possible to argue the complexity of the crystal structure. The cell has an orthorhombic crystal structure, for which the c axis is the main axis. The crystal axis have the following dimensions: a=b=5.4 Å, c=30.6 Å [36]. The Bi-O planes are the most probable fleaking planes for this structure, given the weakness of the chemical bonds between Bi-O layers. Bi2212 is an easily cleavable compound, with the c-axis being orthogonal to the cleaving plane. This reason makes Bi2212 the most studied superconducting compound with photoelectron spectroscopic techniques. The stability of the compound crystal structure made this compound one of the most studied in general, together with the YBCO copper oxide based superconductor. Bi-O planes are also the planes in which the extra Oxygen atoms due to the doping modify the hole concentration. The doping content δ strongly affects the physical properties of BSCCO. Indeed, for $\delta = 0$, this compound is an antiferromagnetic charge transfer insulator. It is only for $\delta > 0$ that the system becomes a (bad) metal. Moreover, it is only for $\delta > \delta_c$, being δ_c a critical doping level, that the system undergoes the superconducting transition, when cooled. The superconductivity then disappears if a maximum doping level, indicated with δ_l, is crossed. Thus, superconductivity exists only for a limited range of doping concentrations, namely $\delta_c \leqslant \delta \leqslant \delta_l$. The doping level for which the compound exhibits its maximum critical temperature, T_{cmax}, is called optimal doping level, δ_{opt}. δ_{opt}=0.16 in Bi2212.

The critical temperature is related to the oxygen doping level p by the phenomenological formula [148]:

$$T_c(p) = T_{cmax}\left[1 - 82.6(p - 0.16)^2\right] \tag{2.6}$$

being T_{cmax}=96 K for our compound.

All cuprates are known for their high anisotropic properties. As an example of this, I may cite the electrical resistivity of Bi2212, equal to $\rho_c \approx 2\ \Omega\cdot$cm along the c axis and equal to $\rho_{ab} \approx 10^{-4}\ \Omega\cdot$cm in the ab plane [43]. In the superconducting phase, both ρ_c and ρ_{ab} drop below the measurability level. Similar anisotropy properties can be found in the thermical conductivity properties. The coherence length, with $\xi_{ab} \approx 30\xi_c$ [55], is the manifestation of the material anisotropy in the superconducting phase.

The values of the electronic and lattice specific heats for these samples, that will be employed in the following chapters of this thesis, has been taken from [94, 118]. For simulations involving the specific heat of the Bi2212 compound (like those reported in Chapters 4, 6, 7, 8), it is important to remember that one Bi2212 mole contains N_A=6.022·10^{23} Bi2212 molecules, with every Bi2212 molecule composed of 15 atoms (2 Bismuth, 2 Strontium, 1 Calcium, 2 Copper, 8 Oxygen). The volume of one Bi2212 primitive cell equals 223 Å^3, while its denisty equals 6.56 g/cm^3, corresponding to 891.15 g/mol.

2.5.1 The Yttrium-doped Bi2212

In $Bi_2Sr_2CaCu_2O_{8+\delta}$, cation disorder at the Sr crystallographic site strongly affects the maximum attainable value for T_c [68]. By minimizing Sr site disorder at the expense of Ca site disorder, it has been demonstrated that the T_c of the two-layered Bismuth-based material can be increased up to 96 K. In particular, this important advance has been achieved by growing a compound in which Ca has been substituted by Y, namely: $Bi_2Sr_2Y_yCa_{1-y}Cu_2O_{8+\delta}$. $T_{c,max}$=96 K has been obtained for y=0.08 (i.e., for 8% Y substitution). The chemical formula for this compound is: $Bi_2Sr_2Y_{0.08}Ca_{0.92}Cu_2O_{8+\delta}$ (Y-Bi2212). Substitution of Y for Ca also helps to enforce Bi:Sr stoichiometry, which reduces chemical inhomogeneities. Moreover, this compound is as easy to prepare as ordinary, nonstoichiometric Bi2212. For our purposes it is worth to note that the electronic properties of this compound are similar to those of the most known Bi2212.

Sample Preparation and Characterization

The superconducting samples I studied in this thesis work are large and high-quality Y-substituted Bi2212 single crystals, grown in an image furnace by the travelling-solvent floating-zone technique with a non-zero Y content [68]. Different annealing procedures have been followed to obtain samples with different doping level. The procedures to obtain an underdoped and an overdoped sample are described. The underdoped samples were annealed at 550 °C for 12 days in a vacuum-sealed glass ampoule with copper metal inside. The overdoped samples were annealed in a quartz test tube under pure oxygen flow at 500 °C for 7 days. To avoid damage of the surfaces, the crystals were embedded in $Bi_2Sr_2Y_{0.08}Ca_{0.92}Cu_2O_{8+\delta}$ powder during the annealing procedure. In both cases, the quartz tube was quenched to ice-water bath after annealing to preserve the oxygen content at annealing temperature.

The critical temperature of the samples has been inferred from the sample magnetic susceptibility curve, measured with a SQUID magnetometer (the magnetic susceptibility curves are reported in Fig. 2.7 for three representative samples). The superconducting transition width has been estimated as follows: $\Delta T_c \equiv \Delta T_{10-90\%}$, i.e., it has been considered the temperature span for which the magnetic susceptibility of the sample passes from 10% to 90% of its minimum value. For the optimally doped sample (OP), the critical temperature reported (T_c=96 K) is the onset temperature of the superconducting phase transition, the transition being very narrow (ΔT_c<2 K). As a meaningful parameter for the underdoped (T_c=83 K, UD) and overdoped (T_c=86 K, OD) samples, which have respectively transition widths of $\Delta T_c \sim$8 K and $\Delta T_c \sim$5 K, I report the transition midpoint temperatures instead. The hole concentration p is estimated through the phenomenological formula 2.6.

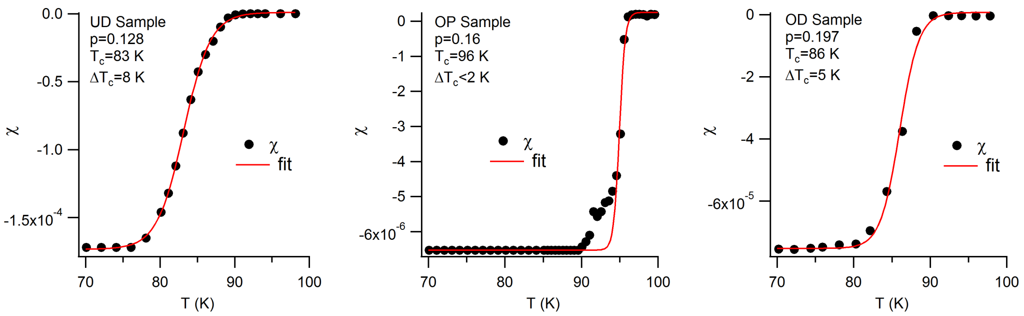

Figure 2.7: The magnetic susceptibility curves for three $Bi_2Sr_2Y_{0.08}Ca_{0.92}Cu_2O_{8+\delta}$ samples are reported. The number of doped holes per Copper ion, p, is: p=0.128 for the UD sample, p=0.16 for the OP sample, p=0.197 for the OD sample.

Chapter 3

Equilibrium Spectroscopy

3.1 Introduction

This chapter reports the description of the static optical properties of HTSC. I'll start with a review of the definitions and models which I will exploit in the subsequent chapters of this work. In particular, the main focus will be about a recently developed version of the Extended Drude formalism, which takes into account the presence of a gap in the density of states (non-constant density of states). A brief review of the relationships among optical properties and of the important sum rules will follow. Finally, the results of the model fitting to the experimental dielectric functions of Y-Bi2212 at T=300 K, T=100 K and T=20 K will be illustrated. The first case allowed us to extract the material bosonic glue, while data at T=100 K allows to discuss the role of a non-constant density of states.

3.2 The dielectric function $\epsilon(\omega)$

The dielectric function, $\epsilon(\omega)$, is a material-dependent complex function describing, in the frequency domain, the response of a material to an externally applied electric field $\overrightarrow{E}(\omega)$: $\overrightarrow{D}(\omega) = \epsilon(\omega)\overrightarrow{E}(\omega)$, being $\overrightarrow{D}(\omega)$ the effective electric field (also known as displacement field), $\overrightarrow{D}(\omega) = \epsilon_0\overrightarrow{E}(\omega) + \overrightarrow{P}(\omega)$. Here ϵ_0 is the vacuum permittivity (ϵ_0=8.85$\cdot$10^{-12} F/m), and $\overrightarrow{P}(\omega)$ the (material dependent) polarization. ω is the frequency of the electric field. $\epsilon(\omega)$ is a response function, since it relates the characteristic response of a system to the externally applied stimulus. Being a response function, it is causal, in the sense that no effect can occur before the cause. As we will see, this intuitive requirement brings very important results. In one sense, the dielectric function establishes the link between the macroscopic world and the microscopic one. From the macroscopic point of view, starting from $\epsilon(\omega)$, all the optical properties can be calculated (see section 3.3). In particular, the reflectivity R(ω), the transmissivity T(ω), the complex index of refraction $n(\omega)$, the complex optical conductivity $\sigma(\omega)$ and the penetration depth $\alpha(\omega)$ can be all inferred from $\epsilon(\omega)$. From the microscopic point of view, $\epsilon(\omega)$ is related to the optical electronic transitions in the material, that depend on the specific material band structure. As a consequence, a detailed knowledge of this function would provide unique information about the underlying electronic properties of the materials.

A detailed description of the key concepts to interpret the electronic optical properties of solids can be found in [185, 59], together with notions on the experimental techniques, the principles of spectroscopy, and the measurement configurations. In the field of equilibrium optical spectroscopy, among the most important experimental works in which the optical properties of noble metals and transition metal oxydes are measured and interpreted, I can cite [65, 66, 67, 39, 155]. A review of the electrodynamics of copper-oxyde-based high-temperature superconductors can be found in [15], while a recent review of the optical properties of strongly correlated electron materials is [16].

In principle, the dielectric function $\epsilon(\omega)$ can be determined from first principles (with the exact electronic structure calculation, but this is the case only for very simple materials [121]), it can be determined with calculations using Density Functional Theory (DFT), for metals, or Dynamical Mean Field Theory (DMFT), for strongly correlated systems, or, finally, it can be modeled, as it is very often the case. Sections 3.4 and 3.5 are enterely devoted to provide an accurate description of the models developed to this aim, and that are the most often used in the literature [15, 16, 179, 90]. An accurate reproduction of the experimentally measured equilibrium dielectric function of Y-Bi2212 by using these models constituted the preliminary task of my work. Results of this analysis are presented in section 3.7.

3.3 Optical Properties

In this section I report some useful expressions relating the dielectric function $\epsilon(\omega) = \epsilon_1(\omega) + i\epsilon_2(\omega)$ to other optical quantities of interest:

- The refraction index $n(\omega) = n_1(\omega) + in_2(\omega)$ of a non-magnetic material is:

$$n(\omega) = \sqrt{\epsilon(\omega)} \tag{3.1}$$

- The optical conductivity $\sigma(\omega) = \sigma_1(\omega) + i\sigma_2(\omega)$ is:

$$\sigma(\omega) = i\frac{\omega}{4\pi}(\epsilon(\omega) - 1) \tag{3.2}$$

- The reflectivity at normal incidence is given by:

$$R(\omega) = \left| \frac{1 - \sqrt{\epsilon(\omega)}}{1 + \sqrt{\epsilon(\omega)}} \right|^2 \tag{3.3}$$

  or:

$$R(\omega) = \frac{(n_1(\omega) - 1)^2 + n_2(\omega)^2}{(n_1(\omega) + 1)^2 + n_2(\omega)^2} \tag{3.4}$$

- For the absorption coefficient $\alpha(\omega)$, entering in $I(z) = I_0 e^{-\alpha(\omega) z}$ (being $I(z)$, I_0, z respectively the absorbed intensity at z, the incident intensity, and the coordinate perpendicular to the sample surface, for a normal incidence geometry), it holds:

$$\alpha(\omega) = 4\pi n_2(\omega)\omega \tag{3.5}$$

  or

$$\alpha(\omega) = 4\pi\sigma_1(\omega)/n_1(\omega)c$$

- $\lambda(\omega) = \alpha^{-1}(\omega)$ is the penetration depth.
- Other useful relations (the frequency dependence is omitted) are:

$$\epsilon_1 = {n_1}^2 - {n_2}^2, \epsilon_2 = 2n_1 n_2$$
$$n_1 = \sqrt{(|\epsilon| + \epsilon_1)/2}, n_2 = \sqrt{(|\epsilon| - \epsilon_1)/2}$$
$$\epsilon = 1 + i\frac{4\pi}{\omega}\sigma(\omega), \epsilon_1 = 1 - 4\pi\sigma_2/\omega, \epsilon_2 = 4\pi\sigma_1/\omega$$

Since $\epsilon(\omega)$, $n(\omega)$, $\sigma(\omega)$ are causal response functions, their real and imaginary parts are not independent, but are mutually related by the Kramers-Kronig (KK) integral relations [185]. The KK relations allow, if for example only the real / imaginary part is experimentally available for any of the above quantities, to calculate the corresponding imaginary / real part. The only requirement is that the measured quantity must be available over a very broad spectral range. Moreover, this fundamental connection allows to find algorithms to infer both real and imaginary parts of $\epsilon(\omega)$ or $\sigma(\omega)$ from the raw reflectivity data. More details about these fundamental relations can be found in [185].

For completeness, the KK dispersion relations for the dielectric function $\epsilon(\omega)$ are:

$$\epsilon_1(\omega) - \epsilon_\infty = \frac{1}{\pi}\mathbb{P}\int_{-\infty}^{+\infty} d\omega' \frac{\epsilon_2(\omega')}{\omega' - \omega} \tag{3.6a}$$

$$\epsilon_2(\omega) = -\frac{1}{\pi}\mathbb{P}\int_{-\infty}^{+\infty} d\omega' \frac{(\epsilon_1(\omega') - \epsilon_\infty)}{\omega' - \omega} \tag{3.6b}$$

Expressions in terms of integrals over positive frequencies only also exist [185].

3.4 Drude and Lorentz dielectric functions

The most common models for reproducing a generic dielectric function are the classical Lorentz and Drude models. The Lorentz model is applicable to insulators, while the Drude model is applicable to free electron metals. They can describe respectively the effect of optical transitions on the optical properties, for direct interband transitions (transitions for which the final state of an electron lies in a different band, but with no change in the k-vector) and intraband transitions (transitions in the same band; in particular, the conduction band). These classical models, describing the response to an external electric field $\overrightarrow{E}(\omega)$ of a bound or a free electron in a solid, have a simple derivation. The idea at their base, in an intuitive and classical picture, is to describe the electronic response to an electric field with an harmonic oscillator, for an electron in an atom or solid. The electron with mass m and charge e, when immersed in an electric field $E(t) = \int_{-\infty}^{\infty} E(\omega)e^{-i\omega t}d\omega$, is subject to a driving force $-eE(\omega)$. The restoring force is modeled through Hooke's law: $-m\omega_0^2 r$. Here ω_0 is not the electron binding energy in the atom / solid, but rather the energy difference of an allowed optical transition. In the Drude model, $\omega_0 = 0$, since there exist no threshold for absorption, for a conduction electron in a free electron metal. Finally, the electron is subject to a viscous damping (representing an energy loss mechanism arising from various scattering mechanisms) modeled as: $-m\gamma(dr/dt)$. This damping term is responsible for the fact that the induced polarizability is complex, thus it differs in phase from the driving field, at all frequencies. In the case of a nearly free electron metal (Drude model), $\gamma = 1/\tau$, being τ the mean free time between collisions, originated from the ordinary scattering of electrons with impurities and phonons, which is the same scattering mechanism determining the value and temperature-dependence of the electrical resistivity. Solving the motion equation, and and calculating the polarization $\overrightarrow{P}(\omega)$, the dielectric functions for the Lorentz ($\epsilon_L(\omega)$) and Drude ($\epsilon_D(\omega)$) models result. They can be written as:

$$\begin{aligned}\epsilon_L(\omega) = 1 + \frac{{\omega_p}^2}{({\omega_0}^2 - \omega^2) - i\gamma\omega} &= \left[1 + {\omega_p}^2 \frac{({\omega_0}^2 - \omega^2)}{({\omega_0}^2 - \omega^2)^2 + \gamma^2\omega^2}\right] + \\ &+ i\left[{\omega_p}^2 \frac{\gamma\omega}{({\omega_0}^2 - \omega^2)^2 + \gamma^2\omega^2}\right]\end{aligned} \tag{3.7}$$

$$\epsilon_D(\omega) = 1 - \frac{{\omega_p}^2}{\omega^2 + i\gamma\omega} = \left[1 - {\omega_p}^2 \frac{1}{\omega^2 + \gamma^2}\right] + i\left[{\omega_p}^2 \frac{\gamma/\omega}{\omega^2 + \gamma^2}\right] \tag{3.8}$$

where ω_p is the oscillator plasma frequency, defined as follows: ${\omega_p}^2 = 4\pi Ne^2/m$. In a realistic situation, the two models must be used simultaneously: the Drude model reproduces the low-energy side of the dielectric function, associated to the metallic behavior; the Lorentz model reproduces the high-energy part of the dielectric function, associated to interband transitions. Usually, a cut-off frequency, ω_c, is defined as the frequency at the crossing of the two behaviors. This choice is arbitrary and lead to some debate, since the tail of the Drude contribution extends well beyond ω_c. In doped cuprates, this cutoff is usually placed at about 10000 cm^{-1}, i.e., 1.25 eV [138]. Thus, in general, a model dielectric function comprises both kinds of oscillators; moreover, often a sum of different Lorentz oscillators is considered, to take into account the fact that many optical transitions from discrete bands or levels can be allowed. The resulting model dielectric function $\epsilon(\omega)$ is written as:

$$\epsilon(\omega) = \epsilon_D(\omega) + \sum_{i=1}^{m} \epsilon_{Li}(\omega) = \epsilon_1(\omega) + i\epsilon_2(\omega) \tag{3.9}$$

where i labels the allowed interband transitions. $\epsilon_1(\omega)$ and $\epsilon_2(\omega)$ are:

$$\epsilon_1(\omega) = \epsilon_\infty - {\omega_{p0}}^2 \frac{1}{\omega^2 + {\gamma_0}^2} + \sum_{i=1}^{m} {\omega_{p_i}}^2 \frac{({\omega_{0i}}^2 - \omega^2)}{({\omega_{0i}}^2 - \omega^2)^2 + {\gamma_i}^2\omega^2} \tag{3.10}$$

$$\epsilon_2(\omega) = {\omega_{p0}}^2 \frac{\gamma_0/\omega}{\omega^2 + {\gamma_0}^2} + \sum_{i=1}^{m} {\omega_{p_i}}^2 \frac{\gamma_i\omega}{({\omega_{0i}}^2 - \omega^2)^2 + {\gamma_i}^2\omega^2} \tag{3.11}$$

In $\epsilon_1(\omega)$, ϵ_∞ takes into account the effect of high-energy interband transitions, which are usually not included in the model. Ideally, if one would include all the possible interband transitions, it would result: ϵ_∞=1.
While the Lorentz model is widely used to reproduce the interband transitions in a variety of materials, the Drude model fails in reproducing the low-energy optical behavior in systems where a strong electron-boson interaction is present [6, 5, 105]. The conventional Drude model is strictly valid only for simple metals, having a constant density of states at E_F and a frequency-independent scattering time τ (the impurity scattering). To interpret the low-energy optical properties of strongly correlated materials, in which quasiparticles strongly interact with bosonic excitations (phonons or other bosonic excitations of electronic origin) or a gap in the density of states opens [166], an extended formalism has been developed by Allen [6, 5], namely, the Extended Drude Model (EDM). On its basis the optical properties of strongly correlated materials are today successfully interpreted [15, 16]. In the next section the EDM in its various forms will be discussed.

3.5 Extended Drude Model

Unless a very simple metallic material is considered, in which conduction band electrons are almost non-interacting with phonons, the Drude model reveals its limits in correctly reproducing the optical properties. Within the Drude model, the effect of band structure is accounted for by considering an effective

mass m^* instead of the bare electron mass m in the expression of the plasma frequency, while the scattering from impurities is accounted for by the damping term γ, which I will now rename as γ_{imp}.
When the electrons are interacting with some bosonic excitations (electron-boson interaction), characterized by a typical spectral distribution, the scattering process and the electron lifetime become strongly frequency-dependent. Sources of electron-boson interaction can be the electron-phonon coupling (either anisotropic, with prefential, strongly coupled modes, or with the whole lattice), or an interaction with bosons of electronic origin, namely, antiferromagnetic spin fluctuations [2, 35, 141] or current loops [180]. This effect is particularly severe in strongly correlated systems and cuprates, where part of the total electron-boson interaction is thought to be the source of coupling for the electrons forming pairs, in the scenario in which the attractive interaction is 'retarded', i.e., mediated by virtual bosonic excitations in the solid [127].

This physics is included in the EDM, which considers the novel sources of scattering, and accounts for a frequency-dependent scattering rate and the renormalization of the electron effective mass due to the interaction. In a metallic system, the physical processes responsible for renormalization of electronic lifetimes and effective masses, are included in the description of the optical properties in a phenomenologic way, by replacing the frequency-independent scattering time τ (where $\tau^{-1} = \gamma$) with a complex and frequency-dependent scattering time, $\tilde{\tau}(\omega)$, given by:

$$\tau^{-1} \Rightarrow \tilde{\tau}^{-1}(\omega) = \tau^{-1}(\omega) - i\omega\lambda(\omega)$$

where $\lambda(\omega) = \frac{m^*}{m} - 1$.

The quantities $\tau^{-1}(\omega)$ and $1 + \lambda(\omega)$ describe the frequency-dependent scattering rate and the mass-enhancement of the electronic excitations, which are due to many-body interactions. The quantity $\tilde{\tau}^{-1}(\omega)$ is equivalently termed optical self-energy, $\Sigma_{opt}(\omega, T)$, or memory function, $M(\omega, T)$ (we explicit the temperature dependence). In the literature, the definition of $M(\omega, T)$ is not univoque. In particular, the most common definitions are: $M(\omega, T) = \tilde{\tau}^{-1}(\omega)$ [15, 132, 174], $\hat{M}(\omega, T) = iM(\omega, T) = i\tilde{\tau}^{-1}(\omega)$ [179, 16], or finally $-2\hat{\Sigma}_{opt}(\omega, T) = \hat{M}(\omega, T)$ [91, 92]. To avoid confusion, in the following I will use the first definition, with:

$$M(\omega, T) = M_1(\omega, T) + iM_2(\omega, T) = 1/\tau(\omega, T) + i\omega\lambda(\omega, T)$$

In this case, the dielectric function $\epsilon_D(\omega, T)$ is given by:

$$\begin{aligned}\epsilon_D(\omega,T) &= 1-\frac{{\omega_p}^2}{\omega(\omega+i/\tilde{\tau}(\omega,T))} = 1-\frac{{\omega_p}^2}{\omega(\omega+iM(\omega,T))} = \\ &= 1-\frac{{\omega_p}^2}{\omega(\omega(1+\lambda(\omega,T))+i/\tau(\omega,T))}\end{aligned} \tag{3.12}$$

In terms of the optical conductivity $\sigma(\omega,T)$, which is most often used in the literature, one obtains:

$$\begin{aligned}\sigma_D(\omega,T) &= \frac{1}{4\pi}\frac{{\omega_p}^2}{1/\tilde{\tau}(\omega,T)-i\omega} = \frac{1}{4\pi}\frac{{\omega_p}^2}{M(\omega,T)-i\omega} = \\ &= \frac{1}{4\pi}\frac{{\omega_p}^2}{1/\tau(\omega,T)-i\omega(1+\lambda(\omega,T))}\end{aligned} \tag{3.13}$$

This can be rewritten in the conventional Drude form as:

$$\sigma(\omega,T) = \frac{1}{4\pi}\frac{\omega_p^{*2}(\omega,T)}{1/\tau^*(\omega,T)-i\omega}$$

after introducing the renormalized scattering time and plasma frequency: $1/\tau^*(\omega,T) = 1/\tau(\omega,T)[1+\lambda(\omega,T)]$, $\omega_p^{*2}(\omega,T) = \omega_p^2/[1+\lambda(\omega,T)]$.
The following relations holds, which indicates that $1/\tau(\omega,T)$ and $1+\lambda(\omega,T)$ are Kramers-Kronig related:

$$1/\tau(\omega) = \frac{\omega_p^2}{4\pi}Re\left(\frac{1}{\sigma(\omega)}\right)$$

$$1+\lambda(\omega) = -\frac{\omega_p^2}{4\pi}\frac{1}{\omega}Im\left(\frac{1}{\sigma(\omega)}\right)$$

After having illustrated the phenomenology at the base of the EDM, I focus on the microscopic scattering mechanisms at the basis of $\tau(\omega)$. In the following, various versions of the formalism, which differs in the way the complex and frequency dependent scattering time $\tilde{\tau}(\omega)$ is expressed, are briefly described.

3.5.1 Extended Drude Model in the case of weak electron-phonon coupling

The EDM form illustrated in this section is the first derived version, as proposed by Allen in 1971 [6], to describe the far-infrared optical properties in metals characterized by a non-negligible, though weak, electron-phonon interaction. The aim of the work was to stimulate a debate about the differences in the optical behavior of normal and supeconducting materials. In fact, it will be soon clear how from this theory the electron-phonon coupling function can be extracted. The first applications of this theory [5] allowed to correctly interpret the departures of NiSb and NiAs intraband optical spectra from the conventional Drude behavior. Allen original theory, valid in the limit $T \to 0$, was later generalized for finite T by Shulga [167]. The theory valid for weak electron-phonon coupling was derived within second order perturbation theory. This theory accounts for the additional photon absorption, with respect to a conventional metal, arising from second order processes involving the creation of both a phonon and an electron-hole pair. This approach is equivalent to a first iteration of the collision term in the Holstein-type Boltzmann equation, and is not as accurate as the full solution of the Boltzmann equation [6].

Within these approximations, the memory function $M(\omega, T)$ can be written as a convolution integral between a transport spectral function, $\alpha^2_{tr}F(\Omega)$, and a Kernel function, $K\left(\frac{\omega}{2\pi T}, \frac{\Omega}{2\pi T}\right)$, which describes the thermal dependence of the phononic excitations coupled with the electrons:

$$M(\omega, T) = -2\int_0^\infty \alpha^2_{tr}F(\Omega)K\left(\frac{\omega}{2\pi T}, \frac{\Omega}{2\pi T}\right)d\Omega \tag{3.14}$$

where the (material independent) Kernel function writes:

$$\begin{aligned} K(x,y) = \frac{i}{y} + &\left\{\frac{y-x}{x}\left[\Psi(1-ix+iy) - \Psi(1+iy)\right]\right\} \\ + &\left\{\frac{y+x}{x}\left[\Psi(1-ix-iy) - \Psi(1-iy)\right]\right\} \end{aligned} \tag{3.15}$$

where $\Psi(z)$ are the Digamma functions, $x = \omega/2\pi T$, $y = \Omega/2\pi T$.
The quantity $\alpha^2_{tr}F(\Omega)$ is related to the transport properties of the material. In 1999 Marsiglio [122] found a method to directly determine $\alpha^2_{tr}F(\Omega)$ from spectroscopic data, with an inversion procedure:

$$\alpha^2_{tr}F(\Omega) = \frac{1}{2\pi}\frac{\omega_p^2}{4\pi}\frac{d^2}{d\omega^2}Re\left(\frac{1}{\sigma(\omega)}\right)$$

It must be pointed out that the quantity $\alpha^2_{tr}F(\Omega)$ is different from the more conventional $\alpha^2F(\Omega)$.
Within the weak-coupling formalism, extended to finite temperatures, the temperature and frequency-dependent scattering time $\tau(\omega, T)$ is written as:

$$\begin{aligned} \frac{1}{\tau}(\omega, T) = \frac{\pi}{\omega}\int_0^\infty d\Omega\alpha^2_{tr}F(\Omega)&\left[2\omega coth\left(\frac{\Omega}{2T}\right) - (\omega+\Omega)coth\left(\frac{\omega+\Omega}{2T}\right) + \right. \\ &\left. +(\omega-\Omega)coth\left(\frac{\omega-\Omega}{2T}\right) + \gamma_{imp}\right] \end{aligned} \tag{3.16}$$

I numericaaly verified this model being KK consistent.

3.5.2 Extended Drude Model in the case of strong electron-phonon coupling

In the case of strong electron-phonon coupling, the Extended Drude formalism is derived starting from the Holstein theory for normal metals, which is the most complete theory for metals. Considering the Kubo formula and using complex diagrammatic techniques to evaluate the electron and phonon thermal Green's functions, if one omits vertex corrections (Migdal approximation), the Memory function $M(\omega,T)$ results:

$$\frac{iM(\omega,T)+\omega}{\omega}=\left\{\int_{-\infty}^{+\infty}\frac{f(\xi,T)-f(\xi+\omega,T)}{\omega+\Sigma^{*}(\xi,T)-\Sigma(\xi+\omega,T)+i\gamma_{imp}}d\xi\right\}^{-1} \tag{3.17}$$

$$M(\omega,T)=-i\omega\left\{\int_{-\infty}^{+\infty}\frac{f(\xi,T)-f(\xi+\omega,T)}{\omega+\Sigma^{*}(\xi,T)-\Sigma(\xi+\omega,T)+i\gamma_{imp}}d\xi\right\}^{-1}+i\omega \tag{3.18}$$

where f is the Fermi-Dirac distribution, $\Sigma(\omega,T)$ and $\Sigma^{*}(\omega,T)$ respectively the electron and hole self-energies. These are obtained averaging $\Sigma(\omega,k,T)$ over the Fermi surface and assuming a constant density of states at E_F.

The optical self energy $M(\omega,T)$ and the one-particle electronic self-energy $\Sigma(\omega,T)$ (averaged over the Fermi surface) have the same analytical properties. However, they are conceptually different quantities. $\Sigma(\omega,T)$ is a quantity measured by a photoemission experiment, since this technique probes the single particle excitations of the (N-1) particle system, which can be described in terms of the spectral function and the single particle self energy. On the contrary, an optical experiment looks at the particle-hole excitations of an N particle system, and gives information about the joint particle-hole density of states.

The electron self-energy $\Sigma(\omega,T)$ is calculated through a convolution integral between the coupling function $\alpha^2F(\Omega)$ and a kernel function $L(\omega,\Omega,T)$, in the following way:

$$\Sigma(\omega,T)=\int_{0}^{\infty}\alpha^2F(\Omega)L(\omega,\Omega,T)d\Omega \tag{3.19}$$

The kernel function $L(\omega,\Omega,T)$ in this formalism is written as:

$$L(\omega,\Omega,T)=\int\left[\frac{n(\Omega')+f(\Omega)}{\Omega-\omega+\Omega'+i\delta}+\frac{1+n(\Omega')-f(\Omega)}{\Omega-\omega-\Omega'-i\delta}\right]d\Omega' \tag{3.20}$$

$n(\Omega)$ being the Bose-Einstein distribution. The integral can be calculated analytically, and results in:

$$L(\omega,\Omega,T)=-2\pi i\left[n(\Omega,T)+\frac{1}{2}\right]+\Psi\left(\frac{1}{2}+i\frac{\Omega-\Omega'}{2\pi T}\right)-\Psi\left(\frac{1}{2}-i\frac{\Omega+\Omega'}{2\pi T}\right) \tag{3.21}$$

where Ψ are the digamma functions. The kernel function describes the thermal excitations of the glue and the electrons. It is important to note that the terms containing the temperature T, are separated into one addend containing the Bose-Einstein distribution n (in which T represents the temperature of the glue excitations) and in two addends containing the Digamma functions Ψ (which are the result of the Fermi-Dirac distribution integration, and in which T is related to the electronic temperature). Thus, the temperatures of electrons and bosons acts on different terms. This will have important implications in the analysis presented in Chapter 6. I numericaaly verified also this model being KK consistent.

3.5.3 Extended Drude Model in the case of a non-constant density of states

A further evolution of the EDM takes into account the possibility of a non-constant electronic density of states, to correctly reproduce the effect of the scattering of electrons with bosonic excitations in systems where a gap is opened in the electronic density of states. This formalism will be relevant in analyzing spectroscopic data in the pseudogap phase. This model was developed by Sharapov and Carbotte in 2005 [166], and applied by Hwang in 2011 to the analysis of HTSC spectroscopic data [90].
In this model, the imaginary part of the electronic self energy is given by:

$$\begin{aligned}\Sigma_2(\omega,T) = -\pi\int_0^\infty \alpha^2F(\Omega)\Bigg\{&\frac{\tilde{N}(\omega+\Omega,T)}{N(0,T)}\left[n(\Omega,T)+f(\omega+\Omega,T)\right]+\\ &+\frac{\tilde{N}(\omega-\Omega,T)}{N(0,T)}\left[1+n(\Omega,T)-f(\omega-\Omega,T)\right]\Bigg\}d\Omega\end{aligned} \tag{3.22}$$

To compute the real part of $\Sigma(\omega,T) = \Sigma_1(\omega,T) + i\Sigma_2(\omega,T)$, we use the Kramers-Kronig relations (see equations 3.6). The calculation of the Memory function is done in the same way as in 3.4.2. The density of states $\tilde{N}(\omega,T)$ can be written in the following form [90]:

$$\tilde{N}(\omega,T) = \begin{cases}\tilde{N}(0,T) + [1-\tilde{N}(0,T)]\left(\frac{\omega}{\Delta_{pg}}\right)^2 & for\ |\omega| \leqslant \Delta_{pg}\\ 1+\frac{2}{3}[1-\tilde{N}(0,T)] & for\ |\omega| \in (\Delta_{pg}, 2\Delta_{pg})\\ 1 & for\ |\omega| \geqslant 2\Delta_{pg}\end{cases} \tag{3.23}$$

Where Δ_{pg} is the energy gap width, while $\tilde{N}(0,T)$ indicates the effectiveness of the gap in reducing the density of states; it is a sort of gap filling. The ratio $\tilde{N}(\omega,T)/N(0,T)$ for Δ_{pg}=350 cm^{-1} and $\tilde{N}(0,T) = 0.5N(0,T)$, representing the pseudogap shape, is shown in Fig. 3.1. The effect of the opening of the pseudogap (i.e., $\tilde{N}(0,T) < N(0,T)$) is a reduction of $1/\tau(\omega,T)$ [166].

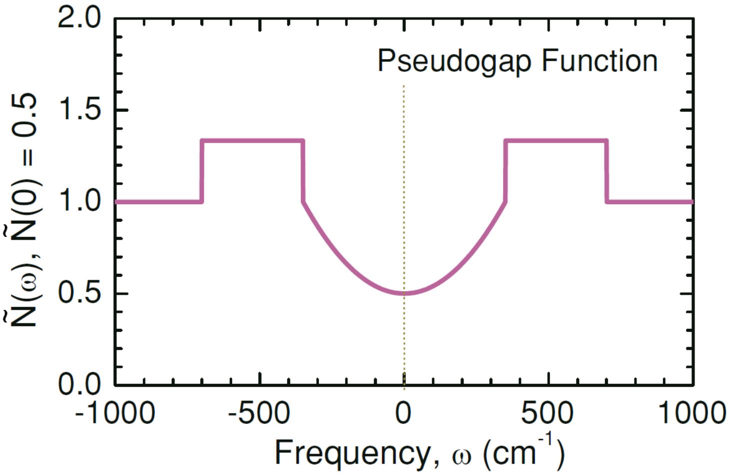

Figure 3.1: The effect of the gap opening on the normalized density of states $\tilde{N}(\omega,T)/N(0,T)$, being $N(0,T)$ the (constant) density of states in the case of no gap, is reported. Here $\tilde{N}(0,T) = 0.5N(0,T)$, which represents the value for the density of state at zero frequency, and Δ_{pg}=350 cm^{-1}. From [90].

This effect must be taken into account in the attempts of extracting a reliable $\alpha^2F(\Omega)$ from spectroscopic data, when a gap in the density of states is opened. I numericaaly verified also this model being KK consistent.

3.5.4 Generalization of the electron-phonon coupling function $\alpha^2F(\Omega)$

In the models reported so far, the function describing the coupling of the electrons with bosonic excitations has been indicated as $\alpha^2F(\Omega)$, mainly for historical reasons: the only scattering mechanism relevant for conventional superconductors is the electron-phonon one, and $\alpha^2F(\Omega)$ is known as the electron-phonon coupling function. A generalization of the theory to a more universal electron-boson interaction (more appropriate to the HTSC field), without any change in the formalism, is possible simply replacing $\alpha^2F(\Omega)$ with a general electron-boson coupling function, usually indicated as $\Pi(\Omega)$, and called the Glue Function. This function takes into account all the possible channels for the electron-boson interaction. The main distinction is between phonons and bosons of electronic origin (such as spin fluctuations and loop currents). One can thus write:

$$\Pi(\Omega) \equiv \alpha^2F(\Omega) + I^2\chi(\Omega) \tag{3.24}$$

where the latter term expresses the electron coupling with all the bosons of electronic origin.

Within this framework, it is instructive to consider the work by van Heumen [179], in which the glue function $\Pi(\Omega)$ is extracted by fitting the EDM to the spectroscopic data (the formalism used is the strong coupling one, in which $\alpha^2F(\Omega)$ has been replaced by $\Pi(\Omega)$). The guess-form for $\Pi(\Omega)$ is a histogram-like function. The Glue Function $\Pi(\Omega)$ of HTSC presents some universal features, as can be argued looking at the results obtained on different materials, at different doping levels and temperatures (Fig. 3.2).

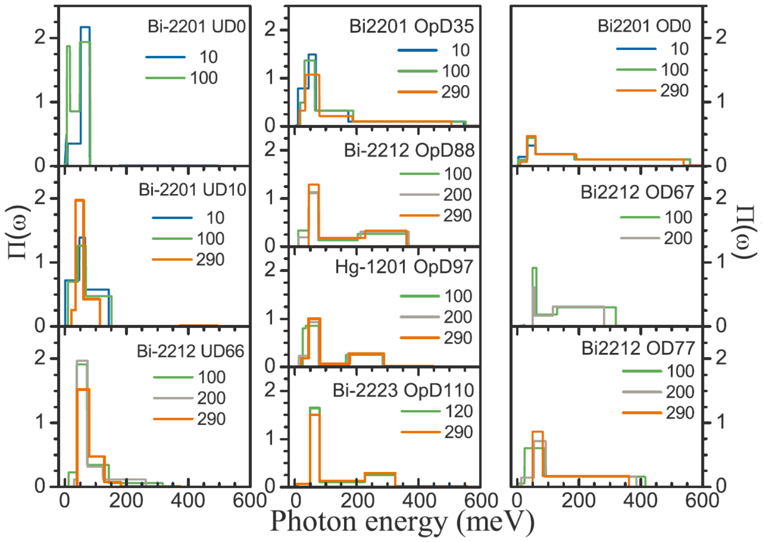

Figure 3.2: The Bosonic Glue $\Pi(\Omega)$ for several cuprate superconductors, at various temperatures and for different doping levels, is reported. From [179].

The universal features of $\Pi(\Omega)$ are a peak at 50-80 meV and a broad continuum extending up to 400-500 meV. The energy at which the peak occurs is in the same energy range of the kink observed in ARPES spectra, in the nodal direction [104]. It must be noted that with a similar form of $\Pi(\Omega)$, the optical properties of a material can be reproduced at all temperatures. Nevertheless, a small temperature-dependence of the Bosonic Glue $\Pi(\Omega)$ has been observed, which is difficult to catch by equilibrium measurements, and which origin is source of debate [92, 179, 15, 16].

In Fig. 3.3, I report the typical spectrum for a $I^2\chi(\Omega)$ spectrum given by electron-boson interaction with spin fluctuations and current loops.

3.6 Useful Sum Rules and Spectral Weight in High-Tc

The requirement of causality for every response function brings to the concept of dispersion relations, which are integral formula relating dispersive processes

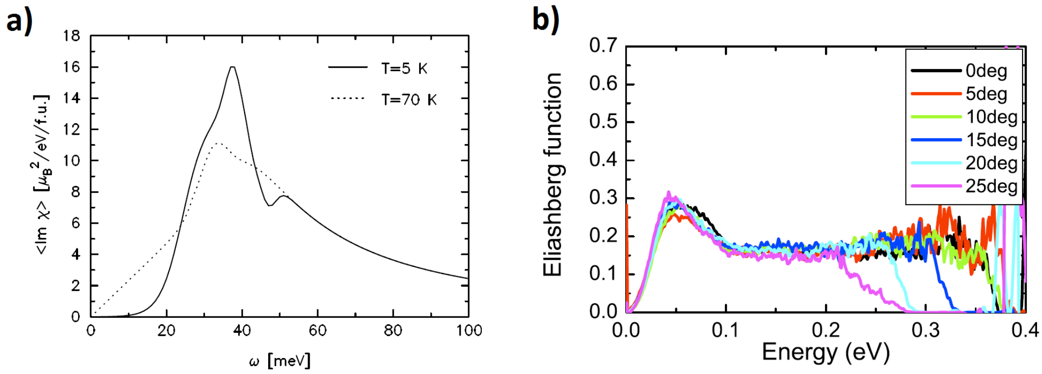

Figure 3.3: a) A typical $I^2\chi(\Omega)$ spectrum for spin fluctuations, measured by inelastic neutron scattering on a YBCO sample, is reported. From [47]. b) A typical $I^2\chi(\Omega)$ spectrum (here labeled as Eliashberg coupling function) for the magnetic excitation modes of the current loop ground state is reported. It is extracted from ARPES data on a slightly under-doped Bi2212 compound. The angle indicates the direction of the cut in the Brillouin zone along which data are extracted; it is measured from the $Y\Gamma$ direction. From [34].

to absorption ones (causality requires that absorption and dispersion processes be intimately related, and cannot be considered as independent). The real and imaginary parts of the dielectric function $\epsilon(\omega)$ or of the refraction index $n(\omega)$ are thus related by a dispersion relation, expressed through the Kramers-Kronig integral relations. However, these relations hold for the real and the imaginary parts of any response function (see equations 3.6).

Starting from these relations, it is possible to derive useful sum rules, the most important of which is the so-called f-sum rule (or global oscillator strength sum rule):

$$\int_0^\infty \omega\epsilon_2(\omega)d\omega = \frac{\pi}{2}\omega_p^2 \tag{3.25}$$

where ω_p is the dressed plasma frequency of the system, i.e.: ${\omega_p}^2 = \frac{4\pi Ne^2}{m}$, being N the total density of electrons participating to the interaction with the electromagnetic wave.

Sum rules indicate conserved quantities, that is, quantities that do no change under a change, for example, of temperature. Analyzing the left hand side of eq. 3.n, it turns out that N must be a conserved quantity.

From this sum rule, the concept of spectral weight (SW) follows straightforwardly: It is defined by:

$$SW \equiv \int_0^\infty \sigma_1(\omega)d\omega = \frac{1}{8}\omega_p^2 \tag{3.26}$$

SW is by definition a conserved quantity.

From this general definition, some particular results about the superconductivity in various materials can be derived, which are of fundamental importance. The fact that the total spectral weight is conserved means that it must be the same at every temperature, and thus, the spectral weight above T_c (for the system in the normal state) must equal the spectral weight below T_c (for the system in the superconducting state). This concept can be expressed by writing: $SW_{SC} = SW_N$, with the two spectral weights referring respectively to the superconducting state and to the normal state. The superconducting state spectral weight is often written separating the regular contribution, given from non-condensed electrons, from the singular contribution, due to the condensed electrons (looking at the system as a two-fluid system). The latter contribution comes from the delta at zero-frequency in the optical conductivity, $\sigma_0(\omega) = \frac{\pi N_s e^2}{2m}\delta(0)$, and writes: $D \equiv \int_0^\infty \sigma_0(\omega)d\omega$. Thus, $SW_{SC} = SW_{SC,reg} + D$.

In principle, nothing prevents spectral weight transfer to occur form one spectral region to another. To extract useful information, it is customary to consider a partial sum rule, calculating the spectral weight up to a cutoff frequency, ω_c; the partial spectral weight is defined as:

$$SW(\omega_c) \equiv \int_0^{\omega_c} \sigma_1(\omega)d\omega = \frac{\pi N_{eff}(\omega_c)e^2}{2m} \tag{3.27}$$

The natural cutoff frequency to be chosen, is the one at the crossover between intraband and interband contributions to the dielectric function. This energy cutoff equals ∼1 eV in cuprates, while it is smaller in conventional, BCS superconductors. For both the normal state and superconducting state spectral weight, one can thus write: $SW_j = A_j + B_j$ (j=N,SC), with $A \equiv \int_0^{\omega_c} \sigma_1(\omega)d\omega$ representing the intraband contribution to the SW, while $B \equiv \int_{\omega_c}^\infty \sigma_1(\omega)d\omega$ represents the intraband contribution to the SW.

For BCS superconductors, with the choice of a proper, low-energy cutoff, the relation $A_N = A_{SC} + D$ holds. This is the famous Ferrell-Glover-Tinkham (FGT) sum rule [175], which states the well known fact that, in BCS superconductors, the spectral weight removed from the gap region is entirely recovered by the singular contribution at zero-frequency, related to the superconducting condensate. Typically, the spectral weight is recovered within a few (∼10) Δ [175]. No modification in B is observed, i.e., $B_N = B_{SC}$. For high-temperature superconductors, on the other hand, it is said that the FGT sum-rule is violated, in the sense that: $A_N \neq A_{SC} + D$. Obviously, the total spectral weight is conserved. This is written as:

$$A_N + B_N = D + A_{SC} + B_{SC} \tag{3.28}$$

or, alternatively:

$$D = A_N - A_{SC} + B_N - B_{SC}$$

This means that the superconductivity-induced spectral weight rearrangement is not recovered within the low-energy, intraband region, but an involvement of high-energy states (in the interband transitions region) is present.
Experimental results [131, 112] indeed suggested that (see Fig. 3.4), in the High-Tc superconductor Bi2212, an increase of the intraband spectral weight upon lowering T (beyond the thermal contribution related to the thermal narrowing of the Drude oscillator [138]) goes on. This happens at the expense of the high energy spectral weight (B term, related to the spectral range 10.000 to 20.000 cm^{-1}), which diminishes upon lowering T. That this peculiar behavior is related to the onset of superconductivity is made clear by observing that the spectral weight trend presents a slope change exactly at $T = T_c$ [112]. These results, referred to both underdoped and optimally doped samples, contrast with what predicted by the BCS theory.

The concept of spectral weight acquires further importance since it is intimately related to carriers kinetic energy. This is exactly true in a limiting case, in which the system can be modeled with a single conduction band, within the nearest-neighbour tight-binding model [86, 139]. It has been demonstrated that the total intraband spectral weight (similar to the A term) can be related to the kinetic energy T_δ of the charge carriers (holes) associated to hopping process in the δ direction, through the following relation [86]:

$$\int_0^\infty \sigma_{1,D}(\omega)d\omega = \frac{\pi^2 a_\delta^2 e^2}{2\hbar^2 V_{Cu}} \langle -T_\delta \rangle \tag{3.29}$$

where $\sigma_{1,D}$ is the real part of the optical conductivity, related only to the intraband region, a_δ is the lattice spacing in the Cu-O plane, projected along the direction determined by the in-plane polarization of the incident light, and V_{Cu} is the volume per Cu atom.
To interpret optical data, often the following relation is assumed:

$$A \equiv \int_0^{\omega_c} \sigma_1(\omega)d\omega \approx \int_0^\infty \sigma_{1,D}(\omega)d\omega$$

meaning that the intraband spectral weight is evaluated integrating optical data up to the cutoff frequency ω_c. Interpreting the observed trend for the superconductivity-induced spectral weight shift in terms of carriers kinetic energy, it turns out that the increase of intraband spectral weight observed for underdoped and optimally doped samples upon crossing T_c, implies a decrease for the carriers kinetic energy (i.e., a kinetic energy gain). This is in contrast to what one expects for conventional, BCS superconductors, where a loss of kinetic energy upon entering the superconducting phase is overcompensated by a potential energy gain. This observation of a possible, direct kinetic energy gain, for High-Tc superconductors, is is agreement with what proposed by Hirsch and Marsiglio [85, 86, 124].

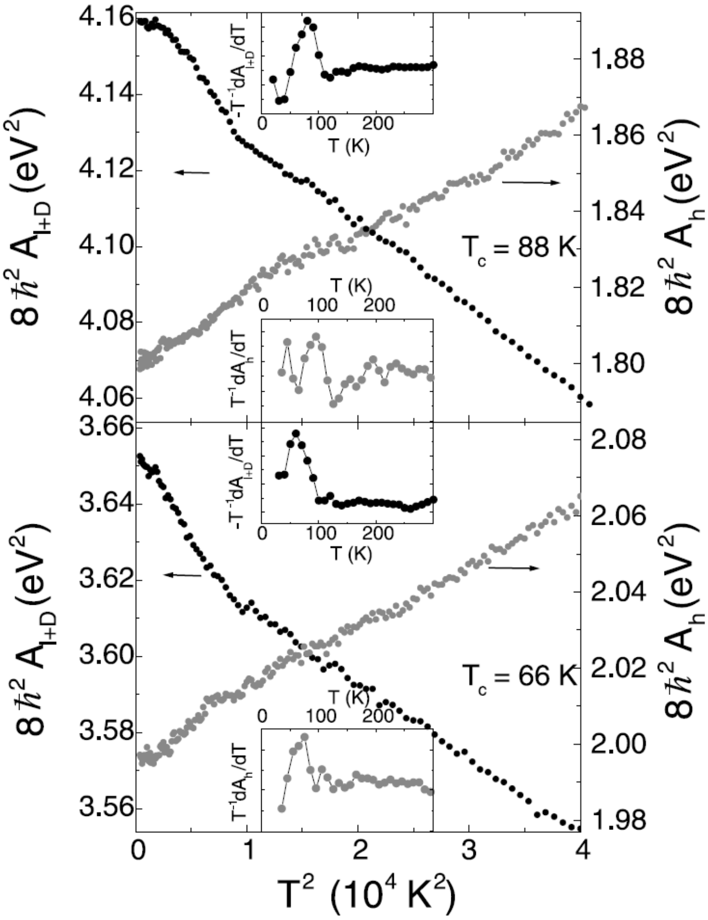

Figure 3.4: The picture shows the lowering of the interband (high-energy, A_h) spectral weight upon lowering the system temperature. Being these data obtained by static optical spectrosocpy, they include the effect of the thermal-narrowing (upon lowering the system temperature) of the Drude component. The component related to the onset of superconductivity, which has the same 'sign', is clearly present and evidenced by a change in the slope of the effect, which happens exactly at T_c. A_{l+D} is the total low-energy (intraband) spectral weight. From [131].

It has to be mentioned that, on the overdoped side of the phase diagram, a behavior more similar to the conventional superconductors has been observed, for High-Tc. This finding suggests that at high doping levels, HTSC superconductivity behaves in a BCS-like manner. Indeed, in this region the system gradually recovers the conventional T^2 law for the electrical resistivity, fingerprint of a Fermi-liquid-like behavior [171].

Concluding, a final remark about what happens in conventional superconductors. Since formula 3.28 is always verified, and an increase of carrier kinetic energy upon lowering temperature below T_c directly follows from BCS theory, a slight transfer of spectral weight to high energies must happen. Thus, though experimentally undetectable, a small spectral weight transfer must exist (a spectral weight transfer has never been observed in BCS superconductors, since it is proportional to the condensation energy [175], in tuurn proportional to Δ^2, which in BCS systems is of the order $\sim$1 meV [175]). In a certain sense, the FGT sum rule is strictly never true. FGT sum rule is indeed a phenomenological relation, and up to now no such spectral weight transfer has been measured in conventional superconductors.

From equilibrium optical measurement, with the help of the illustrated sum rule, very important informations about the mechanisms driving the superconducting transition in copper oxide based superconductors have been extracted [131, 179, 139, 138]. Anyway, these findings are not conclusive, in the sense of assigning these spectral weight shifts a clear physical origin. Moreover, the problem of the thermal narrowing of the Drude peak, upon lowering the temperature, must be faced. Recently it has been demonstrated [138] that the temperature dependence of the optical integral $A \equiv \int_0^{\omega_c} \sigma_1(\omega)d\omega$ in the normal state of the cuprates is due solely to a cutoff-dependent term that accounts for the extension of the Drude peak beyond the upper bound ω_c of the integral, rather than to a true sum-rule violation. This implies that the dominant contribution to the observed sum-rule violation in the normal state is only due to the finite cutoff ω_c and to a thermal effect.
With the help of the recently developed time-resolved spectroscopic technique (see Chapter 5), we were able to clarify that the whole spectral weight transfer observed by static spectroscopies upon entering the superconducting phase comes precisely from two high energy states (at 1.5 and 2 eV), and that a trend form a superconductivity induced kinetic energy gain in the underdoped side of the phase diagram, to a BCS-like superconductivity induced kinetic energy loss in the overdoped side of the phase diagram, exists. More details can be found in Chapter 8. The time-resolution eliminates the problem of the finite cutoff ω_c, being the electronic effects related to the condensate formation and the thermal ones disentangled by their timescales.

3.7 Y-Bi2212 Static Dielectric Functions Analysis

In this conclusive paragraph I present the results of the fitting of the Lorentz and Extended Drude model dielectric function, with the proper formalism, to the optimally doped Y-Bi2212 sample (T_c=96 K) dielectric function experimental data. I will treat singularly the cases of the optical properties for the Y-Bi2212 sample in the normal state phase (T=300 K, section 3.7.1), in the pseudogap phase (T=100 K, section 3.7.2) and in the superconducting phase

(T=20K, section 3.7.3). The main difference in the model dielectric function for the various cases will stand mainly in the Extended Drude formalism chosen to model the low-energy part of the optical properties. This choice has been guided by the relevant effect taking place in the non-equilibrium condition. The *ab*-plane static optical properties of the Y-Bi2212 OP sample, presented in Fig. 3.5 for a number of representative temperatures, present very little differences. It is only the non-equilibrium susceptibility which strongly differs from one phase to the other, as I will demonstrate in Chapters 6, 7, 8. The choice of the static dielectric function to be employed for the static data is thus guided by the non-equilibrium observations. However, the common features of the model dielectric function are described in detail only in 3.7.1.

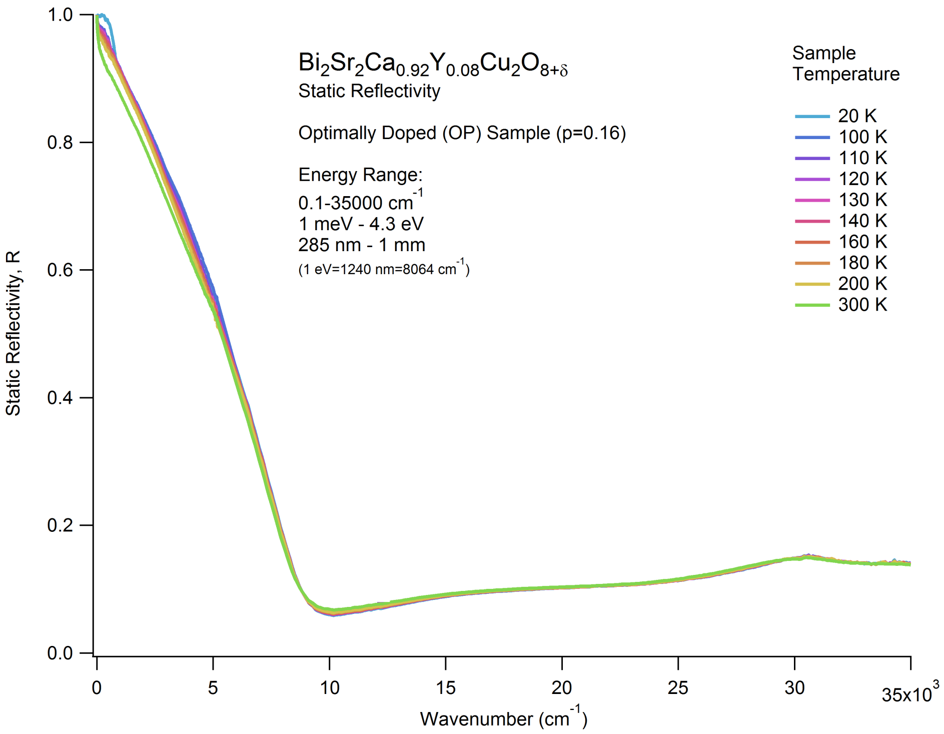

Figure 3.5: Y-Bi2212 Optimally Doped Static Optical Properties. The reflectivity is presented in a broad energy range and in a wide range of temperatures. The low-energy part ($\hbar\omega \lesssim$10000 cm^{-1}) is governed by a metallic-like behavior due to intraband transitions, while the high-energy part ($\hbar\omega \gtrsim$10000 cm^{-1}) presents an insulating behavior, due to interband transitions. The first will be modeled within an Extended Drude model dielectric function, the latter using a proper number of Lorentz oscillators.

In Fig. 3.5 I reported the reflectivity $R(\omega)$ of Y-Bi2212. It has been calculated, through formula 3.3, starting from the ellipsometric data published in [178]. The procedure used to experimentally measure the original data, i.e., $\epsilon_1(\omega)$ and $\epsilon_2(\omega)$, is worth to be described. Indeed, $\epsilon_1(\omega)$ and $\epsilon_2(\omega)$ have been obtained by applying the KramersKronig [185] relations to the measured reflectivity, in the range 50-6000 cm^{-1}, and directly from conventional spectroscopic ellipsometry, in the range 1500-36000 cm^{-1}. This combination allowed a very accurate determination of the dielectric function $\epsilon(\omega)$ in the entire combined frequency range. Due to the off-normal angle of incidence used with ellipsometry, the *ab*-plane pseudo-dielectric function had to be corrected for the *c*-axis admixture.

3.7.1 Equilibrium Optical Properties of Optimally Doped Y-Bi2212 at T=300 K: the Glue Function

In this paragraph I will present the fitting results of the Extended Drude and Lorentz model dielectric function to the optimally doped Y-Bi2212 sample (T_c=96 K) dielectric function, at T=300 K. Among the parameters extracted from the fitting procedure (listed in Table 3.1), of particular importance is the bosonic glue spectrum, $\Pi(\Omega)$, presented as the conclusive result of this paragraph (Fig. 3.8).

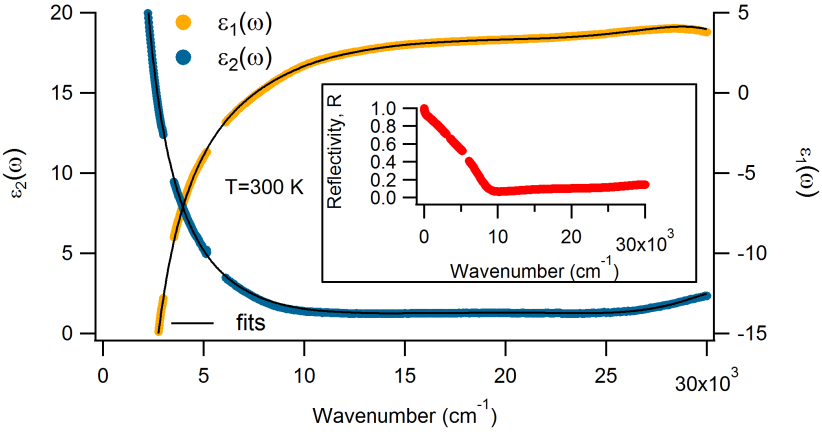

Figure 3.6: The real and imaginary parts of the dielectric function of OP $Bi_2Sr_2Y_{0.08}Ca_{0.92}Cu_2O_{8+\delta}$ (p=0.16) sample, measured by static ellipsometry at T=300 K, is reported. Solid lines are the fit to the data, performed with the model described in the text. In the inset, the sample reflectivity is shown.

Fig. 3.6 reports the real ($\epsilon_1(\omega)$) and imaginary ($\epsilon_2(\omega)$) parts of the optimally doped sample dielectric function, measured by spectroscopic ellipsometry. In the graph inset, the reflectivity $R(\omega)$, calculated from the data with formula 3.3, is presented. From these data we can clearly see that, below 10000 cm^{-1} (1.25 eV), the optical properties are dominated by the Drude response of free carriers coupled to a broad spectrum of bosons [92, 179], whereas in the high-energy region ($\hbar\omega$ >1.25 eV), a major role is played by several interband transitions. The best fit to the data, performed simultaneously on $\epsilon_1(\omega)$ and

$\epsilon_2(\omega)$, is reported on the same graph as thin solid black lines. This fit has been obtained modeling the dielectric function as:

$$\epsilon(\omega, T) = \epsilon_D(\omega, T) + \sum_{i=1}^{m} \epsilon_{Li}(\omega, T)$$

where $\epsilon_D(\omega, T)$ and $\epsilon_{Li}(\omega, T)$ represent Drude and Lorentz oscillators, the latter being indexed by i. We employed six Lorents oscillators, thus i=1-6. $\epsilon_D(\omega, T)$ has been modeled as described in paragraph 3.5.2 (formulae 3.12, 3.18, 3.19, 3.21). The dressed plasma frequency of the system (the frequency for which $\epsilon_1(\omega, T) = 0$), equals 1 eV.

Fig. 3.7 reports the different contributions of the single oscillators to the imaginary part of the dielectric function $\epsilon_2(\omega)$. Three regions are evident: the Intraband one, governed by the Extended Drude contribution, a region of low-intensity transitions, mostly related to transitions between many-body Cu-O states, and finally an intense feature (represented by transitions i=4,5,6, even though only the i=4 one is visible on this wavenumber scale) which represents the reminiscence of the charge-transfer (CT) gap, shifted to higher energies because of the doping effect [51].

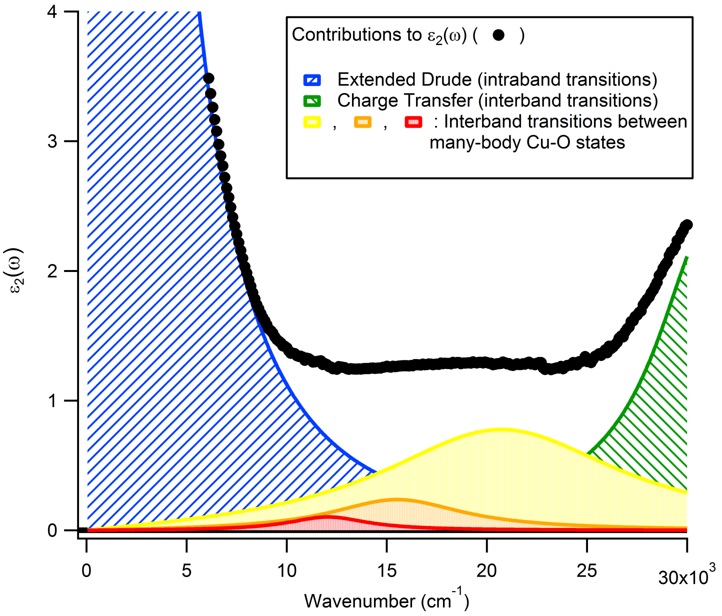

Figure 3.7: The Lorentz oscillators, as resulted from the fitting procedure, are reported. In particular, their single contribution to the imaginary part of the dielectric function is evidenced. Three oscillators represent transitions between many-body Cu-O states, while the remaining three oscillators, here represented as a whole, represent the reminiscence of the charge-transfer gap.

Fig. 3.8 contains the bosonic spectrum $\Pi(\Omega)$, extracted from the fitting procedure. This spectrum, being Ω the boson frequency, represents the electron-boson coupling strength at boson frequency Ω multiplied by the boson density of states at boson frequency Ω. An histogram-like form for the glue function has been assumed [38]. The spectrum is characterized by a low-energy part (up to 40 meV), compatible with the coupling to acoustic phonons [1] and Raman-active optical phonons, involving c-axis motion of the Copper ions [108]; a narrow, intense peak centered at $\sim$60 meV, attributed to the anisotropic coupling to either out-of-plane buckling and in-plane breathing Cu-O optical modes [56] or bosonic excitations of electronic origin, such as spin fluctuations [48], and finally a broad continuum, extending up to 350 meV [141, 92, 179], i.e., well above the characteristic phonon cut-off frequency ($\sim$90 meV). In the determination of this bosonic glue, an upper limit of Ω_{max}=1 eV has been artificially imposed, even if this limit could exclude some high-energy contributions to the electron-boson coupling.

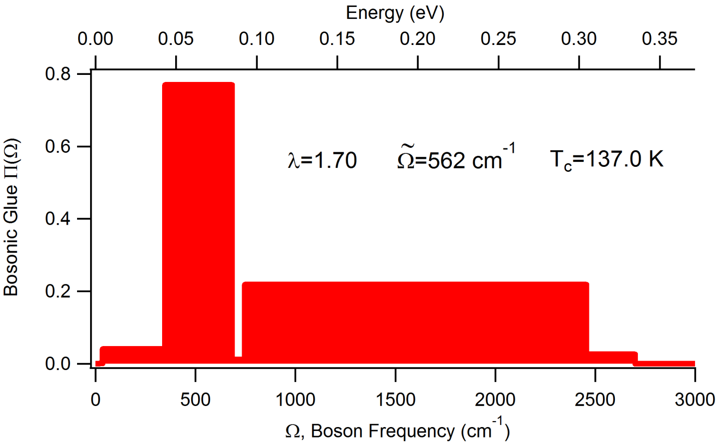

Figure 3.8: The Glue Function $\Pi(\Omega)$, representing the electron-boson coupling strenght at the boson frequency Ω, is reported. This quantity is a result of the fitting procedure to the static data reported in Fig. 3.6. The values of λ, $\tilde{\Omega}$ and T_c have been calculated with expressions 2.3, 2.4, 2.5 respectively, as reported in section 2.4.

As I anticipated, the interband transitions in the near-IR/visible/UV spectral range has been reproduced using six Lorentz oscillators at resonant frequencies ω_{0i}=1.26, 1.64, 2.25, 3.18, 3.60 and 4.17 eV. The number of the interband oscillators is the minimum necessary to obtain a stable fit. Adding more oscillators does not significantly improve the χ^2 of the fit in the 1-5 eV region. The attribution of the 1.26, 1.64, 2.25, 3.18 eV transitions, that are the most relevant to this work, is a subject of intense debate. As a general phenomenological trend, the CT gap edge (hole from the upper Hubbard band with $d_{x^2-y^2}$ symmetry to the O-2$p_{x,y}$ orbitals), peculiar of the undoped compound, is about 2 eV [15]. Upon doping, a structure reminiscent of the CT gap moves to higher energies, while the gap is filled with states at the expense of spectral weight at energy higher than ∼2 eV [15]. Dynamical mean field calculations of the electron spectral function and of the *ab*-plane optical conductivity for the hole-doped three-band Hubbard model recently found that the Fermi level moves into a broad (∼2 eV) and structured band of mixed Cu-O character, corresponding to the Zhang-Rice singlet states [51]. The empty upper Hubbard band, which involves Cu-3d^{10} states, is shifted to higher energies with respect to the undoped compound, accounting for the blue shift of the optical CT edge to 2.5-3 eV. The structures appearing in the optical conductivity at 1-2 eV, that is, below the remnant of the CT gap, are mostly related to transitions between many-body Cu-O states at binding energies as high as 2 eV (for example, singlet states) and states at the Fermi energy. Interpretation of the 1.26 eV structure in terms of a d-d excitation [72] can be ruled out, since the oscillator strength obtained from the fit is incompatible with the temperature dependence of a phonon assisted d-d transition, observed in undoped compounds [17].

The dielectric functions of underdoped and overdoped samples have been extrapolated from the illustrated optimally-doped one following the trend of the optical properties at different dopings, as reported in [26]. In Table 3.1 I report the fitting results for the OP sample.

3.7.2 Equilibrium Optical Properties of Optimally Doped Y-Bi2212 at T=100 K: role of the Gap

Below T^* (onset temperature for the pseudogap), the opening of a gap in the density of states impedes the use of the same EDM formalism used for the T=300 K case to reproduce experimental data. In fact, it is known that in cuprates an energy gap in the density of states opens at the T^* temperature [49]. To correctly interpret equilibrium spectroscopic data below T^*, the Extended Drude part of the previous model has been replaced with the recently developed model presented in section 3.5.3, accounting for the gap opening. This section reports on the results of this new approach.

Taking into account the effect of the opening of a gap in the optical properties is a difficult task, since static measurements are not accurate enough to evidence such small effects. Our best fit has been done by assuming a value of Δ_{pg} equal to 350 cm^{-1} [153]; a value for the gap amplitude $\tilde{N}(0,T)$ of 0.7 allowed us to obtain the best fit. I keep the Glue Function $\Pi(\Omega)$ equal to the one extracted by the fit to the T=300 K data, sice, also in this respect, it is difficult to evidence the small temperature-dependence of the Glue by fitting the EDM to equilibrium ellipsometric data. This EDM formalism accounting for a gap in the density of states will reveal of great importance in the analysis of the time-resolved data taken in the pseudogap, as reported in Chapter 7.

The fitting of the Extended Drude model presented in section 3.5.3, and of six Lorentz oscillators (as I did for the T=300 K case) to the equilibrium ellipsometric data at T=100 K, is presented in Fig. 3.9.

Table 3.1: Fitting Parameters for the Model Dielectric Function of Optimally Doped $Bi_2Sr_2Y_{0.08}Ca_{0.92}Cu_2O_{8+\delta}$ (p=0.16) at T=300 K

Parameter	Value	Unit
ϵ_∞	2.58	
ω_{p0}	18806	cm^{-1}
γ_{imp}	192	cm^{-1}
T	300	K
ω_{01}	12305	cm^{-1}
ω_{p1}	2472	cm^{-1}
γ_1	4872	cm^{-1}
ω_{02}	16026	cm^{-1}
ω_{p2}	5500	cm^{-1}
γ_2	8097	cm^{-1}
ω_{03}	21947	cm^{-1}
ω_{p3}	15603	cm^{-1}
γ_3	14688	cm^{-1}
ω_{04}	31057	cm^{-1}
ω_{p4}	17738	cm^{-1}
γ_4	6190	cm^{-1}
ω_{05}	35146	cm^{-1}
ω_{p5}	15905	cm^{-1}
γ_5	6395	cm^{-1}
ω_{06}	40753	cm^{-1}
ω_{p6}	28647	cm^{-1}
γ_6	6949	cm^{-1}

The effect in the simulated reflectivity obtained by assuming a complete closing of the gap ($\tilde{N}(0,T)$=1) are reported in Fig. 3.10, together with the reflectivity obtained by the fit.

The fitting parameters obtained with this approach are presented in Table 3.2. The Lorentz oscillator parameters are only slightly changed with respect to the values obtained for the fit to the T=300 K data.

3.7.3 Equilibrium Optical Properties of Optimally Doped Y-Bi2212 at T=20 K

Below T_c the superconducting gap 2Δ(T) opens, and a zero-energy peak in the real part of the optical conducibility, representing the 'optical' response of the condensed electrons, appears. Thus, below T_c the far-infrared reflectivity is dominated by the effect of the opening of the superconducting gap and by

Table 3.2: Fitting Parameters for the Model Dielectric Function of Optimally Doped $Bi_2Sr_2Y_{0.08}Ca_{0.92}Cu_2O_{8+\delta}$ (p=0.16) at T=100 K

Parameter	Value	Unit
ϵ_∞	2.62	
ω_{p0}	18666	cm^{-1}
γ_{imp}	213	cm^{-1}
T	100	K
$\tilde{N}(0,T)$	0.7	
Δ_{pg}	350	cm^{-1}
ω_{01}	12305	cm^{-1}
ω_{p1}	2261	cm^{-1}
γ_1	4872	cm^{-1}
ω_{02}	16075	cm^{-1}
ω_{p2}	5296	cm^{-1}
γ_2	8160	cm^{-1}
ω_{03}	21947	cm^{-1}
ω_{p3}	15600	cm^{-1}
γ_3	14688	cm^{-1}
ω_{04}	31057	cm^{-1}
ω_{p4}	16900	cm^{-1}
γ_4	6190	cm^{-1}
ω_{05}	35146	cm^{-1}
ω_{p5}	15905	cm^{-1}
γ_5	6395	cm^{-1}
ω_{06}	40753	cm^{-1}
ω_{p6}	28646	cm^{-1}
γ_6	6949	cm^{-1}

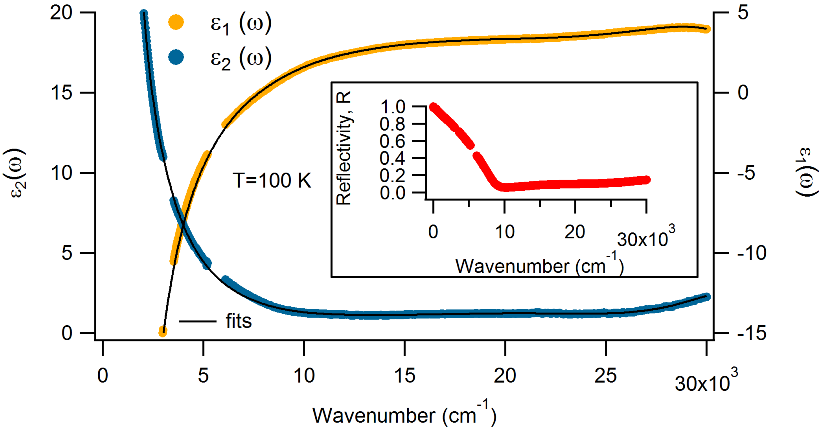

Figure 3.9: The real and imaginary parts of the dielectric function of OP $Bi_2Sr_2Y_{0.08}Ca_{0.92}Cu_2O_{8+\delta}$ (p=0.16) sample, measured by static ellipsometry at T=100 K, is reported. Solid lines are the fit to the data, performed with the model described in the text. In the inset, the sample reflectivity is shown.

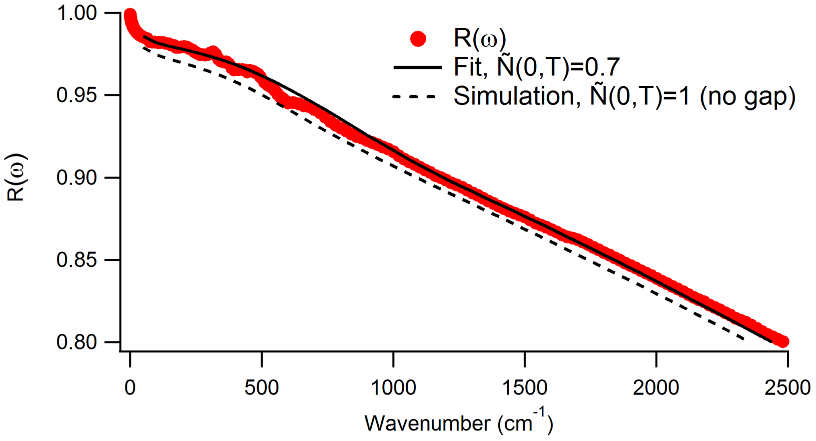

Figure 3.10: The fit to the reflectivity at T=100 K is presented (solid black line). Black dashed line is the result of a simulation for the reflectivity obtained from the same fitting parameters, except for the value of $\tilde{N}(0,T)$, equal to 1, i.e., no gap.

the emergence of the condensate $\delta(0)$ function. The extraction of the boson spectral function in the case $T < T_c$ is difficult [179]. For this reason, our fit to the T=20 K data will prescind from the lowest energy ($\hbar\omega \lesssim$100 meV) region. With the assumption that the electron-boson coupling does not change upon entering the superconducting phase, we will keep the same electron-boson coupling function $\Pi(\Omega)$ determined for the T=300 K case, and the formalism of the EDM without gap in the density of states (section 3.5.2).
The fitting results of the Lorentz (six Lorentz oscillators are enough to obtain the best χ^2 for the fit) and EDM model to the T=20 K ellipsometric data are

reported in Fig. 3.11.

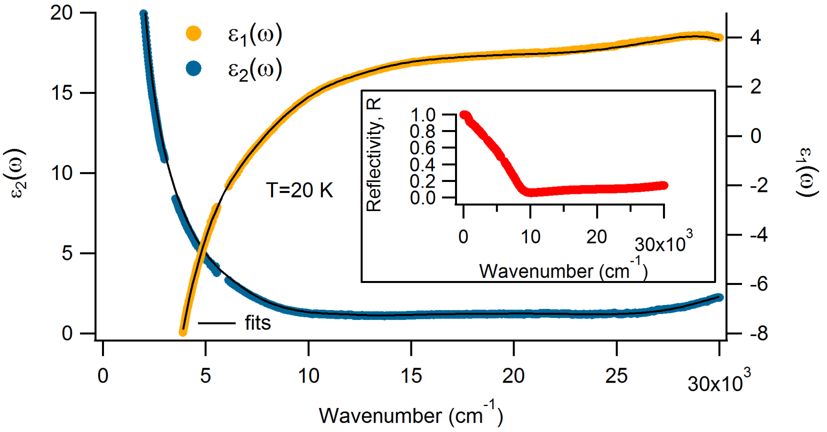

Figure 3.11: The real and imaginary parts of the dielectric function of OP $Bi_2Sr_2Y_{0.08}Ca_{0.92}Cu_2O_{8+\delta}$ (p=0.16) sample, measured by static ellipsometry at T=100 K, is reported. Solid lines are the fit to the data, performed with the model described in the text. In the inset, the sample reflectivity is shown.

The relevant parameters extracted from the fit to the T=20 K data are summarized in Table 3.3. The Lorentz oscillator parameters are only slightly changed with respect to the values obtained for the fit to the T=300 K and T=100 K data.

Table 3.3: Fitting Parameters for the Model Dielectric Function of Optimally Doped $Bi_2Sr_2Y_{0.08}Ca_{0.92}Cu_2O_{8+\delta}$ (p=0.16) at T=20 K

Parameter	Value	Unit
ϵ_∞	2.67	
ω_{p0}	17418	cm^{-1}
γ_{imp}	53	cm^{-1}
T	20	K
ω_{01}	11800	cm^{-1}
ω_{p1}	2358	cm^{-1}
γ_1	3644	cm^{-1}
ω_{02}	16163	cm^{-1}
ω_{p2}	6385	cm^{-1}
γ_2	8304	cm^{-1}
ω_{03}	21947	cm^{-1}
ω_{p3}	15026	cm^{-1}
γ_3	13998	cm^{-1}
ω_{04}	31057	cm^{-1}
ω_{p4}	16989	cm^{-1}
γ_4	6191	cm^{-1}
ω_{05}	35146	cm^{-1}
ω_{p5}	14747	cm^{-1}
γ_5	6396	cm^{-1}
ω_{06}	40421	cm^{-1}
ω_{p6}	27390	cm^{-1}
γ_6	7518	cm^{-1}

Chapter 4

Non-Equilibrium Physics of HTSC

4.1 Introduction

With this chapter I want to underline the importance of non-equilibrium physics, in understanding some aspects which equilibrium physics cannot properly address. In particular, emphasis will be directed to the information which can be gained from non-equilibrium, all-optical time-resolved measurements, based on ultrashort ($\sim$100 fs) laser pulses.
In the field of strongly correlated systems, the non-equilibrium physics can shed light on aspects which at equilibrium are masked and entangled, revealing the true nature of the physical phases. This is achieved thanks to both the temporal resolution of non-equilibrium techniques (which allows to access to the time domain, in which different kinds of excitations are disentangled by their temporal dynamics) and the spectral resolution we have added (which allows to access to the energy domain, in which the different effects are disentangled by their out-of-equilibrium spectral fingerprint). A phase of matter can be characterized thanks to the knowledge of its own intrinsic susceptibility, i.e., its response to a light-induced perturbation, which can be ascribed either to thermal effects, or excited state absorptions, or linear modification of the static dielectric function. These different scenarios can indeed be revealed by time-resolved optical measurements with spectral resolution, which are able to reveal the microscopic changes in the electronic structure, which happen on timescales much faster than those typical of thermal phenomena. The spectral resolution is of paramount importance since it allows to relate a time-resolved optical signal in the energy domain to a peculiar modification of the dielectric function of the material, depending upon its electronic band structure. It is the ability of non-equilibrium physics to temporally and spectrally disentangle thermal effects from electronic ones which allowed us to get new insights on the HTSC physics, revealing the nature of the different phases of the phase

diagram.
This chapter is organized as follows. I will at first present a brief review of the state of the art about the main results of time-resolved optical techniques. Then, I will describe the models (namely, the Two-Temperature Model and the Three-Temperature Model) which are commonly employed to extract the electron-phonon coupling strenght from time-resolved optical measurements in the time-domain. I will also formulate a generalized version of the three temperature model. Finally, I will introduce the differential model used to interpret the time-resolved optical measurements in both the time and energy domains, which constitute the novelty of this work. The combined, simultaneous temporal and spectral rosolution allows finally to unambiguously associate a physical origin to the observed time-resolved optical signals, thanks to the approach we developed, based on the knowledge of the modifications, on ultrafast timescales, of the dielectric function of the material.

4.2 Pump-Probe experiments and QP dynamics in HTSC

Time-resolved optical spectroscopy on copper-oxide based superconductors is a technique that attracted much interest since the knowledge of the quasiparticle dynamics can provide fundamental information on the properties of HTSC.
A pump-and-probe time-resolved optical measurement is conceptually simple: an ultrashort (∼100 fs) pump pulse is used to inject excitations in the system, while a second ultrashort pulse, named probe, analyzes the effect on the optical properties of the system (usually the reflectivity R) induced by the excitation of the system in a non-equilibrium condition. The temporal delay between the pump and the probe beams, τ, can be varied by simply changing the relative optical path difference of the two beams (1 μm=3.3 fs). In this way, the temporal dynamics of the reflectivity signal can be followed after the system excitation. What one measures is the relative, transient (pump-induced) change in the reflectivity R, defined as:

$$\frac{\Delta R}{R}(\omega,\tau)=\frac{R_{excited}(\omega,\tau)-R_{equilibrium}(\omega)}{R_{equilibrium}(\omega)}$$

where $R_{excited}(\omega,\tau)$ and $R_{equilibrium}(\omega)$ are respectively the excited (pumped) and equilibrium (unpumped) reflectivities.
This time-resolved optical signal $\Delta R/R(\omega,\tau)$ depends upon the pump-probe delay τ and the energy of the probe beam, equal to $\hbar\omega$. However, in this section I will present the established results of the literature, which are performed at a fixed probe energy equal to $\hbar\omega$=1.55 eV (λ=800 nm). I will refer to this technique as the one-color pump-probe technique.

The time-resolved optical signal $\Delta R/R(\omega,\tau)$, which is characterized by a magnitude, a sign and a decay time, constitutes a fingerprint of the different phases of the HTSC phase diagram. Modifications of the time-resolved optical signal are observed both upon changing the doping level of the material [78] and upon changing the temperature of the system [117]. As reported in Fig. 4.1, the time-resolved optical signal measured in the superconducting state of Bi2212, changes from positive on the underdoped side of the phase diagram to negative on the overdoped side of the phase diagram, with the sign-change taking place in coincidence with the optimal doping level. The time-resolved optical signal measured in the superconducting phase reveals a decay time of about 2.5 ps, and an amplitude of the order 10^{-4} for a pump fluence in the range 1 μJ/cm^2. The question regarding the nature of the excitations probed by a time-resolved transient reflectivity experiments performed on a HTSC in the superconducting state has been faced in [77]. It has been demonstrated that the time-resolved optical signal is proportional to the density of quasiparticles created by the laser excitation, occupying states close to the antinodal regions of the Brillouin zone. The lifetime of the photoinjected quasiparticle (and thus the time-resolved optical signal) strongly depends on both the temperature and the pump laser intensity (see Fig. 4.2), and diverges in the limit in which both the temperature and the excitation intensity tend to zero. This effect is due to the constraints of momentum and energy conservation, preventing the thermalization of antinodal quasiparticles toward the nodes. Fig. 4.3 shows instead how the time-resolved optical signal evolves, for an underdoped sample, when the temperature of the sample is raised, starting from the superconducting phase. Approaching the pseudogap phase, the positive and slowly-decaying time-resolved optical signal characterizing the optical response in the superconducting phase is gradually quenched, and at T_c a fast, negative

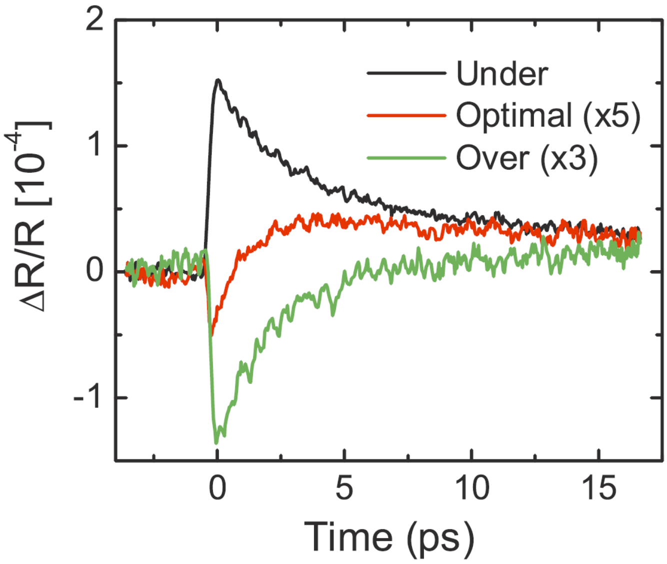

Figure 4.1: Time-resolved optical signal (in reflectivity) measured on three Bi2212 samples, differing for the doping level. The samples are held in the superconducting state, i.e., $T<T_c$. From [78].

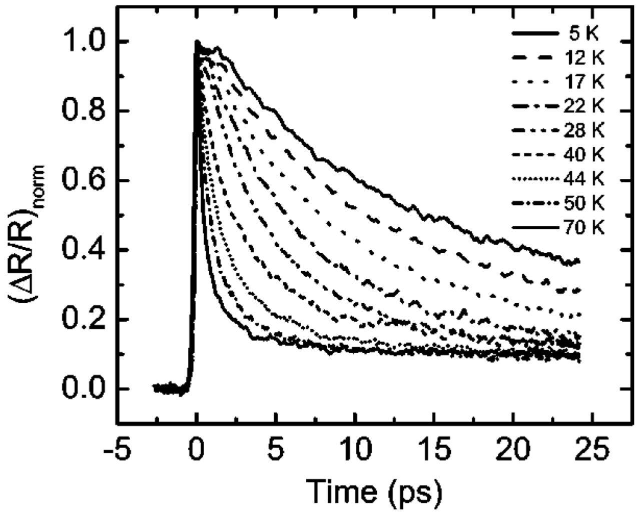

Figure 4.2: Time-resolved optical signal for temepratures in the range 5-70 K, measured on a YBCO sample having T_c=45 K. Curves are normalized to the same value at delay zero to illustrate the variation in the initial decay rate. The decay is most rapid at the highest temperature, and becomes systematically slower as T is reduced. From [77].

and weaker time-resolved optical signal sets in. This kind of optical response is considered the fingerprint of the pseudogap phase. This signal survives till the T^* temperature is reached. For $T > T^*$, the time-resolved optical signal changes sign again, and becomes positive, with a fast decay time (~300 fs) and a small amplitude. This kind of optical response is typical of the normal state phase.

While the meaning of the signal sign and amplitude remains unexplained in this context, the temporal dynamics are usually interpreted on the basis of the two/three temperature model for the normal state dynamics (see section 4.3 for deeper details regarding these models) and on the basis of the Rothwarf-and-Taylor model for the superconducting state dynamics.

The Rothwarf-and-Taylor Model: QP dynamics in the superconducting phase

The dynamics in the superconducting state can be explained taking into account that below T_c, an energy gap of magnitude Δ is opened. The physical process which takes place, and explains the increase of the time-resolved optical signal decay time (as compared to the normal state dynamics), is the following: the pump pulse injects quasiparticles (with rate $I_{qp}(t)$, which is Gaussian in time like the pump pulse) in the system. This lead to a temporal dynamics for the quasiparticle density n and boson density p (density of bosons with energy

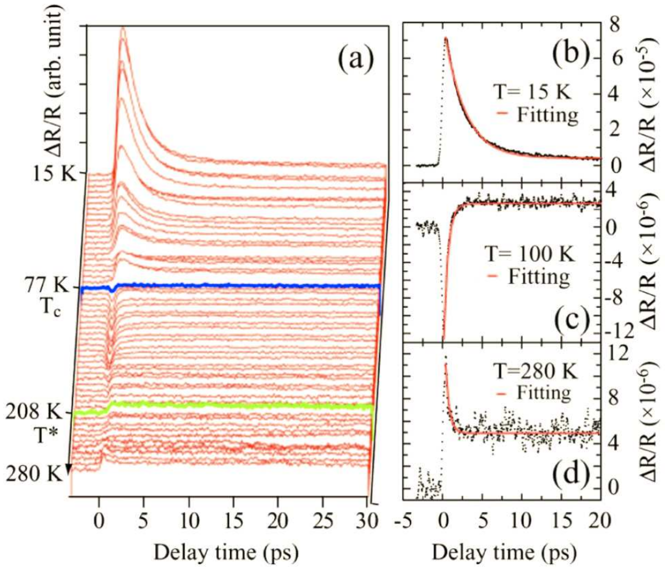

Figure 4.3: a) Temperature dependence of the time-resolved optical signal (in reflectivity), measured on an underdoped Bi2212 sample. Blue line marks the transition from the superconductive phase to the pseudogap. Green line marks the transition from the pseudogap to the normal state. b,c,d) The time-resolved optical signal in the superconductive, pseudogap and normal state is reported, respectively. From [117].

$> 2\Delta$) which is governed by three physical processes, described by the following picture (as illustrated in Fig. 4.4), and which are taken into account in a system of differential equations for $\partial n/\partial t$ and $\partial p/\partial t$. A Cooper Pair, whose

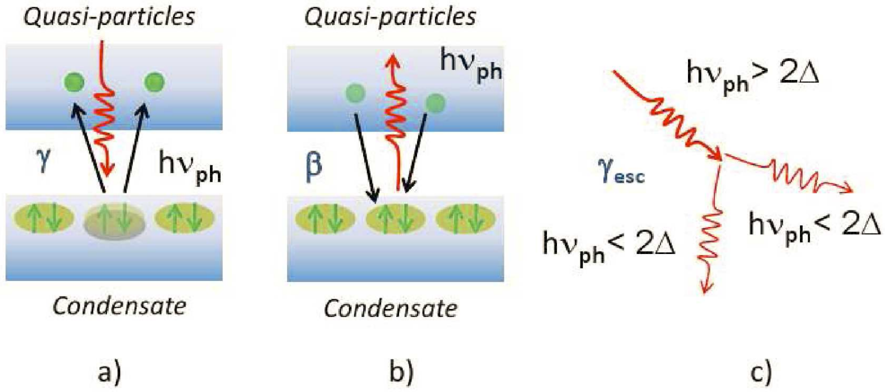

Figure 4.4: This picture sketches the three processes described by the Rothwarf and Taylor model. a) Creation of two quasiparticles above the superconducting gap, by absorption of one high-frequency phonon. b) Annihilation of two quasiparticles and emission of one phonon. c) Anharmonic decay of high-frequency bosons. From [54].

binding energy is 2Δ, can be broken from the absorption of a boson with energy

$> 2\Delta$, generating two quasiparticles: the rate of this process is proportional to $+2\gamma p$ for the increase of quasiparticle density, while is proportional to $-\gamma p$ for the decrease of high-frequency phonons. On the contrary, a Cooper Pair can be formed by annihilating two quasiparticles (rate $-\beta n$); the binding energy of the pair is then freed as a boson of energy 2Δ (rate $+1/2\beta n$). The bosons can then anharmonically decay (through inelastic scattering, or simply leaving the excited area by transport processes), with rate $-\gamma_{esc}(p - p_T)$, being p_T the thermal boson population density and γ_{esc} the coefficient describing the strength of the boson anharmonic decay. This picture is described by the following set of coupled differential (rate) equations.

$$\frac{\partial n}{\partial t} = I_{qp}(t) + 2\gamma p - \beta n^2$$

$$\frac{\partial p}{\partial t} = -\gamma p + \frac{\beta}{2} n^2 - \gamma_{esc}(p - p_T)$$

After quasiparticles are photoinjected in the system by the pump pulse, a quasiequilibirum between the quasiparticles and bosons densities is established. The slow decay time of phonons is responsible for the slowing down of the relaxation dynamics of quasiparticles (this is usually indicated as 'phonon bottleneck'). In particular, when $\gamma > \gamma_{esc}$, the quasiparticle and boson populations result strongly coupled, and both decay with rate γ_{esc} (of the order of few picoseconds^{-1}). All this picture is consistent assuming that the time-resolved optical signal at 1.55 eV is proportional, for the reasons that will be clarified in Chapter 8, to the pump-induced perturbation of the condensate, i.e., to the density of photo-injected quasiparticles.

The model described so far, regards the so-called 'low fluence regime' ($F \lesssim 50$ μJ/cm^2), in which the pump fluence slightly perturbs the superconduting condensate and is not intense enough to photoinduce a non-thermal phase transitions to the normal state, as pointed out in [111, 81, 80]. An interesting review of fluence tresholds for photoinduced phase transitions in HTSC or melting of CDW order in charge-density-wave systems can be found in [168]. A true 'spectroscopy' of a physcial phase from the non-equilibrium point of view (by this statement I mean the study of the peculiar excitations) can only be achieved whether the physical phase is not (partially) vaporized, thus the requirement to perform low-fluence studies.

Disentangling contributions to the signal from different quasiparticles

Once demonstrated that the superconductivity-related signal presents a decay time which is about one order of magnitude larger than the one observed in the normal state and pseudogap phases, the contributions of the different excitations to the time-resolved signal can be disentangled on the basis of their decay times. This observation was used [53] to address the interplay between superconducting and pseudogap phases in YBCO crystals. In Fig. 4.5 the relaxation times associated to the different components of a multicomponent exponential fitting to the data are reported. This successful way of disentangling the different excitation contributions revealed a temperature independent pseudogap and a temperature-dependent superconducting gap, with BCS-like temperature dependence. This also implies a possible coexistence of both gaps below T_c. The fact that the decay of the superconducting component diverges exactly at T_c can be explained on the basis of the Rothwarf and Taylor model: as the gap Δ decreases approaching T_c, an increasing number of phonons can break Cooper Pairs, and this results in a huge number of quasiparticles. Thus a quasiequilibrium between quasiparticles and phonons establishes, which slows down the recombination dynamics, governed only by inelastic processes.

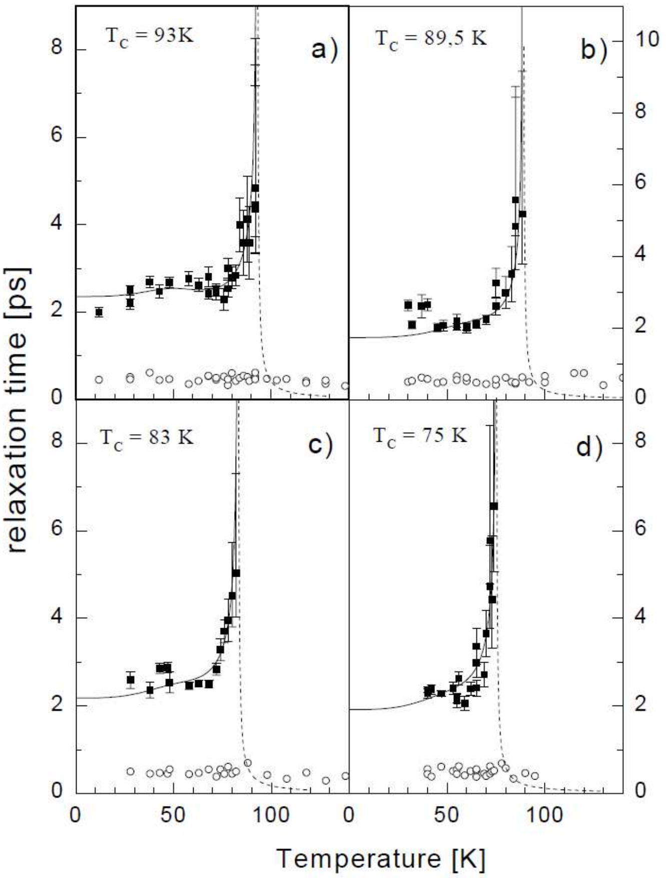

Figure 4.5: Relaxation times resulting from a two component fit of the time-resolved optical signal, on some YBCO samples, differing from the doping level. One component (squares) diverges exactly at T=T_c, while the other (circles) is temperature independent. From [53].

Pump-probe measurements in the THz region

In the superconducting phase, the signal observed at 1.55 eV is intimately related to the low-energy physics associated to the superconducting condensate. This can be directly demonstrated by pump-probe measurements in which the probe is a THz field (1 THz= 4.13 meV). In particular, in the THz range, the optical conductivity is given by the formula [99] (within a two fluid model, for quasiparticle density ρ_{QP} and superfluid density ρ_S):

$$\sigma(\omega) = \rho_{QP} \frac{1}{1/\tau - i\omega} + \rho_S \left(\pi\delta(0) + \frac{i}{\omega} \right)$$

from which it is clear that the imaginary part $\sigma_2(\omega)$ is proportional to the superconducting condensate density, at low frequencies (τ is the conventional Drude scattering time).

The THz probe thus directly accesses the superconducting condensate energy region. Typically, this energy region is 0.1-3 THz, ie, 0.4-12 meV. Examples of this kind of pump-probe measurements are reported in [12, 99]. The measured THz relaxation dynamics is strikingly similar to that observed in the near-infrared, as can be argued by looking at Fig. 4.6 (from [99]). Some difference exist anyway with respect to the optical probing: while elastic scattering with large momentum transfer dominates transport properties of carriers, the transient THz kinetics enables a sensitive measure of the inelastic quasiparticle recombination.

Magnitude of the signal in the different phases of an HTSC

The fact that, in the visible spectral region, the observed transient reflectivity signal magnitude in the superconducting state (of the order of 10^{-4} for fluences of the order of 1 μJ/cm^2) is at least one order of magnitude bigger than the one observed in the normal state and pseudogap phases, has been known by long time [164] (see Fig. 4.7). A clear interpratation of this fact has been proposed only recently [80]. Two scenarios were proposed to explain this experimental evidence: the first consider the $\Delta R/R$ signal as due to an excited state absorption, as it happens in metals and semiconductors. The second, instead, consider the $\Delta R/R$ signal as arising from a true (pump-induced) modification of the band structure of the material, which involves a spectral weight shift between high (in the near-IR) and low (condensate) energy scales (and which justifies the increase of the magnitude of the signal). In this scenario, the band structure at high energy is modified as a consequence of a partial quench of the energy gap, demonstrating an interplay between physics at very different energy scales. We ruled out the first scenario [80], as I explain in Chapter 8.

Beyond one-color optical pump-probe measurements

In concluding this section, I want to remark how single-color measurements, though very powerful in characterizing the peculiar phase of the system and in

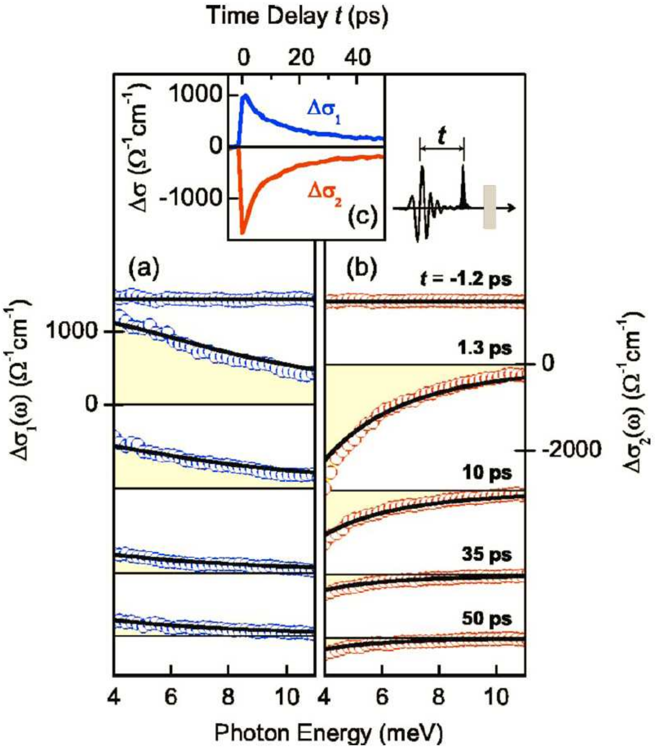

Figure 4.6: Induced THz conductivity changes, for T=6 K and a 0.7 μJ/cm^2 pump fluence, on a OP Bi2212 sample. a), b) Measured changes in the real part of the optical conductivity $\sigma_1(\omega)$ and in the imaginary part $\sigma_2(\omega)$ (circles) at indicated time delays t after the excitation. Solid lines are the fitting results of a two-fluid model, corresponding to a momentary depletion of 16% (1.3 ps), 8% (10 ps), 3.2% (35 ps), 2.7% (50 ps) of the low temperature condensate spectral weight and Drude widths, respectively, of of $1/\tau$=1.35, 1.26, 1.21, and 1.20 THz. c) The transient conductivity changes at center probe energy 5.5 meV, averaged over a 1.6 meV interval, versus pump-probe time delay t. From [99].

extracting very useful information mainly related to the relaxation dynamics, fails in producing a comprehensive physical picture able to explain the microscopic physical origin of the observed transient signals. To overcome this limitation, we developed a novel time-resolved optical spectrosocpy (described in 5) which adds the energy resolution to the usual temporal resolution. This is achieved thanks to a broadband probe pulse. With this technique, the time-resolved signal in the energy domain can be related unambiguously to pump-induced modifications of the dielectric function $\epsilon(\omega)$ of the material, allowing to associate a physical origin to the observed signal, in the various phases of the system. In section 4.4 the approach we employ to interpret time-resolved data in both the time and energy domains is presented.

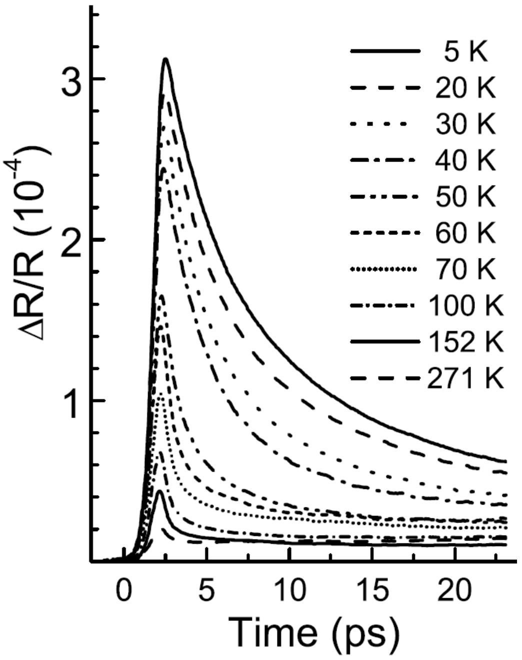

Figure 4.7: Time-resolved optical signal (in reflectivity) at constant pump intensity, for different temperatures, from a YBCO sample. It is evident how the signal intensity increases in the supeerconducting state. From [164].

4.3 Determining the Electron-Boson coupling by pump-probe

Determining the electron-phonon (and more generally the electron-boson) coupling strength is a task of paramount importance to give more insights into the problem of High Temperature Superconductivity. The nature of the glue which binds together electrons forming Cooper Pairs (and its coupling strength) is one of the most debated points in the HTSC field. Time resolved techniques allow to directly measure the electron-phonon coupling λ, as compared to other static (equilibrium) techniques (such as ARPES, tunneling, inelastic neutron scattering). Moreover, the temporal resolution of pump-probe techniques, giving a direct access to the time domain, allows to discriminate among the possible different bosonic populations the electrons scatter with (are coupled to): each electron-boson coupling channel will give origin to a different dynamics in the time-resolved signal, whose decay is related to the electron-boson coupling strenght. This connection is modeled by a number of models which will be carefully analized in the following. The conventional, one-color time resolved pump-probe technique suffices the extraction of the parameter lambda; we will also briefly point out how the spectral resolution can help in determining the nature of the bosons the electrons are coupled to.
The outline of this section will follow a chronological order, with the emphasis

on the experimental findings which motivated or supported the various models. In particular, I will start from the Two-Temperature Model (4.1), and then introduce the Three-Temperature Model (4.5), illustrating the reasons leading to the formlation of this model. I will also formulate a novel, generalized version of the three temperature model, in which a 'parallel' coupling of electrons with all bosonic populations is taken into account (4.8). This model can be naturally extended to include more temperatures, one for each bosonic population the electrons scatter with. On this line, I will present the system of coupled differential equations for a four temperature model. With this model, formulated to explain the experimental evidences presented in 6, all the possible scattering mechanisms which contributes to the total electron-boson pairing, which manifests in the glue function $\Pi(\Omega)$, are taken into account.

4.3.1 The Two-Temperature Model

In this section, the Two-Temperature Model (2TM) is described.
The so-called 'Two-Temperature Model' is the result of the theoretical work done by Anisimov [10] and Allen [7]. The model interprets and describes the electronic non-equilibrium dynamics excited in a material by an ultrashort (∼100 fs) laser light pulse. This model applies to metals and conventional, metallic superconductors. The formulation of this model was stimulated by the development of new laser sources, producing ultrashort pulses in the ps domain. The first systematic experimental studies were those of Brorson [25], who measured λ in several metals.
We can say that the two temperature model describes the physics of a pump-probe experiment carried on a solid state material, in which the electron-phonon scattering is directly observed in the time domain.
The physical picture on which the model was developed is the following. The energy deposited in the system by the laser pulse is absorbed by electrons, which are instantaneously excited above the Fermi level. After a few fs, electron-electron scattering processes, on the 1-10 fs timescale [11], drive the thermalization of the electronic population at an elevated temperature $T_e > T_0$, T_0 being the base temperature. On this timescale, the electrons are practically disentangled from the lattice: the electrons thus reach the maximum temperature $T_e(0)$ determined mainly by their specific heat. On a longer timescale, the electrons start to lose energy through electron-phonon scattering, and reach a common temperature with phonons. Finally, a much slower relaxation process - dominated by heat diffusion - makes the system return to the ambient temperature T_0. It is important to point out that the rate of return to local equilibrium is governed entirely by electron-phonon processes. The model presented assumes that diffusion driven by spatial inhomogeneities is negligible; acceleration due to both external and internal fields is negligible, and no other collision processes are important. The most important requirement is that electron-electron and phonon-phonon (anharmonic) processes are active in keeping the electronic and phononic distributions equal to the local equi-

librium distributions (respectively FD and BE) at the separated temperatures $T_e(t)$ and $T_l(t)$. The metal is looked as a two temperature system at every time t.

The phenomenologic system of coupled differential equations describing the evolution of the electronic and the lattice temperatures, as proposed by Anisimov in 1974 to describe the energy balance for a metal absorbing a laser pulse, is:

$$\frac{\partial T_e}{\partial t} = -\frac{G}{C_e}(T_e - T_l) + \frac{p}{C_e} \tag{4.1a}$$

$$\frac{\partial T_l}{\partial t} = \frac{G}{C_l}(T_e - T_l) \tag{4.1b}$$

Where T_e, T_l are the electronic and lattice (phonon) temperatures, respectively. $G = \gamma_{e-ph} C_e$ is a coupling constant describing the coupling between the electron and the phonon systems. γ_{e-ph} is a different way of expressing the coupling constant, often found in the literaure [7]. $C_e = \gamma_e T_e$ is the electronic specific heat, being γ_e the coefficient of the linear electronic specific heat. C_l is the lattice specific heat. p is the absorbed power, with the same Gaussian profile of the laser pulse. Both the specific heats and the laser power are expressed per unit of volume.

The solution of this system of equations indicates that the electronic temperature evolution follows an exponential decay with time-constant $\tau = (\gamma_{e-ph})^{-1}$. It is worth to point out that this model was developed in order to describe the electron emission from metal surfaces exposed to picosecond laser pulses. It was found that for laser intensities beyond a critical value, the emission current is entirely due to thermoionic emission (while below threshold a competition between photoelectric emission and thermoionic emission exists). The first attempt to measure the electron-lattice relaxation kinetics was done by measuring the thermoionic emission current, proportional to the electronic temperature.

The relation between the experimentally measured τ and the key-quantity λ, expressing the electron-phonon coupling in the superconductivity theory, has been first derived by Allen [7], though in a limit I will discuss in the following. The main result is that λ can be directly inferred from τ, once the electronic temperature T_e and the mean phonon energy $\langle \hbar^2 \omega^2 \rangle$ are known. Allen's formula is:

$$\gamma_{e-ph} = \frac{3\lambda \langle \hbar^2 \omega^2 \rangle}{\hbar \pi k_B^2 T_e} \tag{4.2}$$

thus:

$$G = \gamma_{e-ph} \gamma_e T_e = \frac{3\gamma_e}{\hbar \pi k_B^2} \lambda \langle \hbar^2 \omega^2 \rangle$$

$T_e(0)$ can be easily evaluated starting from the pump laser energy delivered to the electrons, and the electronic specific heat. This value, together with the value of $T_e(\infty)$=$T_l(\infty)$ (which can be estimated from the pump laser energy

and the lattice specific heat), constitute the initial conditions to correctly solve the differential system of equations (while $T_l(0) = T_0$, being T_0 the base system temperature). The mean phonon energy $\langle \hbar^2\omega^2 \rangle$ is more difficult to evaluate; it can be taken from the literature (the phonon spectrum can be measured by scattering techniques), or it can be approximated with $\hbar^2{\omega_D}^2/2$ [24]. Since $T_e(0)$ can be calculated, measuring τ allows to know the product $\lambda\langle \hbar^2\omega^2 \rangle$ without free parameters. For completeness, the experimentally extracted values of λ range from 0.1 to 0.15 for non-superconducting metals (Au, Cu), to 0.25-0.4 for very low-Tc ($\lesssim$1 K) superconductors (W, Ir, Ti, Zn), to 0.8-1 for the most known metallic superconductors (In, Sn, Hg, Pb, Nb), which are in the strong-coupling limit.
Expression 4.2 predicts a direct proportionality between the decay time τ and the electronic temperature T_e. To understand in which limits this formula is applicable, it is worth to follow a few steps, illustrating the approximations used and the derivation of the same expression.
The decay rate of the electron thermal energy (transferred to the phonon system) is given by:

$$\frac{\partial E_e}{\partial t} = 2\pi N_c N(E_F) \int_0^\infty d\Omega \alpha^2 F(\Omega)(\hbar\Omega)^2 \left[N(\Omega, T_l) - N(\Omega, T_e)\right] \tag{4.3}$$

where N_c is the number of cells in the sample, $N(E_F)$ is the density of states of both spins per unit cell, and $N(\Omega, T_j)$ are the BE distribution functions (j=e,l). The electronic energy for the system can be written as: $E_e = \sum_k \epsilon_k F_k \approx E_0 + 1/2\gamma_e T_e^2$ (where F_k is the FD distribution, and E_0 the system point-zero energy, for the system at $T = 0$), while the electronic specific heat writes: γ_e=$\pi^2 N_c N(E_F) k_B^2/3$.
Without any assumption regarding the actual spectrum of the electron-phonon coupling $\alpha^2 F(\Omega)$, and remembering that $\lambda \left\langle \omega^2 \right\rangle = 2 \int_0^\infty \alpha^2 F(\Omega)\Omega d\Omega$, equation 4.3 can be rewritten as:

$$\frac{\partial E_e}{\partial t} = \pi\hbar N_c N(E_F)\lambda \left\langle \omega^2 \right\rangle k_B(T_l - T_e) + ... \tag{4.4}$$

if a Taylor expansion of $N(\Omega, T_j)$ in terms of $\hbar\Omega/k_B T_j$ is carried out, in the **high temperature limit**, that is, when both T_e and T_l are much higher than the phonon energy $\hbar\Omega$.
Finally, expression 4.4 can be recasted in the usual form $\partial T_e/\partial t = \gamma_{e-ph}(T_l - T_e)$ by using the definitions of E_E and γ_e.
Allen Formula 4.2 is thus strictly valid only when the system is considerably heated by the pump pulse energy.

Relation between the optical signal and the temperature increments ΔT_e, ΔT_l

In the context of a pump-probe experiment, the pump-induced change of the electronic temperature T_e modifies the electronic distribution of the material, being the electronic population described by a Fermi-Dirac statistic at an elevated temperature T_e. This effect can be monitored by a subsequent probe pulse, which reflection or transmission is influenced by the change in the electronic population of the material. More considerations about this point are done at the end of this section.

It must be emphasized that, for the optical pump-probe technique to be employed to the study of the electron-phonon coupling, the induced changes in T_j (j=e,l) must have an effect on the sample optical properties (reflectivity or transmittivity), at the probe wavelength. In the more general form, the induced change in reflectivity will be sensitive to both variations in the electronic temperature (ΔT_e) and in the lattice one (ΔT_l): $\Delta R/R = c_1 \cdot \Delta T_e + c_2 \cdot \Delta T_l$. The ratio c_1/c_2 is usually a free fitting parameter.

Changes due to ΔT_l can come from band shifting arising from thermal strain. These lattice-temperature-induced reflectivity changes will decay on very long timescales, determined by the rate at which the heat can diffuse away from the optically excited area. In this model T_e and T_l remain at an elevated temperature with respect to T_0, since the heat diffusion effect is not taken into account. This is not a limitation, being the timescale of this effect of the order of the ns.

Changes induced by ΔT_e instead are due to optical transition from/to states which population is altered by the laser excitation; in particular, any transition involving states near the Fermi level will be sensitive to T_e. The idea is simple: the increase of the electronic population makes the tails of the Fermi distribution smearing, opening states below the Fermi level for transitions. These new states can then absorb probe photons, resulting in an increase of absorption. Alternatively, the promoted electrons of the Fermi distribution can be excited to free states above the Fermi level, resulting in an absorption decrease. The actual sign of the $\Delta R/R$ thus depends upon the material band structure.

Overall, the relative induced change in reflectivity turns out to be very small, of the order of 10^{-4} to 10^{-6}.

Limits of the Two-Temperature Model

Here I will state briefly the main limits of the 2TM, which call for an extension of the model. The main criticism to this model stands in the possibility to define the electronic temperature T_e. Though the optical scattering rate τ_{e-e} is of the order 1-10 fs [11], indicating a very fast electron thermalization, recent photoemission experiments [145] found a small deviation of the actual non-equilibrium electronic distribution with respect to a Fermi-Dirac statistics. The non-thermalized high-energy tail evidenced in [145], to whom the authors didn't give much weight, is instead predicted (as shown in [75]) by exact calculations [96] taking into account the exact analytical solution of the integral Boltzmann equation, without the questionable assumption that electrons are in a quasiequilibrium with a time-dependent temperature. The electron-lattice ralaxation rate within this formalism is: $(\tau_{e-ph})^{-1} = 3\hbar\lambda \left\langle \omega^2 \right\rangle / 2\pi k_B T_l$. Apart the factor of '2' with respect to the 2TM result, more important is the dependence on T_l rather than T_e, which justifies the experimental evidence that the relaxation rate is fluence-independent. A term of difficult evaluation is $\langle\omega^2\rangle$, which is in general taken from the literature. The model by Kabanov et al. [96], which is applicable also when the electron-electron scattering time is bigger than the electron-phonon scattering time (i.e., when $\tau_{e-e}>\tau_{e-ph}$), is the natural model to be employed to interpret the findings described in [144], in which the apex oxygen vibration in YBCO turns out to be strongly excited within 150 fs, demonstrating that the lattice absorbs a major portion of the pump energy before the quasiparticles are thermalized. The evidence of an ultrafast electron-phonon coupling with peculiar phononic modes, evidenced in [144], and the observation of a double exponentially-decaying dynamics in optical measurements on HTSC, are a strong evidence for an anisotropic electron-phonon coupling, which cannot be accounted for by the 2TM. This observation clearly invokes a further coupling term, which is accounted for by the Three-Temperature Model.

4.3.2 The Three-Temperature Model

The Three-Temperature Model (3TM) was initially developed [145] as an extended version of the two temperature model, to interpret recent new results obtained with the time-resolved ARPES technique. In particular, this model well reproduces the time-resolved dynamics observed in systems with a strong anisotropy of the electron-phonon interaction, due to phonon branches with different coupling strength, which results in different timescales in the relaxation dynamics. This is the case of strongly correlated materials, such as the cuprates.

The experimental findings, on an optimally doped Bi2212 single crystal (at T=30K), are the following. A time-resolved ARPES experiment is conceptually simple: the sample excitation is performed with 1.5 eV laser pulses (pump), while the photoelectrons are emitted thanks to a 6 eV probe beam which is delayed with respect to the former. Photoelectrons are collected and analyzed with a time-of-flight (TOF) spectrometer. Time-resolved ARPES 'directly' probes the electronic temperature $T_e(t)$, which is inferred from the photoelectron spectra (collected at the Fermi wavevector) at various pump-probe delays t. A fast thermalization for the electronic population is observed, since the electronic distribution converges to a Fermi Dirac distribution within the pump pulse duration (~50 fs). This is due to a large electron-electron interaction. The novelty of the data stands in the fact that the electronic temperature T_e relaxes with two different timescales: a fast one (which relaxes with an exponential decay with $\tau_\alpha \approx$110 fs) and a slow one (which decays with $\tau_\beta \approx$2 ps).

The physical interpretation the authors gave was the following. After the fast electronic thermalization, the electronic population at the temperature T_e starts to relax transferring energy to a subset of strongly coupled (also called 'hot') phonons, whose temperature is indicated with T_p. The idea is that only a small subset of the total phonon modes (a fraction f of the total, with $0 \leqslant f \ll 1$) contributes to the coupling. After a time $\sim 3\tau_\alpha$, the electrons and the hot phonons reach a common temperature, and their relaxation dynamics becomes similar. Then, the relaxation process of both populations proceeds with a decay on the picoseconds timescale, governed by the phonon-phonon anharmonic scattering. This scattering occurs between two 'independent' phonon subsets: the more strongly coupled ones (f modes) and the nearly non-interacting $1-f$ phonon modes (sometimes called 'cold' phonons or simply 'lattice'), the latter being characterized by the temperature T_l. This is the physical picture described by the so-called (conventional) three temperature model.

Within the approximation of an Einstein model for the phonon spectrum (a non-dispersing distribution for the phononic modes given by $F(\Omega - \Omega_0)$), being $\int_0^\infty d\Omega\Omega^2\alpha^2 F(n_e - n_p)$ the rate of energy transfer from electrons to phonons (with $n_j = (e^{\Omega/k_B T_j} - 1)^{-1}$) and $\lambda = 2\int_0^\infty d\Omega\Omega^{-1}\alpha^2 F$ the dimensionless electron-phonon coupling, the system of rate equations for the temperatures $T_j(t)$ is:

$$\frac{\partial T_e}{\partial t} = -\frac{3\lambda\Omega_0^3}{\hbar\pi k_B^2}\frac{n_e - n_p}{T_e} + \frac{p}{C_e} \tag{4.5a}$$

$$\frac{\partial T_p}{\partial t} = \frac{C_e}{C_p}\frac{3\lambda\Omega_0^3}{\hbar\pi k_B^2} - \frac{T_p - T_l}{\tau_\beta} \tag{4.5b}$$

$$\frac{\partial T_l}{\partial t} = \frac{C_p}{C_l}\frac{T_p - T_l}{\tau_\beta} \tag{4.5c}$$

Where n_j are the Bose-Einstein distributions at the temperatures T_j: $n_j = (e^{\Omega_0/k_B T_j} - 1)^{-1}$. $C_j(T)$ are the electrons ($j = e$), hot phonons ($j = p$) and cold phonons ($j = l$) specific heats, with $C_e(T) = \gamma_e T_e$. The fraction f of strongly coupled phonon modes enters the model through the two phononic specific heats. Finally, τ_β is the (phenomenologic) phonon-phonon anharmonic decay. On the contray to the 2TM, in the derivation of the 3TM a particular form for the electron-phonon coupling, i.e., $\alpha^2 F(\Omega) \propto \delta(\Omega - \Omega_0)$ has been assumed (electrons are coupled with just one phonon mode at frequency $\Omega = \Omega_0$), but no approximations are applied to the BE statistics.

Within this model, the data analysis revealed a weak ($\lambda \approx 0.2$) electron-phonon coupling, for a phonon mode with 40 meV $\leqslant \Omega_0 \leqslant$ 70 meV. Moreover, the fraction of coupled phonons turns out to be $f \approx 0.2$, implying that the interaction is highly anisotropic, and only a few modes are significantly coupled (since 80% of the phonon modes have a weak interaction with the electrons). These findings point toward a scenario in which the electron-phonon interaction is not the main source of coupling in HTSC, even if this weak form of coupling can cooperate with other stronger electron-boson interactions.

This model neglects the electron-phonon scattering with the $1-f$ lattice modes considered more weakly coupled, which thus would barely contribute to the evolution of the electronic temperature $T_e(t)$. Anyway, the distinction between the strongly coupled phonons and the other lattice vibrations is physically meaningful as far as the strongly coupled phonons have a stronger coupling normalized to their density of states (or specific heat).

A few words are worth to be spent on the way the specific heat must be modeled. This is a task of fundamental importance. The authors considered just one phonon frequency (Ω_0, a delta) in the phonon spectrum. All phonon modes have the same frequency. The specific heat within this model follows straightforwardly from the specific heat definition:

$$C = 3N_A k_B \int_0^\infty d\Omega F(\Omega) (\frac{\Omega}{k_B T})^2 \frac{e^{(\Omega/k_B T)}}{(e^{(\Omega/k_B T)}-1)^2}$$

That is:

$$C_p(T) = 3N_A f \frac{\Omega_0^2}{k_B T^2} \frac{e^{(\Omega_0/k_B T)}}{(e^{(\Omega_0/k_B T)}-1)^2} = 3N_A f \Omega_0 \frac{\partial n_p}{\partial T_p}$$

$$C_l(T) = 3N_A(1-f) \frac{\Omega_0^2}{k_B T^2} \frac{e^{(\Omega_0/k_B T)}}{(e^{(\Omega_0/k_B T)}-1)^2} = 3N_A(1-f)\Omega_0 \frac{\partial n_p}{\partial T_p}$$

which satisfies: $C_{tot}(T) = C_p(T) + C_l(T)$.

Here N_A is intended to give the correct normalization for C_{tot}, and must be intended as a number of molecules per cm^3.

An improvement to this method consists in taking into account the true functional form of $C_{tot}(T)$, the total specific heat, as measured from experiments. The phonons specific heat $C_p(T)$ is calculated exactly as before, assuming one phonon frequency as the most coupled one, with the only difference that $C_p(T)$ must be balanced in such a way that, for $f \to 1$, it must be $C_p(T) \to C_{tot}(T)$. Finally, the lattice specific heat $C_l(T)$ is calculated as $C_l(T) = C_{tot}(T) - C_p(T)$. However, the best way of estimating the specific heat would require the knowledge of the whole phonons spectrum $F(\Omega)$. The total specific heat then follows straightforwardly from the definition. The phonon specific heat $C_p(T)$ is calculated by selecting a proper subset of $F(\Omega)$, and balanced in the described way. This ensures the specific heat is modeled taking into account the actual phonons distribution.

To apply this model to the case of all-optical experiments, the problem of connecting the electron and phonon dynamics to the transient dielectric properties arises. In the most general case, the transient reflectivity can be modeled as follows:

$$\Delta R/R = c_1 \cdot \Delta T_e + c_2 \cdot \Delta T_p + c_3 \cdot \Delta T_l \tag{4.6}$$

or

$$\Delta R/R = c_1 \cdot \Delta T_e + c_2 \cdot (f \cdot \Delta T_p + (1-f) \cdot \Delta T_l) \tag{4.7}$$

It must be pointed out that the choice of the coefficients c_j relating the temperature increase to the transient reflectivity is of extreme importance and must be carried out with much care, in order to obtain stable results. Usually the

coefficients c_j (j=1, 2, 3) are free fitting parameters. This lead to a level of uncertainty in the estimation of the value of λ.
Finally, it must be noted that the experimental evidences so far described, obtained with time-resolved ARPES, refer to a system in the superconducting state, at a base temperature T=30 K. With all-optical measurements, it is not possible to obtain the electron-phonon coupling in the superconducting state, since the observed dynamics is slowed down by a bottleneck effect, as described by the Rothwarf-Taylor model [156]. The problem is that on the contrary to photoemission, which directly probes the electronic temperature T_e, the optical transient signal is proportional [111] to the superconducting state excitations, when the system is in the superconducting state. Thus, the electron-phonon coupling with optical techniques can only be inferred measuring the normal state properties. This shouldn't be a problem, since it is thought that the electron-phonon coupling doesn't change upon crossing T_c.

The same conventional Three-Temperature Model has been recently used [27] to interpret experimental results obtained by analyzing the ultrafast electron diffraction by Bi2212 and Bi2223 crystals. Samples are excited by a 1.55 eV - 120 fs ultrashort pulse, while the probing is done by a synchronized electron beam, which produces a diffraction pattern, whose peak intensities are recorded. Here, the lattice (cold phonons) temperature can be directly inferred measuring the relative intensity of the (00) diffraction rod (which gives the structural dynamics along the c axis, along which the 'cold' phonons are supposed to act), and the data are interpreted directly fitting the three temperature model lattice temperature T_l to the same parameter extracted from the data. The latter can be derived by considering the Debye-Waller model, in which $\Delta T_l(\tau) \propto -\ln(I(\tau)/I_0)$, being I_0 the unperturbed (00) spot intensity and $I(\tau)$ the intensity of the same spot at the pump-probe delay τ. The experimental findings evidenced a directional electron-phonon coupling (here I refer to the 'hot' phonons, i.e., the more strongly coupled to electrons, which are thought to be 'in-plane'): the coupling is stronger when the excitation direction (pump electric field polarization) is parallel to the Cu-O bond, while it appears weaker at 45 degrees (along the nodal direction), where the relaxation dynamics slows down. This happens only when the sample is in the superconducting state. The evidence that it exists an anisotropic electron-phonon coupling even in the Cu-O plane (probed analyzing the c-axis phonon dynamics related to the cold-phonons) is explained by the authors with a stronger coupling between the antinodal charge carriers and the out-of-plane buckling vibration of the oxygen ions in the Cu-O planes.

Limits of the Three-Temperature Model

The 3TM is applicable only when a thermal distribution for the excited electrons is reached thanks to electron-electron scatering mechanisms, in such a way an effective temperature T_e can be associated to the excited population.

Thus it is not applicable when a gap in the density of states is opened. The 3TM is thus stictly applicable to HTSC only at room temperature and on the OP and OD regions of the phase diagram. It is well-known that in cuprate superconductors [77], in the superconducting state, the probed excitations are quasiparticles which occupy a precise region of k-space, and namely the antinodal one, where the gap has its maximum. Thus, the probed excitations have a strongly non-thermal distribution, which impedes the application of the 3TM to reproduce the measured dynamics. The fact that a non-thermal distribution of excitations is obtained in the presence of a gap is explained by the blocking of electron-electron scattering away from the node, because of the limited phase space in the antinodal region. Recently, this speculation has been observed experimentally by time-resolved photoemission experiments, analyzing the electronic thermalization in various k-directions of the Brillouin zone of a Bi2212 sample [41].

In the conventional 3TM, electrons are directly coupled only with the so-called strongly-coupled phonons. To take into account the direct coupling of electrons with different kinds of bosonic excitations, we propose a generalized version of the 3TM, accounting for the energy exchange among the different degrees of freedom of a system in a phenomenological way.

4.3.3 A generalized Three-Temperature Model

In order to overcome some of the limitations of the conventional three temperature model, and to provide a model which is able to fully reproduce the relaxation dynamics of a system whose electron-boson coupling is described by a general bosonic glue $\Pi(\Omega)$ made of different contributions, we developed a new model in which we assign a temperature T_j (j=p for storngly coupled phonons, j=l for weakly coupled phonons or lattice) to each different bosonic population the electrons scatter with, and whose coupling λ_j (here again j=p,l) with the electrons derives from a particular subset $\Pi_j(\Omega)$ of the total bosonic glue $\Pi(\Omega)$:

$$\lambda_j = 2\int_0^\infty d\Omega \frac{\Pi_j(\Omega)}{\Omega}$$

where: $\Pi(\Omega) = \sum_{j=1}^{N} \Pi_j(\Omega)$; obviously $\lambda = \sum_{j=1}^{N} \lambda_j$.

The various $\Pi_j(\Omega)$ linearly contribute to the total bosonic glue $\Pi(\Omega)$, which thus accounts for all the possible degrees of freedom the electrons can exchange energy with. N defines the number of temperatures (and degrees of freedom) considered in the model.

If we consider only phonons (both strongly and weakly coupled) as possible mediator bosons, we obtain a three temperature model in which the phonon-phonon anharmonic coupling term is replaced by a direct electron-weakly-coupled-phonon interaction term, which carries a coupling strength λ_l (absent in the conventional three temperature model). The model we propose is the following (here the anharmonic term has been completely neglected, but it can be nevertheless considered in peculiar situations):

$$\frac{\partial T_e}{\partial t} = \frac{G(\Pi_p, T_p, T_e)}{\gamma_e T_e} + \frac{G(\Pi_l, T_l, T_e)}{\gamma_e T_e} + \frac{p}{\gamma_e T_e} \tag{4.8a}$$

$$\frac{\partial T_p}{\partial t} = -\frac{G(\Pi_p, T_p, T_e)}{C_p} \tag{4.8b}$$

$$\frac{\partial T_l}{\partial t} = -\frac{G(\Pi_l, T_l, T_e)}{C_l} \tag{4.8c}$$

Where:

$$G(\Pi_b, T_b, T_e) = \frac{6\gamma_e}{\hbar \pi k_B^2} \int_0^\infty d\Omega \Pi_b(\Omega)\Omega^2[N(\Omega, T_b) - N(\Omega, T_e)] \tag{4.9}$$

and: $N(\Omega, T_j) = (e^{\Omega/k_B T_j} - 1)^{-1}$.
The differential reflectivity can be modeled in the usual way (as reported in 4.6 and) or with the expression:

$$\Delta R/R = c_1 \cdot \Delta T_e + c_2 \cdot (\Delta T_p + (\lambda_l/\lambda_p) \cdot \Delta T_l) \tag{4.10}$$

In order to highlight the differences this model introduces with respect to the conventional Three-Temperature Model, we perform some simulations numerically integrating the systems of coupled differential equations, using the same values for the specific heats (electronic and total) and for the parameters λ_p=0.3, p=2 J/cm^3, f=0.1. I consider also a model in which an anharmonic coupling term of the form $\frac{T_p - T_l}{\tau_\beta}$ couples equations 4.8b and 4.8c, exactly as it enters in equations 4.5b and 4.5c. The main difference with respect to the conventional 3TM stands in the overshoot of the temperature T_p, which

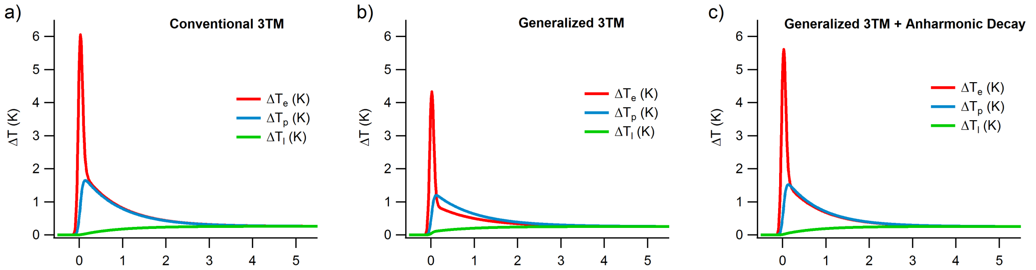

Figure 4.8: a) Numerical integration of the system of equations of the conventional 3TM, 4.5. b) Numerical integration of the system of equations of the generalized 3TM, 4.8. c) The generalized 3TM plus an anharmonic decay term is considered. In the three cases, the electronic temperature evolution ΔT_e (red), the strongly-coupled phonons temperature evolution ΔT_p (blue) and the weakly-coupled phonons temperature evolution ΔT_l (green) are reported. The common parameters are: λ_p=0.3, p=2 J/cm^3, f=0.1. In a), τ_β=800 fs; in b), λ_l=0.2; in c), λ_l=0.15, τ_β=1.2 ps.

is ascribed to the fact that being the electrons directly coupled also to the weakly coupled phonons (lattice), they cool down fastly and the hot phonons remain at an elevated temperature from which they relaxes more slowly with respect to the electrons, given their higher specific heat. As a consequence, the lattice warms up fastly with respect to the conventional 3TM case. In the conventional 3TM, the weakly coupled phonons heating turns out to be small since they directly loose energy (anharmonically) interacting with the lattice. In principle, the effects of an anharmonic (phonon-phonon scattering) term and a direct electron-lattice coupling term can coexist. If both coupling (electron-lattice and anharmonic one) are present (panel c)), the overshoot of the temperature T_p can be removed. The values for λ_l without the anharmonic term must be considered as an upper limit.

The Four Temperature Model (4TM)

This model can be easily extended to take into account the electron scattering with other (than phonons) bosonic populations, which could be of electronic origin, for instance antiferromagnetic spin fluctuations. This is done by simply adding a new (fourth) equation which describes the evolution of this bosonic population temperature, T_{be}. In a natural way, this population will be characterized by its own specific heat, C_{be} (which could be of difficult evaluation, and in general very small) and by its coupling with electrons, λ_{be}, coming from a specific part $\Pi_{be}(\Omega)$ of the total bosonic glue $\Pi(\Omega)$. The implicit assumption of all the previous models was that both spin and charge fluctuations thermalized within the pulse duration (and were thus considered as a whole with the electrons), with the phonons representing the only possible channel for the electrons relaxation. The new equation overcoming this limitation is:

$$\frac{\partial T_{be}}{\partial t} = -\frac{G(\Pi_{be}, T_{be}, T_e)}{C_{be}}$$

Moreover, a coupling term: $+\frac{G(\Pi_{be},T_{be},T_e)}{\gamma_e T_e}$ must be added to the first equation describing the $T_e(t)$ temporal evolution.

The more general way to model the differential reflectivity in this 4TM is the following:

$$\Delta R/R = c_1 \cdot \Delta T_e + c_2 \cdot \Delta T_{be} + c_3 \cdot \Delta T_p + c_4 \cdot \Delta T_l \tag{4.11}$$

In this way, we get a four-temperature-model (the fourth temperature being the one of the electronic bosons *be*) which can be of great importance in order to correctly estimate the coupling of electrons with the different bosonic populations. At this purpose, it becomes of fundamental importance the spectral resolution, which, combined with the temporal resolution, allows to point out whether the electrons are coupled to some bosonic modes of electronic origin. It must be pointed out that, since C_{be} is small (of the same order of the electronic specific heat $C_e = \gamma_e T_e$), the new equation contributes little to

the electronic temperature evolution, and $T_{be} \approx T_e$ (this happens also in the very first part of the relaxation dynamics, during the pulse duration). The point is that the population $j = be$ carries a finite value of λ_{be}. The spectral resolution can help in pointing out what is the true temperature evolution of the system, with the following argument: according to the Extended Drude model, the electronic temperature can be disentangled from the bosonic one (see sections 3.5.2, 3.5.3), and the fact that $T_e \approx T_{be}$ or $T_e > T_{be}$ gives different spectral responses (see the simulations reported in 4.4 and the analysis in Chapter 6). If the spectral response at early pump-probe delays is in agreement with the one simulated in the case $T_e \approx T_{be}$, it means that a bosonic population with small specific heat (and thus of electronic origin) is coupled with the electrons. Indeed, if electrons were coupled only with phonons, it couldn't be $T_e \approx T_{be}$ at early delays, for considerations regarding the phonons specific heat C_p, which makes the phonons warming on longer timescales. The former situation revealed the actual one, as pointed out in Chapter 6. Time resolved spectroscopy thus revealed a powerful technique in order to assign the correct value of λ to the various bosonic populations. The relations $T_c = T_c(\lambda)$ presented in 2.4 finally allowed to clarify which bosonic population is responsible for the actual material T_c. Moreover, the spectral resolution allows both to evaluate the subsets $\Pi_j(\Omega)$ of $\Pi(\Omega)$ related to the various bosonic populations (being $\Pi(\Omega)$ determined from static measurements) and to fix the coefficients c_j in expression 4.11, thus limiting the number of free parameters of the fit.
The results revealed a strong ($\lambda \approx 1$) electron-boson coupling, with bosons which are other than phonons, and must thus be of electronic origin. Concluding, we can say that in HTSC a strong electron-boson coupling is hidden from the point of view of the electron dynamics, but its actual presence is revealed by the spectral resolution. Non-equilibrium spectroscopy thus revealed a very powerful and unique technique in order to shed light on the problem of electron-boson coupling in strongly correlated materials.

4.3.4 Modeling the absorbed power density

In this section some considerations about the power density p [J/(cm^3·s)], deposited by the laser pulse in the system, are done.
The following equalities hold:

$$p(t) = p_0 \frac{2\sqrt{\ln 2}}{\sqrt{\pi}} e^{-4\ln 2 \frac{t^2}{\tau^2}} = \frac{P_0}{V} \frac{2\sqrt{\ln 2}}{\sqrt{\pi}} e^{-4\ln 2 \frac{t^2}{\tau^2}} = \frac{E}{V \cdot \tau} \frac{2\sqrt{\ln 2}}{\sqrt{\pi}} e^{-4\ln 2 \frac{t^2}{\tau^2}}$$

Where p_0 is the pulse mean power density, P_0 is the pulse mean power, E the energy per pulse, V the volume in which the energy is deposited, and τ the pulse temporal $FWHM$, determined for example by auto- or cross-correlation measurements.
Usually, the volume V is calculated as follows: $V = A \cdot d = \pi (FWHM/2)^2 \alpha^{-1}$, that is, the excited volume is a cylinder which top area is that of a disk of diameter $FWHM$ (determined experimentally), and which height is the penetration

depth d, the inverse of the (wavelength dependent) absorption coefficient α. To improve the model and obtain more reliable results, two steps are required. The first is to take into account the actual shape of the pump pulse (Gaussian) and the finite size of the probe pulse, which is Gaussian too. The second is to consider the role of the finite penetration depth of the pump pulse. This is done numerically, calculating $\Delta R/R(\omega)$ through a transfer matrix method, when a graded index with exponential profile proportional to $\exp(-z/d)$ (being d the pump pulse penetration depth) is assumed.

Gaussian Profile for pump and probe beams
As far as the probe lateral size is kept smaller than the pump one (as always happens in pump-probe experiments), the common procedure for calculating the effective power density would be correct if the power distribution were uniform in the beams section (disk). This is not the case, since the lateral pulse profile is Gaussian. Thus, the actual Gaussian power distribution (given by the pump pulse) must be taken into account, together with the Gaussian probe pulse profile. The idea is to calculate which is the effective power density to be considered in the simulations, with respect to the one calculated in the homogeneous case, in order to be more quantitative.
A Gaussian power distribution for the pump pulse has been taken into account, which is normalized in such a way the total absorbed mean power P is the same of the homogeneous case (defined by the relation $P = p\cdot(\pi FWHM^2/4)$, where now I omitted the temporal dependence):

$$p \ln 2 e^{-4\ln 2 r^2/FWHM_{pu}^2}$$

(indeed: $\int_0^{2\pi}\int_0^{\infty} r dr p \ln 2 e^{-4\ln 2 r^2/F_{pu}^2} = P$)
In the same way, a Gaussian distribution for the probe has been taken into account, which is normalized to 'one':

$$\frac{4\ln 2}{\pi F_{pr}^2} e^{-4\ln 2 r^2/F_{pr}^2}$$

(indeed: $\int_0^{2\pi}\int_0^{\infty} r dr \frac{4\ln 2}{\pi F_{pr}^2} e^{-4\ln 2 r^2/F_{pr}^2} = 1$)
The effective power density in the non-homogeneous case thus results:

$$p_{eff} = p \ln 2 \int_0^{2\pi}\int_0^{\infty} r dr e^{-4\ln 2 r^2/F_{pr}^2} \frac{4\ln 2}{\pi F_{pu}^2} e^{-4\ln 2 r^2/F_{pr}^2} = p \ln 2 \frac{F_{pu}^2}{F_{pu}^2 + F_{pr}^2}$$

If one considers the power distribution ratio with respect to that of the homogeneous case, it results:

$$p_{eff}/p = \ln 2 \frac{F_{pu}^2}{F_{pu}^2 + F_{pr}^2}$$

which depends on the relative spot sizes of the pump and the probe beams. This relation indicates that the measured signal (obviously related to the Gaussian case) refers to an effective power which is always smaller than the one calculated in the homogeneous case. This means that in the simulations the actual power density must be reduced by a factor which is at least $\ln 2$ ~0.69, in the case of a delta-like probe. If the probe spot size is one-third the pump one, the factor becomes: $0.9 \cdot \ln 2$ ~0.62; if the probe spot size is half the pump one, the factor results $0.8 \cdot \ln 2$ ~0.55. As far as the probe spot size becomes closer to the pump one, the measured $\Delta R/R$ reduces, and the correction with respect to the homogeneous case is important and important.

Role of the pump-beam finite penetration depth

To get quantitative results in models requiring a precise knowledge of the absolute magnitude of a time-resolved signal, the problem of the finite penetration depth must be faced. This is the case of the two, three and four temeprature models presented so far.

The correction which takes into account this effect must be evaluated in a numerical way. We employed the transfer matrix method. This method is widely used in optics to analyze the propagation of electromagnetic waves (here the probe ones) through a layered medium (in our case, the medium is made optically inhomogeneous by the effect of the laser excitation with a pump pulse whose penetration depth exponentially decays inside the material, and which induces a modulation in the material refraction index). The reflection and transmission of light from an interface between two media is described by the Fresnel equations, and is governed by the refraction index (which will thus be the natural quantity to consider). When multiple interfaces are present, multiple reflections occur. Depending on the geometry of the reflection (which determines the light path length), the reflections can interfere constructively or destructively (for simplicity we will consider the case of normal incidence). The overall reflection and transmission of a layered structure is the result of a huge number of reflections, which is in general difficult to calculate. The transfer matrix method was developed to this purpose. According to Maxwell's equations, there are simple continuity conditions for the electric fields across boundaries from one layer to the next. If the field is known at the beginning of one layer, the resulting one at the end of the layer can be obtained from a simple matrix operation. The effect of a stack of layers can be represented as the product of the individual layer matrices. The final step of the method involves converting the fields back to reflection and transmission coefficients.

We assume the exponentially decaying pump power profile modulates the (complex) refraction index in a linear way: the pump-induced modification of the refraction index will thus decay exponentially too in the direction perpendicular to the sample surface. The fact that $\int_0^\infty dz e^{-z/d} = d$ ensures that the pump-induced modification of the refraction index at the sample surface equals the one calculated in the homogeneous case (in which the excited area is a cylinder of height $d = \alpha^{-1}$). This is helpful since one can consider, as a starting point for the simulation, the transient refraction index values obtained in the homogeneous case. The pump-induced modification of n then drops to zero in a distance of about $3d$, where the equilibrium refraction index is recovered. We make a simulation in which the sample is decomposed in many thin films parallel to the sample surface; each is 1 nm thick and is characterized by a refraction index $n = n_0 + \Delta n_{hom} e^{-z/d}$, where $z = m \cdot 1$ nm, for the m-th layer. The result of the transfer matrix method simulation is (probe) wavelength dependent, and it is directly the new value of the transient reflectivity, to be compared to the one of the homogeneous case. The graph below shows the original transient reflectivity, as obtained in the homogeneous (non-layered) case, and the one corrected for the finite penetration depth, obtained through the simulation described, assuming a pump penetration depth d (we use the value d =166 nm, the Bi2212 penetration depth at the pump wavelength λ =790 nm). The simulation result for the case d=infinity (infinite penetration depth), which superposes to the homogeneous case result (as it should be), is also reported. This ensures we implemented correctly the method.

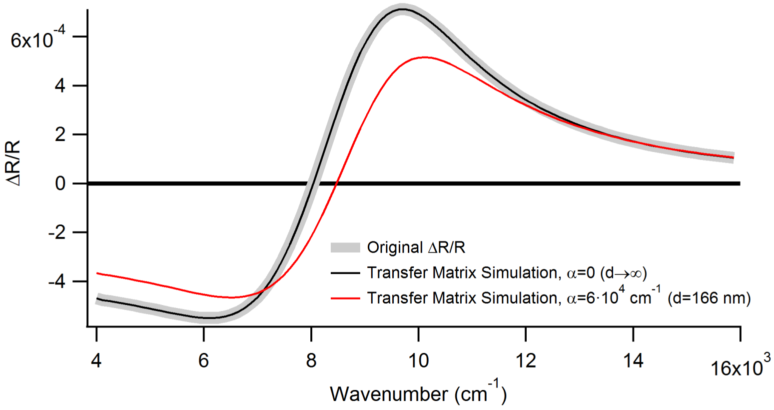

Figure 4.9: The result of the transfer matrix method applied to the time-resolved optical signal in the energy domain is presented. Black line is the original signal. Red line represents the signal corrected for the finite penetration depth of the pump beam (166 nm for Bi2212), which creates in the material a graded index with exponential profile. Thick gray line is a test simulation, performed for an infinite penetration depth of the pump beam, which does not alter the signal, as it should be.

4.4 Differential Model for the Dielectric Function

In this section I introduce a model we developed to interpret the transient spectra measured with the novel time-resolved spectroscopic set-up, described in 5. I anticipate that with this novel pump-probe set-up, the energy resolution is added to the conventional temporal resolution of the optical pump-probe method. This is achieved by exploiting a broadband probe pulse, with a wide spectral content (1 to 2 eV in particular). With this method, the time-resolved signal is measured in both the time domain, as a function of the pump-probe delay τ, and in the energy domain, as a function of the probe pulse energy $\hbar\omega$. The spectroscopic information, which is related to the modification on ultrafast timescales of the dielectric function, allows to better clarify the true physical origin of the observed signals. One important result of this approach is that we will be able to constraint the coefficients c_j appearing in the expressions 4.6, 4.3.3, 4.10, 4.11, thus limiting the number of free parameters in the fitting of the 3TM (or 4TM) to experimental data in both time and energy domains. The coefficients c_j are instead free fitting parameters in the case the 3TM (or 4TM) is fitted to data only in the time domain, impeding reliable results for the electro-boson coupling to be achieved. More details can be found in the analysis done in 6.

In the following, I will refer to this approach as the *differential dielectric function* approach. The term *differential* underlines the fact that this model allows to establish a precise relationship between a time-resolved optical signal in the energy domain and a peculiar (pump-induced) modification of the equilibrium dielectric function of the system, originating the signal itself.

An essential requirement for this approach is that the equilibrium optical properties of the material under investigation are completely understood. This problem has been deeply tackled in section 3.7 for the Y-Bi2212 sample, at various temperatures. In other words, the equilibrium, experimentally measured (usually by ellipsometric techniques) complex dielectric function $\epsilon(\omega,T) = \epsilon_1(\omega,T) + i\epsilon_2(\omega,T)$ must be satisfactorily reproduced by fitting to it a model composed of a Drude oscillator (in the Extended Drude formalism) and a sum of Lorentz oscillators, representing respectively the intraband transitions (low-energy side) and the interband ones (high-energy side). This model will constitute the static, equilibrium dielectric function $\epsilon_{eq}(\omega,T)$, the starting point of our approach. Usually this model is constituted by a huge number of parameters (30-40), as it is clear from section 3.7.

The final quantity we measure with the time-resolved spectroscopic setup is the transient reflectivity $\Delta R/R$, which includes the frequency information ω: $\Delta R/R(\omega,\tau)$, where τ is the pump-probe delay. This quantity is defined as follows:

$$\Delta R/R(\omega,\tau) = \frac{R_{ex}(\omega,\tau) - R_{eq}(\omega)}{R_{eq}(\omega)} \tag{4.12}$$

where $R_{eq}(\omega)$ is the static reflectivity (which does not depend upon τ, since it is measured by blocking the pump beam), related to $\epsilon_{eq}(\omega)$ through formula 3.3, and $R_{ex}(\omega,\tau)$ is the excited reflectivity (which now depends upon the pump-probe delay τ), which analogously will be related to a new, non-equilibrium dielectric function, which we call excited dielectric function, indicated with $\epsilon_{ex}(\omega,\tau)$. This dielectric function will describe the effect on the material electronic structure, induced by the pump beam. In principle, this dielectric function will be as similar as possible to the static one: our approach is to vary the smallest subset of parameters necessary to catch the transient reflectivity spectrum at delay τ, with the great majority of the parameters being unvaried. The number of oscillators is never modified. Only slight perturbations of the parameters are considered throughout this work (as we work in a very low excitation level regime).

The pump excitation effect on the equilibrium dielectric function, resulting in a non-equilibrium dielectric function, can be of different nature. It can be mainly thermal, which means the transient spectrum can be reproduced by varying only the temperatures comparing in the Extended Drude formalism (see section 3.7), or can be of different kind (though a small heating of the system is obviously always present, which is given by the energy deposited in the system by the pump pulse). If we consider other effects related to the low-energy side of the dielectric function, the pump pulse can for example modify the shape of the glue function in the Extended Drude model, or can modify the Gap in the density of states. While if we consider the high-energy part of the dielectric function, a pump-induced modification of the Lorentz oscillator parameters can take place. A plasma frequency modification for some oscillators indicates a spectral weight shift, while a modification in the central frequencies or widths of some oscillators, indicates a modification of the band structure.

It has to be emphasized that even the variations of the dielectric function low-energy side parameters can induce a change in the $\Delta R/R$ at much higher energies, typically around the plasma frequency, which is about 1 eV for Y-Bi2212. On the contrary, the modification of the interband oscillators parameters typically produces changes in the $\Delta R/R$ which are confined around the central frequency of the involved oscillator. Below, a few examples reporting on the effect on the optical properties of an impulsive thermal heating of the system, triggered by the absorption of the pump pulse energy, are presented and commented. I will present at first some exaggerated examples, to point out which is the actual effect even in the static dielectric function. Then, I will show which is the effect on the $\Delta R/R(\omega)$ of a pump-induced only-thermal modification of the dielectric function, in various conditions for the coupling of the electrons with the different bosonic degrees of freedom of the system. These quantitative simulations are performed for an Y-Bi2212 sample at T=100 K.

It is by the differential-dielectric-function method here presented, with the help of the spectroscopic information, that we have been able to understand the microscopic origin of the observed signals, for the normal, pseudogap, and superconducting phases of the Bi2212 family of high temperature superconductors. These information will be presented in detail, respectively, in chapters 6, 7, 8.

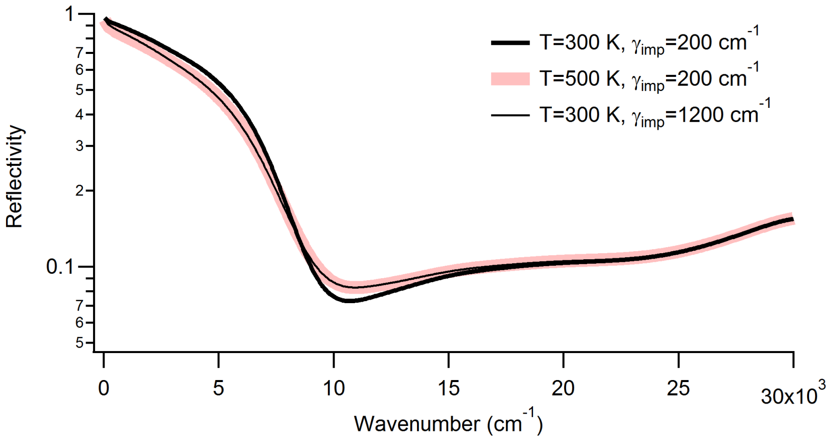

Figure 4.10: Here I report the effect on the static reflectivity of an heating of the system from T=300 K to T=500 K, being T the temperature appearing in the extended Drude model. The effect of the heating can be reproduced by simply increasing, for the lowest temperature situation, the damping term γ_{imp}. This means the heating implies a reduction of the conventional scattering time $\tau = \gamma^{-1}{}_{imp}$. From this simulation, we also argue that the heating effect is not frequency-dependent, since γ_{imp} is constant.

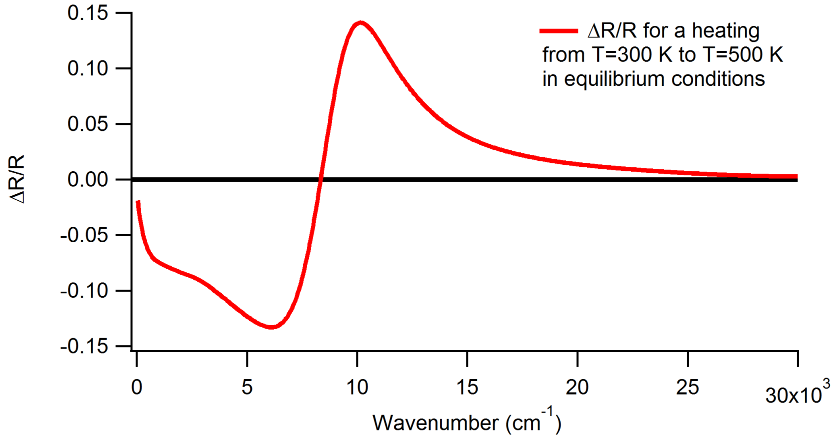

Figure 4.11: Here I report the simulated transient reflectivity variation, $\Delta R/R$, arising from the heating of the system from T=300 K to T=500 K in equilibrium conditions.

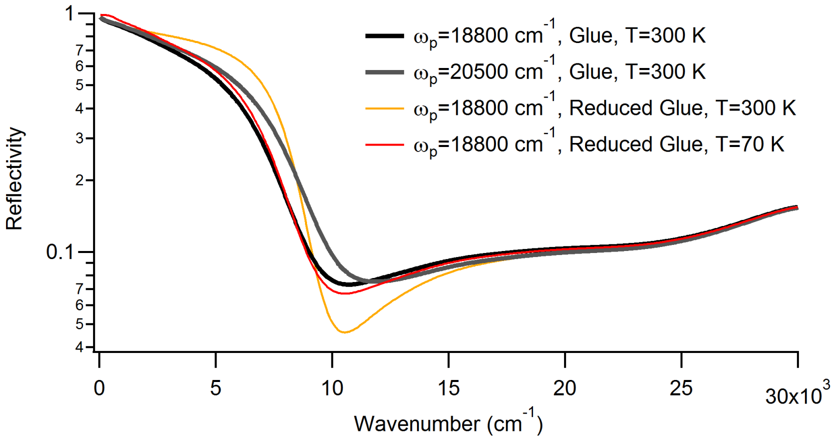

Figure 4.12: Here I report the effect on the static reflectivity arising from a modification of the Drude plasma frequency of the system, ω_p, and by a reduction of the electron-boson coupling, expressed by the Glue Function $\Pi(\Omega)$. This effect cannot be reproduced in an intuitive way. A cooling of the system is not enough to account for a reduced electron-boson coupling strenght.

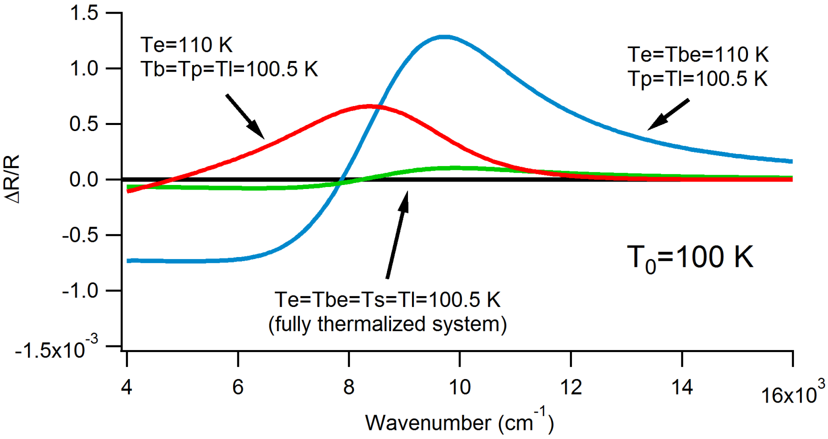

Figure 4.13: Simulation of the $\Delta R/R(\omega)$ induced in Y-Bi2212 at T=100 K by a purely heating effect. T_e, T_{be}, T_p, T_l are respectively the electrons, electronic bosons, strongly coupled phonons and weakly coupled phonons temperatures. The temperature increments ΔT_j are calculated through the 4TM (see section 4.3.3 for further details), for different scenarios: non-thermal scenario, in which the electrons are decoupled from all the bosonic degrees of freedom (red line); quasi-thermal scenario, in which electrons are strongly coupled only with a subset of the bosonic degrees of freedom (blue line); quasi-thermal scenario, in which electrons and all bosons are thermalized at the same elevated temperature with respect to the thermal bath one (green line). The $\Delta R/R(\omega)$ is calculated with the differential dielectric function approach and the Extended Drude model presented in 3.5.2. The aim of this picture is to emphasize how different physical scenarios lead to a completely different spectral response $\Delta R/R(\omega)$.

Chapter 5

Time-Resolved Spectroscopy

5.1 Introduction

The novel results presented in this thesis work have been made possible by a novel experimental technique, the time-resolved optical spectroscopy. This technique constitutes the natural extension of the conventional (one-color) time-resolved ultrafast pump probe technique, in which the spectral (energy) resolution is added to the intrinsic temporal resolution of the technique ($\sim$100 fs). In this way, an effective spectroscopy with temporal resolution is achieved. This chapter, after a brief introduction to the time-resolved methods, describes in detail the techniques developed in this work to obtain the spectral resolution. I can anticipate that I fulfilled this task in two complementary ways: exploiting a white-light supercontinuum pulse to cover the visible region of the electromagnetic spectrum (1.2-2.2 eV, i.e., 1050-550 nm, i.e., 9500-18000 cm^{-1}), and a tunable infrared pulse (obtained through an optical parametric amplifier, OPA), to cover the infrared part of the spectrum (0.5-1.1 eV, i.e., 2450-1100 nm, i.e., 4000-9000 cm^{-1}).

5.2 Motivations

The pump-probe approach is today declined in a wide field of time-resolved measurements, well beyond time-resolved optics. In the pump-probe framework, two synchronized pulses are employed. One is the so-called pump beam, exciting in a non-equilibrium condition the sample, while the other is the so-called probe beam, used to measure, as a function of the time delay with respect to the former, the effect produced by the excitation on one quantity of interest. The first time-resolved experiments, made possible by the advent of pulsed laser sources, were in the field of optics. In these all-optical pump-probe experiments, both the pump and the probe beams are ultrashort ($\sim$100 fs) laser pulses, typically in the near-IR region. They are quasi-monochromatic, in the sense that their bandwidth is typically the minimum required by the indeterminacy principle for the pulse to be ultrashort (∼10 nm for a ∼100 fs, 800 nm pulse). With all-optical pump-probe measurements, the probed quantities are the optical properties of the sample, namely, the reflectivity R or the transmissivity T. On the contrary to the pump beam, which is often the fundamental of the laser source, soon became clear how a different probe could provide new advances. Considering an all-optical pump-probe, the tunability of the optical probe is possible since long time. Usually it is achieved thanks to light-conversion devices, known as Optical Parametric Amplifiers (OPA, see section 5.6). In this way, the spectral range that can be probed is considerably widened (the 200-20000 μm range can be explored). However, the non-equilibrium optical properties can be probed singularly, one-wavelength at a time. Moreover, such light conversion devices work only in combination with high-power laser sources, which are not well suited to perform experiments on fragile materials. However, more recently it was demonstrated that the probe can be tuned in the far-IR or THz (1 THz $\sim$ 4.1 meV) spectral range with conventional, low power sources. This opened the access to the probing of the non-equilibrium optical properties in the infrared spectral range. As an example of application of these techniques to probe the non-equilibrium optical properties of cuprate superconductors, I may cite, respectively for mid-IR and THz: [101, 100, 102, 20, 19] and [12, 99]. The study of the evolution of the optical properties, simultaneously in a wide range of energies, is a possibility that only very recently is encountering an increasing interest. This is made possible thanks to the so-called supercontinuum pulses, i.e., very broadband, white light pulses, which energy content can exceed 1 eV. Joining the spectral resolution to the time-resolved approach considerably helps in the interpretation of the observed non-equilibrium dynamics. Applications of this technique to strongly correlated electronic materials have been recently reported [82, 169]. The problem is that in general such pulses require high-power sources (see section 5.6) to be generated, and are again not well suited to investigate from the non-equilibrium point of view materials which ground state can be easily altered, quenched or vaporized by an excitation.

Only recently it has become possible to generate supercontinuum pulses by using low-energy laser sources, thanks to the use of Photonic Crystal Fibers (see section 5.7 for further details). In this thesis, I developed a set-up exploiting this new possibility. The important result has been that a novel pump-probe system allowing to measure simultaneously the temporal evolution of the time-resolved optical signal in a wide range of energies has been developed. This setup, on the contrary to the ones based on high-power laser sources, is characterized by an enhanced sensibility, and allows to probe the non-equilibrium optical response of a material which is only slightly brought out of its equilibrium condition. This ensures the ground state of the system is not strongly perturbed, with the measured optical response accounting for the typical excitations of the ground state itself. This setup constitutes the perfect match for

materials which ground state is a phase which free energy only slightly differs from the one of the other allowed phases. This is the case of superconductors or materials exhibiting charge density wave or spin density wave ordering. These phases are vaporized for extremely low values of pump fluence [168].
In particular, the spectral resolution combined with the temporal one allows to understand the physical origin, i.e., on the microscopic level, which originated the non-equilibrium optical signal. This is often precluded to conventional time-resolved measurements, probing the time-resolved optical signal at a fixed wavelength. This can be understood by the observation that the spectral resolution allows to interpret the non-equilibrium optical signal by differential models applied to the sample dielectric function. By doing so, being the dielectric function related to the electronic structure and the allowed optical transitions of the material, a close correspondence can be established between a non-equilibrium signal in the energy domain and one excitation-induced effect on the material electronic structure.
It is for this reason that we call this novel experimental technique the time-resolved spectroscopy. It is a spectroscopy, since the spectral resolution has been achieved. It is non-equilibrium, with the peculiarity that the weakly-excited states can be probed, providing information precluded to static spectroscopy, that only the joined spectral and temporal resolutions can provide. The access to the dynamics, from which the effects related to the thermal heating can be disentangled from the purely electronic ones, and the fact that the ground state of the system is not sensibly affected, make this technique the ideal tool to probe the strongly correlated electronic materials, in which an interplay of different phenomena dominate the non-equilibrium optical signal.

For completeness, I must remember that in the last few years the pump-probe approach has been successfully applied also to non-all-optical techniques. Time resolved photoemission and time-resolved electron diffraction are widespreading techniques. The former technique allows to measure the temporal evolution of the electronic structure, while the latter allows to study the temporal evolution of the crystal structure, after the sample is brought out-of-equilibrium by the absorption of a pump pulse. In both situations, the pump pulse exciting the sample is an optical, laser pulse, while the probe pulse is respectively a high-energy photon ($\gtrsim$6 eV) photoemitting electrons or an electron bunch which diffraction pattern from the sample is recorded. Examples of application of these techniques on cuprates are respectively: [145, 41] and [27].

5.3 Time-resolved basics: background, sources, useful definitions and beam diagnostic

It is a long time that time-resolved optical measurements are being carried on on solid state systems. The first examples of such kind of measurements,

that allowed to study the transient, non equilibrium (optical) properties of solid state systems on very short timescales (ps and fs), are dated 1980−1990 [165, 63, 64, 163, 25, 24, 87].
The key-element for this kind of study is an ultrafast laser system capable of producing a train of ultrashort pulses, with a temporal duration of 100-1000 fs. Other important parameters of the laser light pulses are their photon energy (or wavelength) and the number of pulses per unit of time (this quantity is known as *repetition rate* of the source, measured in Hz). For Ti:Sapphire sources, that is, the most common laser systems today available for research purposes, the pulse photon energy equals 1.55 eV (i.e. 800 nm, 12500 cm^{-1}); this is called the fundamental of the laser. Ti:Sapphire, i.e., Ti doped Al_2O_3, is the active medium inserted in the laser cavity.
The majority of time-resolved measurements published up to now, are performed by using the fundamental energy (or its harmonics: 2^{nd} - 3.14 eV (400 nm); 3^{rd} - 4.51 eV (266 nm), 4^{th} - 6.28 eV (200 nm)) to measure the transient optical properties. This is what we call conventional (or one-color) pump-probe measurements. This approach, although capable of revealing the non-equilibrium dynamics of a system on a timescale (< 1 ps) not accessible to other non-optical techniques, has an important limit: the dynamics can be measured at a single and fixed energy. This prevents, in most situations, the understanding of the microscopic origin of the (differential) time-resolved optical signal. To achieve this ambitious goal, the range of energies for which the non-equilibrium dynamics of a system is measured, must be widened. This opens the way to the knowledge of the non-equilibrium dielectric function of a system, from which a great amount of information can be, in general, extracted. The realization of this target will be described in detail in the next sections of this chapter.

Laser sources classification

The average power at the output of a standard laser system is of the order of some (1-4) Watts. Depending on the repetition rate of the source, three classes of lasers can be distinguished today. The key parameter is the energy per pulse, measured in J.

- The so-called oscillators produce train of pulses at 80-100 MHz: this results in an energy per pulse of the order 5-50 nJ/pulse. This source can be coupled to an acousto-optic device to control the repetition rate of the source, from some MHz to single-pulse. This device is called pulse-picker (if it is placed outside the cavity) or cavity-dumper (if it is placed inside the cavity, resulting in a minor amount of losses). Both these devices are useful in reducing the average thermal heating of the sample under study. This is mandatory in the field of low-temperature physics.
- The regenerative-class of laser systems have repetition rate tunable from

10 to 300 KHz, and produce pulses with a typical energy of about 5 μJ.

- Finally, the amplified laser systems, with repetititon rate around 1 kHz (10 Hz to 5 kHz operation is often achievable), produce pulses with energy per pulse in the mJ (1-10) range.

Thus, the three classes of sources differ in the level of the energy-per-pulse: nJ, μJ, mJ. Since we deal with solid state materials which ground state phase can be easily vaporized by laser excitation [168, 81], we employed both a cavity-dumped oscillator and a regenerative system (which enables to take advantage of many non-linear optics phenomena, as we will see). Fig. 5.1 sketches the proper pulse parameters to perform a pump-probe experiment on a solid state system, for the three classes of laser sources. Advantages and drawbacks for each source are pointed out.

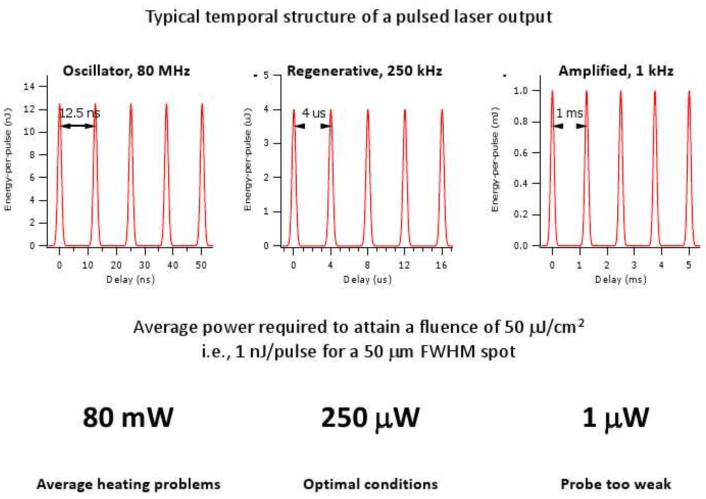

Figure 5.1: This scheme summarizes the main parameters of laser pulses produced by different laser sources. Assuming a spot size of 50 μm and a fluence of the order of 50 μJ/cm^2 (see [168] for the reason), it turns out that the optimal laser system is the one with a repetition rate in the range 0.25-1 MHz. An oscillator would heat the sample too much, while with an amlified system the problem stands in the fact that the probe pulse - which must be less intense than the pump pulse, would be too weak to be detected.

Optical Pump-Probe

Conceptually, the time resolved approach, which in the optics field is realized through the so-called pump-probe technique, is simple. The train of pulses produced by the laser source is divided in two arms by a beamsplitter (a partially reflective mirror). The more intense one (usually from 70% to 90% of the total power) is used to excite the sample, and is called pump beam, while

the less intense one (10% to 30% of the total power) is employed to measure the pump-induced change in the optical properties of the sample, and is called probe beam.
By optical properties I mean the reflectivity R of the sample, or its transmissivity T (if the sample is transparent to the actual probe wavelength), or both. Thus, the probe beam reflected or transmitted from the sample, is collected with a sensing element (usually a photodiode) and the generated electric signal is acquired and digitized. On the contrary, the pump beam is dumped. In the time-resolved approach, the relative change (transient) in the optical properties is measured. This means that the measured quantity is the relative variation induced by the pump. In a typical time-resolved experiment, the measured quantity is the difference between the reflectivity R_{pumped} of the excited (pumped) system and the reflectivity $R_{unpumped}$ of the equilibrium (unpumped) system, divided by the equilibrium reflectivity, that is:

$$\frac{\Delta R}{R}(\omega,\tau)=\frac{R_{pumped}(\omega,\tau)-R_{unpumped}(\omega)}{R_{unpumped}(\omega)} \tag{5.1}$$

τ is the actual delay between the pump and probe beams; expression 5.1, in principle, also depends on ω, the frequency of the probe photon energy $\hbar\omega$.
The $\Delta R/R(\omega,\tau)$ is usually very small with respect to the values R_{pumped} and $R_{unpumped}$. In practice, R is the reflected light intensity from the sample, and not the true reflectivity. However, since, as it is always the case, the incident intensity I_0 on the sample is unchanged, R has the same meaning of the actual reflectivity, in the $\Delta R/R$ expression. The same argument holds for the transmissivity T. Both the quantities $\Delta R/R$ and $\Delta T/T$ have the advantage of being universal, i.e., independent (as far as one works in a linear regime) from the incident probe intensity I_0. Usually, $\Delta R/R$ ranges from 10^{-2} to 10^{-6}. This means that the detection system, described subsequently, must be very accurate. It must have a dynamic range able to reveal signal variations as small as one part over one million, ie, $\sim$1 μV, if the total ligth intensity produces a signal R$\sim$1 V on the detector. The detection system must be characterized by a signal-to-noise ratio (S/N) higher than the $1/(\Delta R/R)$ induced by the pump pulse.

Pump-probe delay, τ

In expression 5.1, τ is the time delay between the arrival of the pump and probe pulses on the sample. It is of the order of tens of fs, and, if one wants to exploit the full temporal resolution of the system, it is of the same order of the pulse duration. The time resolution, as small as the laser pulse duration, comes from the fact that the ultrashort probe laser pulses sample the reflectivity or the transmissivity of the sample, 'integrating' it on a time window equal to that of the pulse duration.
The delay τ is varied, to study the dynamics of the system, simply changing the relative length of the optical path of the pump and the probe arms. This

is achieved with a mechanical delay stage or with a coil, on which a couple of mirrors (to reflect the beam) are mounted. One μm of displacement introduces a delay equal to 6.66 fs between the pump and probe beams ($1\mu\text{m} \cdot 3.33$ fs/μm $\cdot$ 2, where the 2 comes from the doubling of the path upon reflection).

Time-resolved optical trace

To measure a pump-probe trace (a plot of the $\Delta R/R$ or $\Delta T/T$ for a number of pump-probe delays τ), two types of approach are possible.

The first consists in acquiring the $\Delta R/R$ signal point-by-point, modifying the relative delay and subsequently acquiring the signal, for a time long enough to obtain the desired noise level in the measurement (usually, 1 s signal average per point is enough to obtain a S/N of the order 10^5, for a $\sim$1 MHz repetition rate source).

The second approach consists in scanning quickly the delay between pump and probe, and acquiring continuously and synchronously the $\Delta R/R$ signal. The temporal windows of the acquisition should be kept as small as possible not to lower the temporal resolution, thus, to lower the noise in the measurements, many scans are needed, which must then be averaged. Usually, 100-1000 scans are enough to obtain a S/N of the order 10^5, for a $\sim$1 MHz repetition rate source. This method (called 'fast scan') requires a fast (and with the lowest possible inertia) delay stage. This approach constitutes a clear advantage because, since every scan is completed on a time of the order of 1 s, it helps suppressing the disturbing effects related to the laser source fluctuations and the effects of the sample degradation (when the sample is placed inside a cryostat, for example). The drawback is that the delay stages designed for this task have a short travel range, and the amount of data to acquire is huge, thus this approach is limited to small ranges of delay (of the order of 10-50 ps). If one needs to explore a wider range of delays (this depends on the dynamics one wants to analyze), the point-to-point approach is the only one that can be exploited. The speed (in mm/s, or ps/s, if one converts the displacement in delay) of the delay stage, v_D, and the acquisition time window t_W of the acquisition system set the temporal resolution of the measurements according to the following formula: Resolution(ps)=v_D(ps/s)$\cdot t_W$(s). This quantity is often larger than the limit resolution given by the pulse duration, in the case of fs laser; what it is important is that this quantity must be smaller than the dynamics one wants to measure. Some numbers are helpful: if v_D=10 ps/s$\sim$1.5 mm/s for the delay stage, and the acquisition time window t_W is set to 1 ms, the maximum achievable temporal resolution is 10 fs. If a 10 ps pump-probe scan is required, each scan would take 2 s (2$\cdot$1 s, since the delay stage must go back and forth).

Direct digitization of the signal vs Lock-in acquisition

The acquisition of the signal must be done taking in mind that very often, extremely small variations in the signal (less than one μV) must be detected. The direct digitalization of the photodiode electric signal is thus a poor idea in the great majority of the experiments. This would require very high resolution digitizers ($>$ 16 bit: over a 1 V full-scale, 16 bit means $\sim$15 μV, which is too much in many cases), which are rare and expensive. This approach is also very sensitive to the various sources of electrical noise. Anyway, to obtain a differential signal, the procedure is to acquire the reflected signal R with ('pumped') and without ('unpumped') the pump beam, and performing the difference with the correct parity (which must be sensed in some way). The most common way to modulate the pump status is to make use of a so-called optical chopper, a device constituted by a disk with a mask of regular holes (designed in such a way to achieve a 50% duty cycle for the modulation), which is put in rotation by a high speed motor. The laser beam is thus chopped by the disk at a frequency ranging from $\sim$1 Hz to $\sim$100 kHz (with a proper choice of the disk mesh).

The Lock-In amplifier solves the resolution problems coming from a direct digitization of the signal. By using a complex algorithm based on Fourier transforms, multiplications and filtering of the signal, carried on by a fast DSP (digital signal processor), this device can extract, from an electric signal of high intensity, only a component which has a frequency equal to that fed in by an external reference. If one modulates the pump beam with a chopper (whose frequency reference is brought to the lock-in), and the pumping has an effect on the optical properties of the system, detected with a photodiode, connected to the lock-in input, the lock-in output will be only - and directly - the pump induced variation of the optical properties, ΔR. To obtain the quantity $\Delta R/R$, the static signal R must be sampled in some way. This is a minor problem, since R is of the order of 1 V. The advantage of this approach is that all sources of noise (with frequency different from the chopper one) are intrinsically suppressed. In general, the higher the chopper frequency f, the lower the noise level $\propto 1/\sqrt{f}$, for the noise related to the acquisition system. In the case of lock-in acquisition, the acquisition time window t_W defined about the fast scan method equals the lock-in integration time. The chopper frequency must be higher (10 times or more) than t_W^{-1}.

Temporal and Spatial superposition

To perform a pump-probe experiment, the temporal and spatial coincidence conditions, for the pump and probe beams on the sample, must be achieved. The condition for which pump and probe impinges simultaneously on the sample is called temporal coincidence. This means that the pump and probe arms have the same optical length, and thus this particular delay τ is defined $\tau_0 = 0$. Often, but not always, at this particular delay one observes the maximum variation of the optical properties.

For what concern the spatial coincidence condition, the maximum of the time-resolved optical signal is achieved when the probe beam is exactly at the center of the (pump) excited area. To make the measure more reliable, usually the pump spot on the sample is kept larger than the probe spot, and this is obtained by focusing the pump beam on the sample with a lens with focal length bigger than the focal length of the lens on the probe beam. This ensures that the probe probes an area which is uniformly excited. The spatial superposition of the beams on the sample is checked with a CCD camera, equipped with an objective collecting the light scattered by the sample.
To avoid interference effects on the sample, usually the pump and probe beam polarizations are kept orthogonal. This helps also to prevent that the pump light scattered by the sample reaches the detector, simply placing a polarizer in front of it. Another solution to improve the measurements quality is to place the delay stage on the pump path: the fact that the pump spot is bigger, and that the pump should not be collected, drastically reduces the effect of misalignments, that would produce non-physical variations in the signal.

5.3.1 Beam Parameters

Key parameters that must be known in order to correctly set up a measurement and interpret the acquired data are the spot size and the pulse duration, for both the pump and the probe beams, on the sample. Typically, laser pulses are Gaussian both in space and in time. They remain Gaussian up to the sample, if they are properly propagated.

Spot lateral size
Two methods can be employed to measure the spot size. The first consists simply in measuring the intensity profile of the beam itself, when impinging on a scattering material placed at the sample position. This task is achieved by imaging the spot on a CCD (Charge-Coupled-Device) camera. To have a good resolution, since typical spot sizes are of the order of 20-50 μm and the CCD pixel size is of the order of 5 μm, a magnifying objective is often used. Then, a Gaussian profile is fitted to the image, along various directions, to extract the beam size.
The second method is called 'the knife-edge'. The position of a knife, mounted on a precision translation stage, is scanned perpendicularly through the beam, in the same position where the sample would be. By means of a photodiode, the total transmitted intensity is acquired, as a function of the knife position. This intensity equals the integral along one axis (defined by the direction of movement of the knife) of the product of the Gaussian pulse intensity, multiplied by a step function expressing the knife position. The integral of a Gaussian function can thus be fitted to the acquired trace, to extract the actual spot

size. In this work, the spot lateral size equals the spot FWHM (Full-Width-at-Half-Maximum).

Pulse temporal width
The temporal duration of ultrashort laser pulses can be measured by acquiring their sum frequency intensity [93], generated in a non linear crystal (usually BBO, beta-barium borate) placed at the sample position, as a function of the pump-probe delay τ. Sum frequency generation (SFG) is a non-linear process involving the energy mixing of two photons [93]. If pulses are Gaussian in time, their sum frequency signal is Gaussian too. Mathematically, the SFG process is expressed as a convolution of the intensities $I_j(t)$ of the two pulses: $C(\tau) = \int_{-\infty}^{+\infty} I_{pump}(t) I_{probe}(t-\tau)dt$, being $C(\tau)$ the sum-frequency signal.
If the pump and probe optical paths are different, i.e., contain a different number of dispersing optical devices, only the pulses cross-correlation can be determined. The pump-probe cross-correlation sets the lower limit for the temporal resolution the system can provide. If the two optical paths are similar, the measure can be approximated to an auto-correlation. Assuming that the pulses are Gaussian, their individual duration is given by their autocorrelation divided by a deconvolution factor, equal to $\sqrt{2}$ for Gaussian pulses [84].
The cross- (or auto-) correlation sum-frequency signal versus the pump-probe delay τ contains the information of the pulse duration. In practice, to extract this information, a Gaussian function is fitted to the sum-frequency signal. In this work, the pump-probe cross-correlation is expressed as the temporal FWHM (Full-Width-at-Half-Maximum) of the correlation signal.

Fluence
The pump fluence is defined as the energy per pulse divided by the area illuminated by the pump beam spot. It is usually expressed in μJ/cm^2. The spot area is calculated from the pump spot lateral FWHM, which is carefully determined with the methods described above. Indicating the pump fluence is the most common way to express the pump excitation intensity of the system. The probe beam fluence should be always kept orders of magnitude weaker than the pump one, to avoid further perturbations of the system. Typical values for the pump fluence employed in this work are comprised in the range 1-100 μJ/cm^2. Working at the lowest fluence values requires some level of care. As we will se, some interesting physics is learnt just at this (low) level of excitation ($\sim$10 μJ/cm^2), since HTSC are very susceptible to an external perturbation, particularly when they are in the superconducting phase.

Up to now, a general overview on the time-resolved approach has been provided. Anyway, the details of the various optical setups employed are described in the subsequent sections of this same chapter. For what concerns one-color measurements, a basic experimental system requires no more components than those already described. The setup we used is sketched in section 5.4. Sections 5.6 and 5.7 are devoted to the newly developed spectroscopic setups.

5.4 The one-color pump-probe technique

The laser source used for the one-color time resolved experiments is a cavity-dumped Ti:Sapphire oscillator, producing 1.55 eV, 120 fs laser pulses. This source is pumped by a solid state diode-pumped Nd:YVO_4 pump system, the Coherent Verdi V-10 (whose output is limited to 4 W). The main feature of this laser is the cavity dumper device, that allows to continuously tune the repetition rate of the source from about 2 MHz down to single shot, choosing an integer submultiple of the laser cavity repetition rate, equal to 54.3 MHz. This device is fundamental when one needs to reduce the effect of the average heating of the sample under test. This is a key requirement in many experimental conditions. The setup employed is schematized in Fig. 5.1. The description and aim of the various optical components is reported in the figure caption. The acquisition method is based on lock-in detection coupled to a fast scan of the pump-probe delay.

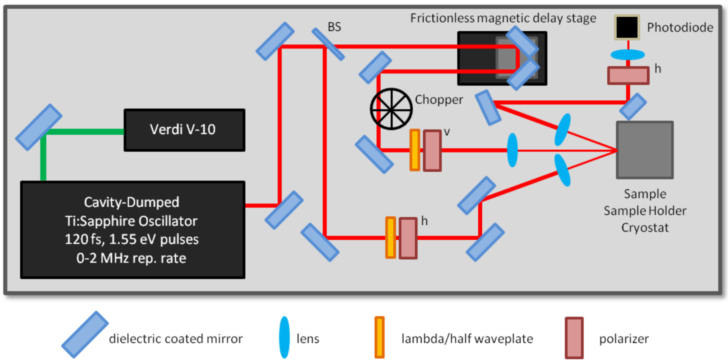

Figure 5.2: The scheme of the one-color pump-probe setup used is reported. Pump and probe beams are generated thanks to a 90%T-10%R beamsplitter. To focus the pump and probe beams on the sample, we employ respectively 20 cm and 10 cm focal lenght lenses, resulting in a spot size of $\sim$40 μm and $\sim$20 μm. This ensures we probe an uniformly excited area.

Important requirements common to all the optical schemes are the manipulation of the polarization state of the laser pulses and their attenuation. Having in mind that the polarization state of the laser output is linear and horizontal, one can rotate this linear polarization by means of a lambda/half ($\lambda/2$) waveplate (the angle of rotation of the linear state, α, is equal to 2θ, being θ the angle of the plate axis with respect to the horizontal), or a circular polarization state can be achieved by means of a lambda/quarter ($\lambda/4$) waveplate (whose axis is oriented at an angle $\theta = \pm 45°$ with respect to the horizontal line). In our setups, for both the pump and the probe beams, we employ linearly polarized fields. The possibility to rotate the relative polarizations of the pump and the probe beams is important since it allows to investigate possible anisotropies in the optical response or in the excitation process. To attenuate a (linearly polarized) laser beam, a lambda/half waveplate plus a polarizer is used. The output polarization is linear, and parallel to the polarizer axis. The output intensity, if the input polarization and the polarizer axis are horizontal, and theta is the same as before, is: $I = I_0(cos^2(\theta) - sin^2(\theta))^2$, being I_0 the incident intensity. The optical components are often designed to work at a single wavelength, but broadband components (which work in a wide range of wavlenghts) also exist.

5.5 Toward the time resolved spectroscopy

So far, I described the pump and probe approach for conventional one-colour (probe) measurements, with the details of the optical layout we employed for this kind of measurements (Fig. 5.1), and I defined some common important concepts which are universal in the field of time-resolved optics. As I anticipate, the novelty of this thesis is to extend this approach to a configuration in which the probe is no more a monochromatic pulse, but rather a broadband pulse which contains a continuum of wavelengths (supercontinuum), or it is a quasi-monochromatic pulse which can be continuously tuned across a wide range of energies. This allowed us to achieve time-resolved spectroscopy, i.e., to combine the temporal resolution with the spectral one. The time-resolved signal of expression 5.1 is indeed wavelength dependent, and this additional information opens the way to a new physics, adding a 'dimension' (the energy resolution) in our measurements. This new dimension finally allowed us to assign a clear physical origin to the measured transient signals, as reported in Chapters 6, 7, 8.
The two different approaches we followed are described in this chapter, starting from the tunable probe configuration, which is a straightforward evolution of the single-color setup. Finally, a comment about the excitation (pump beam) role. In the work reported here, the pump photon-energy is fixed, and equal to 1.55 eV (i.e., 800 nm). A systematic study of the effects of the excitation photon-energy tuning on the transient optical properties is beyond the scope of this work. However, we checked that the results were independent on the pump photon energy, repeating the most meaningful measurements with a SHG pumping. Despite this, a systematic study of the excitation mechanism could reveal some interesting features.

5.6 Tunable-Probe Pump-Probe Setup

The pump-probe setup described in this section was designed to perform time-resolved measurements with a probe energy in the near infrared region of the electromagnetic spectrum. In particular, the probe energy can be continuously tuned in the range 1100-2450 nm (i.e., 1.1-0.5 eV, 9000-4000 cm^{-1}). The pump is kept fixed at the fundamental energy value of 1.55 eV.

While the details of the optical setup are similar to those described in Fig. 5.1, what it is different is the laser source. The conversion of a 1.55 eV beam into a (tunable) infrared beam requires to exploit a non linear phenomenon, called parametric amplification. The device which allows to do this is called optical parametric amplifier, also known as OPA. These non linear phenomena requires energy per pulse of the order of μJ/pulse, thus a regenerative laser source must be employed.

Our laser source is the Coherent RegA 9050 system, a Ti:Sapphire laser system pumped by a Verdi V-18 solid state laser (producing 18W of monochromatic CW (continuous wave) radiation at 532 nm). The final laser output consists of a train of 1.55 eV, 50 fs laser pulses. The repetition rate of this source can be continuously tuned from 10 to 300 kHz. At a 250 kHz repetition rate, the one we used, the output power is about 1.5 W. This gives an energy per pulse of about 6 μJ. Very briefly, the scheme of this complex laser system is as follows: the 532 nm output (18 W) of the Verdi diode-pumped Nd:YVO$_4$ pump system is splitted in two parts: $\sim$6 W are brought to a Ti:Sapphire optical oscillator (Mira Seed), while the remaining $\sim$12 W are borught to the regenerative cavity (RegA). The oscillator produces a train of <100 fs, 1.55 eV pulses, with a fixed repetition rate of 80 MHz. These pulses are fed in a stretcher, a device based on diffraction gratings which aim is to increase the temporal duration of the laser pulses. These pulses are the seed pulses to be amplified by the regenerative cavity, in which they are fed in after having been temporally-stretched. In the regenerative multi-pass cavity the amplification process takes place. This process happens because the seed pulses pass through a Ti:Sapphire active medium for a proper number of times (20 to 30), until the desired energy has been reached for the pulse. The injection of the seed pulse in the cavity and the ejection of the amplified pulse are both obtained with an acousto-optic device (a cavity dumper). This device is a SiO$_2$ cell, whose index of refraction is modulated by a strain wave induced by a piezoelectric element, driven by a proper radiofrequency, in such a way that the beam passing through the cell is diffracted when the radiofrequency is applied. A complex electronics synchronizes the timing of the injection with the 80 MHz pulse train of Mira Seed, and manage the injection and ejection phases of the radiofrequency for the acousto-optic device. The seed pulses and the amplified pulses, which propagate collinearly, are separated thanks to a faraday rotator coupled to a polarizer. The amplified pulse is then recompressed with a grating-based compressor. The seed pulse must be stretched before the amplification, otherwise the peak intensity would be too high for a good amplification process to

occur. Obviously, not all the seed pulses are amplified: the RegA repetition rate is a sub-multiple of the seed laser repetition rate; the actual seed pulse to be amplified is picked by the cavity dumper, the others are dumped.
The 70% of the laser system output is fed to the OPA, for wavelength conversion. The resulting energy per pulse is of the order of 4 uJ. The remaining 30% is employed for the pump in pump-probe experiments. The Optical Parametric Amplifier is the Coherent OPA 9850. Its output consists in two beams, called signal and idler, whose energy can be continuously varied in a specified range. The infrared (1100-1600 nm) part of a white-light supercontinuum, generated focusing 25% of the total power in a Sapphire plate, is amplified in phase-matching conditions in a Type II BBO nonlinear crystal, exploiting a two-pass cavity design. The pump beam used for the amplification process is the remaining 75% of the total power entering the OPA. Two aspects are worth to be described in more detail: the supercontinuum generation and the amplification process itself. The supercontinuum generation is achieved in a 2 mm thick Sapphire plate, on which is focused (with a short focal lenght (30 mm) lens) an energy of about 1 μJ/pulse. In this way, a stable supercontinuum can be obtained. The generation threshold in Sapphire is about 500 nJ/pulse. Over this threshold, a self-focusing effect, related to the Kerr effect, occurs, and the intensity-dependent index of refraction of the material, being the incoming pulse spatially Gaussian, behaves like a lens for the pulse itself. Thus, extremely high pulse intensity develops, and various non linear phenomena cooperate to broaden the spectral content of the seed pulse. The most important non linear phenomena is the self phase modulation. The amplification process takes place in a 1 mm thick BBO non linear crystal. This process in called parametric amplification, and involves three beams (photons). In this process, the energy and momentum conservation relations, for the three photons, are satisfied simultaneously. These three beams / photons are: the seed beam, the one which will be amplified, and which comes from the supercontinuum: this will be the signal, s; the pump beam, which will be depleted after the amplification, indicated with p, and the idler, i, which is generated to match the energy and momentum conservation relations. ω_j and k_j are respectively the angular frequencies and momenta of the three beams. The energy and momentum conservation relations write:

$$\omega_i = \omega_p - \omega_s$$

$$\omega_p = \omega_s + \omega_i$$

$$k_i = k_p - k_s$$

The second expression indicates that one pump photon is annihilated, and two new photons, the signal and the idler, whose energy sum equals the pump one, are generated. There is thus a transfer of energy from the pump, which will be depleted, to the signal and the idler. The seed pulse coming from the supercontinuum 'tells' the system which frequency will be amplified. If the

axis orientation for the crystal matches the momentum conservation relation between the pump and the seed beams (this implies the so-called phase matching condition is satisfied), a good amplification efficiency is achieved. Starting from the sub-nJ energy level of the seed, a mean energy of more than 400 nJ/pulse is obtained for the signal, in a two step amplification process in the same BBO crystal.
Being 1.55 eV, 800 nm the energy of the pump beam, the degeneracy condition for the amplification process will be that for which both the signal and the idler have the same energy of 0.75 eV, 1600 nm. The signal output is comprised in the interval from 1100 to 1600 nm, while the idler output ranges from 2450 to 1600 nm. They are generated in a collinear geometry, and thus are both present at the OPA output. Signal and Idler have (linear) orthogonal polarizations, thus they can be alternatively selected with a polarizer. The energies of the couple of produced signal and idler can be tuned continuously in the range indicated. Once aligned, the tuning of the device is quite simple. It consists in the modification of the phase matching angle of the non-linear crystal, and in the compensation of the delays between the pump and the seed or signal, for both the two amplification steps. The signal and idler pulse duration has been characterized with a cross correlation with a 50 fs 800 nm pulse, when the OPA is seeded with a 50 fs pulse. The result is that the average pulse duration is of about 100 fs. Now that the laser radiation sources have been described, a brief description of the optical layout used to carry the experiments is provided. A schematic of the optical layout is presented in Fig. 5.3. In this configuration, the pump and the probe beams reach the optic bench being already divided. The pump beam comes directly from the RegA output, while the probe beam comes from the OPA output: it is either the signal or the idler pulse. In this way, the probe pulse can be tuned continuously from 1100 to 2450 nm. To switch from signal to idler, a polarizer is used, which is rotated by 90 degress to select the signal (horizontal) or the idler (vertical). To ensure the polarization of the two is the same on the sample, a broadband lambda/half waveplate plus a second polarizer (kept fixed) is employed. To compensate for the optical path of the OPA (about 5 m), the pump path is lengthened exploiting the reflection from some retroreflectors. The probe pulse must be attenuated by an amount of 100 to 10000 (with a neutral density filter with optical density (OD) continuously variable from 2 to 4) to ensure it is weak enough to be employed as a probing beam. To introduce a carefully variable time delay between pump and probe beams, the pump beam is brought to a retroreflector mounted on a coil motor. This device (APE ScanDelay 50) is computer controlled and allows to introduce a delay ranging from 10 to 50 ps in the beam path. Its motion equals a triangular wave, with a rise-time tunable from 0.1 to 5 s. This means that a complete pump-probe scan can be acquired in a time ranging from 0.2 to 10 s (5 to 0.1 Hz rate). This device is designed to allow acquisitions in the 'fast scan' configuration I described in section 5.2. We set the relevant parameters as follows: for a 10 ps scan, a rise time of 0.2 s was chosen. With a lock-in

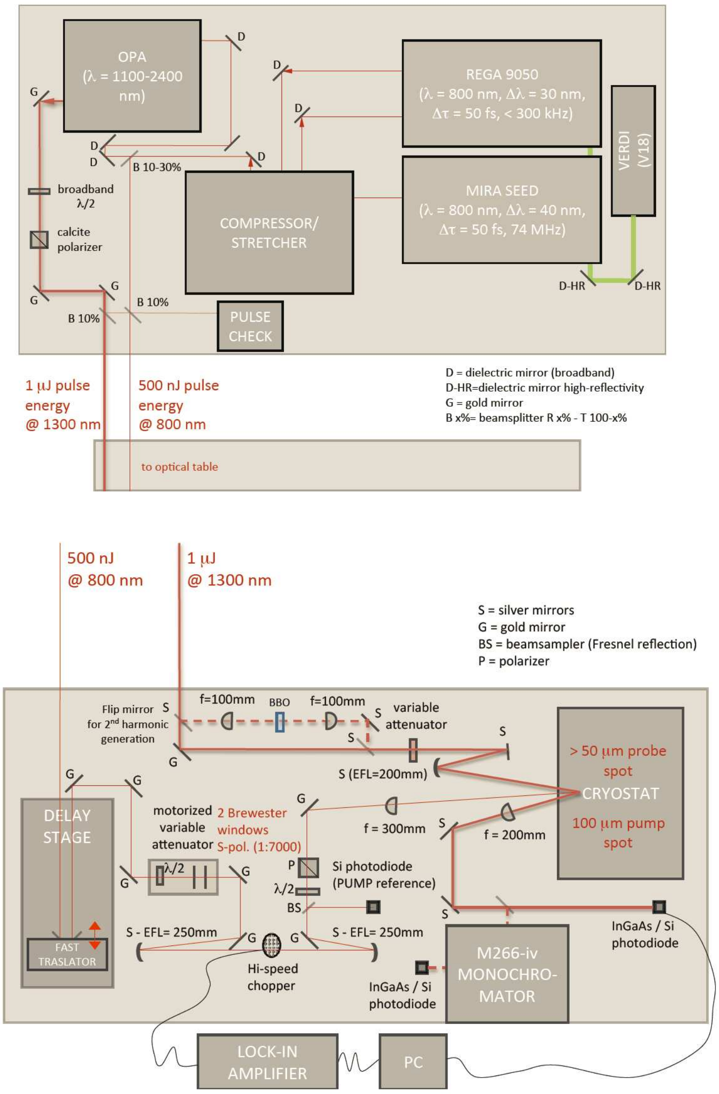

Figure 5.3: Here I report the experimental layout of the pump-probe system. The top panel schematizes the laser system, while the bottom panel describes the optical layout of the system.

acquisition time of 1 ms, this results in a temporal resolution of 50 fs, of the same order of the pump pulse duration. Then the pump pulse passes through a telescope (built with two 25 cm focal lenght sperical mirrors), in which focus is placed the disk of a high speed chopper. The beam need to be focused since we wanted to reach high chopping speeds, and to achieve this the disk mesh to be used is quite small (<500 μm). In particular, we set the chopping speed to 13 kHz. This value has been chosen in such a way it is comprised between the laser repetition rate (250 kHz; doing so, about 10 laser pulses are blocked, and 10 passes) and the lock-in integration time (1 ms, ie, 1 kHz, in such a way that at least 10 modulation cycles are integrated). The pump beam can be attenuated with a computer controlled lambda/half waveplate, placed behind a polarizer made of two Brewster angle windows. In this way, the measurements can be automatically repeated at various values of excitation intensity. Finally, the pump beam is focused on the sample with an anti-reflection coated 40 cm focal length lens. The probe path is much simpler: no particular devices are needed, and the beam is focused with a 25 cm focal length spherical mirror. The choice of a spherical mirror has been done since this optical component is achromatic (the probe can range from 1100 to 2450 nm). This ensures the probe spot size is almost constant in the entire spectral range. We obtained 100±5 um for the pump FWHM and 50±5 um for the probe FWHM, at the sample position. The reflected or transmitted beam from the sample is imaged onto pin photodiodes of the InGaAs type. Two photodiode types (which differ in the doping of the sensing area) help to cover the whole probe energy range. They are Thorlabs DET10C and DET10D, which detect light respectively in the 700-1800 nm and 1200-2600 nm range. Placed in front of the photodiode, an RG 1000 filter blocks the scattered light coming from the 1.55 eV pump beam. The detection system is based on a lock-in acquisition. This allows us to reach a signal to noise level as high as 10^6, averaging about 200 scans (lasting 0.4 s each). To obtain the $\Delta R/R$ signal, the static quantity R is measured averaging the photodiode signal over 10 ms windows, and sampling them with a 16 bit-100 kHz digitizer. The same digitizer acquires the analog X and Y fast outputs of the lock-in amplifier, from which is calculated the ΔR signal, and the position signal coming from the ScanDelay. To obtain a plot of the $\Delta R/R$ signal at the different probe wavelengths, the OPA must be manually tuned. This procedure requires some time (everything must be kept aligned), so that a complete $\Delta R/R$ map requires some hours to be collected (considering a pump fluence of $\sim$100 μJ and 20 lambda-points).

5.7 Supercontinuum-Probe Pump-Probe Setup

In this setup the spectral resolution enters in a natural way, since the probe pulse is itself a broadband pulse, with a wide energy content. No need to manually tune the probe wavelength is necessary anymore, which often results in misalignment problems. The main difference with respect to the setups described till now, stands in the acquisition system. Here, the spectral signal, at a fixed pump-probe delay, is acquired simultaneously in a wide spectral range, thanks to a multichannel linear detector (a linear array of photodiodes on which the spectrum is dispersed) which is digitized using an analog-to-digital acquisition board. No lock-in detection is possible in this setup, and this results in a poorer signal-to-noise ratio with respect to lock-in based acquisitions. But since no dead time dedicated to tuning and realignment is spent, the final result is similar: the acquisition of the transient time-resolved spectra at different pump-probe delays can be repeated many times in a fully automated way. With respect to the tunable-probe approach, the $\Delta R/R$ 2D map is constructed following a different 'filling': transient spectra at a fixed pump-probe delay (which is then scanned in the point-by-point configuration) are collected. On the contrary, different time-resolved traces at fixed wavelength (to be manually tuned) were collected in the previous approach. In our case, the linear array sensors have 128 pixels: this implies that the spectral resolution is much higher than the previous approach, and also narrow spectral features can be detected.

After a brief description of the optical system and the acquisition system we developed for this task, particular importance will be devoted to the characterization methods for the broadband supercontinuum pulses. The next paragraph of this chapter will be entirely devoted to this aim. A brief description of the mechanisms which produce the white light continuum starting from a monochromatic seed pulse, will reveal that the temporal structure of these pulses can be far from trivial. Since the temporal structure of the probe pulse reflects itself in a pump probe spectrally resolved scan, for the data to be correctly interpreted and presented, the temporal structure of the pulse (the temporal distribution of the various wavelengths) must be a priori characterized. In this way, the raw data can be corrected from the unphysical features related uniquely to the probe temporal structure. Thus, a review of some techniques we developed and employed to obtain the supercontinuum pulse spectrograms (time and energy maps of the pulse) will be presented, evidencing pros and cons of each technique.

A supercontinuum pulse can be generated following two different approaches. As a common starting point, an ultrashort ($\sim$100 fs) monochromatic laser pulse must be focalized in a medium, in such a way that very high peak intensities are reached. Depending on the material one chooses, the initial energy per pulse must belong to a completely different energy range. In the case of bulk materials (such as Sapphire, CaF_2, BBO) or liquids (water, ethanol), the threshold for supercontinuum generation is of the order of $\sim$500 μJ/cm^2. Following this approach, the first broadening of a monochromatic ultrashort pulse was demonstrated [3, 4] in 1970. The temporal structure of these pulses is in general quite simple: the various wavelengths have a linear and positive chirp, related to that of the material in which the generation occurs. To generate a supercontinuum following this approach, one needs an amplified laser system, which is a rather complex and expensive machine. On the contrary, supercontinuum pulses can be generated starting from pulses with a much lower energy per pulse, of the order of some nJ/pulse, if one exploits the recently developed photonic crystal fibers (PCF). The first report on a PCF-generated supercontinuum is dated 2000 [152, 107, 158, 61]. Following this approach, supercontinuum pulses can be generated using a standard oscillator laser source. The drawback is that the temporal structure of these pulses is more complicated, and must be known in some way prior to use these pulses as probe pulses in time-resolved experiments. The temporal structure is involved because it follows the effective dispersion characteristic of the fiber, and because of the various physical phenomena which contributes to the broadening of the spectrum. From now on, for dispersion characteristic I mean the behavior of the group velocity dispersion (GVD) versus the radiation wavelength.

A few words about the PCFs are worth to be spent. An optical fiber is constituted by two concentric materials: the internal one, named core, in which the light is guided, and the external one, the cladding. The most common material for both the constituent is fused silica. The light propagation through an optical fiber is made possible by the phenomenon of the total internal reflection: this phenomenon confines the light inside the material with higher refraction index (the core), since the reflectivity at the interface is one if the incident angle θ_i is bigger enough (it must be bigger than the critical angle θ_c, that is $\theta_i > \theta_c = \arcsin(n_{cl}/n_c)$, being n_c and n_{cl} the refraction index of the core and the cladding, respectively). This condition is easily satisfied for a beam propagating inside an optical fiber. In a conventional optical fiber, the (wavelength dependent) refraction index of the core is made bigger than that of the cladding, upon a proper doping of the material. The problem is that the dispersion characteristic of the fiber will be the same of the material, and this makes the conventional optical fibers not well suited to the production of supercontinuum: a short pulse temporally broadens and thus cannot non-linearly interact with the fiber core material (for fused silica, zero dispersion occurs close to 1.5 μm). On the contrary, the dispersion characteristic of photonic crystal fibers is designed in such a way the dispersion is zero close to the seed wavelength (which is usually 800 nm, the fundamentalof Ti:Sapphire lasers). Doing so, the (ultrashort) seed pulse remains short upon propagation in the fiber, and the high peak intensities make it non-linearly interact with the core. The desired dispersion characteristic for the a PCF is obtained (see Fig. 5.4) thanks to a microstructured cladding, which is usually composed of a regular (computer designed) pattern of holes which surround the core. This peculiar design results in an effective refraction index, for the cladding, which is smaller than the core one, with the advantage that the dispersion characteristic can be enginerized as one needs. From the cladding enginerized structure, which resembles that of some crystals, the photonic crystal fibers take their name. Many non linear phenomena, which take place in the fiber core, contribute and cooperate to the broadening of the monochromatic (800 nm) seed pulse into a broadband white light supercontinuum pulse. These phenomena are: the self phase modulation, the Raman scattering, the four wave mixing and the solitonic fission. The last is specific to the light propagation in optical fibers. For a detailed description of these phenomena I suggest Ref. [61]. Since many physically different phenomena participate in the spectral broadening of the seed pulse, the pulse temporal structure will be rather involved, and difficult to be predicted. Anyway, the pulse temporal structure will closely follow the

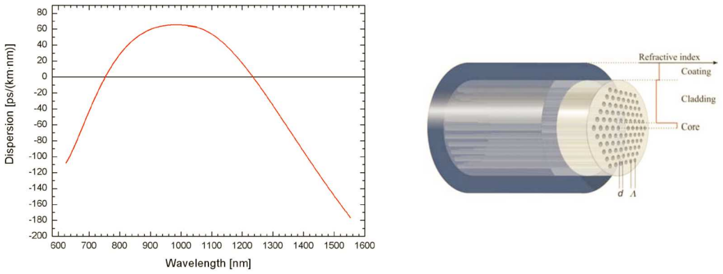

Figure 5.4: The dispersion characteristic of our PCF is reported (left). On the right, a section of the same fiber reveals its actual inner strucure.

fiber dispersion characteristic shape.
The PCF we employed is the CrystalFiber FemtoWhite 800. This fiber is 12 cm long, and its core diameter is 1.6 μm. This ensures extremely high peak intensities develop for an ultrashort (∼100 fs) laser pulse propagating into it (10 nJ/pulse results in an intensity of more than 3 TW/cm^2). This allows the pulse non-linearly interact and broaden into a white-light continuum which ranges from 450 to 1600 nm. The zero-dispersion for this fiber happens at 750 nm. This fiber is polarization maintaining, thus the supercontinuum is linearly polarized, in the same direction of the incoming pulse. The peculiarity of this fiber, enclosed in a solid aluminum housing, is that its end are collapsed up to a diameter of 30 μm: this solution allows an easy coupling of the seed pulse, and ensures a high stability of the coupling condition, resulting in a highly stable output. The fiber numeric aperture (NA) is 0.27. The seed pulse must be focalized in the collapsed end of the fiber with a lens whose focal length ensures no power losses; in our case, we choose an aspheric lens. In the same way, the supercontinuum output must be collimated; for this purpose, we employed an aspheric doublet (which limits chromatic aberrations, since we deal with a broadband pulse).

A PCF based pump-supercontinuum probe setup, seeded by an optical oscillator, offers a great versatility. The spectral resolution of this system is limited to the visible and near infrared regions of the spectrum; in particular, the range 500-1050 spectral region can be explored in the setup we developed. This range is limited entirely by the sensibility range of the detectors. The fiber itself, if correctly aligned, generates a spectrum in the range 500-1600 nm. The detectors instead are sensible in the spectral range 200-1050 nm. Thus, a wide spectral region in the infrared cannot be detected. Only very recently, new linear sensors has been designed which allow to extend the sensibility in the infrared up to 1600 nm. These will constitute a perfect match with the PCF, even if in the infrared region, because of the solitonic fission, the pulse temporal structure is very irregular. Currently, I'm testing a new setup based on these novel sensors (Hamamatsu G11608), which are sensible in the range 500-1700 nm. On the other hand, new PCFs which extend the limit in the infrared up to 3-4 μm (with a conventional 800 nm seeding) has been designed [106, 58]. But the lack of linear sensors working in this range makes the spectroscopy in the mid-IR far to be achieved. The time-resolved spectroscopy in the infrared spectral region (in particular, for λ>1600 nm) is thus, up to now, only possible employing wavelength conversion devices (OPA or DFG) coupled to amplified laser systems, which I described in section 5.6. The pump-supercontinuum probe setup will be now described. The output of a cavity-dumped Ti:Sapphire oscillator (producing ~120 fs, 1.55 eV laser pulses, with a repetition rate easily and continuously tunable from 1 MHz down to single shot) is splitted in two arms by a 70% T, 30% R beamsplitter. The more intense beam constitutes the pump beam. It passes through a magnetic delay stage (Micos LMS-80), which introduces and controls the pump-probe pulse delay, and through a low-frequency chopper (Scitec 300CD, which chopping speed is set to 20 Hz), which aim is to introduce a modulation on the pump beam, necessary to perform the differential measurement of the (pump-induced) transient reflectivity. The status (parity) of the chopped pump beam is sensed through a photodiode, on which a small percent (~4%) of the pump beam, picked by a wedged window, is focused with a short focal length lens. Then, the pump beam passes through a motorized lambda/half waveplate, followed by a fixed polarizer, to allow for a precise pumping intensity control. Finally, the pump beam is focused at the sample position through an achromatic doublet with 20 cm focal length (Thorlabs AC254-200-B). The obtained pump spot FWHM is 38±2 μm. The rest of the splitted intensity constitutes the probe beam. It is focused with an aspheric lens (Thorlabs C230TM-B) into the PCF. The supercontinuum output is collimated thanks to an achromatic doublet (Thorlabs AC010-080-B), designed to work in the wavelength range 650-1050 nm. The alignment of the seed into the PCF requires some level of care; anyway, once done, the day-to-day alignment is a straightforward task. The supercontinuum beam is propagated by means of Silver mirrors. The beam is focused at the sample position thanks to a 10

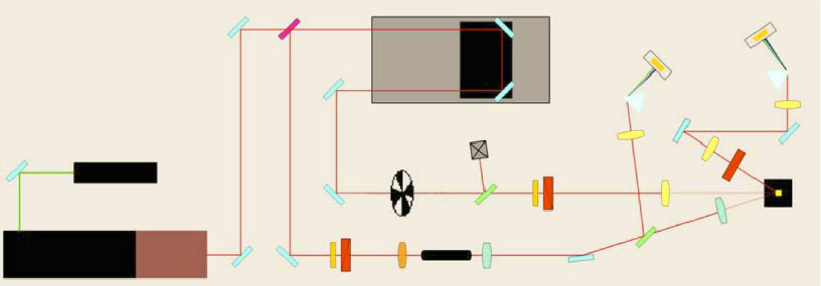

Figure 5.5: Here I report the experimental setup we designed to perform time-resolved spectroscopic measurements. Key elements are the Photonic Crystal Fiber employed to generate the supercontinuum pulse, and the acquisition system based on fast linear array sensors.

cm focal length achromatic doublet (Thorlabs AC254-100-B). We obtained a probe beam FWHM of 20±4 μm, for the whole wavelength range 500-1050 nm. The superposition of the pump and probe beams is cheked with a CCD camera equipped with a 10x magnifying objective. The sample reflected or transmitted supercontinuum beam is collimated with 10 cm focal length spherical mirror (Thorlabs CM254-100-P01). The collimated beam is directed toward an SF11 prism, which disperses the various wavelengths toward different positions in space. A 20 cm focal lenght achromatic doublet is placed after the prism; in the focus of the doublet, the linear array photodiode sensor is placed. The sensor we employed is the Hamamatsu S8380-128Q. It is a device composed of 128 pixels, each 50 μm wide. The total active area, on which the supercontinnuum is dispersed through the prism, is thus 6.4 mm long. The pixel height equals 2.5 mm. The dispersion characteristic of the prism on the sensor is simulated thanks to a numeric simulation (taking into account the prism material (SF11) refraction index and the (refraction index dependent) prism dispersion law). In this way, the calibration of the array (the correspondence pixel-to-wavelenght) is achieved. Some specific wavelengths are selected with interference filters and their position on the sensor is recorded, to allow for the calibration to be performed. To allow an efficient suppression of the supercontinuum intensity fluctuations, the non-interacting (with the sample) beam is sampled with a second linear array sensor. This constitutes the reference sensor. The (pixel-by-pixel) ratio of the signal sensor signal to the reference sensor signal will be a quantity which fluctuates less than the two single quantities. This is the quantity which will be employed for the experiments. To build the reference path, a small amount of the supercontinuum beam (~4%) is picked by an uncoated wedged window. The optical path of this beam toward the second sensor is build in such a way it is as similar as possible with respect to the signal optical path. The acquisition of a transient spectrum $\Delta R/R(\omega,\tau)$ at fixed pump-probe delay τ, is straightforward, if one exactly

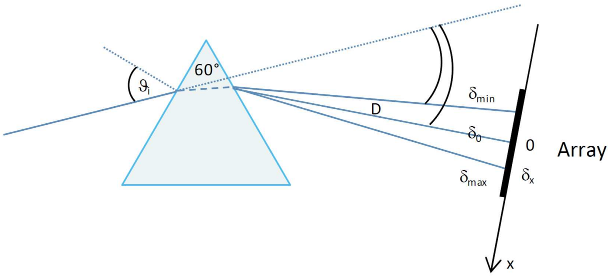

Figure 5.6: The scheme of the dispersion of the white-light pulse onto the linear array sensor, obtained thanks to a prism, is shown in the figure. The calibration procedure for the system consists in the assignment of a wavelenght to every pixel of the array, simulating the actual dispersion of the prism system, which is anchored by measuring the position of several selected wavelenghts.

knows the pump parity. To calculate the $\Delta R/R(\omega,\tau)$, the $R_{pumped}(\omega,\tau)$ and $R_{un-pumped}(\omega,\tau) = R_{un-pumped}(\omega)$ are the only quantities that must be acquired (the 'unpumped' spectrum does not depend on the pump-probe delay). Usually, for each transient spectrum at fixed pump-probe delay, 2000 spectra are recorded and averaged. This takes about 1 s. Part of these spectra will be 'pumped', part 'unpumped'. The pump parity is sampled together with the spectra, thus the $\Delta R/R(\omega,\tau)$ can be computed. To obtain a time and spectrum resolved map of the material optical response, many transient spectra, for different pump-probe delays τ, must be collected. Usually, we record about 250 delay points for a 6.6 ps total delay scan, which results in a temporal resolution of 26.4 fs. The spectral resolution of this system is about 2 nm/pixel toward the visible part of the spectrum (500 nm) and 6 nm/pixel toward the infrared side (1050 nm). This resolution is not constant because of the dispersion characteristic of the prism. Anyway, it is a good value and it is enough to evidence spectral feature in the time-resolved signal. The choice of a grating to disperse light would have produced a linear dispersion, thus a constant resolution (in nm), but at the expense of a much lower intensity efficiency.

A dedicated acquisition system has been developed and constructed to perform this kind of measurements. No commercial systems for this purpose are available yet. The acquisition system is devoted to both the control of the linear array sensors and the acquisition of their outputs. The software part, developed in a LabVIEW environment, controls the acquisition and saves the time and energy resolved maps as 2D matrices. I anticipated that no lock-in acquisition is possible with this acquisition scheme. This is due to the sensors, the Hamamatsu S8380-128Q (plus the control electronics C7883), which make available the data in a serial form: the voltage information (proportional to the illumination level) for the 128 pixels is output on the same electrical line at a 2 MHz rate (if one drives the devices at 8 MHz), thanks to an integrated shift register circuit. Thus, the data acquisition can be performed solely by digitizing (in our case with a National Instruments high speed digitizer, the NI PCI-5922, which offers two independent ADCs with 22 bit of resolution at a 2 MHz acquisition rate) the train of voltage values for the 128 pixels. This limits the final signal-to-noise ratio to a value slightly better than 10^4, with an acquisition time of about 1 s. The acquisition is performed simultaneously for both the sensors, and the pixel-by-pixel ratio of the two voltages is immediately computed. The parity signal for the pump status is acquired with a standard National Instruments M-Series board, the NI PCIe-6251. The Hamamatsu sensors, in order to work, need two control signals: one is an 8 MHz clock, which drives the shift register for the pixel voltage value reading; the other is a lower-frequency signal whose frequency inverse equals the integration time of the sensor, equal for every pixel. The frequency of this signal has an upper bound, which is 15625 kHz (or 64 μs). This is the value needed to complete a scan of the whole array (128 pixels $\cdot$ 0.5 μs/pixel, since the sensors respond at a 2 MHz rate when driven with an 8 MHz clock, which is the maximum allowed value). This signal is fed to both the arrays (in addition to the setting of the integration time, it starts the output of the data toward the video line) and to the acquisition boards, for which acts as trigger for the acquisition of the data. The acquisition is synchronized to the laser trigger, in such a way that the same number of pulses is acquired for every spectrum, and a constant illumination level (thus of signal) is generated, independently of the (tunable) laser repetition rate. Since the range of repetition rates we use is comprised between 100 kHz and 1 MHz, the laser trigger must be divided by some integer value. Single shot acquisition is not possible (it would also result in a signal close to the background level). After some tests, we conclude that an optimal value is 256: this means that every spectrum is the result of the accumulation of 256 laser pulses. With this divider, the laser repetition rate can be as high as 4 MHz for the system to work correctly. Anyway, the maximum repetition rate one can set is about 1 MHz: the limit is given by the acquisition boards, which cannot handle a trigger event rate of more than some (4-5) kHz. All the digital timing signals for the sensors and the acquisition boards are generated by an ad-hoc circuit based on high-speed and low-latency logic gates.

5.8 The characterization of a supercontinuum pulse

This section is devoted to the presentation of some methods to perform the characterization of a supercontinuum light pulse. These methods are recently attracting much interest [37, 184], given the growing appeal and diffusion of pump-probe setups with spectral resoluton, in the time-resolved scientific community. Pulse characterization is indeed a fundamental step to perform whether broadband supercontinuum pulses are going to be employed as probe pulses in time-resolved pump-probe measurements. In fact, the temporal structure of the probe pulse affects the measurements, and, particularly when the temporal structure of the pulse is not trivial (as it is the case for PCF generated supercontinuum pulses), a detailed knowledge of the pulse spectral and temporal intensity distribution (spectrogram) must be obtained, through a careful characterization procedure we present here in detail. The information extracted from the characterization procedure are enough to correct the measurements from the pulse temporal structure, making them pulse-structure-independent as they should be.

The experimental apparatus with which the characterization procedure can be carried on, is the same as presented before; if needed, the specific differences will be highlighted. A comparison of the advantages and drawbacks for each method will be also presented.

5.8.1 Pulse characterization through a VO_2 thin film solid state switch

This technique works in a reflection geometry and requires no modification of the pump-probe setup I described: the pulse characterization can thus be performed in situ, in the same experimental run of the programmed measurements.

The idea is to take advantage of the photoinduced insulator-to-metal phase transition of a vanadium-dioxide (VO_2) high quality thin film sample. In fact, it has been demonstrated that, upon photoexciting a VO_2 sample with ultrashort laser pulses of proper fluence ($F > F_c = 250\ \mu J/cm^2$ [154]), a 2^{nd} order phase transition (both electronic and structural) from the low-temperature ($T < T_c = 340$ K) monoclinic and insulating phase to the high-temperature rutile and metallic phase ($T > T_c = 340$ K) can be photoinduced [31, 29]. This happens on an ultrafast timescale (<100 fs), and is in no way related to the much slower thermal phase transition. After photoexcitation, the system remains in a metastable state for about 1 ns: for this reason the term 'switch' has been employed. The phase transition manifests itself with the collapse of the energy gap, which characterizes the insulating phase. This has an effect on the material optical properties, which change abruptly and by a big amount (many percent for the case of the reflectivity) after the phase transition has been photoinduced. This makes the VO_2 film an optical switch, which activation is triggered by the pump pulse, and which optical properties are probed by the probe pulse, in a pump-probe experiment. Obviously, the transient optical response of the material extends throughout a wide range of energies, allowing to characterize a broadband pulse in the visible and mid-IR spectral region. About VO_2, it has been demonstrated that the exciting radiation couples to the structural degrees of freedom; the induced change in the crystal structure is then followed by the electronic structure, which adapts itself to the new structural configuration. This observation comes from both the observation that the transition can be induced by an exciting wavelength smaller than the material energy gap (~0.6 eV), and that there exist a bottleneck of about 80 fs [30] lasting from the photoexcitation of the system and the change of the optical properties (related to the gap collapse). This 80 fs bottleneck poses a lower limit to the shortest pulse that can be characterized. Anyway, in our case, being the pump pulse of about 120 fs, this limitation is not important: the limit to the temporal resolution achievable from this technique is the bigger among the material response (80 fs) and the actual pump pulse temporal duration (FWHM).

In practice, the (temporal) optical response of the VO_2 sample is regarded as a smeared step function, whose 'activation' is given by the pump pulse. We will thus assume that the VO_2 switching behavior in the time domain can be modeled by a step function (the abrupt change in the optical properties triggered by photoexcitation), convoluted with the 80 fs activation time (the bottleneck) and the 120 fs pump pulse. This results in the smeared step function. The

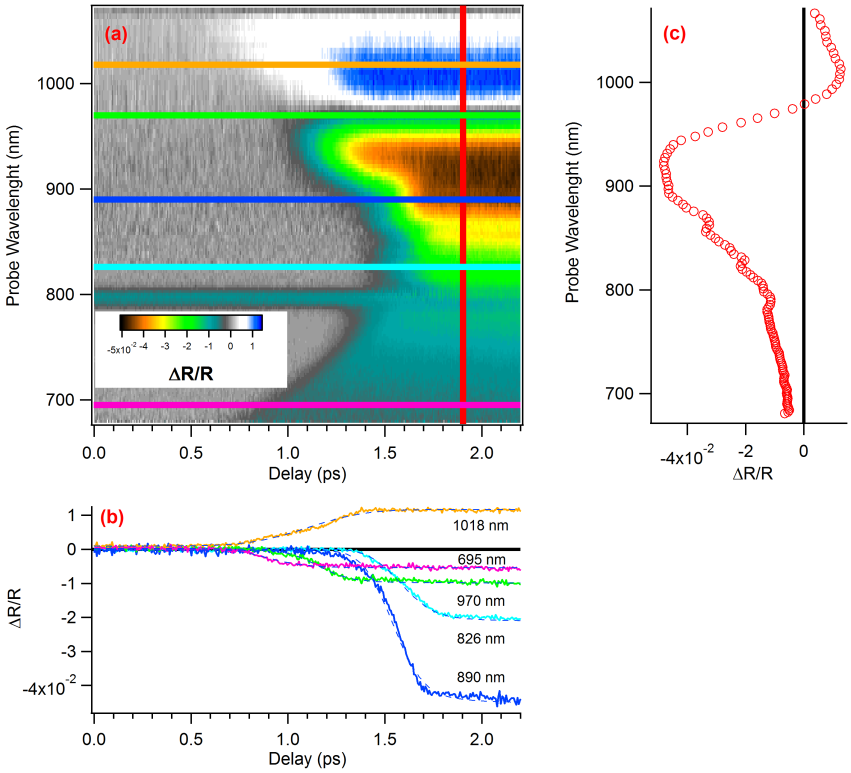

Figure 5.7: Here I report the raw measurement carried on on the VO_2 multifilm sample (panel a)). In panel b) some cuts of the measurement at fixed wavelenght are reported, while panel c) contains a fixed-delay cut, representing the transient spectral response of the system.

time-resolved measurement (reported in Fig. 5.7) can be interpreted as follows: each vertical slice is the normalized difference between the reflectivity of the excited and the unexcited sample (of which we now know the temporal behavior). Depending on the relative temporal position of the pump (which activates the switch) and the (broadband) probe pulses, different situations can occur: if the probe pulse comes before the switch is activated, the $\Delta R/R$ will be zero (on the left side), since the probe sees the unexcited material. On the contrary, if the probe pulse comes after the switch has been excited, for all the wavelength (on the right), there will be a non-zero $\Delta R/R$, because the probe pulse sees the excited optical properties of the sample, since it comes entirely after the phase transition has taken place. In between these limit situations, only some spectral regions of the probe pulse see the pump-excited optical properties. This fact allow to know exactly where the various spectral components of the broadband pulse are temporally located, since one exactly knows where the pump pulse is.

Now, if one fits a function, which is the convolution of a Gaussian function (representing the probe pulse) and the described material response, to the various temporal slices of the pump-probe measurement, it is possible to extract (as fitting parameters) the temporal duration of each spectral slice of the supercontinuum pulse, and its temporal position. The probe intensity cannot be inferred, since the wavelength dependent material response is not known with precision. These two parameters allow for a complete characterization of the spectro-temporal structure of the pulse, and the pulse spectrogram can be calculated starting from those values. The fit results are reported in the graphs below. The temporal duration of the different spectral components of the supercontinuum pulse ranges from 100 fs in the UV to 200 fs in the infrared. With this information in mind, and the relative time-position of the same wavelengths, the time-resolved measurements can be corrected. Making use of a differential dielectric function model, we verified that the VO_2 spectral optical response could be reproduced assuming the closing of the electronic gap after the photoexcitation. To do this, we consider a vertical slice of the data reported in Fig. 5.7, at a pump-probe delay such that the probe pulse entirely comes after the pump pulse. A function described below has been fitted to this trace. For the details of the differential dielectric function approach, we refer to 4.3. Actually, in this context, the model has been adapted: both the equilibrium and the excited reflectivity from the sample have been modeled taking into account the multiple reflections given by the thin multifilm structure of our sample, composed of three layers: a 20 nm thick VO_2 film, a 330 nm thick Si_3N_4 buffer layer, and a Silicon substrate, which thickness has been considered infinite. Each material has its own dielectric function; we assume that only the VO_2 one is changed upon excitation, in the excited model. In particular, the

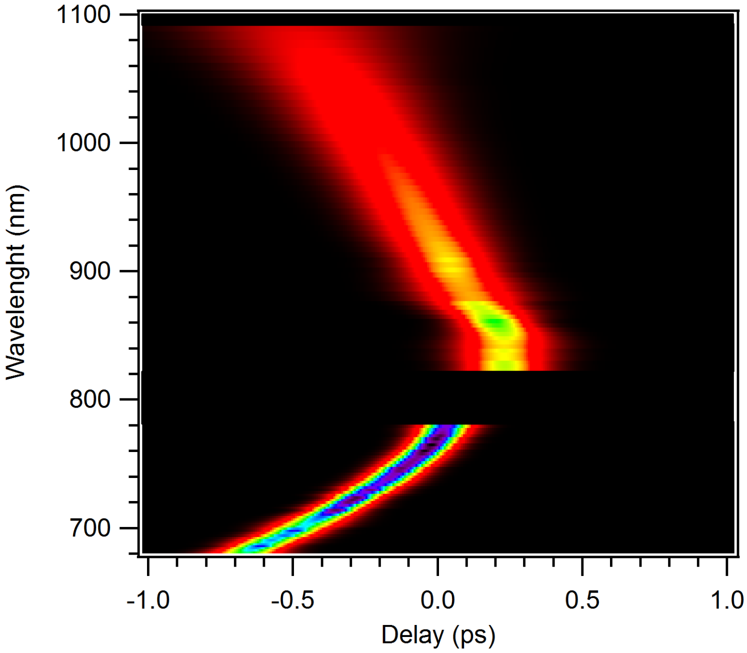

Figure 5.8: Here I report the supercontinuum pulse spectrogram, retrieved with the fitting procedure described in the text.

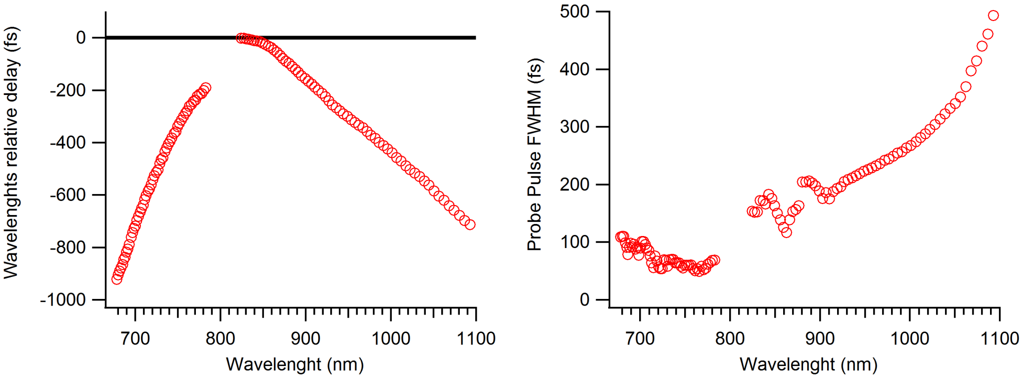

Figure 5.9: The fitting parameters at the base of the pulse spectrogram reported in Fig. 5.8 are here reported.

VO_2 static dielectric function has been modeled with four Lorentz oscillators, which energies are respectively 1.25, 2.8, 3.6, 4.9 eV. The excited dielectric function, characterizing the material in the photoinduced metallic phase, is somewhat modified: the lowest-energy oscillator, related to transitions across the band-gap, has been replaced with a Drude term, modeling the free electron contribution to the dielectric function in the metallic phase. The remaining three oscillators present slight changes in their energies (respectively equal to 2.8, 3.5, 4.5 eV). This reflects the fact that the modified structure slightly modifies the band structure, and thus the optical transitions, of VO_2. The fitting parameters of this complex model are only the ones modeling the VO_2 excited dielectric function. The results are compatible with a photoinduced metallic phase. The best fit of this model to the data is reported in the figure below. Overall, this characterization technique consists in an experimentally simple procedure which can be performed in situ, simply placing a VO_2 film at the samples position. The clear advantage is that the VO_2 switch optical

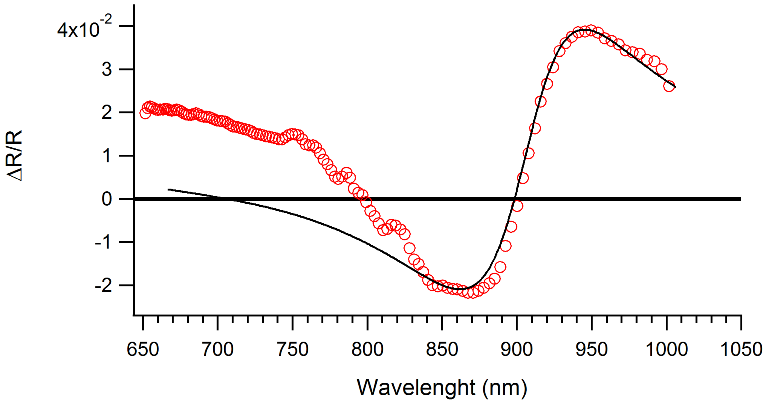

Figure 5.10: Here I report the fit to the fixed-delay time-resolved spectrum, performed as described in the text.

response extends in a wide energy range, thus allowing for the simultaneous characterization of a broadband ultrafast pulse. The drawback is that the extraction of the pulse characteristic parameters, from the raw measurement, is a rather time-consuming procedure, since it requires a non-trivial fitting procedure. Thus, the pulse characterization cannot be an on-line task. It requires some level of post-processing. Also, to obtain a good $\Delta R/R$ signal, allowing for a good signal-to-noise level in a reasonable time, a pump fluence as high as 3-5 mJ/cm^2 must be available, which is not so common if one works with an oscillator laser system.

A unique feature of this technique, coming from the fact that it is developed around a material exhibiting a switching behavior, is that it allows laser diagnostic, in the sense that it can reveal pre- or post- pulses in the laser output, without performing long and time-consuming temporal scans. With this technique indeed we revealed a post-pulse in the laser output, which appears as the flat signal at 800 nm, clearly visible in Fig. 5.7. The weak post-pulse cannot non-linearly interact with the PCF core, thus remains monochromatic, but it is revealed by this technique.

5.8.2 Pulse characterization through two-photon absorption in ZnSe and ZnS

This technique allows for a fast characterization of a broadband pulse, exploiting the two-photon absorption process [109] in an insulating transparent material. It works in a transmission geometry. As we will see, this technique is quasi on-line, but it has the important drawback that the deduced pulse shape is correct as far as the wavelengths to be characterized are far from the visible spectral region. We employed two different materials: ZnSe and ZnS. These two materials allow for a different choice of the gate pulse energy, the fixed-energy pulse (in the two-photon process) employed to induce the absorption: 1.55 eV for ZnSe, 1.55 eV or 3.14 eV for ZnS.

The two-photon absorption process we exploit for this characterization method can be described as follows. The photon absorption in a bulk material is allowed if the photon energy is higher than the material gap energy. This equals 2.55 eV (490 nm) in ZnSe, and 3.45 eV (360 nm) in ZnS (see Fig. 5.11 for a plot of the materials transmission, from which the energy gap for both the materials is inferred). In general, a photon can be either regarded as two physically different photons, coming from two physically different beams, unless they interact in the same position and at the same time (the two beams must reach the interacting area at the same instant). The absorption efficiency will be lower, since in the absorption process a virtual, intermediate state is involved. The application of this idea to a pump-probe experiment, is straightforward. A temporally short, fixed-energy beam, the pump beam of a pump-probe setup, will constitute one of the two pulses. This pulse is named gate pulse. Its temporal duration poses a lower-limit to the temporal

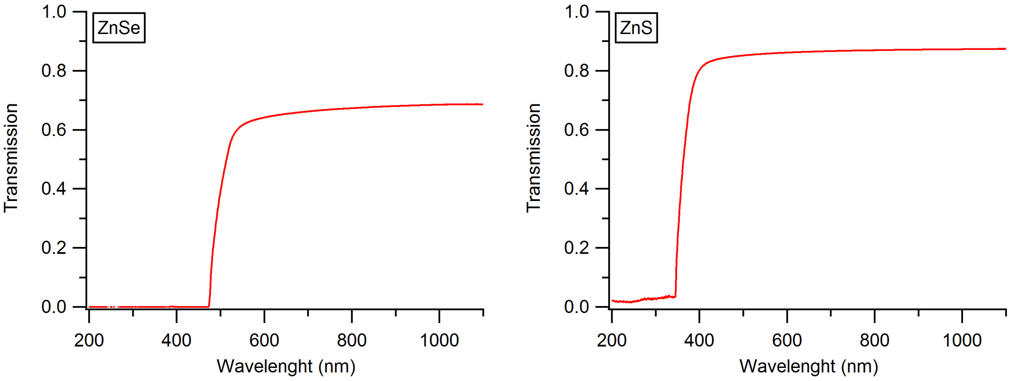

Figure 5.11: Here I report the measured static transmittivity of our ZnSe and ZnS samples.

resolution of the technique. Its energy must be lower than the material energy gap. Also, the more monochromatic the pulse is, the more the energy resolution of the technique will be. The delta-energy missing from the gap material (ΔE=E$_{gap}$-E$_{gate}$) determines the range of photon energies which can be absorbed from the second beam. This is usually the (broadband) probe pulse of a pump-probe setup, which is detected with the broadband setup described in section 5.7. The probe pulse, in general, has a temporal duration which is much higher than the pump, gate pulse. Scanning the relative temporal position of the gate pulse with respect to the broadband probe pulse, the absorption will happen, in principle, at different positions, and will involve different spectral portions of the pulse, depending on the actual pulse shape. The transient absorption is thus a signal which allow to reconstruct the pulse spectrogram. Thus, a negative (since what one measures is the absorption) map of the pulse, which temporal and spectral resolution is limited by the gate pulse characteristics, will be obtained. The ΔE defined above, and the material-dependent gap energy, constitutes the limits of the broadband pulse energy range one can characterize. Energies smaller than ΔE cannot be absorbed; energies bigger than the gap one are absorbed directly and thus can not be timely resolved: they simply cannot be characterized.

I anticipated we employ two different materials for the characterization of the same pulse: ZnSe and ZnS. They appear as polished 2 mm thick optical windows, which we placed at the sample position for pulse characterization. The theoretical range of energies ZnSe allow to characterize is 1-2.55 eV (490-1240 nm): the former equals ΔE=(2.55-1.55) eV= 1 eV. This energy range is in excess of what we need (500-1050 nm). On the contrary, we employed ZnS to perform pulse characterization in the experimental situations in which the pump is the laser 2^{nd} harmonic (3.14 eV). This experiment would not be possible with ZnSe, since it would absorb directly this gate energy. The theoretical energy range allowed for characterization is, in these experimental conditions, 0.31-3.45 eV (390-4000 nm).

The left plots of Fig. 5.12 and 5.13 contain the two-photon absorption measurements (on ZnSe and ZnS respectively), from which I'll retrieve the spectrogram of our supercontinuum probe pulse. In fact, these measurements do not directly represent the spectrograms, since the temporal (and spectral) structure of the pump gate pulse is involved. As it is possible to see, the pulse temporal structure in the visible spectral region (more evident in the ZnSe measurement) is clearly distorted. Moreover, in ZnS the absorption lasts much longer than the pulse duration (even if the pulse shape is preserved, as I'll demonstrate below). Since the (unknown) energy-dependent material absorption efficiency is involved, the true pulse intensity cannot be inferred from these measurements. The fitting of a single-gaussian function (convoluted with the gate pulse Gaussian shape) to the fixed-wavelenght-slices of the above plots allowed

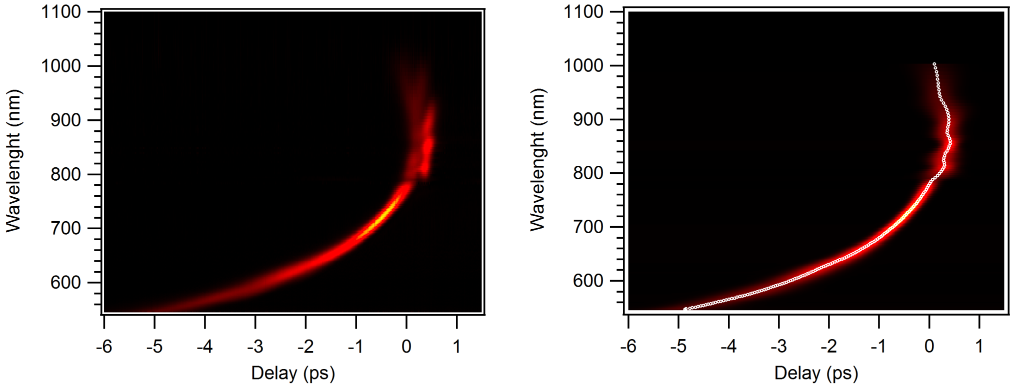

Figure 5.12: Here I report the raw measurement on ZnSe (left) and its reconstruction by a fitting with one Gaussian function (right). White dots represent the center of the Gaussian at different wavelenghts.

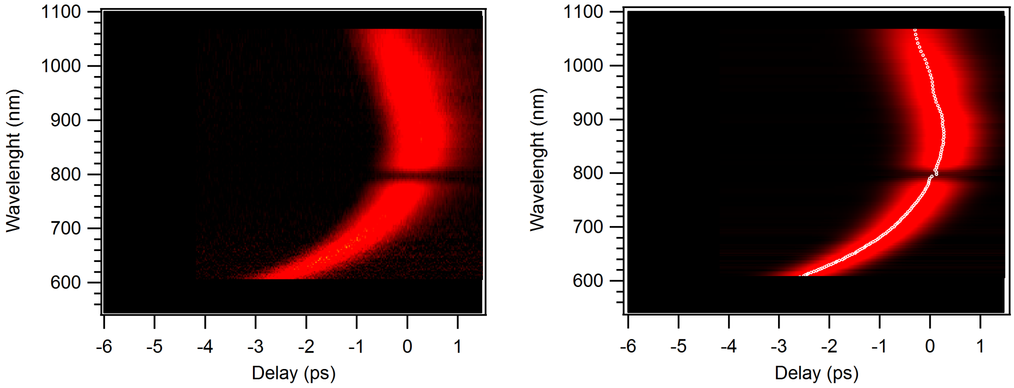

Figure 5.13: Here I report the raw measurement on ZnS (left) and its reconstruction by a fitting with one Gaussian function (right). White dots represent the center of the Gaussian at different wavelenghts.

us to extract both the temporal duration (deconvoluted from the gate pulse one) and the temporal position of the broadband probe pulse spectral slices. The fits to the data are reported in the right plots of Fig. 5.12 and 5.13. The fitting parameters results are reported in Fig. 5.14 (a and b), for what concern the temporal positions of the broadband probe wavelenghts, as obtained by the two materials. I do not report the retrieved temporal duration for such spectral components, instead, since the results are not physically meaningful. Summarizing, the clear advantage of this technique is that it produces a quasi-online result for the spectrogram of an ultrashort, broadband pulse. Since the $\Delta T/T$ signal is quite high even with low gate fluences ($\sim10^{-2}$ with F<1 mJ/cm^2), the actual measurement takes a few minutes to achieve a good signal-to-noise level. On the contrary, the drawback stands in the fact that the results are not reliable for wavelenghts in the visible spectral range (in particular, for $\lambda \lesssim 750$ nm). This can be argued by looking at Fig. 5.15, where the results are compared to that obtained thrugh the VO$_2$ switching technique. The courious thing is that both ZnSe and ZnS behave in the same way, ruling out the possibility the deviation from the actual pulse shape comes from the vicinity of the radiation to the material energy gap or from the energy difference between the gate and the probe energies. Moreover, this method cannot be employed to deduce the pulse temporal width: the extracted temporal durations are misleading (in particular for the ZnS case), probably because of the fact that the absorption process involves some metastable states.

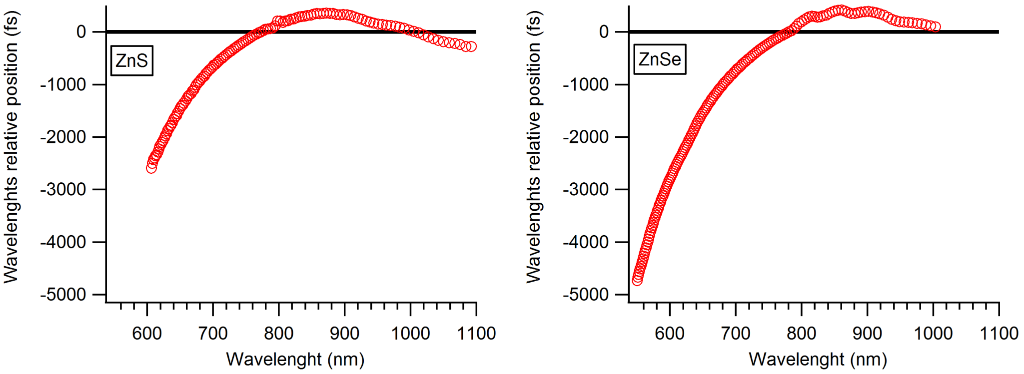

Figure 5.14: The central position of the pulse for each wavelenght is reported here for ZnSe (left) and ZnS (right).

5.8.3 Pulse characterization through XFROG technique

This technique is the most direct way to obtain a spectrogram of a pulse, since the characterization involves only electronic processes which happens on a time-scale much shorter than the pulse durations ($\sim10^{-15}$ s). For this reason, the results obtained with this method constitute a benchmark for every other pulse characterization method. On the contrary to the two techniques

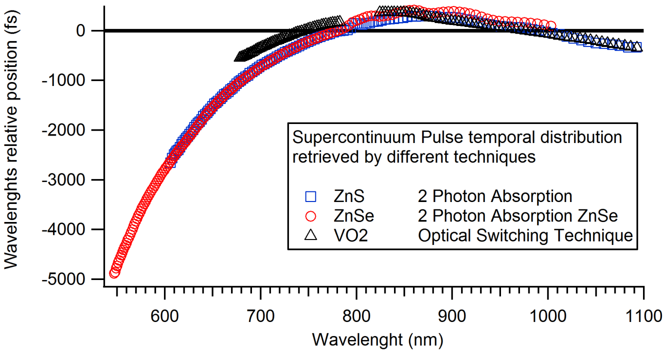

Figure 5.15: A comparison of the results obtained through different techniques is reported: the two-photon absorption method is not accurate in the visible spectral region.

described before, this technique requires a completely different experimental setup, and thus cannot be performed online during a programmed experimental run. Also, it requires a certain level of care.
This technique consists in the generation of the sum frequency between a spectral portion of a broadband pulse and a monochromatic gate pulse, obtained in a non-linear crystal. It is one of the possible applications of the XFROG (cross correlation frequency resolved optical gating) technique [176]. In our case, we employ a 1 mm thick Type I BBO crystal, and record the sum frequency generated between a gate (pump) 1.55 eV pulse and a spectral region of the broadband supercontinuum (probe) pulse. The sum frequency will be generated only in conditions of temporal coincidence for the two pulses. The difference of this technique, with the one described in section 5.8.2, is that a phase matching condition (representing the momentum conservation between the two pulses wavevectors), for the sum frequency to be efficiently generated, must be satisfied. Absorption, instead, requires no phase matching conditions to occur, and different wavelengths can be analyzed (absorbed) at the same time. The phase matching condition, which limits to a (usually) narrow spectral interval the spectral region that can be explored at the same time, is realized upon rotation of the non linear crystal optical axis with respect to the beams linear and parallel polarization axis. The tuning of this angle allows different probe spectral regions to be alternatively found in phase matching condition with the gate pulse, resulting in a high frequency resolution (xFRog).
Performing such a kind of measurement is a time-consuming task: for a fixed pump-probe delay, the crystal axis must be rotated to allow the different spectral regions of the broadband probe pulse to be analyzed. This is obtained through a motorized, computer controlled, rotation actuator. This procedure must be repeated for a proper amount of pump-probe delays, for a good time-resolution. If we suppose to characterize a spectral interval 600-1100 nm, with a 1.55 eV, 800 nm gate, the phase matching angle varies from 25.2° to 34.1° for BBO. Since we employ a common BBO crystal cut for SHG (second harmonic

generation) at 800 nm, characterized by a 29.2° phase matching angle, this means the crystal must be angle-dithered in the interval (-4, +5)°. We divide this interval in 40 discrete steps. The sum frequency is recorded through a high-resolution UV fiber spectrometer (Ocean Optics SD2000), which allows for a spectral resolution better than 1 nm. The energy conservation law, $\hbar\omega_{sf} = \hbar\omega_g + \hbar\omega_{pr}$ (being respectively ω_{sf}, ω_g, ω_{pr} the sum-frequency, gate and probe frequencies), relates the measured wavelength to the corresponding analyzed probe wavelength. For the range 600-1100 nm (2.06-1.13 eV), assuming a 1.55 eV, 800 nm gate, the sum-frequency will mainly be in the UV range: 3.61-2.68 eV (343-463 nm). The need to use a spectrometer comes from the fact that we need a calibrated and high resolution device. The latter requirement follows because the wide analyzed range (600-1100 nm), on which we need a good resolution, is translated into a much narrower spectral range (considering the wavelengths) by the energy conservation law.
The measurements we obtained, with the corrected wavelength axis, is reported in Fig. 5.16. The measurement is obtained with 150 delay steps (with

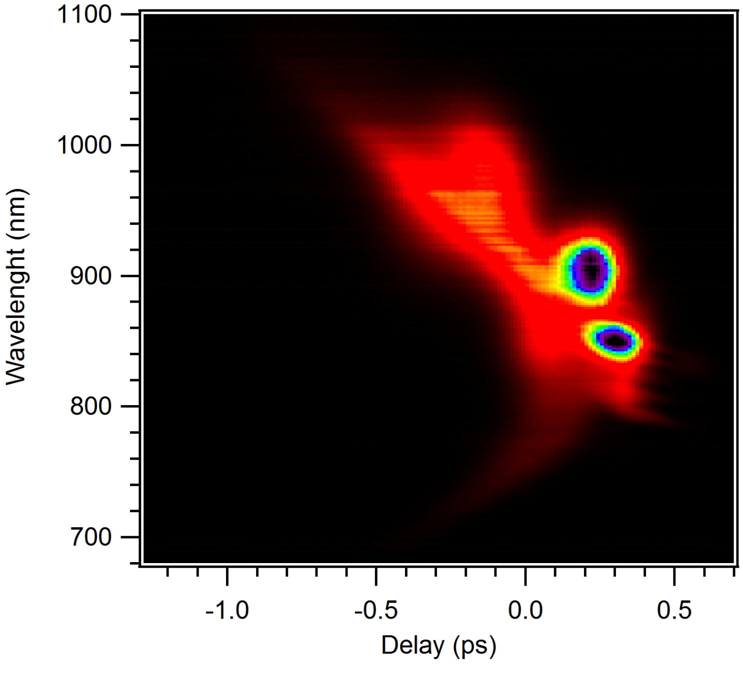

Figure 5.16: The XFROG measurement of the supercontinuum pulse is here reported. The wavelenght axis is corrected acounting for the energy conservation in the wave mixing process.

13.2 fs resolution), and each vertical slice is the mean of the intensities obtained from each of the 40 different selected phase matching conditions. This measurement is proportional to the pulse spectrogram. As usual, the intensity is not proportional to the actual pulse intensity, since the (non-constant) conversion efficiency is involved. It also contains the effect of the gate pulse. Nevertheless, the shape is the same of the probe pulse: we can appreciate the

high spectral and temporal resolution of this technique, when compared to the previous ones. The higher resolution allows to reveal the fine structure of the pulse, evidencing the solitonic features for $\hbar\omega < \hbar\omega_{seed}$, being $\hbar\omega_{seed}$=1.55 eV the PCF seed energy. The pulse extends temporally for about 1 ps in the spectral range 700-1100 nm. The pulse duration, after deconvolving for the 120 fs gate pulse, is about 100 fs around 700 nm, while it increases up to $\sim$300 fs around 1000 nm, due to the presence of solitonic structures.
The clear advantage of this technique is its unbeatable resolution, both in the spectral (thanks to the phase matching condition) and temporal (only electronic processes are involved) domains. On the contrary, it requires a long time to be performed (more than one hour, since the phase matching condition must be continuously tuned), and cannot be performed within the conventional pump-supercontinuum probe setup.

5.9 Cryostat System

We employed an open cycle cryostat (Helitran LT-3-B) to allow the temperature of the samples be varied in the range 10-350 K. This range can be achieved only when the coolant is liquid helium. Also liquid nitrogen can be used as coolant; in this case, the temperature range is limited to the interval 77-350 K. The coolant is transferred from the storing dewar to the cryostat with a transfer arm. The temperature near to the sample region is accurately measured with a calibrated Cernox sensor. A computer controlled heater, with a PID feedback system, stabilizes the sample temperature within ±0.1 K from the set temperature. The system is kept in UHV thanks to a pumping system composed of a Scroll pump plus a Turbomolecular pump. A base pressure as low as $5{\cdot}10^{-9}$ mbar can be reached inside the UHV chamber; this ensures that no sample degradation takes place, even after many hours of measurements at very low temperatures. The UHV chamber is equipped with a CaF_2 UHV optical window, through which the pump and probe beams reach the sample. A copper shield shields the samples region from the rest of the chamber, limiting the heat transfer toward the cold finger area.

Chapter 6

Electron-boson coupling in the normal state

6.1 Introduction

This chapter illustrates the results obtained in the normal state (T=300 K) of a Y-Bi2212 optimally doped sample, by time-resolved optical spectroscopy. Exploiting the spectroscopic information of our technique, and analyzing the experimental results within the differential dielectric function approach, I demonstrate that, in a time interval limited by the temporal resolution of our technique (∼100 fs), the fermionic quasiparticles photoinjected in the system by a pump pulse, quickly interact with bosonic excitations characterized by a very strong coupling to electrons (λ>1), specific heat smaller than the electronic one, and an energy distribution extending to ∼350 meV. In particular, three subsets of the total bosonic glue function ($\Pi(\Omega)$, determined by conventional spectroscopic ellipsometry) have been disentangled: bosonic excitations of electronic origin, strongly-coupled phonons, and the rest of lattice vibrations. The main finding of our analysis on the non-equilibrium optical properties of Y-Bi2212 in the normal state is that the portion of $\Pi(\Omega)$ arising from the electron coupling with bosons of electronic origin, such as spin fluctuations or current loops, fully accounts for the high critical temperature of the compound. This suggests that bosonic excitations of electronic origin are the most important factor in the formation of the superconducting phase at high temperatures in the cuprates.

6.2 Time-resolved optical spectroscopy at T=300 K

In this paragraph I report and discuss the time and frequency resolved pump probe reflectivity measurements performed at T=300 K on three Y-Bi2212 samples with different doping. The probed energy range is 1.2-2 eV, i.e., 600-1000 nm, while the pump fluence is 10 μJ/cm^2. The three samples differ for the doping level. An underdoped (UD, T_c=83 K, p=0.128), an optimally doped (OP, T_c=96 K, p=0.16) and an overdoped (OD, T_c=83 K, p=0.2) sample have been measured, in order to explore the evolution of the pump-induced reflectivity variations as a function of the doping level in the normal state. The measured reflectivity variations, i.e., $\Delta R/R(\omega,\tau)$, as defined in section 4.4, are reported in Fig. 6.1.

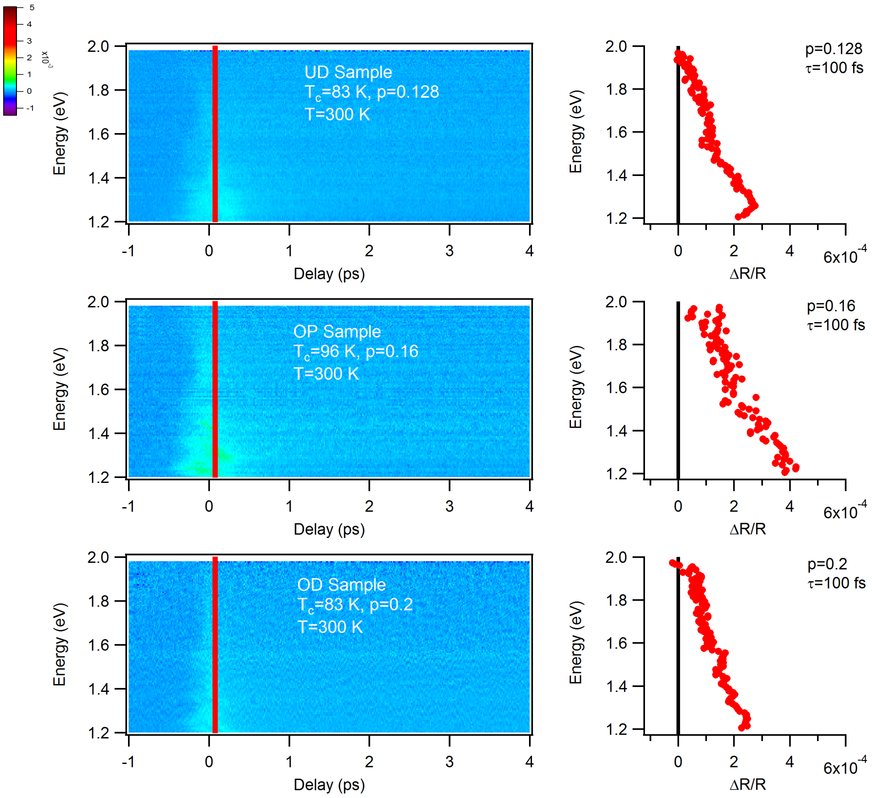

Figure 6.1: The temporally and spectrally resolved plots for the transient reflectivity in the normal state phase (T=300 K) of $Bi_2Sr_2Y_{0.08}Ca_{0.92}Cu_2O_{8+\delta}$ are here reported for three doping levels: p=0.128 (UD sample), p=0.16 (OP sample), p=0.2 (OD sample). The 800 nm, 1.55 eV signal is in agreement with measurements performed with one-color probe. The cuts (evidenced in red) at τ=100 fs pump-probe delay are reported in the right graphs, evidencing the spectral strucutre of the transient signal. The pump fluence is 10 μJ/cm^2.

Looking at the data, the main evidence is that both the spectral shape of the transient reflectivity and its dynamics are doping-independent. All samples exhibit a positive $\Delta R/R(\omega,\tau)$ that monotonically decreases in amplitude in the visible region. I checked by single color measurements at 3.14 eV probe energy that the transient reflectivity vanishes in the UV. The relaxation dynamics is governed by a double exponential decay, with a fast component of about 300 fs, followed by a slower one, with a decay time of about 2 ps. This double relaxation dynamics is usually interpreted [145, 27] as the thermalization of the photoinjected fermionic quasiparticles with a subset of strongly-coupled phonons (sub-ps dynamics) and the rest of the lattice (ps dynamics). The energy-resolved information, in this case, brings the evidence of a structureless spectral response.

To address the microscopic origin of the measured $\Delta R/R(\omega,\tau)$ signal, I extended the probed spectral region to the infrared, exploiting the tunable infrared probe setup described in section 5.6. I used both the signal and idler beams, to cover the spectral range 0.5-1 eV (1200-2400 nm) and add discrete time-traces (one every 50 nm) to our time-and-energy resolved reflectivity plots. Here I present the obtained results only for the OP sample, on which the complete differential analysis will be carried on. Similar results are obtained on the underdoped and overdoped samples. The extended transient spectrum for the OP sample is presented in Fig. 6.2.

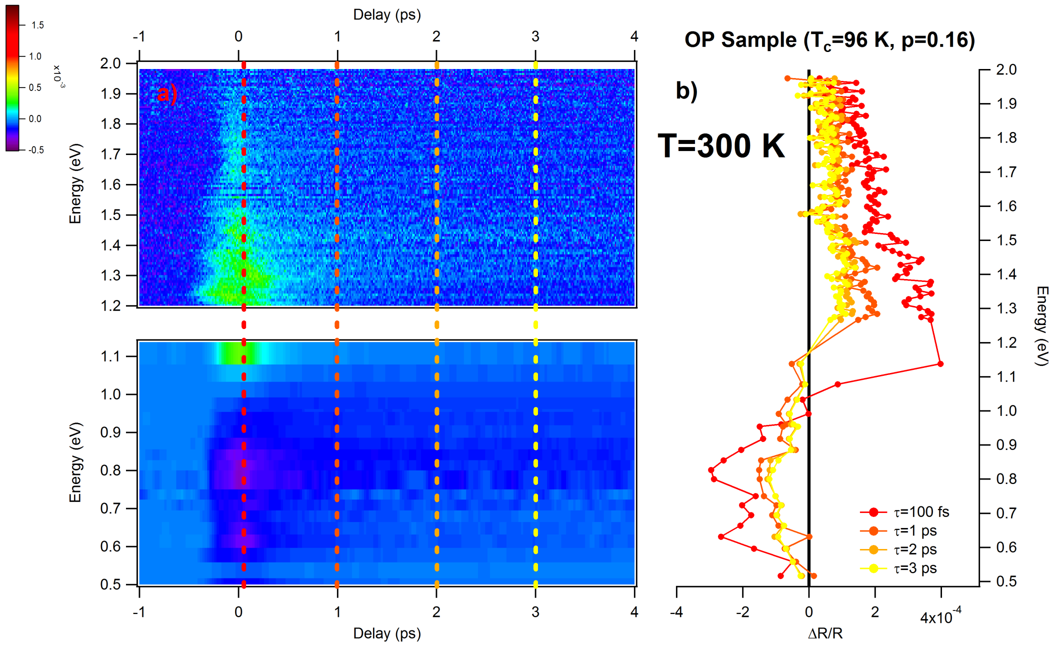

Figure 6.2: a) The measurement on the Optimally Doped sample is extended toward the infrared, up to 0.5 eV. b) The total transient spectra for selected pump-probe delays τ are reported.

Thanks to the extended probed energy range (0.5-2 eV), I observe that the spectral response has a more structured form. It turns from positive in the visible to negative in the infrared, with the crossing point which falls close to the dressed plasma frequency of the system (~1 eV, see Figure 3.6). On the contrary, the dynamics in the infrared is characterized by the same decay rate observed in the visible. In the infrared, the maximum reflectivity variation maintains a value of about $-2 \cdot 10^{-4}$ up the lowest probed energy (0.5 eV).

All the analysis described in the following sections will be carried on on the optimally-doped sample (see Fig. 6.2), since in this system the total $\Pi(\Omega)$ is maximum [179], while the use of the extended Drude formalism (see Chapter 3, section 5.2) still appears a reliable approximation [179, 170]. The physical scenario disclosed by the data will be at first qualitatively described in section 6.3, while a more rigorous and quantitative approach will be adopted in sections 6.4 and 6.5.

6.3 Ultrafast thermalization with bosonic excitations

The aim of this section is to demonstrate that the transient spectrum shown in the left panel of Fig. 6.2 can be reproduced by a quasi-thermal scenario, within the differential dielectric function model described in section 4.4. Quasi-thermal scenario means that the measured pump-induced effect on the optical properties can be accounted for simply by modifying the effective temperatures of the bosonic excitations in the Extended Drude. No other parameter in the non-equilibrium model must be modified to reproduce the data.

The key point to extend the Extended Drude model, extensively discussed in Chapter 3, to non-equilibrium experiments is that the electron self-energy, $\Sigma(\omega, T)$, entering in the calculation of $\epsilon(\omega, \tau)$, can be factorized into [105]:

$$\Sigma(\omega, T) = \int_0^\infty \Pi(\Omega) \, L(\omega, \Omega, T) \, d\Omega$$

where $L(\omega, \Omega, T)$ is the kernel function, already defined in section 3.5.2, that accounts for the thermal activation of the bosonic excitations and of the QPs. The kernel function $L(\omega, \Omega, T_{\mathrm{e,b}})$= $-2\pi i[N(\Omega, T_{\mathrm{b}}) + 1/2] + \Psi(1/2 + i(\Omega - \Omega')/2\pi T_{\mathrm{e}}) - \Psi(1/2 - i(\Omega + \Omega')/2\pi T_{\mathrm{e}})$, where Ψ is the Digamma function and $N(\Omega, T_{\mathrm{b}})$ the Bose distribution at temperature T_b, can be decomposed into different terms depending on the electronic (T_e) and bosonic (T_b) temperatures. The independent variation of T_e and T_b is expected to induce different modifications of the dielectric function.

Fig. 6.3 shows the expected relative variation of the reflectivity, i.e., $\Delta R/R(\omega)$= $[R(\omega, T + \Delta T)$-$R(\omega, T)]/R(\omega, T)$, in the non-thermal ($\Delta T_e$>0, ΔT_b=0) and quasi-thermal ($\Delta T_e = \Delta T_b$>0) scenarios. The difference between the two cases is more significant in the spectral region close to the dressed plasma frequency, $\Omega_{\mathrm{p}} \simeq 1$ eV, i.e., an energy scale much higher than the energy scale of the bosonic

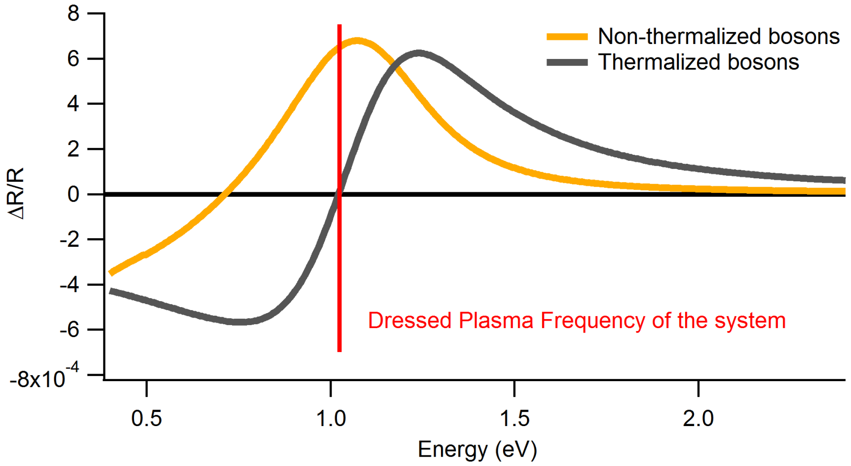

Figure 6.3: The results of a simulation for two electron-boson coupling scenarios are reported. The resulting $\Delta R/R(\omega)$ signals present marked differences. In one case, electrons are decoupled from all bosons (ΔT_e>0, ΔT_b=0, yellow line), while in the other case, electrons are strongly coupled with bosons (ΔT_e=ΔT_b>0, gray line).

function.

In Fig. 6.4 I report two energy-resolved traces of $\Delta R/R(\omega,\tau)$ at fixed delays: a) τ=100 fs, i.e., before the complete thermalization with the small subset of strongly-coupled phonons, b) τ=4 ps, i.e., after the thermalization with all the lattice. In the simple scenario of the conventional three-temperature model described in section 4.3.2, T_e is predicted to be decoupled from the temperature of the phonons (both the subset of strongly-coupled phonons and the rest of the lattice) in the very first instants ($\ll$100 fs) after the pump excitation. On the ps timescale, i.e., after the thermalization with phonons, the quasi-thermal scenario with $T_e \simeq T_b$ is recovered.

Comparing the $\Delta R/R(\omega,\tau)$ measured on the OP sample at τ=100 fs (Figure 6.4a) and τ=4 ps (Figure 6.4b) to the relative variation of the reflectivity calculated in the non-thermal (yellow solid line in Figure 6.4a) and quasi-thermal cases (dashed lines in Figure 6.4a and 6.4b), I come to the major point of this chapter, i.e., on a timescale ($\leq$100 fs) faster than the electron-phonon thermalization, the measured $\Delta R/R(\omega,\tau)$ is related to the variation of the temperature of some bosonic excitations participating to $\Pi(\Omega)$, while the non-thermal scenario with ΔT_e>ΔT_b is never observed. The fast timescale ($\ll$100 fs) of the thermalization with these bosonic excitations implies a very large coupling and a relatively small specific heat, and strongly suggests that this process involves bosonic excitations of electronic origin.

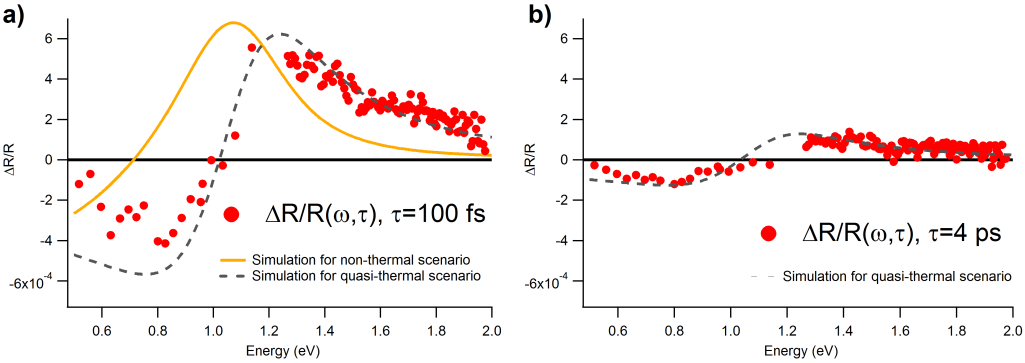

Figure 6.4: a) $\Delta R/R(\omega,\tau)$ experimental data at τ=100 fs pump-probe delay are compared with the simulated $\Delta R/R(\omega)$ obtained both for the non-thermal (yellow solid line) and the quasi-thermal (gray dashed line) scenarios. The latter result agrees with the experimental data. b) $\Delta R/R(\omega,\tau)$ experimental data at τ=4 ps pump-probe delay are compared with the simulated $\Delta R/R(\omega)$ (gray dashed line) obtained for a quasi-thermal scenario, in which ΔT_e=ΔT_b=0.22 K. A perfect match between experimental data and simulation is achieved, indicating that the system is completely thermalized after 4 ps after excitation.

6.4 Dynamics of the energy transfer to bosonic excitations

The qualitative analysis, reported in the previous section, of the measured $\Delta R/R(\omega,\tau)$, demonstrated some important issues:

- on all the timescales, the $\Delta R/R(\omega,\tau)$ signal is mostly determined by the increase of the effective temperature of the bosonic excitations that contributes to the total bosonic glue $\Pi(\Omega)$.
- the temporal dynamics evidences two distinct decays: a fast component of ~300 fs, and a slower one, with a decay time of ~2 ps. These timescales are related to the coupling of electrons with two different subsets of phononic excitations: a small fraction (f<1) of modes (with specific heat $f \cdot C_{tot}$, C_{tot} being the total specific heat) that are strongly-coupled to the electrons (strongly-coupled phonons, p) and determine the fast decay time; the rest of the lattice (l) that regulates the slower dynamics.
- on a timescale ($\leq$100 fs) faster than the electron-strongly coupled phonons thermalization, the fermionic quasiparticles photoinjected in the system by the pump pulse quickly interact with bosonic excitations characterized by a very strong coupling to electrons and a very small specific heat. These features strongly point to an electronic origin of these excitations.

The most straightforward way to reconcile these results is to solve a set of four coupled equations, describing the temporal evolution of the effective electronic

temperature (T_e) during the relaxation process toward equilibrium, through energy exchange with the three subsets of the total $\Pi(\Omega)$, determined through equilibrium spectroscopy (see section 3.7.1 and figure 3.8). This is equivalent to assume that the total bosonic function is given by $\Pi(\Omega)$=$\Pi_{be}(\Omega)$+$\Pi_p(\Omega)$+$\Pi_l(\Omega)$ where Π_{be} refers to the bosonic excitations of electronic origin at the effective temperature T_{be}, Π_p to the small fraction of strongly-coupled phonons (p) at T_p [145] and Π_l to all other lattice vibrations at T_l.
Although the possibility of defining effective temperatures for the electrons and the bosonic excitations is subjected to some limitations that will be discussed in section 6.6, this extension of the more conventional two/three temperature model [7, 145] allows to obtain a fully consistent analysis of the $\Delta R/R(\omega,\tau)$ data both in the time and frequency domains.
In this picture, the rate of the energy exchange among the different populations is given by [7] a four-temperature model (4TM):

$$
\begin{aligned}
\frac{\partial T_e}{\partial t} &= \frac{G(\Pi_{be},T_{be},T_{be})}{\gamma_e T_e} + \frac{G(\Pi_p,T_p,T_e)}{\gamma_e T_e} + \frac{G(\Pi_l,T_l,T_e)}{\gamma_e T_e} + \frac{p}{\gamma_e T_e} \\
\frac{\partial T_{be}}{\partial t} &= -\frac{G(\Pi_{be},T_{be},T_e)}{C_{be}} \\
\frac{\partial T_{scp}}{\partial t} &= -\frac{G(\Pi_p,T_p,T_e)}{C_p} \\
\frac{\partial T_l}{\partial t} &= -\frac{G(\Pi_l,T_l,T_e)}{C_l} \\
G(\Pi_b,T_b,T_e) &= \frac{6\gamma_e}{\hbar\pi k_B^2}\int_0^\infty d\Omega \Pi_b(\Omega)\Omega^2[N(\Omega,T_b)-N(\Omega,T_e)]
\end{aligned}
$$

with b=be,p,l and $N(\Omega,T)$=$(e^{\Omega/k_BT}-1)^{-1}$ the Bose-Einstein distribution at the temperature T. The specific heat (C_p) of strongly coupled phonons is proportional to their density of states and is taken as a fraction f of the total specific heat, i.e., C_p=$f\cdot C_{tot}$.
In principle, the numeric solution of these equations can be fitted to the measured relative reflectivity variation at a fixed wavelength to determine the different fractions ($\Pi_b(\Omega)/\Pi(\Omega)$) of the total $\Pi(\Omega)$. However, since time-resolved optical techniques do not provide a direct measurement of T_e and T_bs, this procedure requires the assumption that the measured $\Delta R/R(\tau)$ is proportional to the electronic and bosonic temperatures through some arbitrary coefficients appearing in expression 4.11, which I recall here:

$$\Delta R/R(\tau) = c_1\cdot\Delta T_e(\tau) + c_2\cdot\Delta T_{be}(\tau) + c_3\cdot\Delta T_p(\tau) + c_4\cdot\Delta T_l(\tau)$$

In Fig. 6.5 I report two time-resolved traces of $\Delta R/R(\omega,\tau)$ at fixed wavelength, i.e., 800 and 2400 nm. The solid lines are the fit to the data, using

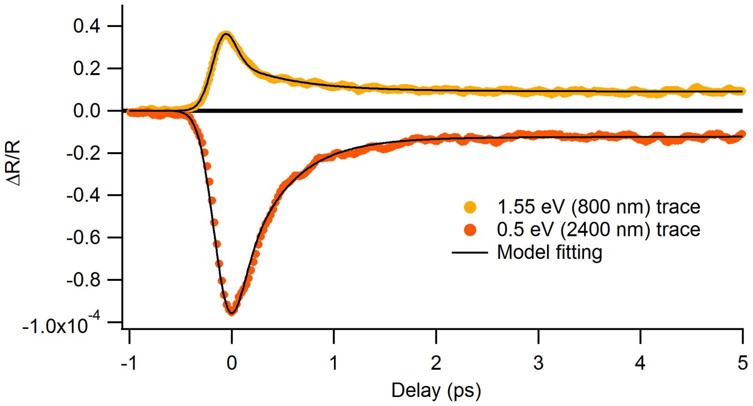

Figure 6.5: Two fixed-wavelenght time-resolved traces, respectively for 800 nm and 2400 nm probe, are reported. Black lines are the fit to the data performed with the 4TM. Fitting results are discussed in the text.

the solutions of the 4TM and fixing the values C_e/T_e=γ_e=10^{-4} Jcm^{-3}K^{-2}, C_{tot}=2.27 Jcm^{-3}K^{-1} and assuming an absorbed power density of 0.6 J/cm^3 and a pulse cross-correlation of 180 fs for the 800 nm measurement and 280 fs for the 2400 nm measurement. The temporal evolution of ΔT_e, ΔT_{be}, ΔT_p and ΔT_l is reported in Fig. 6.6. I note that, during the cooling process, the temperature T_p is transiently larger than T_e and T_{be}. This is related to the lack, in the 4TM, of any term for the anharmonic decay of the strongly coupled phonons [145], that directly couples the 3rd and 4th equations of the 4TM. Including this term, does not significantly alter the results of the fitting procedure. In Table 6.1 typical values of the electronic and bosonic temperatures at τ=0 and τ=4 ps are reported.

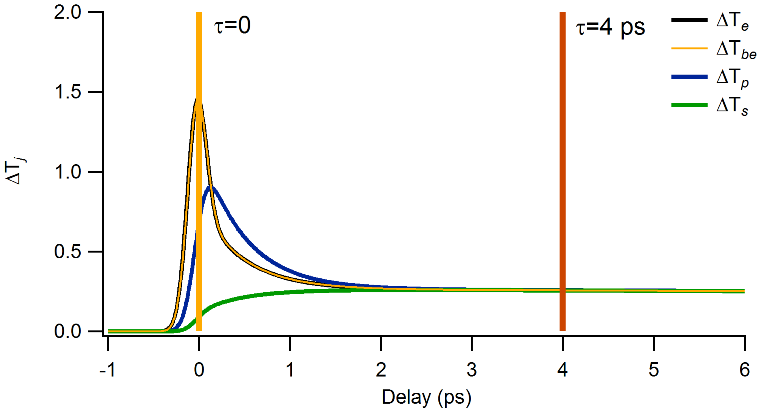

Figure 6.6: The result of the numeric integration of the 4TM equations system, showing the temporal evolution of the temperatures T_e, T_s, T_p, T_l, is reported. The simulation is performed with the paramters extracted by the fitting of the model to the 800 nm data.

Table 6.1: Electronic and bosonic temperatures at particular pump-probe delays τ, from a 4TM simulation at T_0=300 K.

Temperature	τ=0	τ=4 ps
ΔT_e	1.46 K	0.26 K
ΔT_{be}	1.46 K	0.26 K
ΔT_p	0.69 K	0.26 K
ΔT_l	0.09 K	0.26 K

While the temporal dynamics is satisfactorily reproduced (see Fig. 6.5) by the simple 4TM, the determination of the different $\Pi_b(\Omega)/\Pi(\Omega)$ fractions is prevented by the arbitrary assumption of the coefficients c_j that determine the proportionality between $\Delta R/R(\tau)$ and $\Delta T_e(\tau)$, $\Delta T_{be}(\tau)$, $\Delta T_p(\tau)$, $\Delta T_l(\tau)$. To decisively narrow the phase-space of the parameters of the fitting procedure and univocally disentangle the different contributions to the total bosonic glue, the fully consistent and simultaneous analysis of the time- and frequency-resolved data will be developed in the next section.

6.5 Simultaneous spectral and temporal analysis

Within the extended Drude model (see section 3.5.2), the optical conductivity is given by:

$$\sigma\left(\omega,T\right)=\frac{\omega_p^2}{i4\pi\omega}\int_0^\infty \frac{f\left(\omega+\epsilon,T\right)-f\left(\epsilon,T\right)}{\omega-\Sigma\left(\omega+\epsilon,T\right)+\Sigma^*\left(\epsilon,T\right)}\,d\epsilon$$

where ω_p is the plasma frequency and $f\left(\epsilon,T\right)$ the Fermi distribution. $\Sigma\left(\omega\right)$ is the electron self energy depending on the bosonic glue $\Pi(\Omega)$ and on the Kernel function $L(\omega,\Omega,T)$, as described in section 3.5.2.

As a consequence, the relative strengths of $\Pi_b(\Omega)$ (b=be,p,l) determine both the intensity of the reflectivity variation and the temporal evolution of the temperatures T_b, through the 4TM reported in the previous section. The simultaneous fit of the calculated $\Delta R/R\left(\omega,\tau,T_e,T_{be},T_p,T_l\right)$ to the data reported in Fig. 6.2 in the time- and frequency domain, significantly narrows the phase-space of the parameters of the model, as compared to single-color measurements and allows us to unambiguously extract the different contributions to $\Pi(\Omega)$ and to estimate C_{be} and C_p.

This procedure is not trivial from the technical point of view. Considering that the energy distribution of phonons is limited to <90 meV, I assume that, for Ω>90 meV, $\Pi(\Omega)\simeq\Pi_{be}(\Omega)$. Within this assumption, the functional dependence

of $\Delta R/R(\omega,\tau)$ on $\Pi_b(\Omega)$ is simplified as a parametric dependence on the coefficients p_b, where $\Pi_{be}(\Omega)=p_{be}\Pi(\Omega<90\text{ meV})+\Pi(\Omega>90\text{ meV})$, $\Pi_p(\Omega)=p_p\Pi(\Omega<90\text{ meV})$ and $\Pi_l(\Omega)=p_l\Pi(\Omega<90\text{ meV})$.
Considering the constraints given by the relations $\Delta R/R(\omega,\tau)=F(p_{be},p_p,p_l,C_{be},C_p,C_l;\omega,\tau)$ (F being the generic function expressing the dependence on the parameters contained in the definition of the $\sigma(\omega)$, see expression 3.13) and $\Pi(\Omega)=\sum_b\Pi_b(\Omega)$ ($\Pi(\Omega)$ being the total glue function determined through equilibrium spectroscopy and reported in the Figure 3.8), the free parameters of the fitting are four. From the fit to the rise time of the time-resolved signal, it is possible to obtain an upper limit to the value of the specific heat of the electronic excitations, i.e., $C_{be}\leq 0.1C_e$. Fixing the values $C_e/T_e=\gamma_e=10^{-4}$ Jcm^{-3}K^{-2} and $C_{tot}=2.27$ Jcm^{-3}K^{-1}, I am able to simultaneously perform the fit to the data reported in Fig. 6.2 in the time and frequency domain with only two free parameters, i.e. C_p and any of the p_b. Furthermore, the small influence of the variations of C_p on the fit results (i.e. $\partial F/\partial C_p\ll\partial F/\partial p_b$), significantly narrows the parameters phase-space of the model, allowing to unambiguously haul out the different contributions to $\Pi(\Omega)$. The result of the fitting procedure in the frequency domain, is shown in Fig. 6.7 for the $\Delta R/R(\omega,\tau)$ spectrum at $\tau=100$ fs. The black lines are the maximum and minimum $\Delta R/R(\omega,\tau=100$ fs), considering the experimental uncertainty in the laser fluence and spot dimensions. The values of $\Delta R/R(\tau=100$ fs) measured at each wavelength, satisfactorily fall within the two lines.

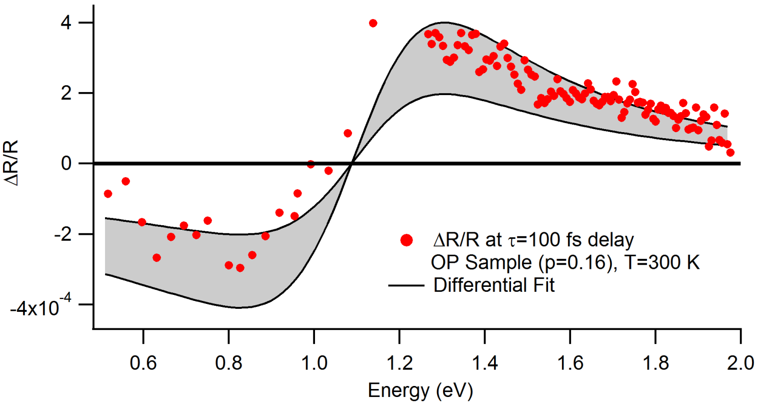

Figure 6.7: The $\Delta R/R(\omega,\tau)$ signal at $\tau=100$ fs pump-probe delay is reported. The gray shadowed area accounts for the experimental uncertainties in the both the measurement of the incident pump fluence and in the determination of the pump and probe spot sizes, which have been considered in the fitting procedure.

Figure 6.8 summarizes the main results of this analysis. The 10 μJ/cm^2 pump pulse gently increases the electronic temperature by $\Delta T_e\sim 2$ K. The entire high-energy part and ~46% of the peak (yellow areas) instantaneously thermalize with electrons at a temperature $T_{be} \simeq T_e$. The spectral distribution and the value of the specific heat of these excitations ($C_{\mathrm{be}} < 0.1 C_{\mathrm{e}}$) demonstrate their electronic origin and are compatible with both the spin fluctuations and current loops scenarios, described in section 3.5.4. On a slower timescale (100-300 fs), the electrons thermalize with the strongly coupled phonons, that represent ∼20% of the phonon density of states ($C_p = 0.2 \cdot C_l$), but are responsible for ∼34% of the coupling (blue area) in the peak of the bosonic function at 40-75 meV. Prominent candidates as strongly coupled phonons are the buckling and breathing Cu-O optical modes (see section 3.7.1). The third and last measured timescale is related to the thermalization with all other lattice modes (80% of the total) that include all acoustic modes and the IR- and Raman-active modes involving c-axis motion of the Cu ions and provide ∼20% of the coupling (green area) in the peak of $\Pi(\Omega)$.

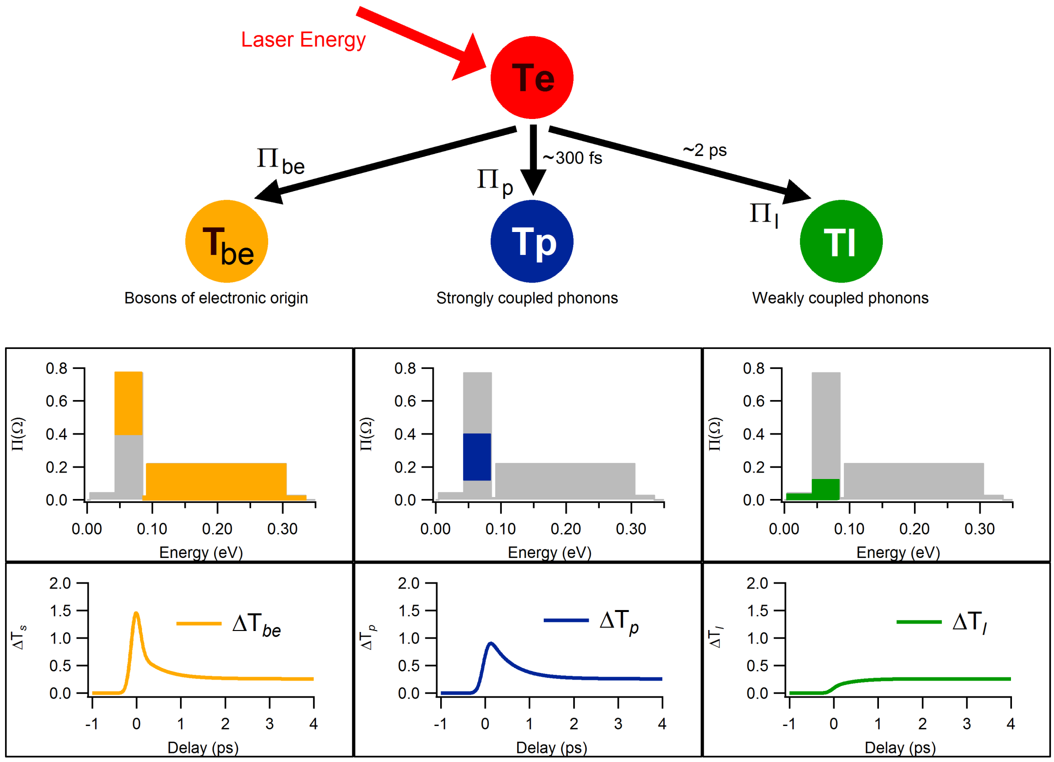

Figure 6.8: This scheme summarizes the scenario taking place in the normal state (T=300 K) of $\mathrm{Bi_2Sr_2Y_{0.08}Ca_{0.92}Cu_2O_{8+\delta}}$ for the electron-boson coupling, as determined by the combined spectral and temporal analysis of time-resolved spectroscopic measurements. The total bosonic glue $\Pi(\Omega)$ has been disentangled in three subsets, evidenced by different colors: yellow for the area arising from coupling with bosons of electronic origin (be); blue for the area related to the coupling with strongly coupled phonons (p); green for the area related to the coupling with weakly coupled phonons (l). The evolution of the three bosonic temperatures is also reported.

Table 6.2: Important parameters for the electron-boson coupling in the normal state, from the combined spectral and temporal analysis of time-resolved spectroscopic data.

Boson	λ_j	$\tilde{\Omega}_j$	C_j	T_c
j=p, strongly coupled phonons	0.4±0.2	60 meV	$0.2 \cdot C_{tot}$	2-30 K
j=l, weakly coupled phonons	0.2±0.2	47 meV	$0.8 \cdot C_{tot}$	0-12 K
j=be, electronic bosons	1.1±0.2	87 meV	$<0.1 \cdot C_e$	105-135K
Total	1.7	69 meV	$(C_{tot} + C_e)$	137 K

6.6 The bosonic glue and T$_c$

These results have fundamental implications for the identification of the pairing mechanism in cuprates. The electron-boson coupling λ_b=2 $\int \Pi_\mathrm{b}(\Omega)/\Omega\, d\Omega$ is calculated for each subset b of the bosonic excitations, considering the experimental uncertainties. In the strong-coupling regime (λ_b<1.5), the critical temperature for d-wave pairing [128] in a Fermi liquid with pseudopotential μ^*=0 is approximately given by an extended version of the Mc Millan's equation [8]:

$$T_c = 0.83\tilde{\Omega}\exp[-1.04(1+\lambda_b)/g\lambda_b]$$

where ln$\tilde{\Omega}$=$2/\lambda_b\int_0^\infty \Pi_b(\Omega)\ln\Omega/\Omega d\Omega$, λ_b=2 $\int \Pi_b(\Omega)/\Omega\, d\Omega$ is the electron-boson coupling constant and $g\in$[0,1] is a parameter that accounts for the d-wave nature of the superconducting gap. The upper bound g=1 corresponds to the case in which $\Pi_b(\Omega)$ entirely contributes to the d-wave pairing.

The coupling with strongly coupled phonons (λ_p=0.4±0.2) is in complete agreement with the values measured on similar materials via different techniques, such as time-resolved photoemission spectroscopy [145], time-resolved electron diffraction [27] and single-color high-resolution time-resolved reflectivity [75]. Although this value is rather close to the threshold of the strong-coupling regime [129, 159], the small value of $\tilde{\Omega}$ gives T_c=2-30 K, that is far from being able to account for the high-temperature superconductivity of the system. The coupling of electrons with all other lattice vibrations is even smaller in strength (λ_l=0.2±0.2) and provides an upper bound of the critical temperature of $T_c\simeq$12 K. Finally, the large coupling constant (λ_{be}=1.1±0.2) and the larger $\tilde{\Omega}$ value of the electronic excitations, give T_c=105-135 K, and hence accounts alone for the high-critical temperature. All the λ_b values, the $\tilde{\Omega}$ values, the specific heats and the maximum attainable critical temperatures T_c are reported in Table 6.2.

The measured value of λ_{be} and the spectral distribution of the electronic excitations constitute a benchmark for theories of superconductivity in the cuprates. In particular, they indicate that the antiferromagnetic spin fluctuations [48, 170] and the loop currents [182] are the most probable mediators for the formation of Cooper Pairs. I remark that our results are rather independent of the assumption of the histogram-like form of $\Pi(\Omega)$ and robust against modifications of the details of the equilibrium dielectric function. In fact, the outcome of this work strongly supports the factorization of the self energy into a temperature-dependent kernel function and a temperature-independent function $\Pi(\Omega)$ (see Eq. 3.19) even under non-equilibrium conditions. Although I do not exclude *a-priori* that: i) $\Pi_{\mathrm{be}}(\Omega)$ may be modified and new magnetic excitations emerge at low temperatures, particularly in the pseudogap phase [116]; ii) the upper limit used in the determination of the bosonic function can hide possible contributions to $\Pi(\Omega)$ even above 1 eV; iii) the electron-phonon coupling may cooperate in driving the superconducting phase transition, our results suggest that bosonic excitations of electronic origin are the most important factor in the formation of the superconducting state at high temperatures in the cuprates.

6.7 Limits of the N-temperature model and uncertainty in the determination of λ

The applicability of the two/three temperature models and their extension to the four 4 temperature model (reported in sections 4.3.1, 4.3.2, 4.3.3), relies on the assumption of a quasi-thermal electronic and bosonic distribution, thermodynamically defined by the effective temperatures T_e and T_b (with b=be,p,l). This model has been used to satisfactorily interpret both time-resolved photoemission [145] and time-resolved electron diffraction [27] data on Bi2212. In particular, the time-resolved ARPES data reported in Fig. 6.9 have been often considered as the evidence of the formation of a Fermi-Dirac electron distribution at an effective temperature, within 50-100 fs from the pump excitations. The departure from the quasi-thermal distribution is limited to a high-energy tail with an intensity of about 2 order of magnitude smaller than the Fermi-Dirac function. This hot electron tail is usually considered negligible in terms of the time-domain dynamics described by the generic N-temperature model.

Nevertheless, the basic assumption of all these quasi-thermal approaches is that the electron-electron scattering time (τ_{e-e}) is much smaller than the electron-phonon scattering time (τ_{e-ph}). In standard metals this condition is not always fulfilled. In particular, the electron-electron scattering time is determined by the Pauli principle and is given by (see equation 17.66 in [11]): $1/\tau_{e-e}$=$A(k_BT)^2/\hbar E_F$, where A is of the order of 1. Considering the typical values of the parameters for metals, I obtain τ_{e-e}∼10^{-10} s, which is signifi-

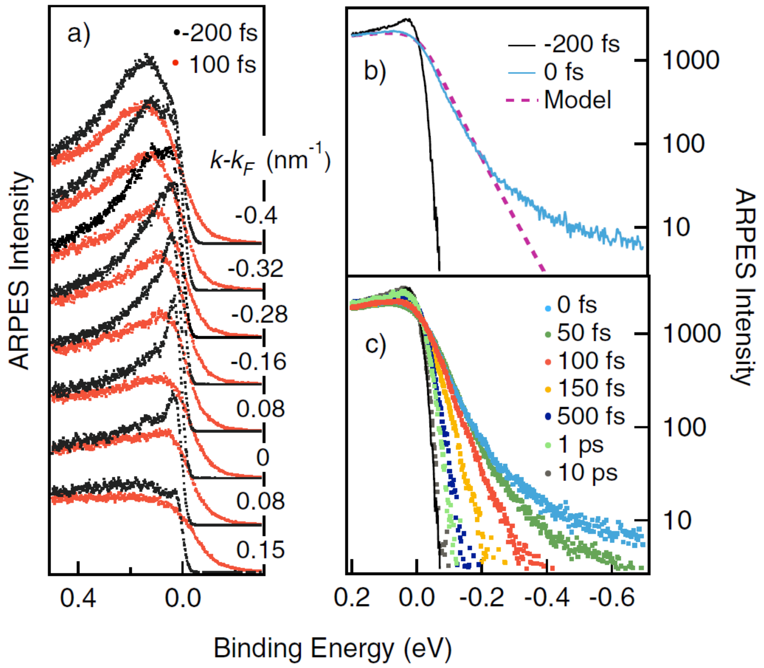

Figure 6.9: a) The time-resolved ARPES spectra acquired 200 fs before (black dots) and 100 fs after (red dots) the arrival of the pump pulse (T_0=30 K) are reported. b) The time-resolved ARPES spectra acquired at τ=0 fs (azure line) and at τ=200 fs (black line) are reported. The hypothetical spectrum of an electronic system that has fully thermalized at T_e=770 K (dashed violet line) is superimposed. c) The logarithmic plot of the k_F spectrum, collected at several pump-probe delays, is reported. From [145].

cantly larger than the typical relaxation time (10^{-12} s) at room temparature in metals. To overcome this problem, an analytical approach to the Boltzmann equation [96], which is free of any quasi-equilibrium approximation, has been recently developed. In this work, two-different regimes have been discussed: the high-temperature (T_e,$T_b$$\gg$$T_D$, where T_D is the Debye temperature) and the low-temperature (T_e,$T_b$$\ll$$T_D$) regime.
In the high-temperature case, the analytical treatment yields the relation:

$$\lambda_{e-ph} < \omega^2 >= \frac{2\pi}{3} \frac{k_B T_l}{\hbar \tilde{\tau}_{e-ph}} \tag{6.1}$$

where $\tilde{\tau}_{e-ph}$ is the exponential decay time of the time-resolved signal related to the electron-phonon coupling. This relation is applicable also when τ_{e-e}>τ_{e-ph}. As compared to the similar formula by Allen [7] (see formula 4.2), the electron-phonon coupling λ_{e-ph} is predicted to be linearly dependent on T_l instead of T_e, with a factor 2 that is absent on the original relation.
In the low-temperature case, it is calculated that the N-temperature model overestimates λ_{e-ph} of a factor $8/(5{\cdot}c(r))$, $c(r)$ being a coefficient ranging from 8/5, when the ratio r=τ_{e-e}/τ_{e-ph} is 0, to 1 in the limit $r\rightarrow\infty$. In other words,

when $\tau_{e-e} \ll \tau_{e-ph}$ the N-temperature model is fully valid, while in the conditions $\tau_{e-e} \gg \tau_{e-ph}$ the quasi-thermal model overestimates λ_{e-ph} of a factor $8/5=1.6$.
This approach based on the Boltzmann equations has been used to reassess [76] the electron-phonon coupling values, previously estimated through the simple 2TM, in metals. Slightly smaller values of λ_{e-ph} are found for the most common metals, with the maximum difference in NbN and V_3Ga, where λ_{e-ph} must be corrected of a factor 2.

In contrast to simple metals, the evaluation of τ_{e-e} in strongly-correlated systems and in cuprates, in particular, is a subtle problem, since the applicability of arguments based on the Fermi-liquid theory is questionable. It has been recently demonstrated [74] that below the value p=0.2 of hole-doping in cuprates, the strong electronic correlations drive a suppression of the coherent part (the quasiparticles) of the nodal ARPES spectra. This marks a clear departure from Fermi-liquid behaviour and a more rapid than expected crossover to Mott physics, where the elementary excitations are strongly localized on the Cu-O sites. Close to the optimal-doping ($0.1<p<0.2$), the system does not have completely lost the concept of quasi-particle, but is very close to the Mott behavior dominated by incoherent excitations. In other terms, the strong Coulomb repulsion among the conducting electrons strongly decreases the scattering time τ_{e-e} eventually driving the complete failure of the Fermi-liquid picture in the uderdoped side of the phase diagram. At optimal doping, the extended Drude model can be recovered, provided that the effect of strong electronic correlations is accounted for by a bosonic glue $\Pi(\Omega)$ of electronic origin.
In Ref. [76], $\tau_{e-e} \simeq 1.4$ ps is estimated considering a Fermi-liquid with an electron effective mass $m^*=4m$ and an effective dielectric constant $\epsilon_{eff} \simeq 30$. This estimation, based on the possibility of defining quasiparticles as in a conventional Fermi Liquid, appears rather crude, and completely neglects the role of the electronic correlations in the material. Furthermore, the concept of effective dielectric function appears questionable in systems dominated by localized excitations with very short coherence length. A value of τ_{e-e} at least two-order of magnitude smaller can be easily obtained assuming a slightly larger effective mass and a smaller ϵ_{eff}. Accidentally, the use of the analytical solutions of the Boltzmann equations in cuprates [75] provides exactly the same value of λ than the one obtained through the conventional three-temperature model, i.e., $\lambda \sim 0.5$ in $La_{1.85}Sr_{0.15}CuO_4$ and ~ 0.25 in $YBa_2Cu_3O_{6.5}$, casting further doubts on the conjecture that $\tau_{e-e} \gg \tau_{e-ph}$ in these systems. The same authors argue that the values of the electron-phonon coupling in $La_{1.85}Sr_{0.15}CuO_4$ and $YBa_2Cu_3O_{6.5}$ does not account for the very high-critical temperature of the system.

In the most pessimistic limit, i.e., $\tau_{e-e} \gg \tau_{e-ph}$, the use of the solution of the Boltzmann equations to evaluate λ even strengthen the main conclusions of this chapter. Since in Y-Bi2212 $T_D \sim$ 300 K, our experiment falls between the low- and high-temperature regimes discussed above. Nevertheless, I can use the two limits to estimate the possible corrections to λ_p, in the case of complete failure of the N-temperature model, i.e. $\tau_{e-e} \gg \tau_{e-ph}$.
Adopting the expression 6.1, I obtain a value of $\lambda_p < \omega^2 >$=360-440 meV^2 for the OP sample, corresponding to λ_p=0.22-0.28 for a phonon frequency ω=40 meV.
Assuming the low-temperature limit, the maximum overestimation of λ_p is given by a factor 8/5. In our case, the fit of the 4TM to the time-resolved data (see Figure 6.5) gives λ_p=0.4 that, multiplied by 5/8, gives 0.25. These values are well within the estimated range of λ_p=0.4±0.2, reported in section 6.5. The large error bars associated to this value include: i) the experimental uncertainty in the pump fluence; ii) the possibility of adding to the 4TM a term that accounts for the anharmonic coupling of strongly-coupled phonons and the lattice (see section 4.3.3); iii) the possibility of the failure of the 4TM in the limit $\tau_{e-e} \gg \tau_{e-ph}$. Therefore, all the conclusions about the role of the bosonic excitations of electronic origin in the formation of the superconducting condensate are robust even against the failure of the 4TM used to reproduce the temporal dynamics of the $\Delta R/R(\omega, \tau)$.

I note that from the analysis of the equilibrium optical spectroscopy data on Y-Bi2212 [178] (see Fig. 6.10), the frequency-dependent scattering time ranges from 5 fs at very low frequencies to a constant value <1 fs at about 1 eV. On the basis of the results reported in this chapter, these very fast scattering processes are dominated by the scattering of fermionic quasiparticles with bosonic excitations of electronic origin. Therefore, the non-equilibrium population created by the pump pulse, instantaneously interacts with these excitations [183] before the electron-phonon scattering processes. The role of this very fast electronic processes in quickly establishing a quasi-thermal population is an open fundamental question in the field of strongly-correlated systems out-of-equilibrium.

I conclude this section presenting the results of the numeric integration of the systems of equations for both the 2TM and the 4TM. The results shown in Fig. 6.11 are the $\Delta R/R(\tau)$ (obtained by formula 4.11 for the 4TM), normalized to the incident pump fluence. The electronic and the total specific heats have the same values in both models. From the numeric solution of the system of coupled differential equations, it is possible to argue that only in a limit of very high pump fluence the decay rate predicted by the 2TM ceases to be fluence-independent. On the contrary, in the 4TM case, this effect is almost completely suppressed. I ascribe this result to the fact that, when the electrons are considerably heated by the absorption of an high fluence laser pulse, their

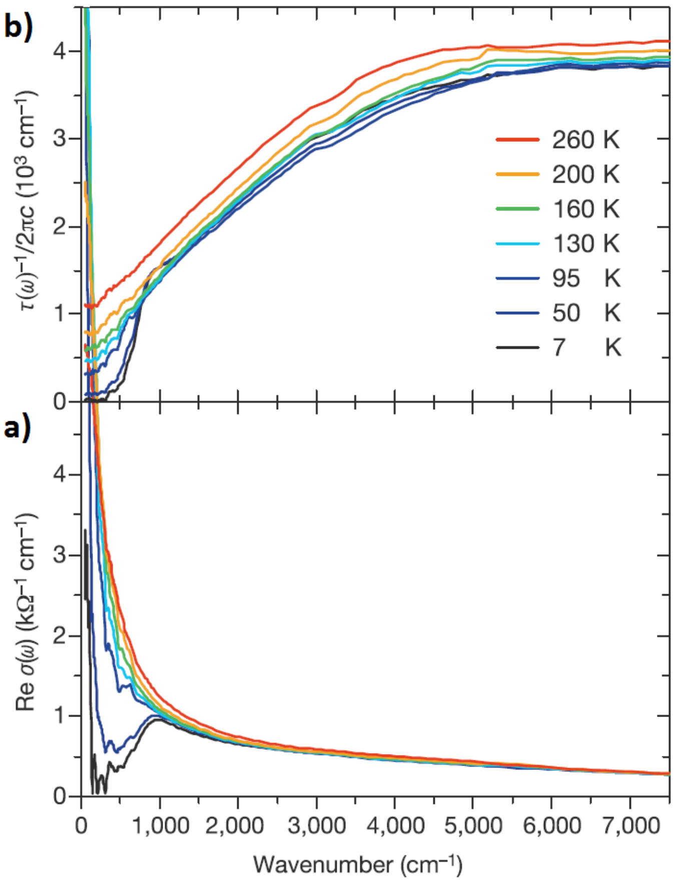

Figure 6.10: a) The in-plane optical conductivity of Y-Bi2212 for a number of selected temperatures is reported. b) The resulting frequency dependent scattering rate, defined as $1/\tau(\omega)$=Re$\left[\omega_p^2/4\pi\sigma(\omega)\right]$ (see Methods in [178]), is reported. From [178].

specific heat C_e=$\gamma_e \cdot T_e$ (being γ_e=10^{-4} Jcm^{-3}K^{-2}) becomes similar (C_e ~0.2 Jcm^{-3}K^{-1} at T_e ~2000 K, the maximum electronic temperature of the system in the case I_{pump}=10000 μJ/cm^2) to the strongly coupled phonons (10% of the total phonons) specific heat, C_p ~0.227 Jcm^{-3}K^{-1}. Thus, in the 4TM, electrons heat less than what predicted by the 2TM, with the relaxation dynamics which is a complex interplay of the contributions from the electrons and strongly coupled phonons relaxation. For the 2TM, the decay rate evolution, resulting from the numeric integration of the equations, is in agreement with the limit of applications of Allen Formula 4.2, which predicts a fluence-dependent decay rate at very high temperatures. By this simulation, it is also possible to argue that the limit in which the decay rate is linear with fluence is extremely high as compared to conventional metals, since in cuprates the penetration depth of light at 800 nm is about one order of magnitude larger than in metals (I remember that our measurements are performed with I_{pump}=10 μJ/cm^2).

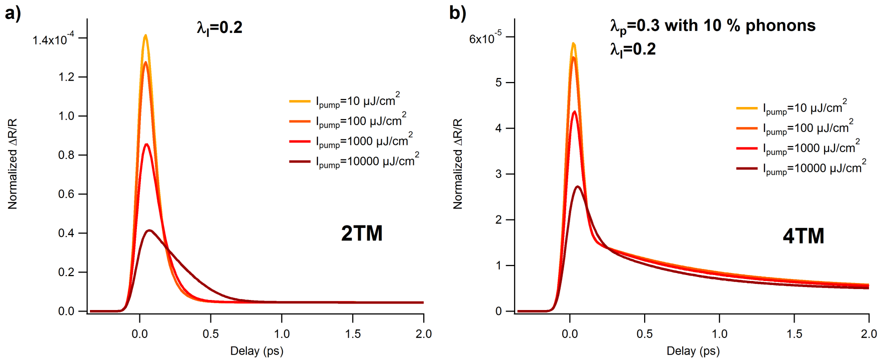

Figure 6.11: a) Simulation of the $\Delta R/R(\tau)$, as predicted by the 2TM. b) Simulation of the $\Delta R/R(\tau)$, as predicted by the 4TM. In both cases, the results are normalized to the incident pump fluence. The departure from a constant decay time starts only at very high pump fluences. For the 4TM, this effect is further reduced.

6.8 Conclusions

The results of the novel time-resolved optical spectroscopy and the related differential analysis reported in this chapter, have fundamental implications in the comprehension of the mechanisms leading to unconventional superconductivity in cuprates. Here I summarize the main conclusions of the analysis:

- On a timescale faster than electron-phonon thermalization, I demonstrated that the measured $\Delta R/R(\omega, \tau)$ signal is caused by the variation of the temperature of bosonic excitations of electronic origin, characterized by a strong coupling with electrons and a very small specific heat.

- The temporal dynamics exhibit two dynamics (respectively on the ~300 fs and ~2 ps timescales), revealing that two subset of phonon populations are coupled, with different coupling strength (λ_p=0.4±0.2, λ_l=0.2±0.2), to the electrons.

- By simultaneously fitting in the time and frequency domains an extended Drude model, in which the temperature evolution is governed by the 4TM rate equations, to the $\Delta R/R(\omega, \tau)$ signal, a fully self-consistent picture is obtained.

- The quantitative results of this analysis reveal that electrons are strongly coupled with a subset of the bosonic glue ($\Pi(\Omega)$) extending up to ~350 meV. The coupling λ_{be}=1.1 and the high mean-frequency $\tilde{\Omega}$=87 meV of this subset alone, account for the high critical temperature of the system. Possible candidates as a source of coupling for the formation of Cooper pairs, compatible with the evidenced characteristics, are either antiferromagnetic spin fluctuations [48, 170] or current-loops [182].

Chapter 7

Excitation-dependence of the bosonic glue in the pseudogap phase

7.1 Introduction

The pseudogap state is the most exotic and elusive phase of the phase diagram of HTSCs, and the comprehension of the microscopic electronic mechanisms behind is of paramount importance to reveal the nature of this intriguing phase. Here I demonstrate that the non-equilibrium dynamics underlying this phase are more complex than those observed for the normal state phase, suggesting that the pseudogap in HTSCs is a state of matter where the fermionic quasiparticles and the bosonic excitations are strongly intertwined.

This chapter illustrates the results obtained by probing, with time-resolved optical spectroscopy, the non-equilibrium dynamics of Y-Bi2212 samples in the pseudogap phase. Measurements are performed at T=100 K, the pseudogap extending between T^* (∼140 K for OP samples and ∼200 K for UD samples) and T_c. In this region of the p-T phase-diagram, the transient frequency-resolved optical response is different from what observed in the normal state and the simple quasi-thermal scenario does not account for the results.

Exploiting the time- and frequency-resolution of our technique and the differential analysis I demonstrate that, on the femtosecond timescale, the transient optical response at T=100 K is dominated by an excitation-dependent bosonic glue.

7.2 Time-resolved spectroscopic measurements at T=100 K

In Fig. 7.1 the time- and energy-resolved transient reflectivities $\Delta R/R(\omega,\tau)$ collected at T=100 K for five Y-Bi2212 samples, are reported. The samples span the p-T phase diagram from the underdoping to the overdoping regime, as the oxygen content δ is varied. The doping levels p of the samples are: p=0.128, p=0.16, p=0.176, p=0.197, p=0.2, corresponding to T_c values respectively of 83 K, 96 K, 94 K, 86 K, 83 K. In contrast to the results obtained at room temperature (see Fig. 1 of chapter 6), when the system is in the normal state, here the spectral response is more structured and exhibits a clear, doping dependent, evolution, when moving from the underdoped to the overdoped side of the phase diagram.

The time-trace extracted from the $\Delta R/R(\omega,\tau)$ plot in Fig. 7.1, for the UD sample and at 1.55 eV energy, exactly reproduces the negative signal observed by conventional single-colour pump-probe measurements on underdoped samples [117], at 1.55 eV probe energy. The negative time-resolved optical signal characterizing the non-equilibrium optical response in the visible spectral region, for UD and OP samples, tends to vanish upon increasing the doping level, as is evident from the right panels of Fig. 7.1. However, the $\Delta R/R(\omega,\tau)$ signal reveals a positive feature toward the infrared spectral region, which is almost doping-independent and is different in intensity from the normal state signal. The picture emerging from the $\Delta R/R(\omega,\tau)$ plots of Fig. 7.1 is that at T=100 K, the time resolved optical signal exhibits strongly doping-dependent spectral features. The spectroscopic information reveals mandatory for the comprehension of the intriguing interplay of physical processes which are taking place in this intriguing phase of matter. In this chapter I will demonstrate that the negative time-resolved optical signal in the visible spectral region is associated to the onset of the pseudogap. To address the origin of the transient $\Delta R/R(\omega,\tau)$ at T=100 K, I extended the probed spectral range to the near infrared (0.5 eV) through an Optical Parametric Amplifier-based setup (described in section 5.6).

Fig. 7.2 reports the measurements performed on the optimally doped sample, along with some cuts of the $\Delta R/R(\omega,\tau)$ plot at fixed delay times, from which the evolution of the transient spectral response is obtained. The full transient spectrum shows two sign-change points. The first, evident from the visible-range measurements alone, is at ~1.35 eV (i.e., ~900 nm), whereas the second is in the infrared part of the probed spectral range, at ~0.6 eV (~2050 nm), where the positive signal associated to the almost-doping-independent feature vanishes, and the impulsive reflectivity variation becomes negative on the sub-ps timescale. Although noisy, the transient signal at longer pump-probe delays (the τ=3 ps trace of Fig 7.2b can be considered) reveals an interesting feature:

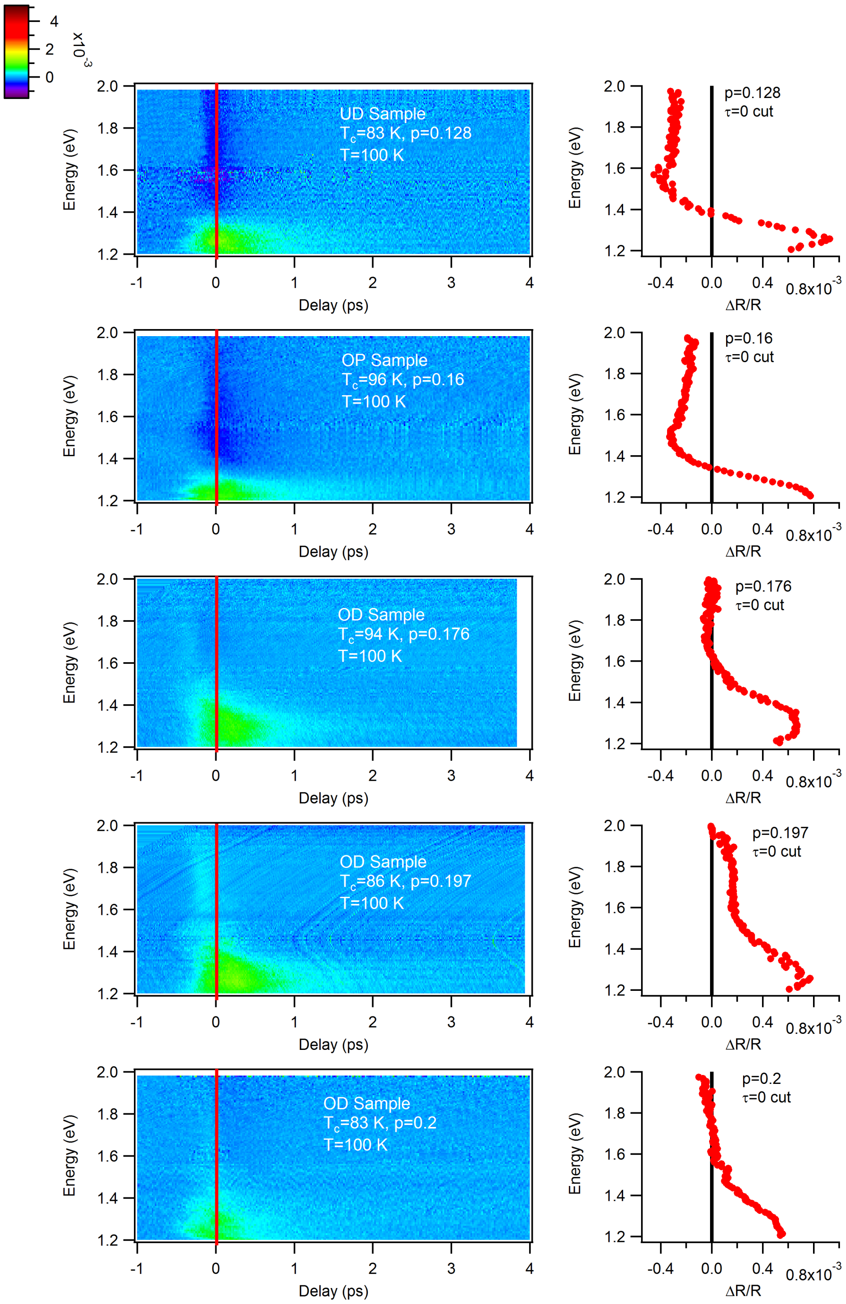

Figure 7.1: The temporally and spectrally resolved plots of the transient reflectivity in the pseudogap phase (T=100 K) of $Bi_2Sr_2Y_{0.08}Ca_{0.92}Cu_2O_{8+\delta}$ are here reported for five doping levels: p=0.128 (UD sample), p=0.16 (OP sample), p=0.176 (OD sample), p=0.197 (OD sample), p=0.2 (OD sample). The cuts (evidenced in red) at τ=0 pump-probe delay are reported in the right graphs, evidencing the spectral strucutre of the transient signal. The pump fluence is set to 10 μJ/cm^2.

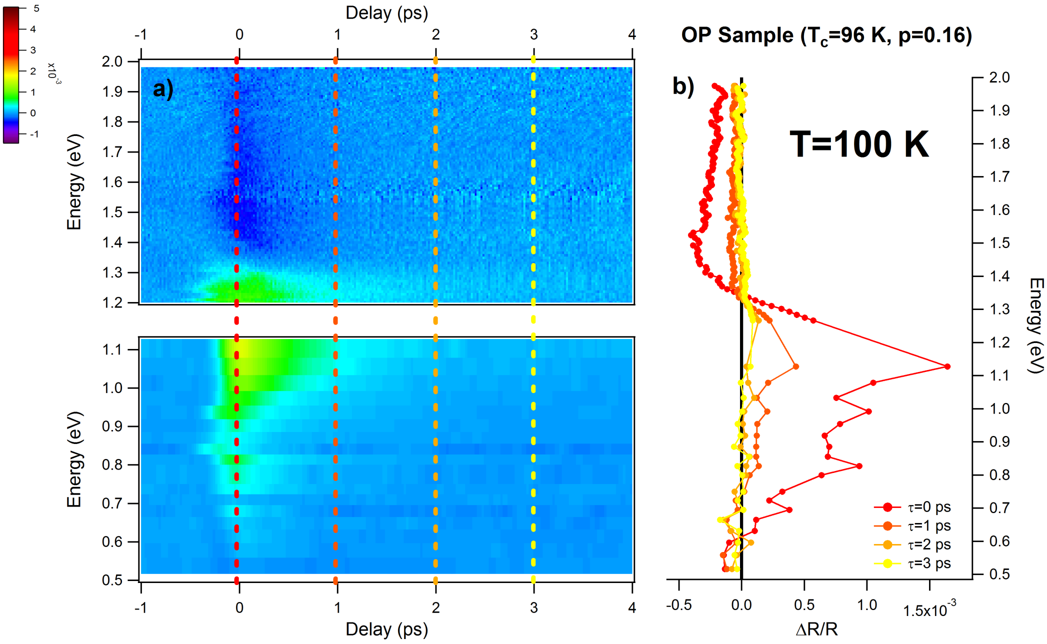

Figure 7.2: a) The measurement on the Optimally Doped sample is extended toward the infrared, up to 0.5 eV. b) The total transient spectra for selected pump-probe delays τ are reported.

its sign is positive in the visible, while it is negative in the infrared. This experimental evidence will be rationalized in section 7.3, as originating from a thermal heating effect. The time-resolved transient signals reported in panel b) of Fig. 7.2, extending in the energy range 0.5-2 eV, will constitute the basis for our analysis, illustrated in the rest of the chapter.

7.3 Pump-induced heating of the bosonic excitations

In this paragraph I simulate the transient reflectivity variation in the energy domain, as expected in the pseudogap phase assuming a quasi-thermal heating of the system. I will show that, while this thermal effect does not account for the $\Delta R/R(\omega, \tau)$ for $\tau <$ 1 ps (i.e., in the sub-ps timescale), it well reproduces the transient spectrum for longer delays ($\tau \gtrsim$3-4 ps), when the bosonic excitations of the system are thermalized. To estimate the temperature evolution of the system in the pseudogap phase, I use the 4TM already exploited in Chapter 6, assuming that the electron-boson coupling has not changed upon cooling down the sample from T=300 K to T=100 K (i.e., that the total glue function $\Pi(\Omega)$ and the various λ_j have not changed). I remind that I demonstrated that the electrons are coupled with three different bosonic populations: bosons of electronic origin (i.e., antiferromagnetic spin fluctuations or current

Table 7.1: Electronic and bosonic temperatures at particular pump-probe delays τ, from the 4TM simulation at T_0=100 K.

Temperature	τ=0	τ=4 ps
ΔT_e	9.45 K	0.61 K
ΔT_{be}	9.45 K	0.61 K
ΔT_p	1.13 K	0.72 K
ΔT_l	0.11 K	0.43 K

loops), that I indicate with subscript j=be, strongly coupled phonons (j=p) and weakly coupled phonons (j=l). For the simulation, I use the same values for λ_j reported in Chapter 6 (see Table 6.2). At a base temperature of T=100 K the specific heats, both the electronic and the total ones, have a non constant value, which is fully accounted for by the simulation. This provides different values for the temperature increments ΔT_j (here j=e for electrons, and j=be, p, l for the temperatures associated to the bosonic populations I recalled before) with respect to those obtained for the system in the normal state, for the same absorbed energy density of 0.6 J/cm^3. The expected temperature evolution profile is reported in Fig. 7.3 for ΔT_e, ΔT_{be}, ΔT_p and ΔT_l. From the simulation I extract the ΔT_j values at τ=0 and τ=4 ps, respectively, for the system in non-equilibrium condition and in the quasi-thermal regime, when the bosons are thermalized. These values are reported in table 7.1.

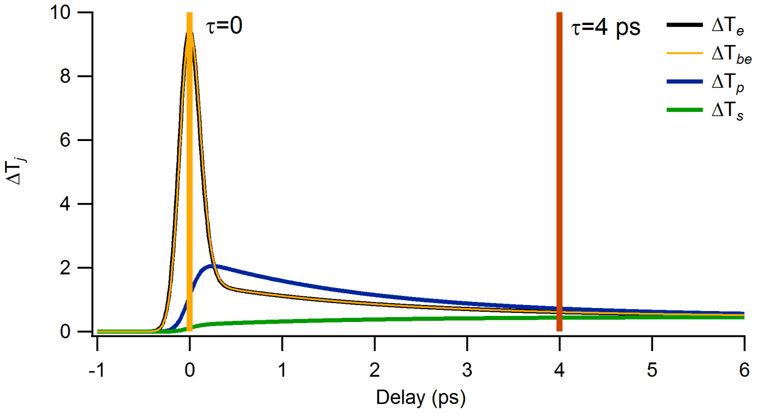

Figure 7.3: The results of the numeric integration of the 4TM equations system, for the temporal evolution of the temperatures T_e, T_{be}, T_p, T_l are reported. The simulation is performed with the parameters determined from the analysis of the $\Delta R/R(\omega, \tau)$ spectra at T=300 K (see section 6.5) From the obtained temperature values, the system heatng in the pseudogap phase is inferred.

The calculated values for the electronic and bosonic temperatures are used to simulate the $\Delta R/R(\omega, \tau)$ traces at τ=0 and τ=4 ps, expected for a quasi-thermal scenario. This simulation has been done with the differential dielectric function approach (see section 4.4) and the EDM presented in section 3.5.2. For clarity, I recall here the main expressions of this model. The Drude part of the model dielectric function, related to the reflectivity by formula 3.3, is given by:

$$\epsilon_D(\omega, T) = 1 - \frac{{\omega_p}^2}{\omega(\omega + iM(\omega, T))} \tag{7.1}$$

Where the Memory function $M(\omega, T)$, given by:

$$M(\omega, T) = -i\omega \left\{ \int_{-\infty}^{+\infty} \frac{f(\xi, T) - f(\xi + \omega, T)}{\omega + \Sigma^*(\xi, T) - \Sigma(\xi + \omega, T) + i\gamma_{imp}} d\xi \right\}^{-1} + i\omega \tag{7.2}$$

is a function of the electronic self-energy $\Sigma(\omega, T)$, which is given by (in the model presented in 3.5.2):

$$\Sigma(\omega, T) = \int_0^\infty \alpha^2 F(\Omega) L(\omega, \Omega, T) d\Omega \tag{7.3}$$

where the Kernel function $L(\omega, \Omega, T)$ writes:

$$L(\omega, \Omega, T) = -2\pi i \left[n(\Omega, T) + \frac{1}{2} \right] + \Psi\left(\frac{1}{2} + i\frac{\Omega - \Omega'}{2\pi T}\right) - \Psi\left(\frac{1}{2} - i\frac{\Omega + \Omega'}{2\pi T}\right) \tag{7.4}$$

It must be noted that in our simulations, the Glue Function $\Pi(\Omega)$, appearing in equation 7.3 and expressing the electron-boson coupling is held constant (i.e., independent from the heating given by the laser excitation), while only the temperatures appearing in the BE (n) and FD (f) distributions of the Kernel function (equation 7.4), which describes the thermal excitations of the electrons and the glue, are changed. Values from Table 7.1 are considered. The Glue Function $\Pi(\Omega)$ is factorized in three subsets, as illustrated in Fig. 6.8. Each one has its own bosonic temperature T_b: T_{be}, T_p, T_l, entering the Kernel function $L(\omega, \Omega, T)$.

The temporal traces obtained by the simulation described are reported in Fig. 7.4 and Fig. 7.5, respectively for $\tau = 0$ and $\tau = 4$ ps, together with the experimental data. Comparing the results of the simulation to the measured $\Delta R/R(\omega, \tau)$ traces, I come to the major point of this section. That is, while the spectrum obtained for the system 4 ps after excitation is well reproduced by a quasi-thermal scenario, the spectrum at zero delay requires a more complex picture than that of a purely (non-thermal) heating effect.

Fig. 7.4 clearly shows that the experimental and the simulated spectra, for a pump-probe delay of τ=0 ps, are significantly different. In particular, a negative time-resolved optical signal is observed in the visible spectral region, and

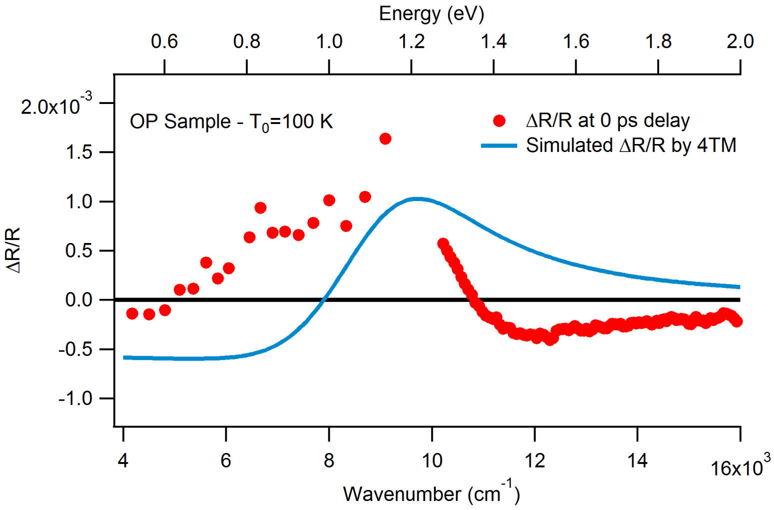

Figure 7.4: The simulation performed for a quasi-thermal scenario, assuming that the electron-boson coupling constants λ_j are unchanged with the respect to the ones determined for the normal state, is reported. The temperatures are taken from Table 7.1. Comparison with data for τ=0 pump-probe delay shows that a non-thermal heating effect alone is not enough to reproduce transient data in the pseudogap phase, at small pump-probe delay.

cannot be reproduced by the simulation described, whereas the time-resolved optical signal is positive in the infrared.
Therfore, in the pseudogap phase, other effects than a purely non-thermal heating are likely taking place, in the first instants after excitation. These effects should be of non-thermal nature, given their fast dynamics. Their correct interpretation is mandatory to shed light on the nature of the pseudogap phase. The problem of assigning a physical origin to the $\Delta R/R(\omega,\tau)$ at τ=0 will be tackled in the next section, making use of the differential dielectric function approach (see section 4.4).
On the contrary, the fact that the spectrum measured at τ=4 ps pump-probe delay is well reproduced by the simulation is supported by two high-resolution one-color pump-probe measurements at probe energy of 1.55 and 0.6 eV, reported in Fig. 7.5. This further confirms that at long pump-probe delays (τ ~3-4 ps) the system time-resolved optical response is quasi-thermal.

7.4 Excitation dependance of the Bosonic Glue

To properly reproduce the time-resolved optical signal at $\tau = 0$, my strategy will be to assume the thermal contribution calculated as described in section 7.3 as a fixed starting background. Then, the other physical contributions necessary to correctly reproduce the experimental signal will be added, modifying the related parameters in the excited dielectric function entering the differential dielectric function model.

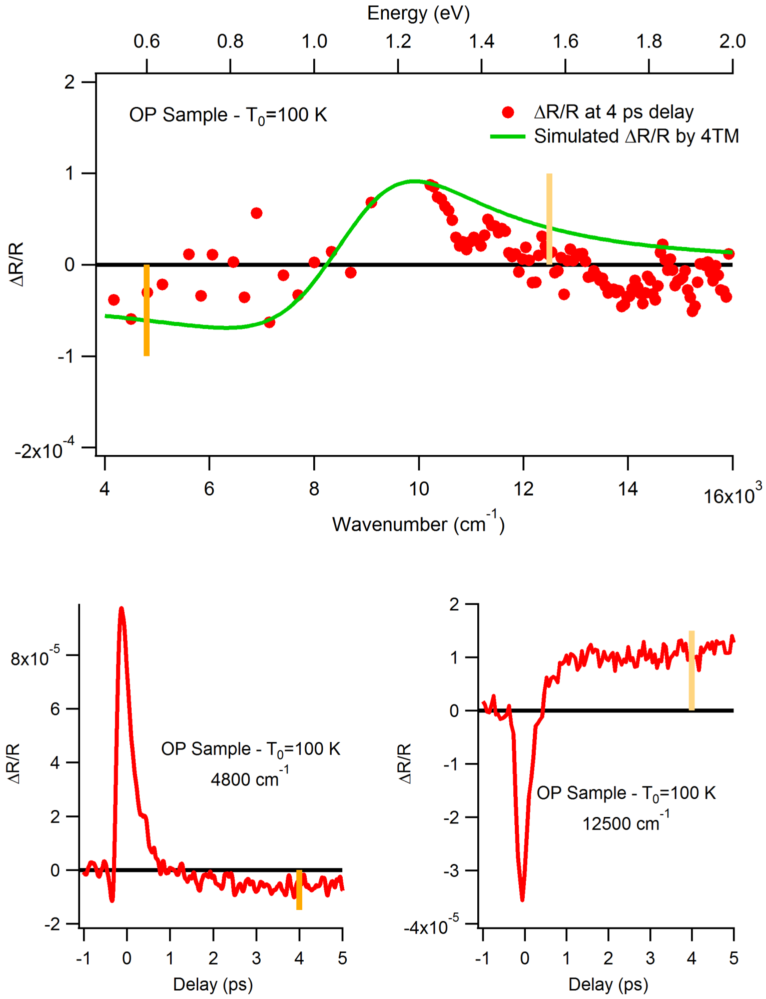

Figure 7.5: This graph demonstrates how the transient spectrum for τ=4 ps pump-probe delay is well-reproduced by a simulation in which the system temperature is increased by 0.5K, that is, ΔT_e=ΔT_b=0.5 K. This indicates that for pump-probe delays $\tau \gtrsim$4 ps, the system is completely thermalized at an elevated temperature with respect to the thermal bath one. The signal is thus dominated purely by a quasi-thermal heating effect, while signals arising from other mechanisms are quenched. Two single-color pump probe measurements confirm this scenario.

In particular, I will demonstrate that the measured $\Delta R/R(\omega,\tau)$ can be reproduced by taking into account the following two contributions:

i) the impulsive quench of a gap in the density of states;

ii) the impulsive modification (decrease) of a low-energy peak of the Glue function $\Pi(\Omega)$.

Some comments are needed about these points. The point i) is accomplished by replacing the Extended Drude strong coupling formalism with the formalism described in 3.5.3, that is also strong coupling and accounts for a non-constant DOS arising from the opening of an energy gap in the pseudogap phase [49]. It is worth to point out that the models described in 3.5.2 and 3.5.3 coincide in the limit of zero-gap, as I verified numerically, therfore I use the model in 3.5.3 without changing the parameters. Point ii) implies that the glue-function, thus the electron-boson coupling, is no more insensible to external perturbations, that is, it is no more fluence-independent, as it was proved to be in the normal state phase. Thus, from now on I will assume that the Glue function $\Pi(\Omega)$ can be directly modified by laser excitation. This will turn out to be a clue observation, to address the origin of the $\Delta R/R(\omega,\tau)$ signal in the pseudogap. Finally, a comment about our procedure. All the transient reflectivity changes arise from the modifications of the Extended Drude model parameters, thus are intrinsically entangled. However, since the variation of the parameters is small (few percents), it has been possible to simulate the transient response arising from each physical contribution alone, by considering individually each contribution. I carefully checked that the sum of the three contributions is exactly the same than the result of the three being considered together. With this in mind, I illustrate which is the expected $\Delta R/R(\omega,\tau)$ arising from contributions i) and ii) alone. Finally, i), ii) and the thermal effect are brought together to reproduce the measured signal, after having considered the effect of the pump beam finite penetration depth (see section 4.3.4).

i) Effect of the gap closing on the $\Delta R/R(\omega,\tau)$

Having photoinjected excitations in the system with the pump pulse, it is reasonable to assume that the gap opened in the density of states is partially quenched. I start from the results of the fitting procedure of the equilibrium model (section 3.5.3) to the experimental dielectric function at T=100 K, presented in 3.7.2, where I fixed a reasonable value for the gap width of Δ_{pg}=350 cm^{-1} [153] and where I found a value for the gap amplitude of $1-\tilde{N}(0,T)=0.3$ (i.e., $\tilde{N}(0,T)=0.7$). In the differential model, I assumed that the excitation effect is that of increasing $\tilde{N}(0,T)$, which corresponds to a pump-induced filling of the gap. However, I verified that an identical $\Delta R/R(\omega,\tau)$ is obtained upon decreasing the Δ_{pg} value.

The transient spectra obtained for $\tilde{N}(0,T)$ equal to 0.74, 0.78, 0.82, 0.86 respectively, are reported in Fig. 7.7. The simulated $\Delta R/R(\omega,\tau)$ presents a positive spectral feature in the spectral range 5000-11000 cm^{-1}, while it vanishes outside this range. Reducing a gap in the density of states implies that carriers gain kinetic energy. This corresponds to an increase of the Drude plasma frequency of the system (see the sum rule in section 3.6). I verified this simple argument by performing a simulation for the expected $\Delta R/R(\omega,\tau)$, assuming an increase of the (Extended) Drude oscillator plasma frequency. The result is that in the spectral range of interest, the transient spectra are similar.

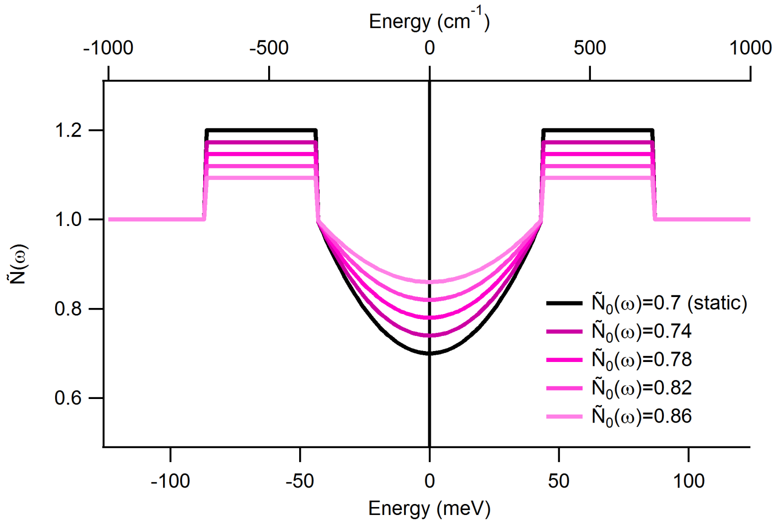

Figure 7.6: The effect of the laser excitation on the gap intensity $\tilde{N}(0,T)$ is pictorially sketched. The effect of this modification on the $\Delta R/R(\omega)$ is reported in Fig. 7.7.

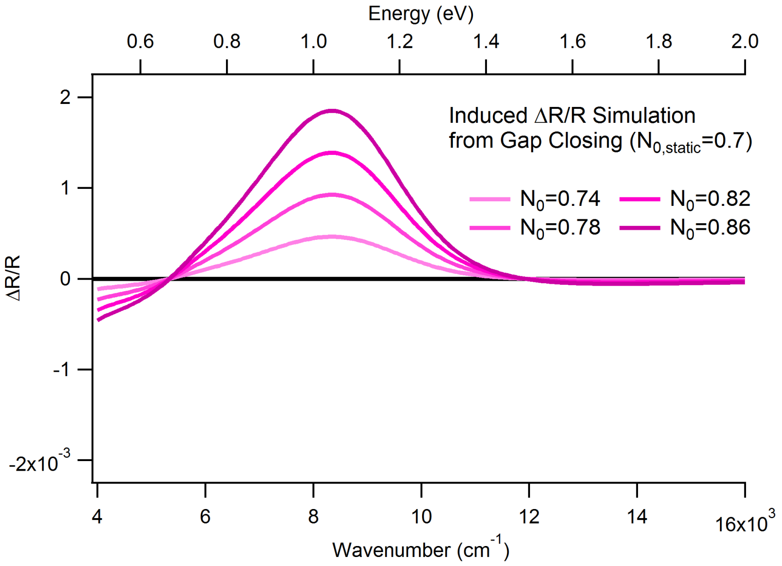

Figure 7.7: Here I show the simulated differential spectra obtained by only modifying the value of the gap in the density of states. Values are reported on the graph itself.

ii) Effect of the $\Pi(\Omega)$ excitation on the $\Delta R/R(\omega,\tau)$

The signal originating from the impulsive modification of the lowest-energy peak intensity in the glue function $\Pi(\Omega)$ leads to a completely different and peculiar $\Delta R/R(\omega,\tau)$. The value of the intensity of peak '1' of the Bosonic Glue $\Pi(\Omega)$, 0.041, is obtained from the fitting of the Extended Drude model to the equilibrium spectroscopic data. In Fig. 7.9 I report the simulated $\Delta R/R(\omega,\tau)$ obtained changing this intensity to the values 0.040, 0.039, 0.038, 0.037, respectively. It must be noted that the modification of the higher peak intensity would lead to similar results.

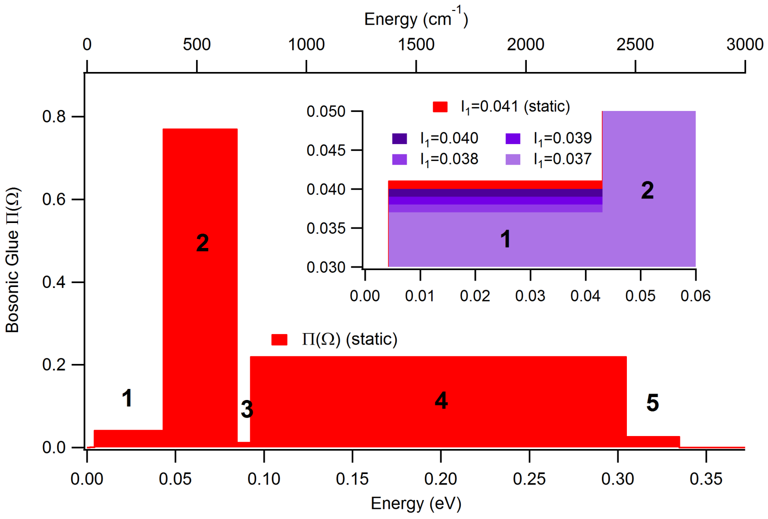

Figure 7.8: The effect of the laser excitation on the $\Pi(\Omega)$ lowest-energy peak intensity (I_1) is pictorially sketched. The effect of this modification on the $\Delta R/R(\omega)$ is reported in Fig. 7.9.

The resulting $\Delta R/R(\omega,\tau)$ shows a significantly different spectral shape, when compared to the $\Delta R/R(\omega,\tau)$ related to the gap filling (Fig. 7.7). In fact, it is negative in the visible spectral range, whereas it is positive in the infrared. The sign changes around 8000 cm^{-1}, i.e., ~1 eV.

Our choice of modifying the lowest-energy peak in the Glue Function will be now discussed in detail.
My argument is based on recent findings I will summarize here. Li et al. [116] revealed the existence of a fundamental collective magnetic mode, which intensity onset is associated with the T^* temperature, and with characteristic energy of 52-56 meV. The measurements have been performed with the inelastic neturon scattering technique, on a $HgBa_2CuO_{4+\delta}$ sample. Measurements on both underdoped and optimally doped samples revealed the same phenomenon, but at different onset temperatures, compatible with the actual T^* of the material. These findings further support previous results [73, 115] obtained by the polarized neutron diffraction technique, that demonstrated the existence of an unusual magnetic order below T^*. The magnetic mode observed by Li et al. [116] (see Fig. 7.10) could be assigned to a typical excitation of this magnetic

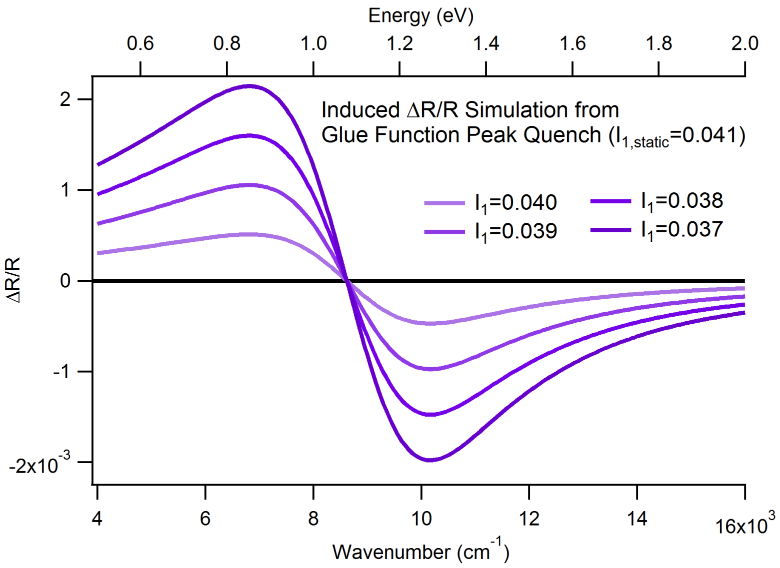

Figure 7.9: Here I show the simulated differential spectra obtained by only modifying the value of the lowest-energy peak in the bosonic glue. Values are reported on the graph itself.

order. All these results point toward a picture where the pseudogap regime (which we found being a set of anomalous physical properties) constitutes a genuine phase of matter, rather than a crossover phenomenon. The experimental findings by Li et al. are summarized in Fig. 7.10.

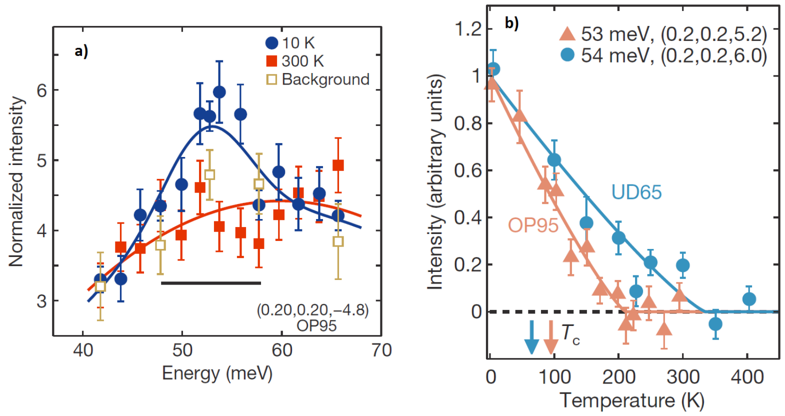

Figure 7.10: a) A weakly dispersing collective magnetic mode (which intensity is reported) has been identified on a $HgBa_2CuO_{4+\delta}$ sample. Its energy is ∼50 meV. b) The temperature dependence of the collective mode demonstrates its connection to the pseudogap phenomenon. The mode onset temperature is ∼210 K for an OP sample and ∼350 K for an UD sample.

Since it has been experimentally demonstrated that in a copper-oxyde based high-temperature superconductor, a new, temperature-dependent excitation mode, with electronic origin, rises at a temperature compatible with the sample actual T^*, I assume that the lowest-energy peak of the bosonic glue can be fluence-dependent. The correctness of this assumption is tested in the next section, where I present the model fitting results to the experimental data. I have to remark that this is only an assumption: I will not be able to reveal which (low-energy) peak of the bosonic glue actually varies.

$\Delta R/R(\omega,\tau)$ fitting to the experimental data.

Having addressed the individual effect on the $\Delta R/R(\omega,\tau)$, originating from the photoinduced heating of the system, from the photoinduced gap filling and from the photoinduced quench of one peak in $\Pi(\Omega)$, I consider them together. In particular, I fit the total $\Delta R/R(\omega,\tau)$ arising from the three contributions to the time-resolved data (at τ=0) in the energy domain.
The fit to the data is thus performed with only two free parameters, i.e., the gap amplitude $(1-\tilde{N}(0,T))$ and the lowest peak intensity (I_1), being the thermal effect simulated a priori and fixed. The result is reported in Fig. 7.11. The contribution of the finite pump penetration depth to the signal is also taken into account (see section 4.3.4). The fit result for the two parameters is: $1-\tilde{N}(0,T)$=0.2 and I_1=0.0377.

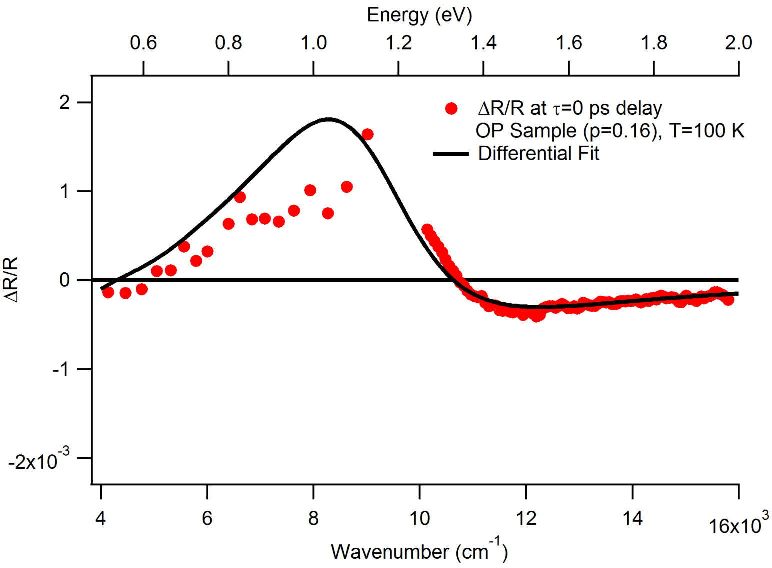

Figure 7.11: Here I show the energy-resolved spectrum at a fixed pump-probe delay τ=100 fs. The black line is the fit to the data, obtained as described in the text. Fitting parameters are collected in Table 7.2.

Therfore, the experimental data are satisfactorily reproduced by assuming the simultaneous presence of three effective physical processes in the pseudogap phase. The three relevant spectral contributions, calculated considering the fitting results, are shown in Fig. 7.12. Table 7.2 summarizes the differential

Table 7.2: Differential fitting results for the pseudogap state.

Parameter	Static	Dynamic (from Fit)
$\tilde{N}(0,T)$	0.7	0.8
I_1	0.041	0.0377

fitting results.

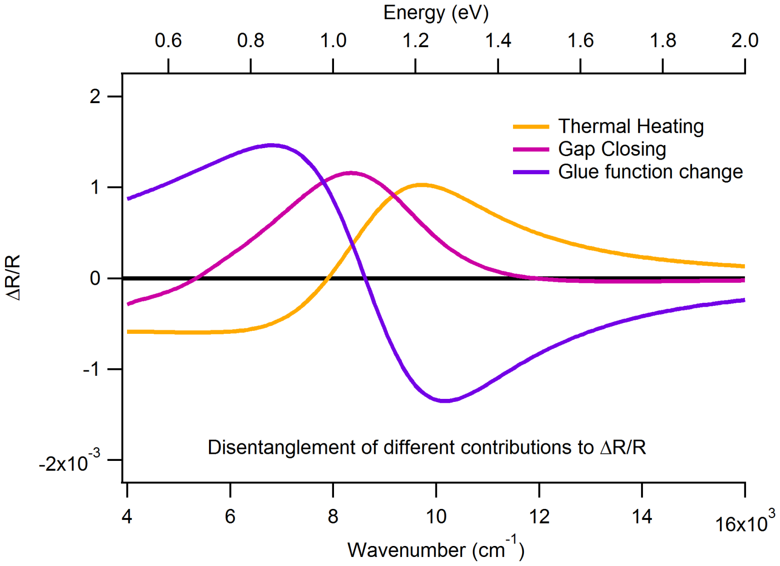

Figure 7.12: Here I show singularly the effect on the transient reflectivity arising from the different 'ingredients' of the fit. Values obtained are those extracted by the fitting procedure.

Final remarks about the fitting procedure

- I want to emphasize that it does not exist another simple way of reproducing the experimental $\Delta R/R(\omega,\tau)$, by varying other parameters in the dielectric function.
- I use only two fitting parameters to reproduce the experimental values of $\Delta R/R(\omega,\tau)$. The fitting procedure described requires the minimum number of parametrs to correctly reproduce the experimental $\Delta R/R(\omega,\tau)$.
- The fact that the differential signal associated to the fluence dependence of the Glue Function $\Pi(\Omega)$ is negative in the visible spectral range, where the contribution related to the gap filling has a negligible effect, and the

> quasi-thermal heating effect gives a positive sign, is a clear evidence that the signal observed by both single or broadband color measurements in the near-IR / visible originates from this contribution. No other way of reproducing this negative signal in the visible spectral range has been found. In the next chapter, the onset of this signal is investigated, by exploiting high-resolution single color measurements at 1.5 eV, in a wide temperature range.

I leave to the next chapter the section devoted to the finding of the onset of the effect related to the fluence-dependence of the Glue Function $\Pi(\Omega)$, related to the first peak intensity (I_1) modification, sice the results provide clue information for the formulation of a phase diagram. As a concluding remark of this section, it must be emphasized that in the pseudogap phase, a peculiar mixture of different effects has been observed, having different origin and properties. This observation is of paramount importance for reconstructing the non-equilibrium phase diagram for copper oxide based high temperature superconductors.

7.5 Conclusions

Thanks to the combined spectral and temporal resolutions, I have been able to disentangle the physics underlying the pseudogap phase of an high temperature copper oxide based superconductor. Two important effects, respectively related to the impulsive quench of an energy gap present in the electronic density of states, and to the impulsive reduction of the intensity of one peak appearing in the bosonic glue, have been revealed, for an optimally doped sample. The negative $\Delta R/R(\omega,\tau)$ originating from the impulsive modification of the lowest-energy peak intensity in the glue function $\Pi(\Omega)$ is dominant in the underdoped side of the phase diagram. The scenario changes in the overdoped side of the phase diagram, as will be pointed out in the next chapter. It must be emphasized that in the pseudogap phase, the bosonic glue is no more fluence-independent, in contrast to what demonstrated in the normal state. Here, the fluence dependence of the bosonic glue in the pseudogap has been revealed. The most straightforward interpretation of this experimental evidence is that new bosonic modes are effective in this phase. This is compatible with the findings reported in [116, 180], where a ground state for the system in the pseudogap phase, governed by circulating orbital currents has been claimed. These bosonic modes could be the ones originating from the (magnetic) fluctuations of the system among the four degenerate ground states predicted by the model reported in [116, 180]. This picture is summarized in Fig. 7.13.

As a concluding remark, it must be emphasized that the temporal resolution is mandatory to disentangle the different effects in the pseudogap phase. By spectroscopic measurements at equilibrium, performed at different temperatures,

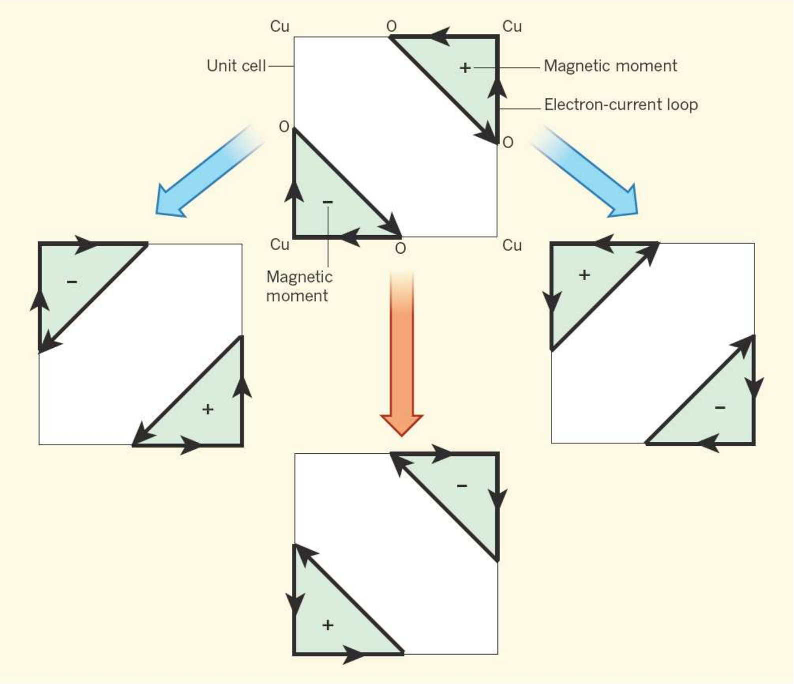

Figure 7.13: The loop-current electronic order is sketched. A copper-oxide based material with loop-current electronic order has four possible ground-state configurations. In each configuration, pairs of electron-current loops flow within each of the material unit cells, and produce a pair of oppositely directed magnetic moments (plus and minus symbols denote a magnetic moment with a direction that is perpendicular out of and into the plane of the page, respectively). If the material condenses into the top configuration, it can locally quantum-mechanically oscillate back and forth between it and the other three configurations. This gives rise to three possible collective modes of oscillation. From [180].

it is not possible to reveal such effects, since their contribution to the reflectivity variation is completely overwhelmed by the dependence of the optical properties on the temperature. The simulated reflectivity variation expected for an increase in the temperature of the system in equilibrium conditions is presented in Fig. 7.14. This signal has an intensity which is one order of magnitude higher than the contributions related to the gap filling and to the bosonic glue variation, over the same temperature range.

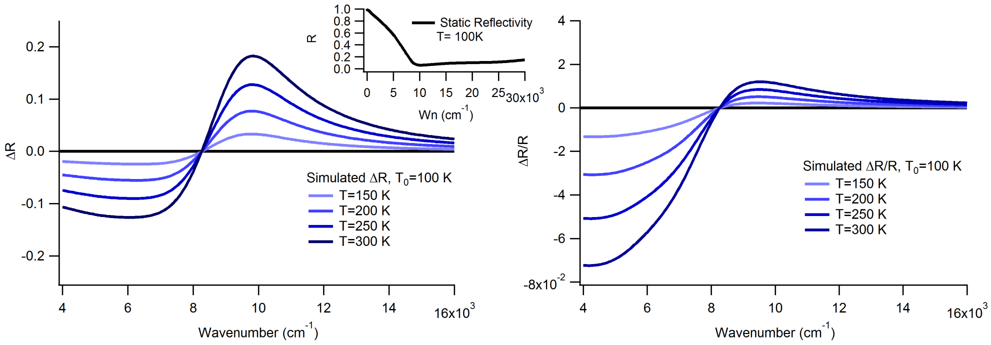

Figure 7.14: In the left plot, I calculate the difference in reflectivity obtained by heating the system, from T_0=100 K, to 150, 200, 250, 300 K. In the right plot, the ΔR/R arising from the same effect is calculated. In the inset, the static reflectivity for T_0=100 K is shown.

Chapter 8

The Phase Diagram from Non-Equilibrium Spectroscopy

8.1 Introduction

The aim of this final chapter is to summarize all the results of the novel time-resolved spectroscopy developed and used in this work. The response to an ultrashort excitation of the normal, pseudogap and superconducting phases of the copper-oxide high-temperature superconductor $Bi_2Sr_2Ca_{0.92}Y_{0.08}Cu_2O_{8+\delta}$, provides a new comprehensive picture of the phase diagram of this system. The chapter will start with the description of the non-equilibrium properties of the system in the superconducting state, that have not been presented yet. In contrast to what observed in the normal state and pseudogap phases, in the superconducting phase the transient optical response in the near-IR / visible spectral range can only be interpreted by assuming a pump-induced modification of the high-energy dielectric function. I demonstrate that two optical interband transitions at 1.5 and 2 eV are intimately related to the condensate formation at T_c. The long-standing debate about the interplay between high- and low-energy physics in these compounds, as a function of doping, is finally addressed. In the superconducting state, the optical response is strongly doping-dependent, with a clear crossover close to the optimal doping level required to attain the maximum critical temperature T_c for the BSCCO family. This crossover delimits two regions in which superconductivity is driven by an opposite mechanism: on the underdoped side of the phase diagram, superconductivity is driven by a direct kinetic energy gain (lowering), while on the overdoped side of the phase diagram, superconductivity is accompanied by a BCS-line kinetic energy loss, overcompensated by a gain in potential energy. In this context, the superconductivity-induced variation of the spectral weight of the interband transitions at 1.5 and 2 eV, fully accunts for the kynetic energy variation over the whole phase diagram.

This observation will be extremely helpful to the construction of a non-equilibrium phase diagram. The non-equilibrium p-T phase diagram we propose (non-equilibrium indicating the way in which it has been obtained) is characterized by a T^* line delineating a region in which the glue function is temperature-dependent. This line intersects the superconducting dome close to optimal doping, delimiting two p-T regions in which superconductivity is driven by a different mechanism. This non-equilibrium phase diagram strongly points towards a quantum critical point (QCP) within the superconducting dome, at T=0. Nevertheless, the signature of a gap is found above T_c, over the whole phase diagram. The onset of the gap is very broad in temperature, and follows a line tangent to the superconducting dome, in the overdoped region.

8.2 Time-resolved optical spectroscopy at T=20 K

In Fig. 8.1 the $\Delta R/R(\omega,\tau)$ plots collected at T=20 K on four Y-Bi2212 samples (an underdoped (UD, T_c=83 K, p=0.128), an optimally doped (OP, T_c=96 K, p=0.16) and two overdoped (OD, T_c=86 K for p=0.197 and T_c=83 K for p=0.2)) are reported. The pump fluence is kept at the low level of 10 μJ/cm^2, to avoid the complete vaporization of the superconducting condensate [81, 42] when photoexciting the system.

The measured $\Delta R/R(\omega,\tau)$ signal shows many peculiar features. The reflectivity variation is about one order of magnitude more intense than the one observed in the normal state and pseudogap phases. The decay time of the $\Delta R/R(\omega,\tau)$ signal slows down to about one picosecond. Finally, the $\Delta R/R(\omega,\tau)$ spectroscopic signal is strongly doping-dependent, with rich and complex spectral features. The right plots of Fig. 8.1, reporting the signals in the energy domain, obtained by vertically-cutting the $\Delta R/R(\omega,\tau)$ plots at τ=400 fs pump-probe delay, clearly show the doping dependence of the signal. I choose to consider a pump-probe delay τ equal to 400 fs, since the maximum signal variation is detected. In Fig. 8.2, the results from a number of samples are compared.

The slowing down of the temporal dynamics of the time-resolved optical signal in the superconducting phase ($T<T_c$) has been observed in many experimental works [97, 53, 98, 164, 79, 77, 117], and it is explained within the Rothwarf-Taylor model, accurately described in section 4.2. The sudden slowing down of the temporal dynamics for $T<T_c$ is due to a bottleneck effect originating from the quasiequilibrium between the population of excited quasiparticles and of high-frequency bosons (having energy $>2\Delta$), when the superconducting gap 2Δ is opened.

The signal at 1.55 eV probe energy, in the time domain, extracted by the $\Delta R/R(\omega,\tau)$ plots (not shown), perfectly reproduces the results obtained by the one color pump-probe measurements reported in the literature [78, 117],

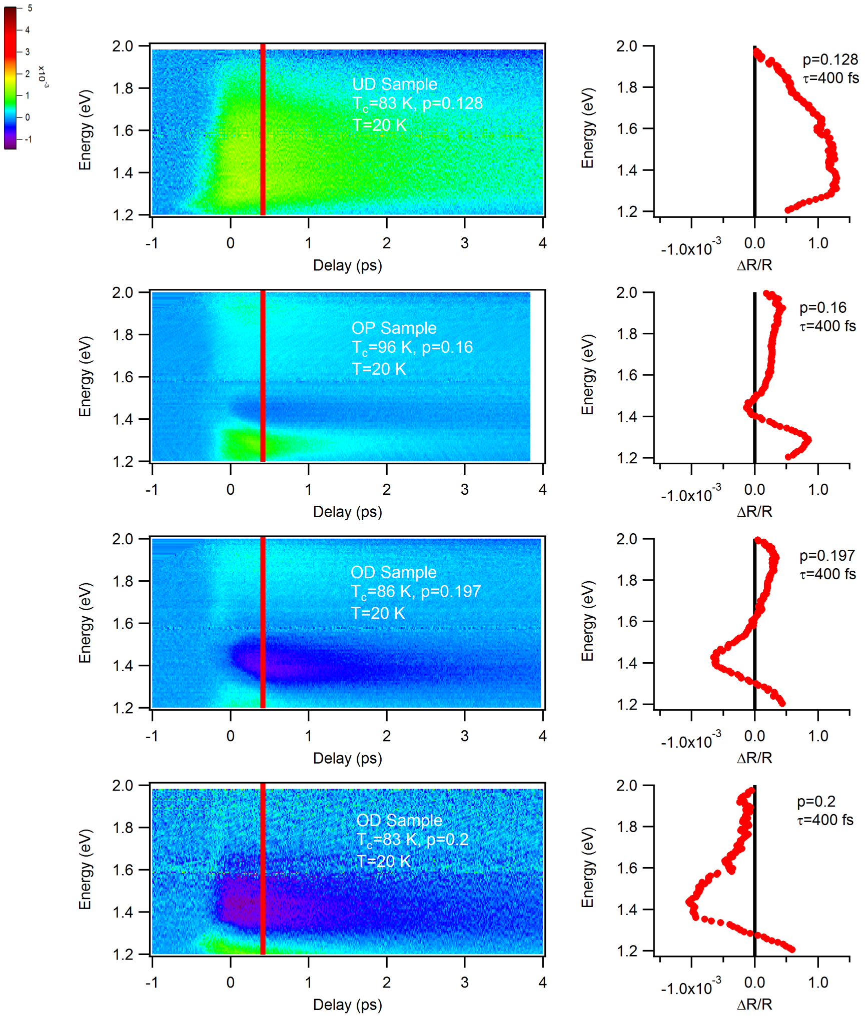

Figure 8.1: The temporally and spectrally resolved plots for the transient reflectivity $\Delta R/R(\omega,\tau)$ in the superconducting state (T=20 K) of $Bi_2Sr_2Y_{0.08}Ca_{0.92}Cu_2O_{8+\delta}$ are here reported for four doping levels: p=0.128 (UD sample), p=0.16 (OP sample), p=0.197 (OD sample), p=0.2 (OD sample). The 800 nm, 1.55 eV signal is in agreement with measurements performed with one-color probe. The cuts (evidenced in red) at τ=400 fs pump-probe delay are reported in the right graphs, evidencing the spectral strucutre of the transient signal. The pump fluence is 10 μJ/cm^2.

for all doping levels. I also verified that the amplitude of the transient reflectivity signal at 3.14 eV probe energy (i.e., 400 nm) is negligible, by performing monochromatic pump-probe measurements with a second-harmonic probe beam. This information will be useful to correctly address the pump-induced spectral weight transfer.

To check that the phenomenology observed in the superconducting phase, and described so far, is independent from the excitation mechanism, I repeated the measurements with a 3.14 eV pump beam. No differences with respect to the

measurements reported in Fig. 8.1, performed with a 1.55 eV pump beam, emerged. This ensures what we observed is related to an intrinsic response of the superconducting phase, independent of the excitation mechanism.
In Fig. 8.2, I show the transient reflectivity spectra for a pump-probe delay equal to τ=400 fs, for a number of samples with different dopings. The traces for the samples with p=0.128 (UD sample), p=0.16 (OP$_1$ sample (red dots), the same sample which reslts are presented in Fig. 8.1), and p=0.197 (OD sample) will constitute the basis for our differential analysis.

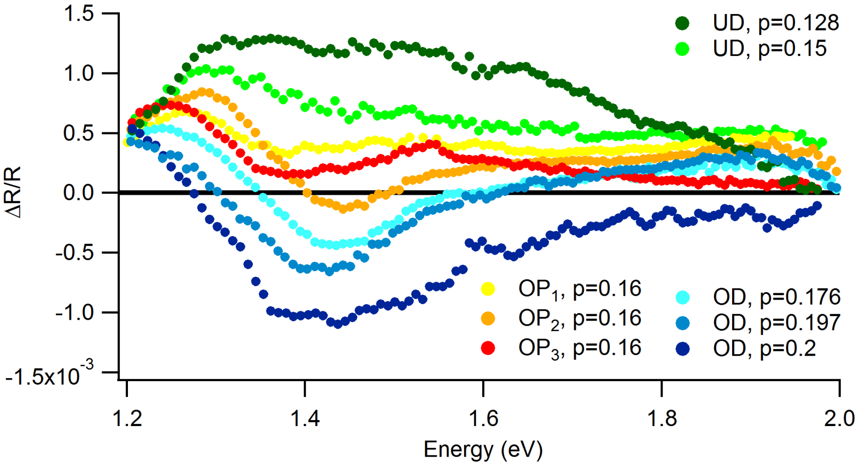

Figure 8.2: The spectrally resolved reflectivity traces at T=20 K, for a pump-probe delay equal to τ=400 fs and a pump fluence equal to 10 μJ/cm^2, are reported here for a number of different samples. While OP samples OP$_1$, OP$_2$, OP$_3$ have the same nominal doping (p=0.16), sample OP$_3$ has been exposed to air for a longer time, resulting in a slight increase of the Oxygen content.

By directly comparing the $\Delta R/R(\omega,\tau)$ cuts at τ=400 fs pump-probe delay, the evolution of the spectroscopic signal with doping can be argued. By increasing the doping level, the all-positive reflectivity variation characterizing the underdoped sample is gradually modified by a suppression of the signal around 1.4 eV, which eventually evolves into a negative feature in the 1.1-1.5 eV energy range for the overdoped sample.

8.3 Transient reflectivity in the superconducting phase

In this paragraph I present the results of the fitting of the differential dielectric function model (described in 4.4) to the $\Delta R/R(\omega,\tau)$ traces at fixed pump-probe delays, for the UD (p=0.128), OP$_1$ (p=0.16) and OD (p=0.197) samples. Experimental data and the fitting results are presented in Fig. 8.3.
For all doping levels, the interpretation of the structured $\Delta R/R(\omega,\tau)$ in the

1.2-2 eV energy range, cannot be accounted for by only assuming a modification of the Extended Drude model parameters, as it happens in the normal state and in the pseudogap. On the contrary, I have been able to account for the structured variation of the reflectivity at high energies by only assuming a modification of the first two interband oscillators, at 11800 cm−1 (1.46 eV) and 16163 cm−1 (2 eV), of the material dielectric function (the six oscillators used to reproduce the high-energy part of the material dielectric function are listed in section 3.7.3). The signals measured in the superconducting phase are the fingerprint of a genuine modification of the dielectric function as excitations are photo-injected, well beyond a simple broadening of the Drude function. The fits to the data automatically satisfy the KramersKronig relations, because they are obtained as a difference between KramersKronig-constrained Lorentz oscillators. The conservation of the total spectral weight is guaranteed by the constraint that the sum of the squared plasma frequencies of the Extended Drude model ($\omega^2_{p,0}$) and of the interband oscillators ($\omega^2_{p,1}$, $\omega^2_{p,2}$) is the same (i.e., $\omega^2_{p,0}+\omega^2_{p,1}+\omega^2_{p,2}$=const) in both the static and the excited dielectric function (the spectral weight of a Drude or Lorentz oscillator being dependent only on its squared plasma frequency), as the FGT sum rule requires. Table 8.1 reports the parameters modified in the non-equilibrium dielectric function to obtain the best fit to the data (only for the OP$_1$ sample and for τ=400 fs), reported in Fig. 8.3.

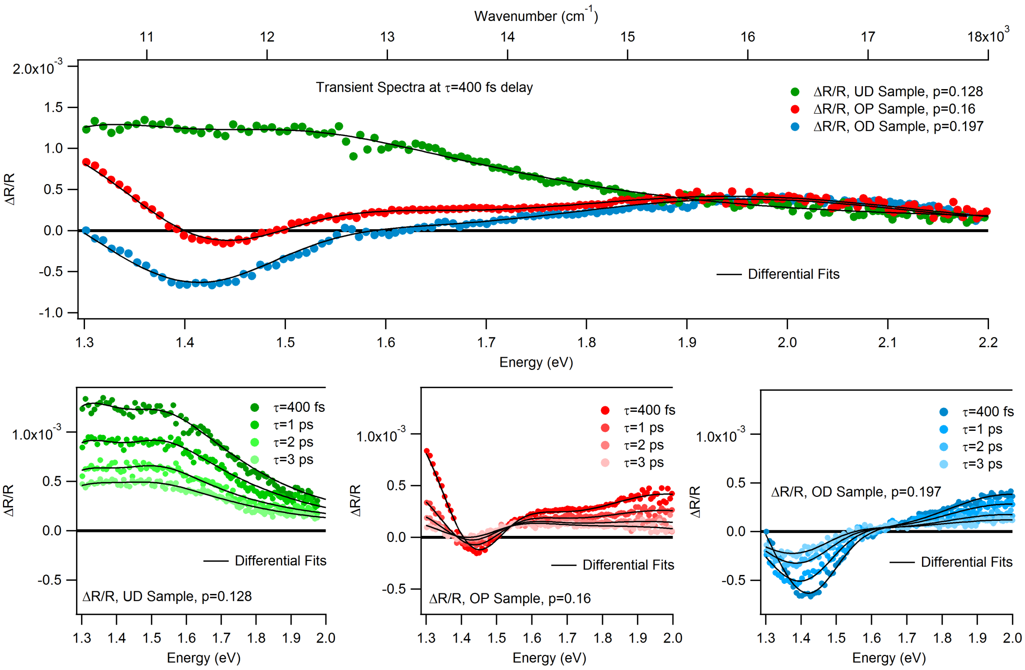

Figure 8.3: The main plot shows the fitting results to the τ=400 fs traces for the UD, OP, OD samples. Below, the fit to the τ=400, τ=1 ps, τ=2 ps, τ=3 ps pump-probe delay traces is reported singularly for the three samples.

Table 8.1: Fitting results for the OP sample, at T=20 K, at τ=400 fs pump-probe delay

Quantity	Static	τ=400 fs
T	20 K	38.8 K
ω_{01}	11800 cm^{-1}	11799 cm^{-1}
ω_{p_1}	2358 cm^{-1}	2383 cm^{-1}
γ_1	3644 cm^{-1}	3698 cm^{-1}
ω_{02}	16163 cm^{-1}	16176 cm^{-1}
ω_{p_2}	6385 cm^{-1}	6372 cm^{-1}
γ_2	8304 cm^{-1}	8283 cm^{-1}

Beyond the effect related to the modification of the high-energy oscillators, I include in the fit the thermal heating of the system associated to the extra energy deposited by the pump pulse in the system. The increase in the system temperature has been calculated by considering the 4TM, with the same Glue Function, subsets and coupling strengths argued by the analysis carried on on the normal state phase data. Because of the smaller specific heats of the system (both electronic and total) at T=20 K, the increase in temperature is much higher than in the pseudogap or in the normal state. We estimated it to be 38.8 K, for the OP$_1$ sample at τ=400 fs. I underline that this effect does not affect the total spectral weight.
The results of the differential fitting procedure are very stable on the choice of the equilibrium dielectric function (our best fit to equilibrium data is reported in 3.7.3). Indeed, the same results are obtained assuming a different equilibrium dielectric function (for example with a different number of interband oscillators or a different glue function). For this reason, the equilibrium dielectric function used can be considered as a ”realistic” dielectric function, even if, possibly, not the best dielectric function one can get (since the procedure to obtain it is often questionable).

The fits are employed to calculate the relative variation of the optical conductivity $\Delta\sigma_1(\omega)/\sigma_1(\omega)$, reported in Fig. 8.4. The trend from positive $\Delta\sigma_1(\omega)/\sigma_1(\omega)$ in the underdoped to a slightly negative $\Delta\sigma_1(\omega)/\sigma_1(\omega)$ in the overdoped samples reveals that the interband spectral weight variation, defined by $\Delta SW_{tot} \equiv \Delta\omega_{p,1}^2/8 + \Delta\omega_{p,2}^2/8$ (see section 3.6), being $\omega_{p,1}^2$ and $\omega_{p,2}^2$ the squared plasma frequencies of the 1.46 and 2 eV oscillators, strongly depends on the doping. I remember that, at higher probe energies (3.14 eV), a negligible $\Delta R/R(\omega,\tau)$ value for OP$_1$ is observed, confirming that the interband transitions at energies larger than 2 eV are not significantly affected by the suppression of the superconducting gap.

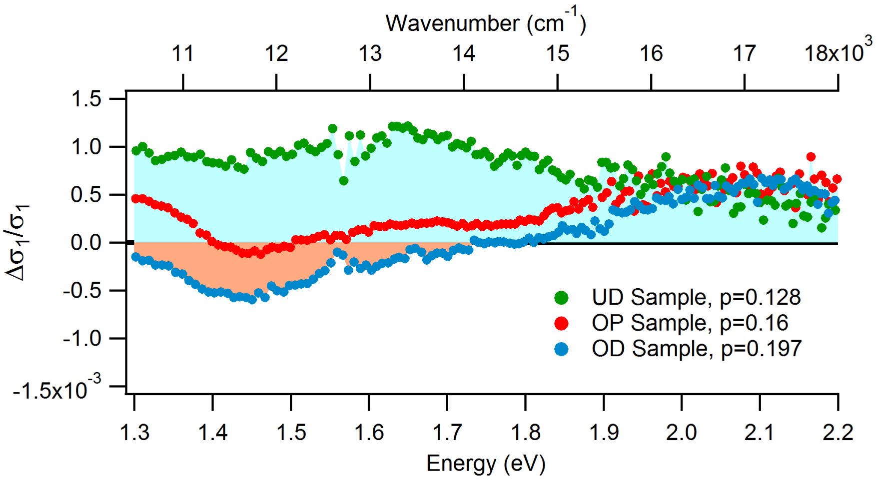

Figure 8.4: The quantity $\Delta\sigma_1(\omega)/\sigma_1(\omega)$ has been calculated and reported for the three samples, for the τ=400 fs situation. The relative spectral weight transfer to/from the intraband spectral region is proportional to the integral of the shadowed area.

Discussion of the results

In the simple energy-gap model for conventional (BCS) superconductors [60, 57], small changes of the interband transitions, over a narrow frequency range of the order of $\omega_{0,i} \pm \Delta_{SC}/\hbar$ can arise from the opening of the superconducting gap at the Fermi Energy. In contrast to this model, the partial suppression of $2\Delta_{SC}$, photoinduced by the pump pulse, induces a change of the optical properties over a spectral range (~1 eV) which is significantly broader than $2\Delta_{SC}$<80 meV [187]. This result reveals a dramatic superconductivity-induced modification of the Copper-Oxygen electronic excitations at 1.5 and 2 eV.
The photoinduced modification of ΔSW_{tot} vanishes as T_c is approached from below, demonstrating that this effect is exclusively related to the impulsive partial suppression of $2\Delta_{SC}$. This is shown in Fig. 8.5 for the OP$_1$ sample.

A further evidence of the direct relation between $2\Delta_{SC}$ and ΔSW_{tot} is obtained by comparing the results obtained with the visible probe with the results of time-resolved experiments with probe energy in the mid-infrared [102] and THz [99, 12] regions. The findings reported therein directly show a recovery time of the superconducting gap and condensate ranging from 2 to 8 ps, for different families of cuprates, temperatures and pump fluences. From our results, the temporal dynamics of ΔSW_{tot}, reported in Fig. 8.6 for UD, OP$_1$ and OD samples, is nearly exponential with a time constant $\tilde{\tau}$=2.5±0.5 ps. The ΔSW_{tot} variation is completely washed out at longer times (τ>5 ps), when the complete electron-boson thermalization broadens the Drude peak, overwhelming the contribution of ΔSW_{tot}. The correspondence between the timescales observed in the mid-IR and THz spectral regions and the recovery time of ΔSW_{tot} finally demonstrates the interplay between the excitations at 1.5 and

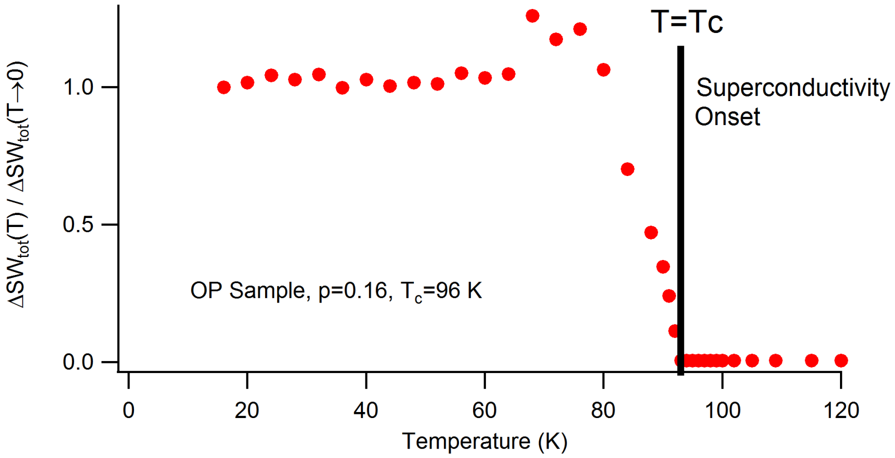

Figure 8.5: The pump-induced modification of the spectral weight is a phenomenon related to the onset of the superconducting state. This result, here reported for the OP sample, is common to all doping levels. The interplay between high and low energy scale physics is thus effective only in the superconducting phase. No spectral weght transfer have indeed been revealed either in the normal state, or in the pseudogap phase.

2 eV and the superconducting gap $2\Delta_{SC}$.
For completeness, I report briefly on the results obtained for the energy gap $2\Delta_{SC}(\tau)$ temporal evolution (being τ the pump-probe delay), calculated within a time-dependent Rothwarf-Taylor model. More details can be found in [42]. The minimum value for $2\Delta_{SC}(\tau)$ with respect to the unperturbed gap $\Delta(0)$, which indicates the maximum gap closing, is achieved 400 fs after excitation, when the gap amplitude is 80% of the maximum. This justifies our choice of performing the data analysis on a spectrum measured at a pump-probe delay τ=400 fs, when the effect related to the superconducting condensate quench is expected to be maximum. It has to be pointed out that the gap suppression and the density of broken CP are not in a linear relation. The evolution of the measured total interband spectral weight variation ΔSW_{tot} shows a clear proportionality with the gap closing calculated within this model, i.e., with the quenching strenght of the superconducting consensate induced by the pump pulse. ΔSW_{tot} and $2\Delta_{SC}(\tau)/2\Delta_{SC}(\tau < 0)$ are compared in Fig. 8.6.

Concluding remarks

The results of the analysis I described in this paragraph shed light on one of the unsolved problems of high-temperature superconductivity, and namely, whether and how the electronic many-body excitations at high-energy scales are involved in the condensate formation in the under- and over-doped regions of the superconducting dome. I remember that within the BCS theory for con-

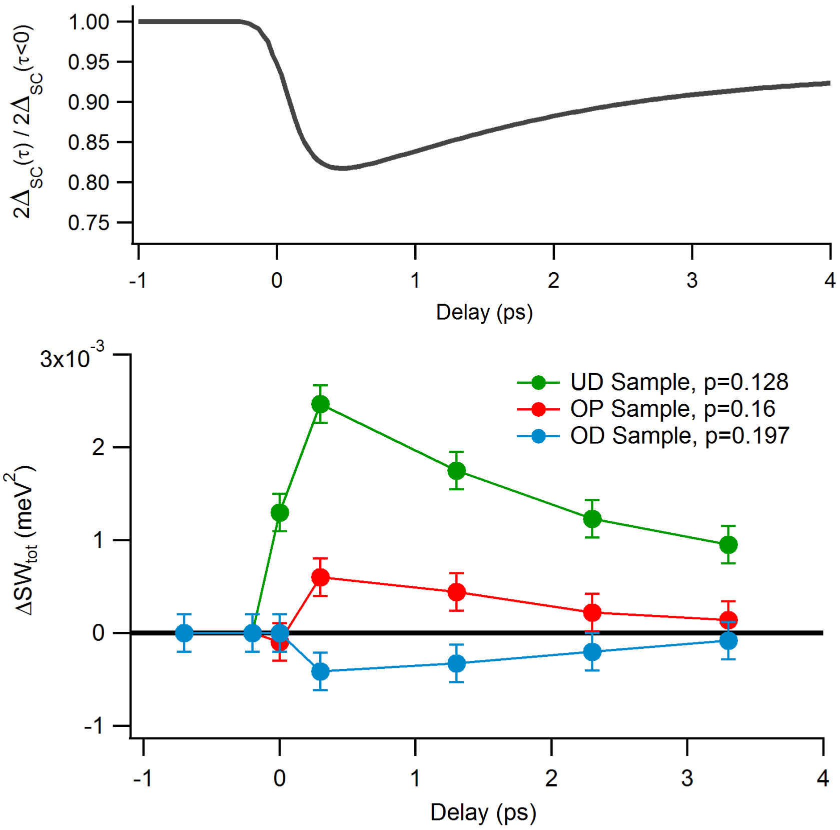

Figure 8.6: The pump-induced spectral weight change ΔSW_{tot} as a function of pump-probe delay τ, for the three samples, follows the temporal evolution of the superconducting gap, calculated within a time-dependent Rothwarf-Taylor model [42].

ventional superconductors, the opening of the superconducting gap induces a significant rearrangement of the quasiparticle excitation spectrum only over an energy range of $\sim 10\Delta$. Here I demonstrated that on HTSC, the picture is considerably different: an interplay between many-body electronic excitations at 1.5 and 2 eV and the onset of superconductivity, both below and above the optimal hole concentration required to attain the maximum T_c, has been addressed, for all doping levels.

Recently, equilibrium techniques revealed a superconductivity-induced modification of the CuO_2 plane optical properties involving energy scales in excess of 1 eV [88, 157, 131, 22, 160, 112]. These results suggested a possible superconductivity-induced gain in the in-plane kinetic-energy on the underdoped side of the phase diagram [123, 71, 26]. However, the identification of the high-energy electronic excitations involved in the onset of high-temperature superconductivity (HTSC) remained elusive, since they overlap in energy with the temperature-dependent narrowing of the Drude-like peak.

The temporal-resolution provided by our non-equilibrium spectroscopy allowed to disentangle the ultrafast modifications of the high-energy spectral weight ($\Delta SW_{tot} \equiv \Delta\omega_{p,1}^2/8 + \Delta\omega_{p,2}^2/8$) from the slower broadening of the Drude-like peak induced by the complete electron-boson thermalization. Time-resolved optical spectroscopy is thus one the most promising experimental techniques to be used as a benchmark for unconventional models of HTSC.

Finally, these results shed light on the long-standing question [77, 52] about the origin of the doping- and temperature-dependent $\Delta R/R(\hbar\omega = 1.55eV, \tau)$ measured in one-colour time-resolved reflectivity experiments at high probe-energies [78, 117]. The measured signal is not originated by an excited state absorption, related to the variation of the electronic distribution within the unvaried electronic bands, but to a real modification of the underlying electronic structure, and in particular, of the interband transitions at 1.5-2 eV. Nonetheless, the measured $\Delta R/R(\omega, \tau)$ is proportional to the density of photo-injected quasiparticles, as commonly assumed [111]. The dynamics of $2\Delta_{SC}(\tau)$ can thus be reconstructed exploiting the $\Delta R/R(\omega, \tau)$ signal measured in the visible / near-IR spectral range.

8.4 Discontinuity of the dynamics at optimal doping

In this paragraph, the change in the high-energy spectral weight determined by the fitting procedure described in the previous section, will be related to the superconductivity-induced change in the carriers kinetic energy, in a few simple steps I will sketch below. Fundamental information about the mechanisms leading to superconductivity will be argued. This will provide us fundamental information in the attempt to formulate a 'non-equilibrium' phase diagram.
The conservation of the total spectral weight, imposed by the global oscillator strength sum rule (see section 3.6), implies that: $SW_D^N + SW_L^N = SW_D^{SC} + SW_L^{SC}$, where the subscripts D and L indicate respectively the spectral weight of the intraband and interband regions, and the superscripts N, SC indicate respectively the spectral weigth in the normal and superconducting phases. Here SW_D^{SC} includes the contribution of the zero-frequency delta describing the condensate contribution to the spectral weight.
The total interband spectral weigth is given by (for either $j = N$ or $j = SC$, and being $(\sigma_{L,i}(\omega))^j$ the optical conductivity of the i-th Lorentz oscillator in the phase j):

$$SW_L^j \equiv \sum_i \int_0^\infty (\sigma_{L,i}(\omega))^j d\omega$$

Similarly, for the intraband part, it holds:

$$SW_D^j \equiv (1/4\pi i) \int_0^\infty \omega(\epsilon_D(\omega))^j d\omega$$

For the conservation of the total spectral weight, the spectral weight change of the intraband region must be compensated by an equal but opposite change of the spectral weight of the interband transitions. Moreover, since I did not observe a superconductivity-induced modification of the high-energy oscillators, except the 1.5 and 2 eV ones, the following equalities hold (see also formula 3.26):

$$\Delta SW_D = -\Delta SW_L = -\Delta\omega_{p,1}^2/8 - \Delta\omega_{p,2}^2/8$$

Where the 'Δ's I defined in this chapter follow in a natural way by considering the effect of the laser excitation on the system held in the superconducting phase, i.e., the partial suppression of the superconducting condensate. Since $\Delta R/R(\omega,\tau) \equiv \frac{R_{pumped}(\omega,\tau)-R_{unpumped}(\omega)}{R_{unpumped}(\omega)}$, it results: $\Delta\omega_p^2 \equiv \omega_{p,pumped}^2 - \omega_{p,unpumped}^2$ and $\Delta SW_L = SW_L^N - SW_L^{SC}$. Since I want to estimate the superconductivity-induced spectral weigth change instead ($N \to SC$), the correct quantity to consider is $-\Delta SW_D = +\Delta SW_L$.

In the special case of a single conduction band within the nearest-neighbour tight-binding model [86, 139], the total intraband spectral weight SW_D can be related to the kinetic energy T_δ of the charge carriers (holes) associated to an hopping process in the δ direction, through the relation [86]:

$$\frac{1}{4\pi i}\int_0^\infty \omega\epsilon_D(\omega)d\omega = \frac{\pi^2 a_\delta^2 e^2}{2\hbar^2 V_{Cu}}\left\langle -T_\delta\right\rangle$$

where a_δ is the lattice spacing in the Cu-O plane, projected along the direction determined by the in-plane polarization of the incident light, and V_{Cu} is the volume per Cu atom. I obtain $\langle K\rangle = 2\langle T_\delta\rangle$ from the spectral weight variation of the interband oscillators, through the relation:

$$\langle K\rangle = 2\langle T_\delta\rangle = \frac{4\hbar^2 V_{Cu}}{\pi^2 a_\delta^2 e^2}\Delta SW_L$$

A finite value of ΔSW_L thus implies a superconductivity-induced variation of the kinetic energy.

To extract quantitative information about the actual superconductivity-induced kinetic energy change, the values obtained for the kinetic energy change related to a pump fluence of 10 μJ/cm^2, must be extrapolated to the case of a complete thermal collapse of the superconductive state (100% gap closing). In non-equilibrium conditions, the collapse of the superconducting state happens for a finite value of the superconductive gap 2Δ, since the photoinduced phase transition has a first order character, as predicted by the μ_{eff} model [143, 136], and clearly demonstrated in [42, 81]. The intuitive reason for this being the intrinsic non-equilibrium character of the photoinduced phase transition, which cannot be interpreted within equilibrium models, according to which the phase transition happens only for a complete collapse of the superconducting gap 2Δ.

I thus estimated the actual density of broken CP (related to an incident fluence of 10 μJ/cm^2) starting from the knowledge of the critical CP density at which

the superconductive state collapses. This happens, accordingly to our measurements, for a pump fluence of 60 μJ/cm^2 [42, 81]. The measured kinetic energy change can then be extrapolated to the superconductivity induced change for 100% CP breaking. The critical broken CP density (in non-equilibrium conditions) making the superconductive state collapse, accordingly to [136], is in the range 15-20%. At our typical pump fluence of 10 μJ/cm^2, the density of broken CP is thus $\sim$ 3%. The total, superconductivity induced kinetic energy change will be $\sim$33.3 times the one I estimated from the measured change of spectral weight.
Considering V_{Cu}=$V_{unit-cell}/8$ $\sim$1.1$\cdot$10^{-22} cm^3 and $a_\delta = a_{unit-cell}/\sqrt{2}$ $\sim$3.9 Å, I obtain that the kinetic energy can be calculated as $\langle K \rangle = 8\hbar^2 \Delta SW_L$$\cdot$(83.3 meV/eV^2), where $8\hbar^2 \Delta SW_L$ is the total interband spectral weight variation expressed in eV^2. To obtain the total kinetic energy variation related to the condensate formation, the measured $\Delta SW_L = \Delta SW_{tot}$ value has been extrapolated to the value corresponding to the breaking of 100% of the Cooper Pairs, being $\sim$3% the actual estimated photo-induced breaking of CPs.

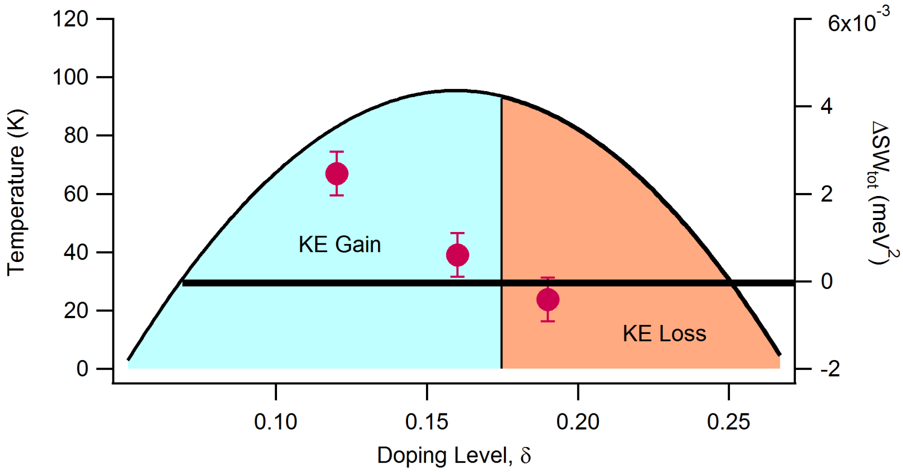

Figure 8.7: The maximum change in the spectral weight (measured for a pump-probe delay equal to τ=400 fs) is reported for the three samples. A clear evolution with the doping level is observed: a scenario in which superconductivity is driven by a direct kinetic energy gain for the charge carriers evolves toward a BCS-like scenario in which superconductivity is accompained by a kinetic energy loss for charge carriers. Error bars take into account the stability of the differential fit over a diffrent choice of the equiibrium dielectric function.

For the UD sample, I estimated a superconductivity-induced kinetic energy decrease of $\sim$1-2 meV per Cu atom. This value is very close to the superconductivity-induced kinetic energy gain predicted by several unconventional models [86, 139].

Concluding remarks

Exploiting the temporal resolution of the novel pump supercontinuum-probe optical spectroscopy, I unambiguously demonstrated that in Y-Bi2212, the superconductive transition is strongly unconventional both in the under- and in the over-doped side of the superconducting dome, since it involves the modification of high-energy states at 1.5 and 2 eV. This has profound implications for the comprehension of the actual phase diagram of copper-oxyde based high-temperature superconductors. Indeed, the sign change of ΔSW_L upon crossing the optimal doping concentration p_{opt} affects the superconductivity-induced change in the carriers kinetic-energy. In particular, when moving from below to above the optimal hole doping p_{opt}, the spectral weight variation ΔSW_L of the high-energy oscillators entirely accounts for a crossover from a superconductivity-induced gain (reduction) to a BCS-like loss (increase, which must be overcompensated by a gain in potential energy of the carriers for the superconductivity to occur) of the carrier kinetic energy, estimated by equilibrium optical spectroscopies directly measuring the low-energy optical properties [175, 131, 123, 71, 26], or by one-color time-resolved reflectivity measurements [78]. This opposite behavior has implications on the mechanisms leading to superconductivity in copper oxide based superconductors, which could be different in different regions of the superconductive dome. While on the overdoped side, BCS-like mechanisms are likely to occur, on the underdoped side other mechanisms must be invoked. In the 1990s, Hirsch and Marsiglio [85, 86, 124] proposed a model, called 'hole superconductivity', which predicts the charge carriers (holes) can directly lower their kinetic energy when paired. In this model the pairing is expected between oxygen holes, with an asymmetric behavior for electrons and holes near the Fermi Energy. Below a critical temperature related to a critical hole density, the model predicts the development of an attractive interaction between nearest neighbor holes with antiparallel spin. Two coupled holes reduce their effective mass and can delocalize more efficiently, thus reducing their kinetic energy.

8.5 Onset of the signal from the temperature dependent glue function

In the previous chapter (see section 7.4) it has been demonstrated that the negative $\Delta R/R(\omega,\tau)$ component measured at T=100 K in the visible spectral range is the fingerprint of an excitation dependence of the bosonic glue, characterizing the pseudogap phase. In particular, I demonstrated this signal being successfully reproduced invoking a temperature induced modification of the intensity of the lowest energy peak of the Bosonic Glue $\Pi(\Omega)$, I_1. To address the evolution of the pseudogap phase as a function of the temperature, high-resolution single-color time-resolved reflectivity measurements have been performed on under-doped, optimally doped and over-doped samples, at a probe energy of 1.55 eV (λ=800 nm).

In Fig. 7.8 I present a temperature scan (the temperature range 100-300 K is explored with more than 25 measurements) performed at very low pump fluence ($\sim$4 μJ/cm^2), on the UD, OP and OD samples. The transient reflectivity measurements are offsetted to make the picture more clear.

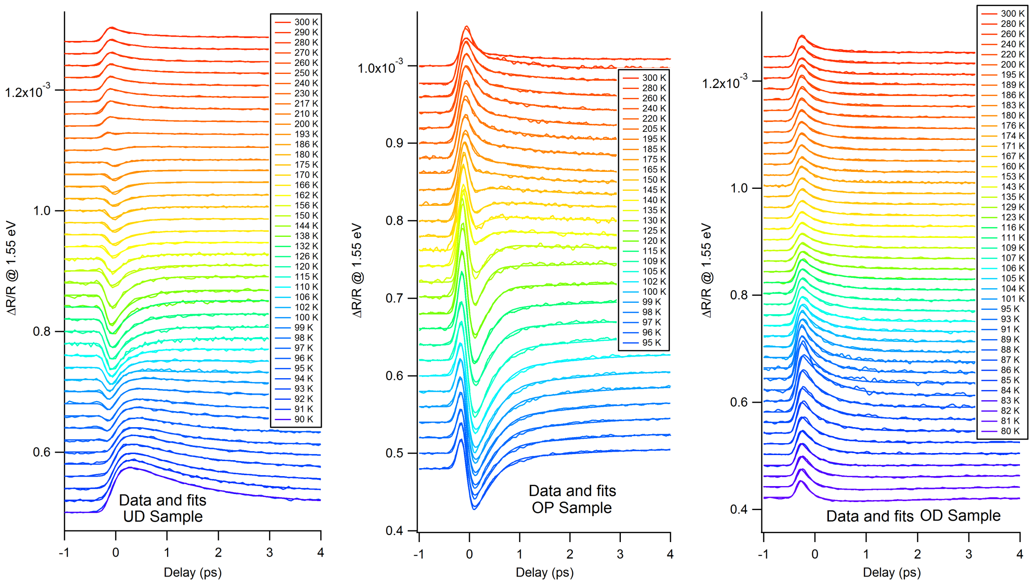

Figure 8.8: The temperature scans in a wide range of temperatures, performed at a fixed probe wavelenght of 1.55 eV, 800 nm, on an underdoped (p=0.128), an optimally doped (p=0.16) and an overdoped sample (p=0.2) are reported. The fit to the time resolved reflectivity traces are superimposed to the experimental data.

To extract quantitatively the temperature onset of the negative signal, I perform a multicomponent fit to the time resolved traces. The fitting function $f(\tau)$ (equation 8.1) is given by the sum of three exponentially-decaying functions, and it is convoluted with a Gaussian profile representing the experimental pump-probe temporal cross-correlation (equal to 180 fs).

$$f(\tau) = I_1 \cdot e^{-\tau/\tau_1} + I_2 \cdot e^{-\tau/\tau_2} + I_3 \cdot e^{-\tau/\tau_3} \tag{8.1}$$

The three exponential decays represent respectively the fast and positive dynamics of the normal state phase, the fast and negative dynamics of the pseudogap phase, and a slow, positive or negative dynamics to catch the signal evolution at longer decay times. The fits are superimposed to the experimental data of Fig. 7.8. The intensity of the negative and fast component (I_2) is represented in Fig. 7.9 for the three samples. Error bars take into account the uncertainties in the fitting procedure.

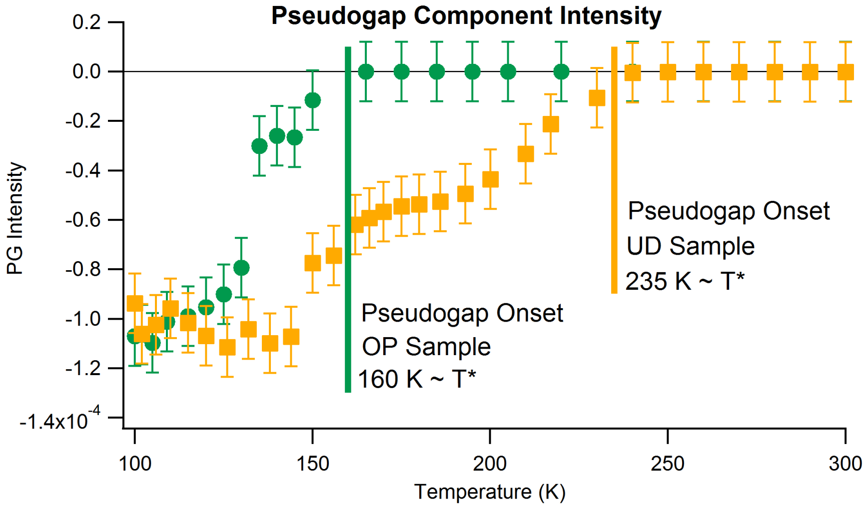

Figure 8.9: The intensity of the negative component I_2, extracted from the fit, is reported. The onset of the negative signal associated to an impulsive quench of the lowest-energy peak of the bosonic glue has been inferred from these data. Error bars take into account the fit uncertainty.

It is evident how the onset of this effect is rather narrow in temperature: 150 to 165 K for the OP sample, 230 to 240 K for the UD sample. Moreover, this onset temperature scales with doping. No negative component has been detected on the OD sample.

Summarizing, our findings clearly show that for UD and OP samples a negative component in the $\Delta R/R(\omega,\tau)$ appears at a temperature which is compatible with the material T^*. The onset of this effect is doping-dependent, and scales as T^* does. This negative component is absent in the OD sample. This negative component in the $\Delta R/R(\omega,\tau)$ has been successfully reproduced (see section 7.4) assuming that one peak in the material Bosonic Glue $\Pi(\Omega)$ depends on the excitation, that is, it is temperature dependent. Electron-Boson coupling is thus no-more temperature-independent in the pseudogap.
As I carefully stated in section 7.4, Li et al. [116] revealed, on the $HgBa_2CuO_{4+\delta}$ copper-oxyde based high-temperature superconductor, a collective magnetic mode of excitation (with energy in the range ~55 meV), which onset temperature shows a temperature evolution similar to that observed in our time-resolved optical data.
Our analysis indicates that the scenario of a temperature independent Glue Function must be overcame to correctly reproduce the experimentl results obtained in the pseudogap phase. Provided that the feature we observed in the bosonic glue is in a relation with the magnetic mode observed by Li et al. (as it is reasonable to assume), we can say that not only a new magnetic excitation mode appears at T^*, but it turns out that this peculiar mode is also

actively coupled to the electrons. This picture is compatible with a phase diagram governed by a quantum critical point. However, the crossing of the line of finite temperature phase transition (the critical line) should produce divergences in many physical quantities, which have not been yet observed. In conclusion, this magnetic excitation mode with energy of ∼55 meV constitutes an important point to be clearified for the comprehension of high temperature superconductivity in copper oxide based superconductors.

8.6 Overdoped side of the phase diagram

With this section I want to briefly discuss which is the scenario in the overdoped side of the phase diagram. To this aim, I collected in Fig. 8.10 the τ=0 spectra measured on several samples, at T=100 K. It is evident how, upon crossing the optimal doping level, the negative signal associated to an impulsive modification of the bosonic glue disappears. Further work is required to correctly interpret the origin of the $\Delta R/R(\omega,\tau)$ signal observed in the overdoped region of the phase diagram. Qualitatively, I can anticipate that the $\Delta R/R(\omega,\tau)$ arising from a thermal heating of the system, alone, is not sufficient to interpret the observed time-resolved signals. A spectral contribution arising from the gap closing (as described in section 7.4) must be invoked.

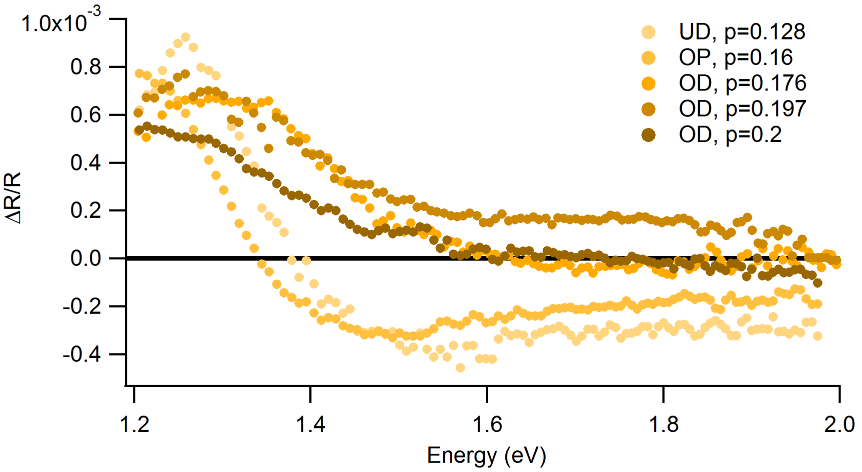

Figure 8.10: The spectrally resolved reflectivity traces in the pseudogap phase (T=100 K) of $Bi_2Sr_2Y_{0.08}Ca_{0.92}Cu_2O_{8+\delta}$ are collected here for five doping levels: p=0.128 (UD sample), p=0.16 (OP sample), p=0.176 (OD sample), p=0.197 (OD sample), p=0.2 (OD sample).

8.7 The Non-Equilibrium phase diagram

The experimental evidences I collected by probing with the time-resolved optical spectroscopy technique the normal state, the pseudogap and the superconducting state of underdoped, optimally-doped and overdoped samples, allowed me to formulate a phase diagram for the Y-Bi2212 copper-oxide based high-temperature supercondutor, based enterely on non-equilibrium evidences. That is, the phase diagram I propose is deducted by only analyzing how the time-resolved optical signal (with both energy (ω) and time (τ) resolutions) $\Delta R/R(\omega, \tau)$, induced by a non-perturbing, low-fluence excitation done by a pump-pulse, evolves in the p-T space.

The most important experimental evidence, coming from the analysis of the time-resolved optical signal in the pseudogap phase, is that it exists a line, at temperatures $T^*(p)$, which enters the superconducting dome, and which delimits a region of p-T space in the underdoped region in which the electron-boson coupling is temperature-dependent, in contrast to what happens in the normal state. The superconducting state is characterized by a non-conventional interplay between high-energy states (precisely at 1.5 and 2 eV) and the formation of the superconducting condensate. The behavior inside the superconducting dome is delimited by the T^* line in two regions, showing a different sign of the induced spectral weight transfer from low to high energy scales. In particular, while in the underdoped side of the superconducting dome, superconductivity is accompained by a direct kinetic energy gain of the carriers, in the overdoped side of the superconducting dome superconductivity is accompained by a BCS-like loss of kinetic energy. This crossover happens close to the optimal hole concentration p required to attain the maximum critical temperature T_c (0.16 for Y-Bi2212).

The rise of a collective magnetic excitation mode related to the onset temperature of the pseudogap, T^*, as recently demonstrated by Li et al. [116], suggests that the pseudogap is indeed a true phase of matter, characterized by a long-range order. Varma [180] proposed this mode to be associated to a current-loop order, being the ground state of the pseudogap phase.

I observed that below the T^* temperature, the Glue Function $\Pi(\Omega)$ acquires a fluence-dependence, affecting a low-energy peak intensity. This fluence-dependence is responsible for the negative $\Delta R/R(\omega, \tau)$ signal in the visible spectral region, which is commonly associated to the pseudogap. Not only this finding confirms that a new mode rises at the temperature corresponding to the onset of the pseudogap phase, but it adds a fundamental ingredient, that is, this mode is coupled to the electrons.

This latter observation opens fundamental questions about the possible interplay between the superconductivity and the pseudogap in copper-oxyde based high-temperature superconductors.

The T^* line entering the superconducting dome suggests the phase diagram in governed by a quantum critical point within the superconducting dome, at T=0, as it is predicted by the theories predicting a circulating-current magnetic order [95].

The phase diagram I propose is sketched in Fig. 8.11.

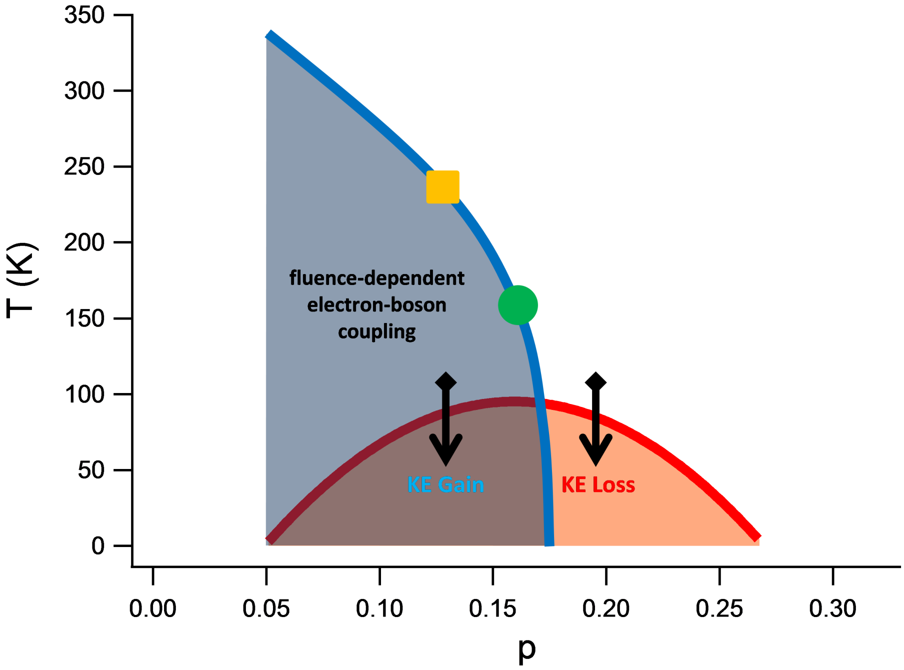

Figure 8.11: The phase diagram I propose, based enterely on the non-equilibrium evidences from the time-resolved optical spectroscopy, is sketched. Red line delimits the superconducting dome. Blue line is the T^{*} line, related to the onset of the pseudogap. This line delimits a region in which the electron-boson coupling is fluence-dependent. The yellow square and the green dot represent respectively the onset temperature of the fluence-dependence of the electron-boson coupling, for the p=0.128 (UD) and the p=0.16 (OP) samples. Entering the superconducting dome, superconductivity is accompained by a doping-dependent change of the carriers kinetic energy, that changes sign close to the optimal doping concentration.

Chapter 9

Conclusions

My PhD work started with the task of developing and setting up novel time-resolved spectroscopies, with the idea that only the knowledge of the non-equilibrium optical response of complex materials, in a wide range of energies, could lead to a true comprehension of the physics at the microscopic level, originating the non-equilibrium optical signal. We brought a fundamental contribution to this nascent field, actively developing the basis for this approach, which is nowadays achieving great success and is quickly spreading around the time resolved scientific community. Many difficulties had to be overcome, mainly related to the need to obtain a very high sensitivity for the measurements, related to the fact that phases of matter which 'vaporizes' at very low fluence levels had to be investigated. This is the peculiarity of our approach: the systems under study are only gently brought out-of-equilibrium by laser excitation. In this respect we call our technique time-resolved spectroscopy, since a true spectroscopic analysis of the phase can be achieved only when the phase itself is not 'vaporized'. Temporal resolution allowed to reveal the characteristic non-equilibrium optical response to a small perturbation of the phase, which strongly depends on the ground state of the system.
In the specific, I developed two complementary experimental set-ups. The first exploits a broadband, supercontinuum white light pulse as probe pulse. The spectral range that can be probed by this setup is 1.2-2.5 eV (i.e., 500-1000 nm). The supercontinuum pulse employed in this set-up is generated by a photonic crystal fiber, which is seeded by a cavity-dumped Ti:Sapphire oscillator. This allowed to obtain very high signal-to-noise ratios, thanks to the high statistic due to the high repetition rate of the source. The drawback has been that the temporal structure of pulses produced in this way presents a pronounced chirp, and this lead us to the development of several characterization techniques to measure the spectro-temporal structure of this pulse, and correct measurements accordingly. The second setup is developed around an optical parametric amplifier, seeded by a regenerative amplified laser system. The probe pulse of this setup is a quasi-monochromatic but widely tunable infrared pulse, obtained as the signal and idler output of the parametric amplifier. This

technique allowed us to extend the probed spectral range toward the infrared, covering the spectral region 0.5-1 eV (i.e., 1200-2400 nm). The two set-ups developed, together with a brief review of the characterization techniques, are presented in chapter 5. After some years these systems have been working, it is possible to say that time and spectral resolved measurements constitute a fundamental improvement over the conventional one color, monochromatic optical pump-probe techniques. Up to now, the lack of spectral resolution prevented to achieve a true comprehension of the physical origin of the observed optical signals. Other improvements can be done to the technique, mainly related to the extension of the probed spectral range. For the systems studied in this work, the infrared part of the spectrum revealed of greater relevance as compared to the ultraviolet one. Extending the probed spectral range toward the infrared is however not simple, because of the actual lack of broadband sources, except for the THz range. Also the achievement of even better signal-to-noise ratios is important, to perform measurements more quickly, thus opening the way to follow the signal evolution in time. This would be extremely useful to map for example the evolution of chemical reactions from the non-equilibrium point of view. In the field of strongly correlated electron systems (transition metal oxides, copper and iron based superconductors) or other complex materials (manganites, ruthenates), time-resolved spectroscopy is one of the most promising techniques to provide new insights on the microscopic mechanisms underlying the phases of these materials and new benchmarks for the non-equilibrium theories which are being developed.

With regard to my research, this novel powerful technique allowed to clarify some open questions about the physics of copper oxide based high temperature superconductors. The sample chosen is the two-layer member of the Yttrium substituted BSCCO family, that is, $Bi_2Sr_2Ca_{0.92}Y_{0.08}Cu_2O_{8+\delta}$, where δ controls the doping level. We have samples with different doping, in such a way we could explore the evolution of the non-equilibrium optical signal in the δ-T phase diagram. The analysis and characterization - by the non-equilibrium spectroscopic point of view - of the phases composing the system phase diagram, allowed us to obtain the first all-optical non equilibrium phase diagram of a strongly-correlated electronic material. In particular, the normal state, the pseudogap and the superconducting state exhibited sensibly different time-resolved optical signals. These non-equilibrium spectrally resolved signals have been interpreted within a differential dielectric function approach (formulated and described in chapter 4), to assign a clear microscopic origin to the signal itself. When excited by an ultrashort laser pulse, each physical phase manifests a peculiar, intrinsic response, mainly due to the excitations produced by the pulse, which are meaningful in understanding the ground state of the phase. Each physical mechanism has its own spectral fingerprint, as it has been demonstrated with several simulations. Moreover, the temporal resolution revealed fundamental since it allows to disentangle the fast electronic processes from the slow, thermal (phonon related) ones. The thermal contribution often overwhelms the signal of electronic origin. This is the reason why equilibrium spectroscopy failed in evidencing the effects revealed by the non-equilibrium approach.

Briefly, what we found about the microscopic nature of the normal (Chapter 6), pseudogap (Chapter 7) and superconducting (Chapter 8) phases can be summarized as follows:

- The time-resolved optical signal measured by time-resolved spectroscopy in the normal state of Y-Bi2212, unambiguously revealed that, after a time shorter than the electron-phonon thermalization, the electrons are already thermalized with some bosonic degrees of freedom, having a small specific heat and a strong coupling with the electrons. This finding suggests that these bosonic excitations are of electronic origin. The time-resolved optical signal in the energy domain is only compatible with a quasi-thermal scenario, in which electrons are never decoupled from a boson subset. The simultaneous analysis of experimental data in both the time and the energy domains revealed that the subset of bosonic excitations of electronic origin can account, alone, for the high critical temperature of the material. This finding suggests that pairing in HTSC is mainly of electronic origin. Possible candidates for the bosons of electronic origin are antiferromagnetic spin flucutations or current loops. In the normal state, the Bosonic Glue $\Pi(\Omega)$ expressing electron-boson coupling is fluence-independent.

- In the pseudogap phase the transient reflectivity signal requires a more complicated explanation. It is doping dependent, in contrast to the normal state signal. A quasi-thermal scenario, alone, is not enough for explaining the observed signal. The further contributions which has to be invoked to correctly reproduce the time-resolved optical signal are the pump-induced impulsive quench of a gap in the electronic density of states, and the impulsive decrease of the intensity of one low-energy peak of the Bosonic Glue $\Pi(\Omega)$. The onset of this fluence-dependent contribution, which is responsible for the negative signal commonly associated to the presence of the pseudogap phase, is exactly at T^*. These experimental observations suggest that in the pseudogap phase one bosonic mode, rising exactly at T^*, is also coupled with the electron system. The pseudogap phase is thus a complex phase, in which the fermionic quasi-particles and the bosonic excitations are strongly intertwined. The doping-dependent temperature onset of the effect related to the fluence-dependence of the electron-boson coupling allowed to formulate the phase diagram of the Y-Bi2212 compound.

- The superconducting state shows a very peculiar optical response with respect to an external excitation by ultrashort laser pulses. The main effect of the excitation is to partially quench (working in a low fluence regime) the superconducting gap. On the contrary to what happens in BCS, conventional superconductors, in which the effect on the optical properties of the superconducting gap is limited in a spectral range very close to the gap itself, in strongly correlated copper oxide based superconductors, an effect at energies much higher than the gap energy is observed in the optical properties. It exists an interplay between high and low energy physics. Some high energy states, and the relevant optical transitions, are intimately related to the condensate formation. In contrast to what observed in the normal state and in the pseudogap phases, here the time-resolved optical signal, which shows a strong doping dependence, can be interpreted only by invoking a pump-induced modification of two Lorentz oscillators at 1.5 and 2 eV, which are present in the equilibrium dielectric function and associated to transitions between many-body Cu-O states. The superconducting signal exhibits a strong doping dependence, from which useful information about the superconductivity driving mechanism can be extracted. Close to the optimal doping level required to attain the highest T_c, a crossover from a direct kinetic energy gain in the underdoped side of the phase diagram to a BCS like kinetic energy loss in the overdoped side of the phase diagram is observed.

All the reported findings can be matched to provide a phase diagram enterely based on all-optical non-equilibrium evidences. The scenario proposed is that of a phase diagram governed by a quantum critical point at T=0, located inside the superconducting dome. A line entering the superconducting dome delimits the pseudogap behavior associated to a fluence-dependent electron-boson coupling. This evidence suggests the pseudogap is indeed a true phase of matter. The T^* line delimits, within the superconducting dome, two regions in which superconductivity is accompained by an opposite superconductivity-induced change for the carriers kinetic energy.

Bibliography

[1] S. Johnston et al. Evidence for forward scattering and coupling to acoustic phonon modes in high-T_c cuprate superconductors. arXiv:1101.1302v1 (2011).

[2] A. Abanov, A. V. Chubukov, and J. Schmalian. Fingerprints of spin mediated pairing in cuprates. *J. Electron Spectrosc. Relat. Phenom.*, 117:129, 2001.

[3] R. R. Alfano and S. L. Shapiro. Emission in the region 4000 to 7000 Ã via four-photon coupling in glass. *Phys. Rev. Lett.*, 24:584, 1970.

[4] R. R. Alfano and S. L. Shapiro. Observation of self-phase modulation and small-scale filaments in crystals and glasses. *Phys. Rev. Lett.*, 24:592, 1970.

[5] J. W. Allen and J. C. Mikkelsen. Optical properties of CrSb, MnSb, NiSb, NiAs. *Phys. Rev. B*, 15:2952, 1977.

[6] P. B. Allen. Electron-phonon effects in the infrared properties of metals. *Phys. Rev. B*, 3:305, 1971.

[7] P. B. Allen. Theory of thermal relaxation of electrons in metals. *Phys. Rev. Lett.*, 59:1460, 1987.

[8] P. B. Allen and R.C. Dynes. Transition temperature of strong-coupled superconductors reanalyzed. *Phys. Rev. B*, 12:905, 1975.

[9] P. W. Anderson. Is There Glue in Cuprate Superconductors? *Science*, 316:1705, 2007.

[10] S. I. Anisimov, B. L. Kapeliovich, and T. L. Perel'man. Electron emission from metal surfaces exposed to ultrashort laser pulses. *Zh. Eksp. Teor. Fiz.*, 66:776, 1974.

[11] N. W. Ashcroft and N. D. Mermin. *Solid state physics*. Harcourt College Publishers, Orlando FL, 1976.

[12] R. D. Averitt, G. Rodriguez, A. I. Lobad, J. W. L. Siders, S. L. Trugman, and A. J. Taylor. Nonequilibrium superconductivity and quasiparticle dynamics in $YBa_2Cu_3O_{7-\delta}$. *Phys. Rev. B*, 63:140502.

[13] J. Bardeen, L. N. Cooper, and J. R. Schrieffer. Microscopic Theory of Superconductivity. *Phys. Rev.*, 106:162, 1957.

[14] J. Bardeen, L. N. Cooper, and J. R. Schrieffer. Theory of Superconductivity. *Phys. Rev.*, 108:1175, 2008.

[15] D. N. Basov and T. Timusk. Electrodynamics of high-T_c superconductors. *Rev. Mod. Phys.*, 77:721, 2005.

[16] D.N. Basov, R.D. Averitt, D. van der Marel, M. Dressel, and K. Haule. Electrodynamics of Correlated Electron Materials. *Rev. Mod. Phys.*, 83:471, 2011.

[17] M. Bassi, P. Camagni, R. Rolli, G. Samoggia, F. Parmigiani, G. Dhalenne, and A. Revcolevschi. Optical absorption of $CuGeO_3$. *Phys. Rev. B*, 54.

[18] B. Batlogg, H. Y. Hwang, H. Takagi, R. J. Cava, H. L. Kao, and J. Kwo. Normal state phase diagram of $(La,Sr)_2CuO_4$ from charge and spin dynamics. *Physica C*, 130:235, 1994.

[19] M. Beck, M. Klammer, S. Lang, P. Leiderer, V. V. Kabanov, G. N. Goltsman, and J. Demsar. Energy-gap dynamics of superconducting NbN thin films studied by time-resolved terahertz spectroscopy. *ArXive*, 1102.

[20] M. Beck, H. Schafer, G. Klatt, J. Demsar, S. Winnerl, M. Helm, and T. Dekorsy. Impulsive terahertz radiation with high electric fields from an amplifier-driven large-area photoconductive antenna. *Opt. Express*, 18:9251, 2010.

[21] J. G. Bednorz and K. A. Müller. Possible high T_c superconductivity in the Ba-La-Cu-O system. *Z. Phys. B: Condens. Matter*, 64:189, 1986.

[22] A. V. Boris, N. N. Kovaleva, O. V. Dolgov, T. Holden, C. T. Lin, B. Keimer, and C. Bernhard. In-plane spectral weight shift of charge carriers in $yba_2cu_3o_{6.9}$. *Science*, 304:708, 2004.

[23] N. B. Brookes, G. Ghiringhelli, O. Tjernberg, L. H. Tjeng, T. Mizokawa, T. W. Li, and A. A. Menovsky. Detection of Zhang-Rice Singlets Using Spin-Polarized Photoemission. *Phys. Rev. Lett.*, 87:237003, 2001.

[24] S. D. Brorson, A. Kazeroonian, D. W. Face, T. K. Cheng, G. L. Doll, M. S. Dresselhaus, G. Dresselhaus, E. P. Ippen, T. Venkatesan, X. D.

Wu, and A. Inam. Femtosecond thermomodulation study of high-t$_c$ superconductors. *Solid State Commun.*, 74:1305, 1990.

[25] S. D. Brorson, A. Kazeroonian, J. S. Moodera, D. W. Face, T. K. Cheng, E. P. Ippen, M. S. Dresselhaus, and G. Dresselhaus. Femtosecond room-temperature measurement of the electron-phonon coupling constant γ in metallic superconductors. *Phys. Rev. Lett.*, 64:2172, 1990.

[26] F. Carbone, A. B. Kuzmenko, H. J. A. Molegraaf, E. van Heumen, V. Lukovac, F. Marsiglio, and D. van der Marel. Doping dependence of the redistribution of optical spectral weight in $Bi_2Sr_2CaCu_2O_{8+\delta}$. *Phys. Rev. B*, 74:064510, 2006.

[27] F. Carbonea, D.-S. Yanga, E. Giannini, and A. H. Zewail. Direct role of structural dynamics in electron-lattice coupling of superconducting cuprates. *Proc. Natl. Acad. Sci.*, 105:20161, 2008.

[28] J. P. Carbotte. Properties of boson-exchange superconductors. *Rev. Mod. Phys.*, 62:1027, 1990.

[29] A. Cavalleri, H. H. W. Chong, S. Fourmaux, T. E. Glover, P. A. Heimann, J. C. Kieffer, B. S. Mun, H. A. Padmore, and R. W. Schoenlein. Picosecond soft x-ray absorption measurement of the photoinduced insulator-to-metal transition in VO_2. *Phys. Rev. B*, 69:153106, 2004.

[30] A. Cavalleri, Th. Dekorsy, H. H. W. Chong, J. C. Kieffer, and R. W. Schoenlein. Evidence for a structurally-driven insulator-to-metal transition in VO_2: A view from the ultrafast timescale. *Phys. Rev. B*, 70:161102.

[31] A. Cavalleri, C. Toth, C. W. Siders, J. A. Squier, F. Raksi, P. Forget, and J. C. Kieffer. Femtosecond Structural Dynamics in VO_2 during an Ultrafast Solid-Solid Phase Transition. *Phys. Rev. Lett.*, 87:237401, 2001.

[32] Tsuei CC. *Phys. Rev. Lett.*, 73:593, 1994.

[33] S. Chakravarty, R. B. Laughlin, D. K. Morr, and C. Nayak. Hidden order in the cuprates. *Phys. Rev. B*, 63:094503, 2001.

[34] Han-Yong Choi, C. M. Varma, and Xingjiang Zhou. Superconductivity in the Cuprates: Deduction of Mechanism for D-Wave Pairing Through Analysis of ARPES. *ArXive*, 1110.

[35] A. V. Chubukov and J Schmalian. Superconductivity due to massless boson exchange in the strong-coupling limit. *Phys. Rev. B*, 72:174520, 2005.

[36] Ye Chuntang, Yang Jilian, Zhang Baisheng, Li Jizhou, Kang Jian, Jin Lan, Ding Yongfan, He Yusheng, Zhang Jincang, He Aisheng, and Xiang Jiong. Structure Refinement of $Bi_2Sr_{1.855}Ca_{1.145}Cu_2O_8$ from Neutron Data. *Chin. Phys. Lett.*, 8:521, 1991.

[37] F. Cilento, C. Giannetti, G. Ferrini, S. Dal Conte, T. Sala, G. Coslovich, M. Rini, A. Cavalleri, and F. Parmigiani. Ultrafast insulator-to-metal phase transition as a switch to measure the spectrogram of a supercontinuum light pulse. *Appl. Phys. Lett.*, 96:021102, 2010.

[38] S. Dal Conte. *Time-resolved optical spectroscopy on $Bi_2Sr_2Ca_{0.92}Y_{0.08}Cu_2O_{8+\delta}$*. PhD thesis, Universitá degli Studi di Pavia, March 2011.

[39] B. R. Cooper, H. Ehrenreich, and H. R. Philipp. Optical Properties of Noble Metals. II. *Phys. Rev.*, 138:494, 1965.

[40] Leon N. Cooper. Bound Electron Pairs in a Degenerate Fermi Gas. *Phys. Rev.*, 104:1189, 1956.

[41] R. Cortes, L. Rettig, Y. Yoshida, H. Eisaki, M. Wolf, and U. Bovensiepen. Momentum-Resolved Ultrafast Electron Dynamics in Superconducting $Bi_2Sr_2CaCu_2O_8$. *ArXive*, 1011.

[42] G. Coslovich, C. Giannetti, F. Cilento, S. Dal Conte, G. Ferrini, P. Galinetto, M. Greven, H. Eisaki, M. Raichle, R. Liang, A. Damascelli, and F. Parmigiani. Evidence for a photoinduced nonthermal superconducting-to-normal-state phase transition in overdoped $\mathrm{bi_2sr_2ca_{0.92}y_{0.08}cu_2o_{8+\delta}}$. *Phys. Rev. B*, 83:064519, 2011.

[43] M. F. Crommie and A. Zettl. Thermal-conductivity anisotropy of single-crystal $Bi_2Sr_2CaCu_2O_8$. *Phys. Rev. B*, 43:408, 1991.

[44] T. Cuk, D. H. Lu, X. J. Zhou, Z.-X. Shen, T. P. Devereaux, and N. Nagaosa. A review of electron-phonon coupling seen in the high-T_c superconductors by angle-resolved photoemission studies (ARPES). *Phys. Stat. Sol. b*, 242:11, 2005.

[45] Wollman DA. *Phys. Rev. Lett.*, 71:2134, 1993.

[46] E. Dagotto. Correlated electrons in high-temperature superconductors. *Rev. Mod. Phys.*, 66:763, 1994.

[47] T. Dahm, V. Hinkov, S. V. Borisenko, A. A. Kordyuk, V. B. Zabolotnyy, J. Fink, B. Buchner, D. J. Scalapino, W. Hanke, and B. Keimer. Strength of the Spin-Fluctuation-Mediated Pairing Interaction in a High-Temperature Superconductor. *ArXive*, 0812.

[48] T. Dahm, V. Hinkov, S. V. Borisenko, A.A. Kordyuk, V.B. Zabolotnyy, J. Fink, B. Büchner, D.J. Scalapino, W. Hanke, and B. Keimer. Strength of the spin-fluctuation-mediated pairing interaction in a high-temperature superconductor. *Nature Physics*, 5:217, 2009.

[49] A. Damascelli, Z. Hussain, and Z.-X. Shen. Angle-resolved photoemission studies of the cuprate superconductors. *Rev. Mod. Phys.*, 75:473, 2003.

[50] Johnston DC. *Phys. Rev. Lett.*, 62:957, 1989.

[51] L. de Medici, X. Wang, M. Capone, and A. J. Millis. Correlation strength, gaps, and particle-hole asymmetry in high-T_c cuprates: A dynamical mean field study of the three-band copper-oxide model. *Phys. Rev. B*, 77:014518, 2009.

[52] J. Demsar, R. A. Averitt, V. V. Kabanov, and D. Mihailovic. Comment on Photoinduced Changes of Reflectivity in Single Crystals of $YBa_2Cu_3O_{6.5}$ (Ortho II). *Phys. Rev. Lett.*, 91:169701, 2003.

[53] J. Demsar, B. Podobnik, V. V. Kabanov, T. Wolf, and D. Mihailovic. Superconducting Gap Δ_c, the Pseudogap Δ_p, and Pair Fluctuations above T_c in Overdoped $Y_{1-x}Ca_xBa_2Cu_3O_{7-\delta}$ from Femtosecond Time-Domain Spectroscopy. *Phys. Rev. Lett.*, 82:4918, 1999.

[54] J. Demsar, J. L. Sarrao, and A. J. Taylor. Dynamics of photoexcited quasiparticles in heavy electron compounds. *J. Phys.:Condens. Matter*, 18, 2006.

[55] G. Deutscher. *Coherence in High Temperature Superconductors.* World Scientific, 1995.

[56] T.P. Devereaux, T. Cuk, Z.-X. Shen, and N. Nagaosa. Anisotropic Electron-Phonon Interaction in the Cuprates. *Phys. Rev. Lett.*, 93:117004, 2004.

[57] A. L. Dobryakov, V. M. Farztdinov, Y. E. Lozovik, and V. S. Letokhov. Energy gap in the superconductor optical spectrum. *J. Am. Chem. Soc*, 105:309, 1994.

[58] P. Domachuk, N. A. Wolchover, M. Cronin-Golomb, A. Wang, A. K. George, C. M. B. Cordeiro, J. C. Knight, and F. G. Omenetto. Over 4000 nm Bandwidth of Mid-IR Supercontinuum Generation in sub-centimeter Segments of Highly Nonlinear Tellurite PCFs. *Opt. Express*, 16:7161, 2008.

[59] M. Dressel and G. Grunner. *Electrodynamics of solids: optical properties of electrons in matter.* Cambridge University Press, Cambridge, 2002.

[60] G. Dresselhaus and M. S. Dresselhaus. Interband transitions in superconductors. *Phys. Rev.*, 125:1212, 1962.

[61] J. M. Dudley, G. Genty, and S. Coen. Supercontinuum generation in photonic crystal fiber. *Rev. Mod. Phys.*, 78:1135, 2006.

[62] R. Dynes. . *Solid State Commun.*, 10:615, 1972.

[63] G. L. Eesley. Observation of Nonequilibrium Electron Heating in Copper. *Phys. Rev. Lett.*, 51:2140, 1983.

[64] G. L. Eesley. Generation of nonequilibrium electron and lattice temperatures in copper by picosecond laser pulses. *Phys. Rev. B*, 33:2144, 1986.

[65] H. Ehrenreich and H. R. Philipp. Optical Properties of Ag and Cu. *Phys. Rev.*, 128:1622, 1962.

[66] H. Ehrenreich, H. R. Philipp, and D. J. Olechna. Optical Properties and Fermi Surface of Nickel. *Phys. Rev.*, 131:2469, 1963.

[67] H. Ehrenreich, H. R. Philipp, and B. Segall. Optical Properties of Aluminum. *Phys. Rev.*, 132:1918, 1963.

[68] H. Eisaki, N. Kaneko, D. L. Feng, A. Damascelli, P. K. Mang, K. M. Shen, Z.-X. Shen, and M. Greven. Effect of chemical inhomogeneity in bismuth-based copper oxide superconductors. *Phys. Rev. B*, 69:064512, 2004.

[69] G. M. Eliashberg. *Sov. Phys. JEPT*, 11:696, 1960.

[70] V. J. Emery and S. A. Kivelson. Importance of phase fluctuation in superconductors with small superfluid density. *Nature*, 374:4347, 1995.

[71] G. Deutscher et al. Kinetic energy change with doping upon superfluid condensation in high-temperature superconductors. *Phys. Rev. B*, 72:092504, 2005.

[72] N. B. Brookes et al. A determination of the pairing interaction in the high Tc cuprate superconductor $Tl_2Ba_2CaCu_2O_8$ (Tl2212). *Physica C*, 40:460, 2007.

[73] B. Fauque, Y. Sidis, V. Hinkov, S. Pailhes, C. T. Lin2, X. Chaud, and P. Bourges. Magnetic order in the pseudogap phase of high-Tc superconductors. *Phys. Rev. Lett.*, 96:197001, 2006.

[74] D. Fournier, G. Levy, Y. Pennec, J.L. McChesney, A. Bostwick, E. Rotenberg, R. Liang, W.N. Hardy, D.A. Bonn, I.S. Elfimov, and A. Damascelli. Loss of nodal quasiparticle integrity in underdoped $\mathrm{YBa_2Cu_3O_{6+x}}$. *Nature Physics*, 6:905, 2010.

[75] C Gadermaier, A Alexandrov, V Kabanov, P Kusar, T Mertelj, X Yao, C Manzoni, D Brida, G Cerullo, and D Mihailovic. Electron-Phonon Coupling in High-Temperature Cuprate Superconductors Determined from Electron Relaxation Rates. *Phys. Rev. Lett.*, 105(25), December 2010.

[76] C Gadermaier, A Alexandrov, V Kabanov, P Kusar, T Mertelj, X Yao, C Manzoni, D Brida, G Cerullo, and D Mihailovic. Electron-Phonon Coupling in High-Temperature Cuprate Superconductors Determined from Electron Relaxation Rates. Supplementary material. *Phys. Rev. Lett.*, 105(25), December 2010.

[77] N. Gedik, P. Blake, R. C. Spitzer, J. Orenstein, R. Liang, D. A. Bonn, and W. N. Hardy. Single-quasiparticle stability and quasiparticle-pair decay in $YBa_2Cu_3O_{6.5}$. *Phys. Rev. B*, 70:014504, 2004.

[78] N. Gedik, M. Langner, J. Orenstein, S. Ono, Y. Abe, and Y. Ando. Abrupt Transition in Quasiparticle Dynamics at Optimal Doping in a Cuprate Superconductor System. *Phys. Rev. Lett.*, 95:117005, 2005.

[79] N. Gedik, J. Orenstein, R. Liang, D. A. Bonn, and W. N. Hardy. Gedik *et al.* Reply:. *Phys. Rev. Lett.*, 91:169702, 2003.

[80] C. Giannetti, F. Cilento, S. Dal Conte, G. Coslovich, G. Ferrini, H. Molegraaf, M. Raichle, R. Liang, H. Eisaki, M. Greven, A. Damascelli, D. van der Marel, and F. Parmigiani. Revealing the high-energy electronic excitations underlying the onset of high-temperature superconductivity in cuprates. *Nature Communications*, 3:253, 2011.

[81] C. Giannetti, G. Coslovich, F. Cilento, G. Ferrini, H. Eisaki, N. Kaneko, M. Greven, and F. Parmigiani. Discontinuity of the ultrafast electronic response of underdoped superconducting $Bi_2Sr_2CaCu_2O_{8+\delta}$ strongly excited by ultrashort light pulses. *Phys. Rev. B*, 79:224502, 2009.

[82] C. Giannetti, G. Zgrablic, C. Consani, A. Crepaldi, D. Nardi, G. Ferrini, G. Dhalenne, A. Revcolevschi, and F. Parmigiani. Disentangling thermal and nonthermal excited states in a charge-transfer insulator by time- and frequency-resolved pump-probe spectroscopy. *Phys. Rev. B*, 80:235129, 2009.

[83] Alloul H. *Phys. Rev. Lett.*, 63:1700, 1989.

[84] E. Hecht. *Optics.* Addison Wesley, 2002.

[85] J. E. Hirsch and F. Marsiglio. Superconducting state in an oxygen hole metal. *Phys. Rev. B*, 39:11515, 1989.

[86] J. E. Hirsch and F. Marsiglio. Optical sum rule violation, superfluid weight, and condensation energy in the cuprates. *Phys. Rev. B*, 62:15131, 2000.

[87] J. Hohlfeld, S.-S. Wellershoff, J. Güdde, U. Conrad, V. Jähnke, and E. Matthias. Electron and lattice dynamics following optical excitation of metals. *Chem. Phys.*, 251:237, 2000.

[88] M. J. Holcomb, J. P. Collman, and W. A. Little. Optical evidence of an electronic contribution to the pairing interaction in superconducting $Tl_2Ba_2Ca_2Cu_3O_{10}. Phys. Rev. Lett., 73:2360, 1994.$

[89] S. Hüfner, M. A. Hossain, A. Damascelli, and G. A. Sawatzky. Two gaps make a high-temperature superconductor? *Rep. Prog. Phys*, 71:062501, 2008.

[90] J. Hwang. Electron-boson spectral density function of underdoped $Bi_2Sr_2CaCu_2O_8$ and $YBa_2Cu_3O_{6.50}$. *Phys. Rev. B*, 83:014507, 2011.

[91] J. Hwang, T. Timusk, and G. D. Gu. High-transition-temperature superconductivity in the absence of the magnetic-resonance mode. *Nature*, 427:714, 2007.

[92] J. Hwang, T. Timusk, E. Schachinger, and J. P. Carbotte. Evolution of the bosonic spectral density of the high-temperature superconductor $\mathrm{bi_2sr_2cacu_2o_{8+\delta}}$. *Phys. Rev. B*, 75:144508, 2007.

[93] W. Rudolph J. C. Diels. *Ultrashort Laser Pulse Phenomena.* Academic Press, 1996.

[94] A. Junod, K.-Q. Wang, T. Tsukamoto, G. Triscone, B. Revaz, E. Walker, and J. Muller. Specific heat up to 14 tesla and magnetization of a $Bi_2Sr_2CaCu_2O_8$ single crystal. Thermodynamics of a 2D superconductor. *Physica C*, 229:209, 1994.

[95] A. Junod, K.-Q. Wang, T. Tsukamoto, G. Triscone, B. Revaz, E. Walker, and J. Muller. Non-Fermi-liquid states and pairing instability of a general model of copper oxide metals. *Phys. Rev. B*, 55:14554, 1997.

[96] V. V. Kabanov and A. S. Alexandrov. Electron relaxation in metals: Theory and exact analytical solutions. *Phys. Rev. B*, 78:174514, 2008.

[97] V. V. Kabanov, J. Demsar, B. Podobnik, and D. Mihailovic. Quasiparticle relaxation dynamics in superconductors with different gap structures: Theory and experiments on $\mathrm{YBa_2Cu_3O_{7-\delta}}$. *Phys. Rev. B*, 59:1497, 1999.

[98] V. V. Kabanov and J. Demsarand D. Mihailovic. Kinetics of a Superconductor Excited with a Femtosecond Optical Pulse. *Phys. Rev. Lett.*, 95:147002, 2005.

[99] R. A. Kaindl, M. A. Carnahan, D. S. Chemla, S. Oh, and J. N. Eckstein. Dynamics of Cooper pair formation in $Bi_2Sr_2CaCu_2O_{8+\delta}$. *Phys. Rev. B*, 72:060510, 2005.

[100] R. A. Kaindl, F. Eickemeyer, M. Woerner, and T. Elsaesser. Broadband phase-matched difference frequency mixing of femtosecond pulses in GaSe: Experiment and theory. *Appl. Phys. Lett.*, 75:1060, 1999.

[101] R. A. Kaindl, D. C. Smith, M. Joschko, M. P. Hasselbeck, M. Woerner, and T. Elsaesser. Femtosecond infrared pulses tunable from 9 to 18 μm at an 88-MHz repetition rate. *Opt. Lett.*, 23:861, 1998.

[102] R. A. Kaindl, M. Woerner, T. Elsaesser, D. C. Smith, J. F. Ryan, G. A. Farnan, M. P. McCurry, and D. G. Walmsley. Ultrafast mid-infrared response of $YBa_2Cu_3O_{7-\delta}$. *Science*, 287:470, 2000.

[103] Yoichi Kamihara, Hidenori Hiramatsu, Masahiro Hirano, Ryuto Kawamura, Hiroshi Yanagi, Toshio Kamiya, and Hideo Hosono. Iron-Based Layered Superconductor:â LaOFeP. *J. Am. Chem. Soc*, 128:10012, 2006.

[104] A. Kaminski, H. M. Fretwell, M. R. Norman, M. Randeria, S. Rosenkranz, U. Chatterjee, J. C. Campuzano, J. Mesot, T. Sato, T. Takahashi, T. Terashima, M. Takano, K. Kadowaki, Z. Z. Li, and H. Raffy. Momentum anisotropy of the scattering rate in cuprate superconductors. *Chem. Phys.*, 71:014517, 2005.

[105] H. J. Kaufmann, E. G. Maksimov, and E. K. H. Salje. Electron-Phonon Interaction and Optical Spectra of Metals. *Journal of Superconductivity*, 11:755, 1998.

[106] Jae Hun Kim, Meng-Ku Chen, Chia-En Yang, Jon Lee, Stuart (Shizhuo) Yin, Paul Ruffin, Eugene Edwards, Christina Brantley, and Claire Luo. Broadband IR supercontinuum generation using single crystal sapphire fibers. *Opt. Express*, 16:4085, 2008.

[107] J. C. Knight. Photonic crystal fibres. *Nature*, 424:847, 2003.

[108] N.N. Kovaleva, A.V. Boris, T. Holden, C. Ulrich, B. Liang, C.T. Lin, B. Keimer, C. Bernhard, J.L. Tallon, D. Munzar, and A.M. Stoneham. c-axis lattice dynamics in Bi-based cuprate superconductors. *Phys. Rev. B*, 69:054511, 2004.

[109] Todd D. Krauss and Frank W. Wise. Femtosecond measurement of nonlinear absorption and refraction in CdS, ZnSe, and ZnS. *Appl. Phys. Lett.*, 65:1739, 1994.

[110] V.Z. Kresin and S.A. Wolf. Colloquium: Electron-lattice interaction and its impact on high T_c superconductivity. *Rev. Mod. Phys.*, 81:481, 2009.

[111] P. Kusar, V.V. Kabanov, J. Demsar, T. Mertelj, S. Sugai, and D. Mihailovic. Controlled Vaporization of the Superconducting Condensate in Cuprate Superconductors by Femtosecond Photoexcitation. *Phys. Rev. Lett.*, 101:227001, 2008.

[112] A. B. Kuzmenko, H. J. A. Molegraaf, F. Carbone, and D. van der Marel. Temperature-modulation analysis of superconductivity-induced transfer of in-plane spectral weight in $bi_2sr_2cacu_2o_8$. *Phys. Rev. B*, 72:144503, 2005.

[113] A. Lanzara, P. V. Bogdanov, X. J. Zhou, S. A. Kellar, D. L. Feng, E. D. Lu, T. Yoshida, H. Eisaki, A. Fujimori, K. Kishio, J.-I. Shimoyama, T. Noda, S. Uchida, Z. Hussain, and Z.-X. Shen. Evidence for ubiquitous strong electron-phonon coupling in high-temperature superconductors. *Nature*, 412:510, 2001.

[114] Jinho Lee, K. Fujita, K. McElroy, J. A. Slezak, M. Wang, Y. Aiura, H. Bando, M. Ishikado, T. Masui, J.-X. Zhu, A. V. Balatsky, H. Eisaki, S. Uchida, and J. C. Davis. Interplay of electron-lattice interactions and superconductivity in $\mathrm{Bi_2Sr_2CaCu_2O_{8+\delta}}$. *Nature*, 442:546, 2006.

[115] Y. Li, V. Baledent, N. Barisic, Y. Cho, B. Fauque, Y. Sidis, G. Yu, X. Zhao, P. Bourges, and M. Greven. Unusualmagnetic order in the pseudogap region of the superconductor $HgBa_2CuO_{4+\delta}$. *Nature*, 455:372, 2008.

[116] Y. Li, V. Balédent, G.Yu, N. Barišić, K. Hradil, R. A. Mole, Y. Sidis, P. Steffens, X. Zhao, P. Bourges, and M. Greven. Hidden magnetic excitation in the pseudogap phase of a high-T_c superconductor. *Nature*, 468:283, 2010.

[117] Y. H. Liu, Y. Toda, K. Shimatake, N. Momono, and M. Odaand M. Ido. Direct Observation of the Coexistence of the Pseudogap and Superconducting Quasiparticles in $\mathrm{Bi_2Sr_2CaCu_2O_{8+y}}$ by Time-Resolved Optical Spectroscopy. *Phys. Rev. Lett.*, 101:137003, 2008.

[118] J. W. Loram, J. L. Luo, J. R. Cooper, W. Y. Liang, and J. L. Tallon. The Condensation Energy and Pseudogap Energy Scale of Bi2212 from the Electronic Specific Heat. *J. Phys. Chem.*, 62:59, 2001.

[119] J. W. Loram, K. A. Mirza, J. R. Cooper, and J. L. Tallon. Specific heat evidence on the normal state pseudogap. *J. Phys. Chem. Sol.*, 59:2091, 1998.

[120] E. G. Maksimov. High-temperature superconductivity: the current state. *Physics Uspekhi*, 43:965, 2000.

[121] E. G. Maksimov, I. I. Mazin, S. N. Rashkeev, and Yu A. Uspenski. First-principles calculations of the optical properties of metals. *J. Phys. F: Met. Phys.*, 18:833, 1988.

[122] F. Marsiglio. Inversion of Optical Conductivity Data in Metals. *J. Supercond*, 12:163, 1999.

[123] F. Marsiglio. Optical sum rule anomalies in the high-Tc Cuprates. *J. Supercond. Nov. Magn.*, 22:269, 2009.

[124] F. Marsiglio and J. E. Hirsch. Hole superconductivity and the high-T_c oxides. *Phys. Rev. B*, 41:6435, 1990.

[125] W. L. McMillan. Transition Temperature of Strong-Coupled Superconductors. *Phys. Rev.*, 167:331, 1968.

[126] A. Migdal. *Sov. Phys. JEPT*, 7:996, 1957.

[127] A.J. Millis, H. Monien, and D. Pines. Phenomenological model of nuclear relaxation in the normal state of $YBa_2Cu_3O_7$. *Phys. Rev. B*, 842:167, 1990.

[128] A.J. Millis, S. Sachdev, and C. Varma. Inelastic scattering and pair breaking in anisotropic and isotropic supercondnctors. *Phys. Rev. B*, 37:4975, 1988.

[129] A.S. Mishchenko and N. Nagaosa. Electron-Phonon Coupling and a Polaron in the t-J Model: From theWeak to the Strong Coupling Regime. *Phys. Rev. Lett.*, 93:036402, 2004.

[130] N. Miyakawa, P. Guptasarma, J. F. Zasadzinski, D. G. Hinksand, and K. E. Gray. Strong dependence of the superconducting gap on oxygen doping from tunneling measurements on $Bi_2Sr_2CaCu_2O_{8+\delta}$. *Phys. Rev. Lett.*, 80:157, 1998.

[131] H. J. A. Molegraaf, C. Presura, D. van der Marel, P. H. Kes, and M. Li. Superconductivity-Induced Transfer of In-Plane Spectral Weight in $\mathrm{Bi_2Sr_2CaCu_2O_{8+\delta}}$. *Science*, 295:2239, 2002.

[132] H. Mori. . *Prog. Theor. Phys.*, 34:399, 1965.

[133] N. Nagaosa and P. A. Lee. Ginzburg-Landau theory of the spin-charge-separated system. *Phys. Rev. B*, 45:966, 1992.

[134] Y. Nambu. Quasi-Particles and Gauge Invariance in the Theory of Superconductivity. *Phys. Rev.*, 117:648, 1960.

[135] Mott NF. *Proc. Phys. Soc. (London) A*, 62:416, 1949.

[136] E. J. Nicol and J. P. Carbotte. Comparison of s- and d-wave gap symmetry in nonequilibrium superconductivity. *Phys. Rev. B*, 67:214506, 2003.

[137] M. R. Norman, , D. Pines, and C. Kallin. The pseudogap: friend or foe of high T_c? *Adv. Phys*, 54:715, 2005.

[138] M. R. Norman, A. V. Chubukov, E. van Heumen, A. B. Kuzmenko, and D. van der Marel. Optical integral in the cuprates and the question of sum-rule violation. *Phys. Rev. B*, 76:220509.

[139] M. R. Norman and C. Pepin. Quasiparticle formation and optical sum rule violation in cuprate superconductors. *Phys. Rev. B*, 66:100506.

[140] M. R. Norman and C. Pepin. The Electronic Nature of High Temperature Cuprate Superconductors. *Rep. Prog. Phys*, 66:1547, 2003.

[141] M.R. Norman and A.V. Chubukov. High-frequency behavior of the infrared conductivity of cuprates. *Phys. Rev. B*, 73:R140501, 2006.

[142] H. Kamerlingh Onnes. The disappearance of the resistivity of Mercury. *Comm. Leiden.*

[143] C. S. Owen and D. J. Scalapino. Quantum critical behaviour in a high-T_c superconductor. *Phys. Rev. Lett.*, 28:1559, 1972.

[144] A. Pashkin, M. Porer, M. Beyer, K. W. Kim, A. Dubroka, C. Bernhard, X. Yao, Y. Dagan, R. Hackl, A. Erb, J. Demsar, R. Huber, and A. Leitenstorfer. Femtosecond Response of Quasiparticles and Phonons in Superconducting $YBa_2Cu_3O_{7-\delta}$ Studied by Wideband Terahertz Spectroscopy. *Phys. Rev. Lett.*, 105:067001, 2011.

[145] L. Perfetti, P. A. Loukakos, M. Lisowski, U. Bovensiepen, H. Eisaki, and M. Wolf. Ultrafast Electron Relaxation in Superconducting $\mathrm{Bi_2Sr_2CaCu_2O_{8+\delta}}$ by Time-Resolved Photoelectron Spectroscopy. *Phys. Rev. Lett.*, 99:197001, 2007.

[146] P. Phillips. Identifying the propagating charge modes in doped Mott insulators. *Rev. Mod. Phys.*, 82:1719, 2010.

[147] W. E. Pickett. . *Rev. Mod. Phys.*, 61:433, 1989.

[148] M. Presland, J. Tallon, R. Buckley, R. Liu, and N. Flower. General trends in oxygen stoichiometry effects on T_c in Bi and Tl superconductors. *Physica C*, 176:95, 1991.

[149] A. V. Puchkov, P. Fournier, D. N. Basov, T. Timusk, A. Kapitulnik, and N. N. Kolesnikov. Evolution of the pseudogap state of high-tc superconductors with doping. *Phys. Rev. Lett.*, 77:3212, 1996.

[150] Anderson PW. *Solid State Phys.*, 14:99, 1963.

[151] Anderson PW. *Science*, 235:1196, 1987.

[152] J. K. Ranka, R. S. Windeler, and A. J. Stentz. Visible continuum generation in air-silica microstructure optical fibers with anomalous dispersion at 800 nm. *Opt. Lett.*, 25:25, 2000.

[153] Ch. Renner, B. Revaz, J.-Y. Genoud, K. Kadowaki, and Ã. Fischer. Pseudogap Precursor of the Superconducting Gap in Under- and Overdoped $Bi_2Sr_2CaCu_2O_8$. *Phys. Rev. Lett.*, 80:149, 1998.

[154] M. Rini, Z. Hao, R. W. Schoenlein, C. Giannetti, F. Parmigiani, S. Fourmaux, J. C. Kieffer, A. Fujimori, M. Onoda, S. Wall, and A. Cavalleri. Optical switching in VO_2 films by below-gap excitation. *Appl. Phys. Lett.*, 92:181904, 2008.

[155] P. Romaniello, P. L. de Boeij, F. Carbone, and D. van der Marel. Optical properties of bcc transition metals in the range 0â40 eV. *Phys. Rev. B*, 73:075115, 2006.

[156] A. Rothwarf and B. N. Taylor. Measurements of recombination lifetimes in superconductors. *Phys. Rev. Lett.*, 19:27, 1967.

[157] M. Rubhausen, A. Gozar, M. V. Klein, P. Guptasarma, and D. G. Hinks. Superconductivity-induced optical changes for energies of 100Δ in the cuprates. *Phys. Rev. B*, 63:224514, 2001.

[158] J. C. Russell. Photonic crystal fibers. *Science*, 299:358, 2003.

[159] G Sangiovanni, O Gunnarsson, E Koch, C Castellani, and M Capone. Electron-Phonon Interaction and Antiferromagnetic Correlations. *Phys. Rev. Lett.*, 97(4), July 2006.

[160] A. F. Santander-Syro, R. P. S. M. Lobo, N. Bontemps, W. Lopera, D. Giratá, Z. Konstantinovic, Z. Z. Li, and H. Raffy. In-plane electrodynamics of the superconductivity in $Bi_2Sr_2CaCu_2O_8$: Energy scales and spectral weight distribution. *Phys. Rev. B*, 70:134504, 2004.

[161] G. A. Sawatzky and J. W. Allen. . *Phys. Rev. Lett.*, 53:2339, 1984.

[162] D. J. Scalapino, E. Loh, and J. E. Hirsch. d-wave pairing near a spin-density-wave instability. *Phys. Rev. B*, 34:8190, 1986.

[163] R. W. Schoenlein, W. Z. Lin, J. G. Fujimotor, and G. L. Eesley. Femtosecond Studies of Nonequilibrium Electronic Processes in Metals. *Phys. Rev. Lett.*, 58:1680, 1987.

[164] G. P. Segre, N. Gedik, J. Orenstein, D. A. Bonn, R. Liang, and W. N. Hardy. Photoinduced Changes of Reflectivity in Single Crystals of $YBa_2Cu_3O_{6.5}$ (Ortho II). *Phys. Rev. Lett.*, 82:3054, 2002.

[165] C. V. Shank, R. Yen, and C. Hirlimann. Time-Resolved Reflectivity Measurements of Femtosecond-Optical-Pulse-Induced Phase Transitions in Silicon. *Phys. Rev. Lett.*, 50:454, 1983.

[166] S. G. Sharapov and J. P. Carbotte. Effects of energy dependence in the quasiparticle density of states on far-infrared absorption in the pseudogap state. *Phys. Rev. B*, 72:134506, 2005.

[167] S.V. Shulga, O. V. Dolgov, and E. G. Maksimov. Electronic states and optical spectra of HTSC with electron-phonon coupling. *Physica C*, 178:266, 1991.

[168] L. Stojchevska, P. Kusar, T. Mertelj, V. V. Kabanov, Y. Toda, X. Yao, and D. Mihailovic. Mechanisms of nonthermal destruction of the superconducting state and melting of the charge-density-wave state by femtosecond laser pulses. *ArXive*, 1109.

[169] S.Wall, D. Brida, S. R. Clark, H. P. Ehrke, D. Jaksch, A. Ardavan, S. Bonora, H. Uemura, Y. Takahashi, T. Hasegawa, H. Okamoto, G. Cerullo, and A. Cavalleri. Quantum interference between charge excitation paths in a solid-state Mott insulator. *Nature Physics*, 7:114, 2011.

[170] M. Le Tacon, G. Ghiringhelli, J. Chaloupka, M. Moretti Sala, V. Hinkov, M.W. Haverkort, M. Minola, M. Bakr, K. J. Zhou, S. Blanco-Canosa, C. Monney, Y. T. Song, G. L. Sun, C. T. Lin, G. M. De Luca, M. Salluzzo, G. Khaliullin, T. Schmitt, L. Braicovich, and B. Keimer. Intense paramagnon excitations in a large family of high-temperature superconductors. *Nature Physics*, 7:725, 2011.

[171] Louis Taillefer. Scattering and Pairing in Cuprate Superconductors. *Annu. Rev. Condens. Matter Phys.*, 1:51, 2010.

[172] H. J. Tao, F. Lu, and E. J. Wolf. Observation of pseudogap in $Bi_2Sr_2CaCu_2O_{8+\delta}$ single crystals with electron tunneling spectroscopy. *Physica C*, 282:1507, 1997.

[173] T. Timusk and B. Statt. The pseudogap in high-temperature superconductors: an experimental survey. *Rep. Prog. Phys*, 62:61, 1999.

[174] T. Timusk and D. B. Tanner. *Physical Properties of High Temperature Superconductors I.* World Scientific, Singapore, 1989.

[175] M. Tinkham. *Introduction to superconductivity.* McGraw-Hill, New York, 1975.

[176] R. Trebino. *Frequency-Resolved Optical Gating: The Measurement of Ultrashort Laser Pulses.* Springer, New York, 2002.

[177] T. Valla, A. V. Fedorov, J. Lee, J. C. Davis, and G. D. Gu. The ground state of the pseudogap in cuprate superconductors. *Science*, 314:1914, 2006.

[178] D. van der Marel, H. J. A. Molegraaf, J. Zaanen, Z. Nussinov, F. Carbone, A. Damascelli, H. Eisaki, M. Greven, P. H. Kes, and M. Li. Quantum critical behaviour in a high-T$_c$ superconductor. *Nature*, 425:271, 2003.

[179] E. van Heumen, E. Muhlethaler, A. B. Kuzmenko, H. Eisaki, W. Meevasana, M. Greven, and D. van der Marel. Optical determination of the relation between the electron-boson coupling function and the critical temperature in high-T$_c$ cuprates. *Phys. Rev. B*, 79:184512, 2009.

[180] C. Varma. Mind the pseudogap. *Nature*.

[181] C. M. Varma. Pseudogap Phase and the Quantum-Critical Point in Copper-Oxide Metals. *Phys. Rev. Lett.*, 83:3538, 1999.

[182] C.M. Varma. Theory of the pseudogap state of the cuprates. *Phys. Rev. B*, 73:155113, 2006.

[183] L. Vidmar, J. Bonca, T. Tohyama, and S. Maekawa. Quantum Dynamics of a Driven Correlated System Coupled to Phonons. *Phys. Rev. Lett.*, 107:246404, 2011.

[184] D. Wegkamp, D. Brida, S. Bonora, G. Cerullo, J. Stahler, M. Wolf, and S. Wall. Phase retrieval and compression of low-power white-light pulses. *Appl. Phys. Lett.*, 99:101101, 2011.

[185] F. Wooten. *Optical properties of solids.* Academic Press, New-York, 1972.

[186] Warren WW. *Phys. Rev. Lett.*, 62:1193, 1989.

[187] G. Yu, E. M. Motoyama, and M. Greven. A universal relationship between magnetic resonance and superconducting gap in unconventional superconductors. *Nature Physics*, 5:873, 2009.

[188] F.C. Zhang and T. Rice. Effective Hamiltonian for the superconducting Cu oxides. *Phys. Rev. B*, 37:3759, 1988.

List of publications

- C. Giannetti, F. Cilento, S. Dal Conte, G. Coslovich, G. Ferrini, H. Molegraaf, M. Raichle, R. Liang, H. Eisaki, M. Greven, A. Damascelli, D. van der Marel, and F. Parmigiani
  Revealing the high-energy electronic excitations underlying the onset of high-temperature superconductivity in cuprates
  Nature Communications **2**, 353 (2011) and http://arxiv.org/abs/1105.2508

- G. Coslovich, C. Giannetti, F. Cilento, S. Dal Conte, G. Ferrini, P. Galinetto, M. Greven, H. Eisaki, M. Raichle, R. Liang, A. Damascelli, and F. Parmigiani
  Evidence for a photoinduced nonthermal superconducting-to-normal-state phase transition in overdoped Bi2Sr2Ca0.92Y0.08Cu2O8+d by ultrashort laser pulses
  Phys. Rev. B **83**, 052907 (2011) and http://arxiv.org/abs/1005.4320

- G. Galimberti, S. Pagliara, S. Ponzoni, S. Dal Conte, F. Cilento, G. Ferrini, S. Hofmann, M. Arshad, C. Cepek, and F. Parmigiani
  The photoinduced charge transfer mechanism in aligned and unaligned carbon nanotubes
  Carbon **49**, 5246 (2011)

- F. Cilento, C. Giannetti, G. Ferrini, S. Dal Conte, T. Sala, G. Coslovich, M. Rini, A. Cavalleri, and F. Parmigiani
  Ultrafast insulator-to-metal phase transition as a switch to measure the spectrogram of a supercontinuum light pulse
  Appl. Phys. Lett. **96**, 021102 (2010) and http://arxiv.org/abs/0910.3785

- G. Coslovich, C. Giannetti, F. Cilento, G. Ferrini, and F. Parmigiani
  Quasi-particles dynamics in underdoped Bi2212 under strong optical perturbation
  AIP Conference Proceedings **1162**, pp. 177-185 (2009)

- C. Giannetti, G. Coslovich, F. Cilento, G. Ferrini, H. Eisaki, N. Kaneko, M. Greven, and F. Parmigiani

Discontinuity of the ultrafast electronic response of underdoped superconducting Bi2 Sr2CaCu2O8+d strongly excited by ultrashort light pulses
Phys. Rev. B **79**, 224502 (2009) and http://arxiv.org/abs/0804.4822
This paper was selected for the Virtual Journal of Applications of Superconductivity.
This paper was selected for the Virtual Journal of Ultrafast Science.

- C. Giannetti, B. Revaz, F. Banfi, M. Montagnese, G. Ferrini, F. Cilento, S. Maccalli, P. Vavassori, G. Oliviero, E. Bontempi, L.E. Depero, V. Metlushko, and F. Parmigiani
  Thermo-mechanical behavior of surface acoustic waves in ordered arrays of nanodisks studied by near infrared pump-probe diffraction experiments
  Phys. Rev. B **76**, 125413 (2007) and http://arxiv.org/abs/cond-mat/0701666
  This paper was selected for the Virtual Journal of Nanoscale Science Technology.
  This paper was selected for the Virtual Journal of Ultrafast Science.

Submitted or In preparation

- S. Dal Conte, C. Giannetti, G. Coslovich, F. Cilento, D. Bossini, T. Abebaw, F. Banfi, G. Ferrini, H. Eisaki, M. Greven, A. Damascelli, D. van der Marel, and F. Parmigiani
  Disentangling the electronic and phononic glue in a high-Tc superconductor
  Accepted for Publication on Science (February 2012)

- G. Coslovich, C. Giannetti, F. Cilento, S. Dal Conte, G. Ferrini, M. Raichle, R. Liang, A. Damascelli, and F. Parmigiani
  The relation between pseudogap and superconductivity: Causality or Casualty?

- F. Cilento, C. Giannetti, S. Dal Conte, G. Coslovich, A. Damascelli, and F. Parmigiani
  Pseudogap Phase: temperature dependent glue function

- F. Cilento, C. Giannetti, S. Dal Conte, G. Coslovich, A. Damascelli, and F. Parmigiani
  Non-equilibrium phase diagram of Bi2212 cuprate superconductors revealed by ultrafast optical spectroscopy

Ringraziamenti

I want to end this work with some acknowledgments. First of all, I want to thank my supervisor, Prof. Fulvio Parmigiani, who stimulated and made possible this project. I thank all the people working in the T-ReX Group in Trieste, and in the Ultrafast Group in Brescia. A special thank to Claudio Giannetti, who constitutes a reference for me since many years. He thougth and supervised this complex research project with enthusiasm, professionality and patience, coordinating a team of young researchers. I want in particular to thank Stefano dal Conte and Giacomo Coslovich, as component of this team. With them I spent a significative and pleasant part of my PhD. The amount of data and models presented in this work are also the result of their scientific efforts. Thanks also to Prof. Andrea Damascelli for providing samples, and to Prof. Dirk van der Marel for providing the static optical data.